Geophysical constraints on the nature of geological domains of continental rifted margins: examples from the West Iberia margin and Ligurian Basin

Irene Merino Perez

Geophysical constraints on the nature of geological domains of continental rifted margins: examples from the West Iberia margin and Ligurian Basin

Memòria de tesis doctoral presentada per

Irene Merino Perez

Per optar al Grau de Doctor per la Universitat de Barcelona

Aquesta memòria s'ha dut a terme dins del Programa de Doctorat de Ciències de la Terra de la Universitat de Barcelona sota la direcció del Dr. César Rodríguez Ranero i el Dr. Valentí Sallarès Casas i ha estat tutelada pel Dr. Juanjo Ledo.

Barcelona, maig de 2021

Dinanzi a me non fuor cose create
se non etterne, e io etterno duro.
Lasciate ogne speranza, voi ch'intrate'.

– Dante Alighieri, *Inferno*

Agraïments / Acknowledgements

En primer lloc, vull agrair als meus directors de tesi la confiança depositada en mi des del primer fins l'últim dia. Vull agrair-vos el temps i dedicació que heu invertit per a que aquest projecte tirés endavant. Gràcies per haver-me donat l'oportunitat de conèixer el món complex que és la ciència i transmetrem la vostra passió per ella.

Un agraïment especial a en Manel, qui ha estat per a mi com un guia més. Per la seva dedicació, però sobretot per la seva paciència a l'hora d'ensenyar-me els misteris de la modelització (i molt més!).

A l'Alci per iniciar-me al processat sísmic i no dubtar en donar-me un cop de mà en qualsevol moment. Agrair també a tota la gent (científics, tècnics, tripulació, ..) que va formar part de les campanyes FRAME. Per fer més amenes les guàrdies i les estones d'esbarjo. Tots ells han fet que cadascuna de les experiències viscudes a bord hagin estat inoblidables.

A la meva còmplice d'experiència, gràcies Cristina per haver-hi estat sempre, el teu recolzament ha estat essencial per a mi. Perquè vinguin nous projectes i bons moments juntes. A les *Wirlies*: Marta, Estela i Clàudia. Gràcies per tots els moments compartits física i telemàticament. La vostra presència, els consells i les converses compartides han fet que m'endugui molts bons records d'aquests anys.

A tots els companys del ICM, als que hi són i els que han pres camins diferents, gràcies. En particular al Davide, *gracias por las risas, los buenos momentos por California, en los congresos, y también por las conversaciones menos optimistas*. A la Sonia per la seva paciència i per les converses al despatx.

Però sobretot gràcies a la meva família, als meus pares i el meu germà Manel. Vull agrair-vos el vostre suport incondicional des del principi en totes les decisions que he anat prenent, per estimar i apreciar la geologia i per l'interès que sempre heu mostrat envers el que faig. Moltes gràcies pel recolzament que m'heu donat, aquesta tesi ha estat possible també gràcies a vosaltres! *A mi yaya Encarna por enseñarme las cosas más importantes, a las que cada vez tengo más en consideración.*

Finalment, a en Giulio. *Gracias por tu paciencia y por tu ayuda. Estas palabras se quedarían siempre cortas.*

Gràcies a tots els que d'una manera o altra han compartit aquest camí amb mi.

Funding

The author of this thesis has benefited from a four-year “Formación de Personal Investigador” (FPI) fellowship (reference BES-2016-077786) in the framework of the FRAME project (reference CTM2015-71766-R), funded by the “Ministerio de Ciencia e Innovacion” (MICINN) between 2016 and 2021. The author carried out, within the framework of the FPI, a 3 months-stay at the Geophysics Section of the DIAS Dublin Institute for Advanced Studies (Dublin, Ireland).

For the first part of this thesis, the seismic data used in this study was collected by French R/V L’Atalante in 2006. We do not use any new data. All data come from previously published sources, and are available through (Gallier et al., 2009) and (Moulin et al., 2015). For the second part of the thesis, the data used was acquired within the framework of the FRAME project (reference CTM2015-71766-R) onboard of the R/V Sarmiento de Gamboa.

This work was carried out within the Grup de Recerca Consolidat de la Generalitat de Catalunya Barcelona Centre for Subsurface Imaging (B-CSI) (2014SGR940). The group computer and software facilities have been largely funded with the projects Kaleidoscope, CO-DOS, Geomargen-2, Geomargen-3, Geomargen-4, Geomargen-5, Geomargen-6, and CODOS-Phase2 funded by Repsol.

Contents

Summary

In this PhD work, I carried out a geophysical and geological study of two classical examples of rifted continental margins: the Gulf of Lions, located in the Western Mediterranean, and the Tagus Abyssal Plain, located in the West Iberia margin. Despite the numerous previous studies performed in these two margins, there is an open debate on their crustal structure and on the processes that led to their formation. My study aims to 1) determining the nature of rocks forming the main geological domains of the basin based on a new methodological approach, 2) defining the tectonic structure of the basement and 3) placing constrains and discussing the kinematics and tectonic and magmatic mechanisms involved in the formation of these basins.

To study the Gulf of Lions and Ligurian basin, I used a geophysical data set acquired during the SARDINIA-2006 survey. It was conducted on board the French R/V L'Atalante, by the L'Institut Français de Recherche pour l'Exploitation de la Mer (Ifremer) (France). In particular, I used seismic records along three spatially consecutive Multi-Channel Seismic (MCS) lines and a collocated Wide-Angle Seismic (WAS) profile recorded by a set of Ocean Bottom Seismometers (OBS) during the shooting of the MCS lines. Altogether, these lines cover a 300-km-long seismic transect that runs NW-SE across the Gulf of Lions until the central part of the Liguro-Provençal basin.

The geophysical data used to study the Tagus Abyssal Plain were collected during the FRAME-2018 survey, performed within the framework of the FRAME project. The main goal of this project was to improve our understanding of the origin and evolution of rifted margins, with particular focus on the West Iberia margin. In this work, I present spatially coincident MCS and WAS data recorded at a set of OBS, along a 350 km-long, E-W trending profile located at 38º N, crossing the basin in the North-West Iberian margin.

The analysis, processing, modelling and interpretation of these data sets allowed proposing a novel interpretation of a series of aspects regarding the structure and nature of the crust, and discussing new hypotheses concerning the tectonic processes that led to the current configuration of these two margins.

I apply a novel joint refraction and reflection travel-time tomography (TT) approach that combines travel-times from MCS data reflections and WAS data refractions and reflections to provide new constraints on the structure and petrological nature of basement domains across the two margins. Including travel-times from reflections identified in the MCS data provides improved constraints to determine the P-wave velocity (Vp) structure of the sediment cover, as well as the geometry of the top of the basement, with unprecedented resolution. The detailed shallow Vp structure reduces the uncertainty in the determination of the Vp distribution within the underlying basement and on the Moho geometry. The result of this joint WAS-MCS tomography is a Vp model of the margin that is fully consistent with the MCS image along the profile, making the geological interpretation much less subjective. In addition, these datasets allowed using state of the art processing and imaging techniques to obtain a deep image of the tectonic structures, and also a relatively good resolution of

the sedimentary infill of the basin. The processing of MCS data provides excellent information on the tectonic structure and geometry of the sedimentary basins.

The final Vp models from both margins obtained by joint MCS and WAS inversion constrain the different basement domains with a higher resolution and lower uncertainty than previous works, so that we have been able to redefine their lateral extent, petrological nature, limits and mode of transition.

The results from the Gulf of Lions support the existence of three geological domains that are: 1) a continental domain formed by normal faults that tilted the continental basement with syn-rift sediment infill. 2) A ~100 km-wide domain between continental and ultra-thin continental crust, showing a 3-4 km thick layer with high velocity and steep gradients (5.5-7.5 km/s). We interpret this layer, whose nature has been widely debated in the literature, as a lens-shaped body made of oceanic crust. 3) A thin continental crust (~5 km). This configuration implies that the COT occurs abruptly, within <10 km along profile, at each side of the oceanic domain.

In the case of the Tagus Abyssal Plain, the models show that the crustal structure is more complex than previously thought, presenting sharp boundaries between five different domains at the base of the continental slope and across the J-anomaly. Thus, the profile across the Tagus Abyssal Plain shows that Domain I and Domain III are made of 4-6 km thick continental crust. Domain III shows a lower crust with comparatively higher Vp possibly caused by the presence of local magmatic intrusions. Domain II, previously interpreted as oceanic crust, is shown to constitute a ~70 km-wide domain of exhumed and serpentinized mantle rocks. The westernmost 200 km of the profile include Domain IV and Domain V with a basement made of oceanic crust. The new Vp model and seismic images support that the COT is located ~300 km offshore and that occurs abruptly in a narrow, 10-15 km-wide segment representing the transition between Domain III and Domain IV. Based on these results, I propose a new geodynamic scenario that has two main phases of crustal extension. According to the interpreted configuration of crustal domains, rifting in the Tagus Abyssal Plain would have started with continental crust extension, continued with exhumation of the mantle, followed by westward a jump on the extensional axis that lead to the formation of the oceanic crust of the J-magnetic anomaly. Then the process continued with the establishment of the Mid-Atlantic spreading centre and the formation of 2-4 km thick oceanic crust of the Cretaceous Magnetic Quiet Zone.

My interpretation challenges current, well-established conceptual models concerning the formation of both examples of rifting systems. The integration of all the results presented in this thesis offers the opportunity to review these conceptual models for the formation of extensional margins, in which mantle exhumation occurs after continental rifting and precedes oceanization. Our models indicate that the response of the continental lithosphere to extensional processes may be more complex than assumed in current paradigms.

Part I
INTRODUCTION

Chapter 1

Basic concepts

In this Chapter, we introduce the basic concepts necessary to understand the geological context of the processes studied in this PhD work. We present general concepts of plate tectonics, and specifically, we focus on the structure of rifted margins and in regard to their characteristics, we focus on the different types of basement rock affinity. The reason is that in the last two decades, geophysical methods have had major leaps increasing resolution and decreasing uncertainty on the definition of the rock bodies that can be found in this geological context. This definition is critical to better understand the basis of the petrological classification of the geological domains of rifted margins, and thus the necessary step to fully understand their formation processes and evolution.

1.1. Fundamentals of plate tectonics

The theory of *Plate Tectonics* was developed during the 60's with a series of seminal articles (e.g. Heezen, 1960; Dietz, 1961; Vine and Matthews, 1963; Wilson, 1963, 1965; Isacks et al., 1968; Le Pichon, 1968; Morgan, 1968), that provided the first model to explain the observations gathered in the earlier Continental Drift theory (Wegener, 1915). Advances in the surveys of bathymetry and magnetic confirmed the existence and improved the definition of structures and lineaments in the seafloor relief and the magnetic stripes of the oceanic rocks that were critical evidences that contributed to the definition of the concept of seafloor spreading (e.g. Hess, 1962; Vine and Matthews, 1963). Those data and the establishment of the global seismological network provided the observations to better understand the global seismicity distribution. All this knowledge, together with the proposal of convection currents in the mantle as driver mechanism and its capacity to explain paleogeography and paleobiologic data, prompted the rise of the Plate Tectonics Theory, which was accepted as dominating paradigm in the early 70's (Smith, 1973; Cox and Hart, 1986; Hamblin, 1992; Kearey et al., 2009). The theory of plate tectonics states that the Earth's outermost rigid layer, the *lithosphere*, is fragmented into a number of nearly rigid *plates* that move relative to each other above a highly viscous, mechanically weak layer known as the *asthenosphere*, which is part of the upper mantle and has a plastic behaviour (e.g. Cox and Hart, 1986; Hamblin, 1992) (Fig. 1.1). Tectonic

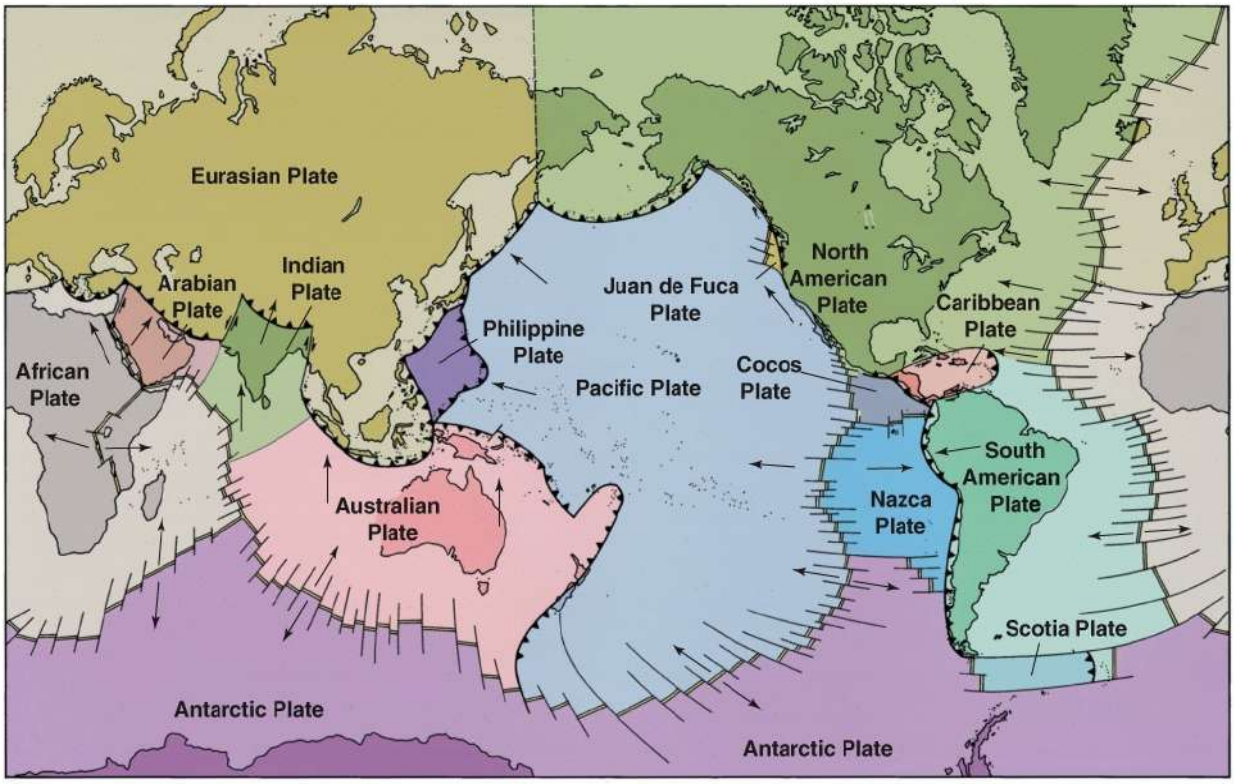

Figure 1.1- Map of the main tectonic plates of the Earth showing the different types of plate boundaries, and the name of each tectonic plate (extracted from http://www.crystalinks.com/tectonicplate.png).

interactions between plates occur at plate boundaries, where most seismic and volcanic activity takes place (Fowler, 2005).

There are three types of plate boundaries as a function of the relative plate motion (e.g. Hamblin, 1992; Whitsmarsh et al., 1996; Kearey et al., 2009) (Fig. 1.2):

i. Transform or conservative: lithospheric plates are not created nor destroyed. They move laterally to each other, generating transform faults. A well-known example is the San Andreas fault in California, USA.

ii. Divergent or constructive: lithospheric plates move away from each other, producing the thinning of the lithosphere and concomitant mantle melting that builds up new oceanic lithosphere (i.e. oceanic accretion). These boundaries are represented by **rifted margins** and Mid-Oceans Ridges in oceanic areas. Examples of this type of boundaries in an oceanic setting are the Mid-Atlantic Ridge, while examples in continental settings are the Red Sea and the East African Rift.

iii. Convergent or destructive: lithospheric plates converge to each other. When the two plates have a similar density, they collide building up mountain ranges like the Himalayas (Indian-European plates). On the other hand, when there is a density contrast, the densest lithosphere (typically an oceanic plate) plunges beneath the lightest one. This entails a subduction process that causes arc volcanism and the most intense seismic activity on earth. One example of this process occurs in the Circum-Pacific Ring of Fire.

In the next section, we focus on the divergent or constructive plate boundaries and the continental rifting process, because they are the focus of this PhD work.

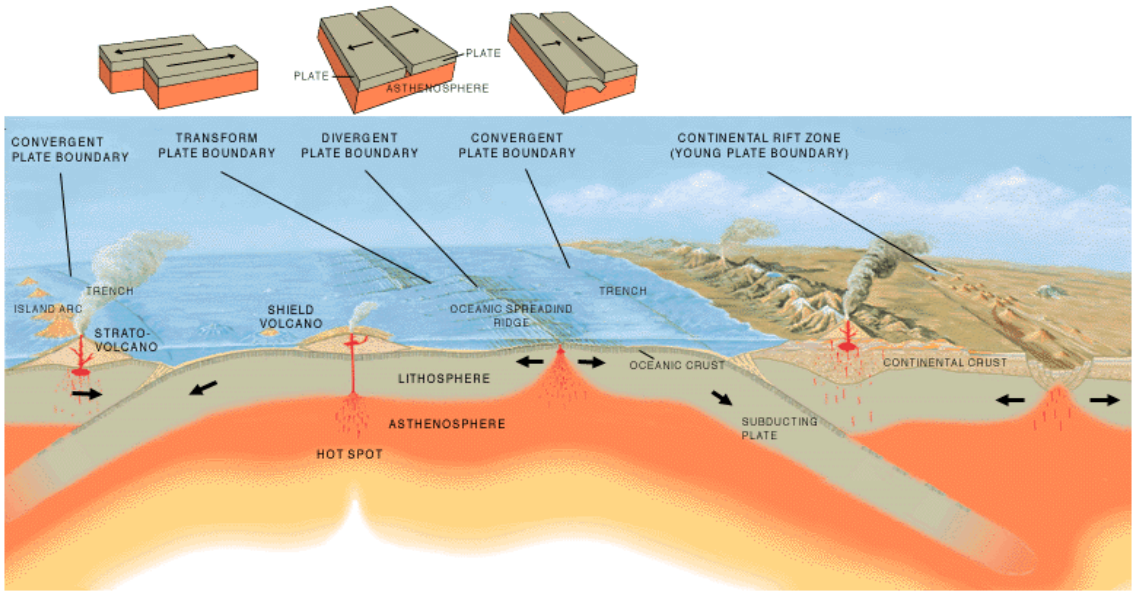

Figure 1.2- Cartoon of the different interactions between plates. At transform boundaries (right upper sketch), plates are moving in a lateral way in relation to each other. At divergent boundaries (middle upper sketch), they are moving away from each other. At convergence boundaries (left upper sketch), they are approaching (extracted from http://www.crystalinks.com/tectonicplate.png).

1.2. Rifted margins

The transition between continental and oceanic lithosphere occurs in active margins and rifted continental margins. The continent-ocean (COT) boundary along rifted margins occurs along progressively rifted and extended continental crust that ultimately breaks apart and transitions to oceanic crust. The formation and evolution of rifts depend on many factors including the thermal structure of the mantle, and the mechanical structure of the lithosphere (e.g. McKenzie, 1978; Pluijm and Marshak, 2004). Traditionally, rifted margins have been classified in two end-member types, namely volcanic or magma-rich and non-volcanic or magma-poor, depending on the degree of extension-related magmatism that is produced during the extension (e.g. Franke, 2013). Figure 1.3 summarizes the overall crustal structure along magma-rich and magma-poor rifted margins.

Magma-rich rifted margins are characterized by thick wedges (up to 15 km) of volcanic flows identified in seismic reflection data as seaward dipping reflectors (SDRs), and the presence of a high P-waves velocity (Vp) > 7.3 km/s lower crust seaward of the continental rifted margin (e.g. Franke, 2013). These geophysical observations are interpreted to indicate that these margins are associated with the generation of large volumes of magmatism during their formation, which is emplaced on top or at the base of the crust. Three primary hypotheses exist that account for the amount of magma produced in these types of margins: 1) mantle plume with elevated temperatures (White and McKenzie, 1989; White et al., 2008); 2) small-scale convection at the base of the lithosphere (Mutter et al., 1988; King and Anderson, 1995); and 3) heterogeneities in mantle source composition

(Korenaga and Kelemen, 2000; Korenaga, 2004). Independently of the process involved in the formation of the margin, continental lithosphere thinning of the magma-dominated margins typically occurs over a considerably short distance (50-100 km) and for that reason the COT is abrupt and narrow, located in the vicinity of the SDRs (e.g. Franke, 2013).

In contrast, **magma-poor rifted margins** do not present such features. Boillot et al. (1980) propose that in this case the margin is divided into a proximal and distal margin. The proximal margin is characterized by the presence of high-angle and listric faults related to the fault-bounded rift basins, while the distal margin is characterized by an extremely thinned crust that is often separated from the oceanic crust by a domain made of unroofed mantle rocks (i.e the "exhumed mantle"). In this case, the COT occurs more progressively along a wider region of ~100-200 km, where the mantle can be exhumed with minor associated melting due to a slow extension that allows mantle cooling (Boillot et al., 1980; Sawyer et al., 1994; Pérez-Gussinyé et al., 2001). In many models, an intracrustal detachment is interpreted somewhere between the brittle upper crust and the mantle at the proximal margin, while at the distal margin brittle upper crust and upper mantle are separated by only a thin lower crustal layer or are juxtaposed. This leads to coupling and the formation of a detachment at the crust-mantle boundary, allowing the exhumation of the mantle further seaward (e.g. Pérez-Gussinyé et al., 2001).

In both types of margins, the COT is a complex and not fully understood region that has proved to be difficult to locate and characterize with geophysical methods in the past. Ground truthing of COT

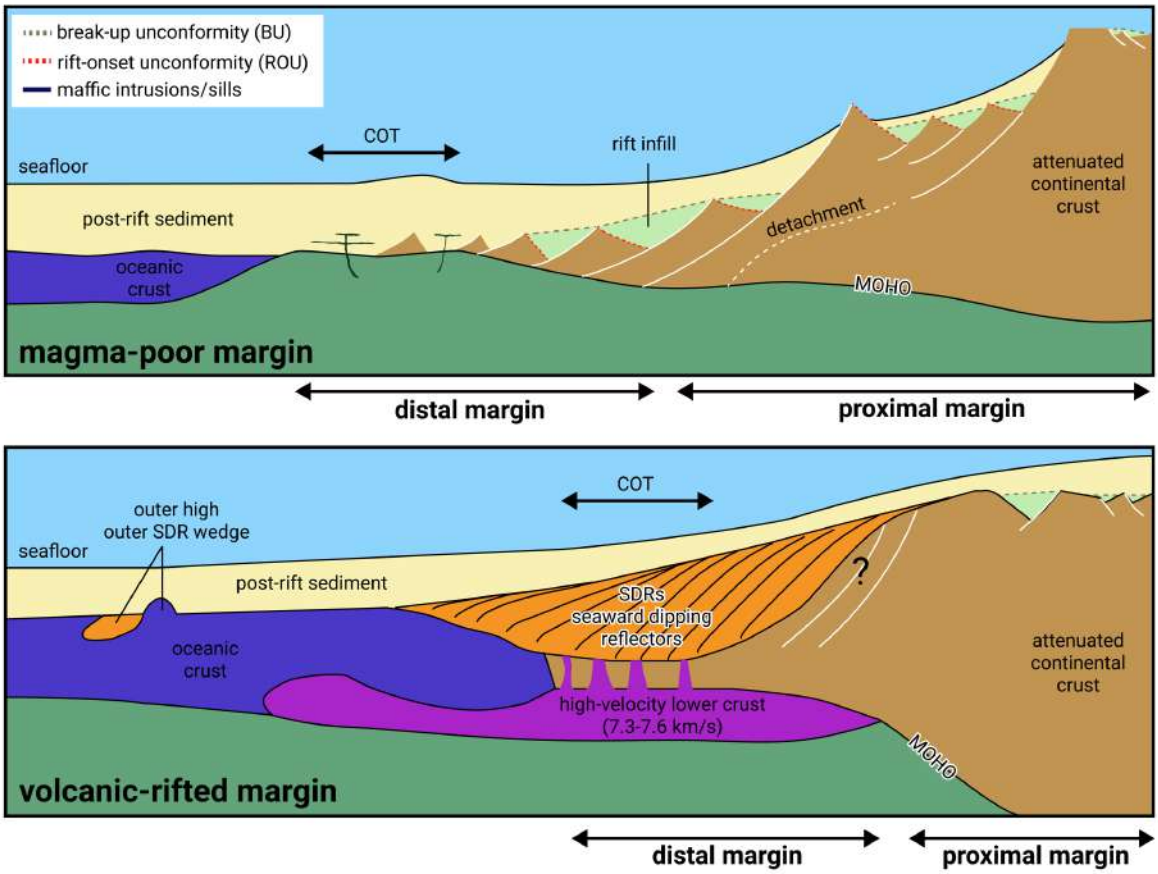

Figure 1.3 - Conceptual sketch of the end-member extremes of passive continental margins: (a) magma-poor or non-volcanic margins and (b) magma-rich or volcanic-rifted margins. Both sketches show the location of the COT zone. Modified from Franke, 2013.

rocks has provided unanticipated results in several locations (Ryan et al., 1973; Boillot et al., 1987; Sawyer et al., 1994; Whitmarsh et al., 1998). However, borehole sample studies are discrete and limited to a few locations, so they do not provide a broad data set to characterize the COT along most of the world margins. Therefore, our understanding of how the transitional domain, commonly interpreted as exhumed mantle, transitions into oceanic crust is still partial and limited. The nature of the basement, and thus the origin of the structures, is still debated, partly due to the lack of appropriate geophysical data.

Due to the scarcity of direct rock samples, most studies concerning rifted margins and their interpretation are based on the observations and interpretation of Multi-Channel Seismic (MCS) images from streamer data. These images provide accurate information about the structure of the basement and the geometry of the tectonic boundaries but not on the petrological nature of the different geological domains. This gives room for subjective judgement and increases the uncertainty on the final interpretation (Fig. 1.4).

The use of novel geophysical methods in our analysis has allowed us to constrain the nature of the rocks of the basement with higher objectivity, than previous approaches, applying indirect methods. Our new approach provides the tools to infer physical parameters that are characteristic of different types of rocks and thus to better constrain the interpretation of the seismic images. The major scientific questions in rifting, include the determination of the variations of the structure, rock properties, and tectonic style of the crust and uppermost mantle across rifted continental margins, and the location and nature of the COT. Characterizing these structures is the key to understand how the lithosphere deforms under extension and to place constraints on its rheology and its dynamic behaviour under different thermodynamic settings.

1.3. Nature of the crust and upper mantle

The lithosphere is composed of the crust and upper mantle, being both chemically different. The crust is constituted by a variety of igneous, metamorphic and sedimentary rocks, while the underlying rigid mantle is thought to be more homogeneous and mainly formed by peridotite, a rock denser than those commonly found in the crust. The term basement is generally used to define those metamorphic or igneous rocks that underlie the sedimentary cover (Allaby, 2008).

The nature of the basement is defined by its rock's composition, which can be determined by direct rock sampling and geochemical analysis. However, most rift systems are covered by several km of sediments and basement is not directly accessible. In the absence of rock samples, as in our study regions, the composition can be inferred using indirect geophysical measurements, which allow estimating physical rock properties of the basement to compare them with the properties of different rock types such as seismic velocity, rock density, or the gradients of these properties with depth (Prada, 2014). However, those properties are not univocal, meaning that different rock types have similar velocity and density values (e.g. Carlson and Herrick, 1990). One way to evaluate the most likely lithology is compare the model results from the field experiment to the empirical relationships that associate different physical properties to a single rock type. There exist a number of such relationships for seismic velocity and density for the most common oceanic and continental rock

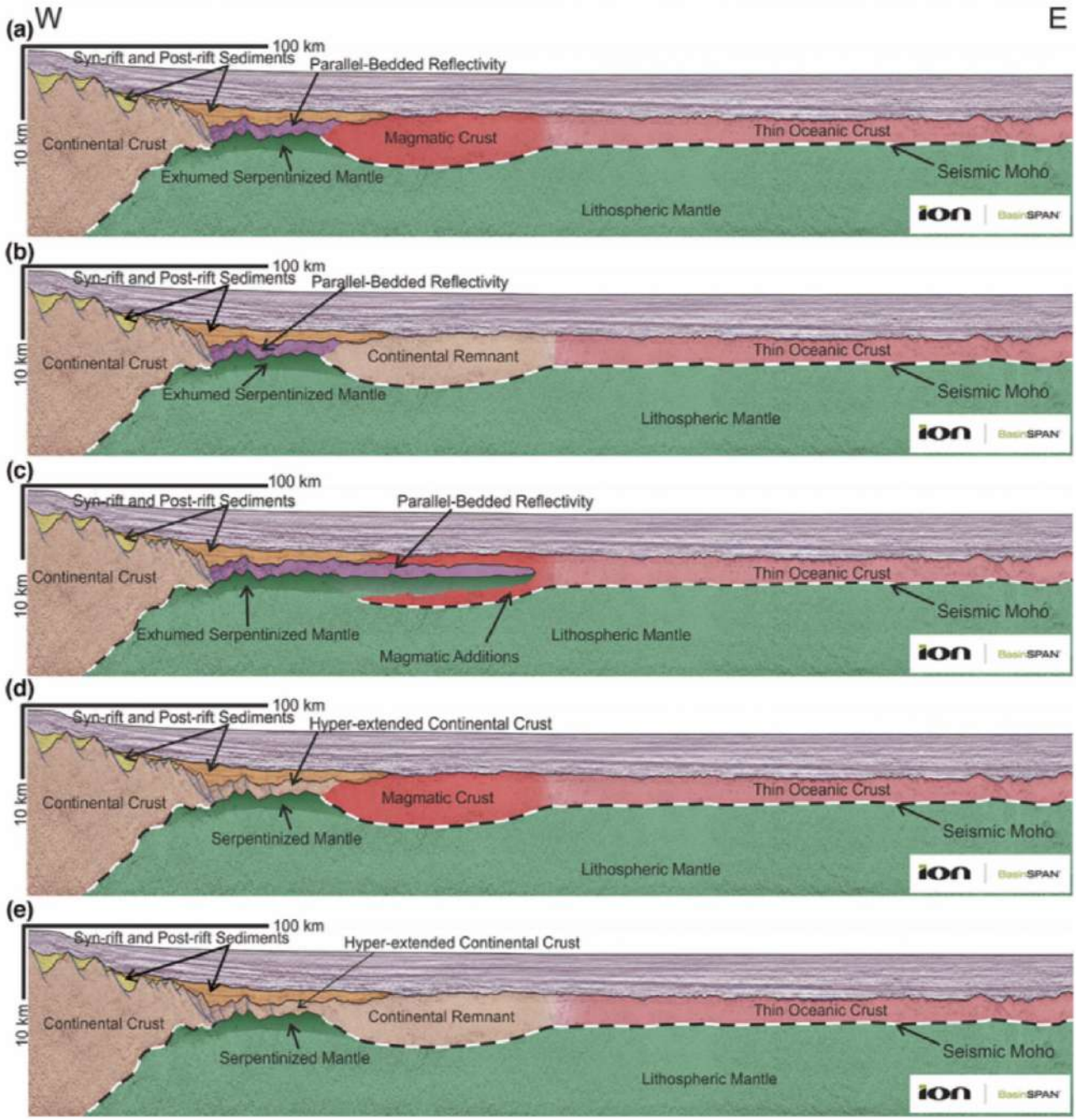

Figure 1.4 – Example of multiple interpretations of the SE Indian rifted margin. The author illustrates five different scenarios with different nature of the domains, based on in seismic observations, for the same seismic line. From Harkin et al. (2017).

types and mantle rocks (e.g. Carlson and Herrick, 1990; Christensen and Mooney, 1995; Carlson and Miller, 2003).

Based on geophysical and geological observations the most common affinities of the basement found in rifted margins are continental crust, oceanic crust, and mantle often partially serpentinized (e.g. Boillot et al., 1980, 1987a; Beslier et al., 1993; Taylor et al., 1995; Benes et al., 1997). In the following section, we describe all of them.

1.3.1. Continental crust

The lithological composition of continental crust includes a wide variety of igneous, metamorphic, and sedimentary rocks. In general, continental crust presents a felsic bulk composition, which means that is relatively rich in elements that form feldspar and quartz (i.e. Si, Al, O, K, and Na). Despite all this variability, the continental crust generally consists basically of two layers: the continental upper crust, with a composition close to granodiorite, and the continental lower crust, with a composition close to granulite (Prada, 2014).

Christensen and Mooney (1995) inferred an overall composition for continental crust by comparing results from a large number of seismic experiments, acquired in different tectonic settings, with high-pressure laboratory measurements of Vp of a wide range of rocks commonly found in continental crust. In summary, the authors conclude that there is an upper-crust layer, which is ~10 km-thick, with P-wave seismic velocities range between 5.9 km/s and 6.3 km/s, indicating that they are composed of granitic and low-grade metamorphic rocks. Deeper in the crust, the middle and lower crust have average velocity increasing from 6.5 km/s to 6.8 km/s, indicating that the dominant rock types are metamorphic rocks like gneiss and amphibolites in the mid-crust, and gabbros at the lower crust. Therefore, the authors attribute the increase of velocity gradient to an increase in the metamorphic grade and a decrease in the silica content. Finally, the net compositional difference between the felsic crust and mantle peridotite is represented by sharp velocity contrast, where velocities jump from ~6.8 km/s to 8.0-8.2 km/s (Christensen and Mooney, 1995; Fowler, 2005) (Fig. 1.5). Crustal density for this compositional model increases from 2.6 $g \cdot cm^{-3}$ at the surface to 3.1 $g \cdot cm^{-3}$ at the base of the crust (Christensen and Mooney, 1995), which is in agreement with Allaby (2008) which states that the average density for continental crust ranges between 2.7-3.0 $g \cdot cm^{-3}$.

The global average thickness for emerged continental crust ranges between 30 and 40 km (Christensen and Mooney, 1995; Fowler, 2005; Allaby, 2008). However, in continental margins, the

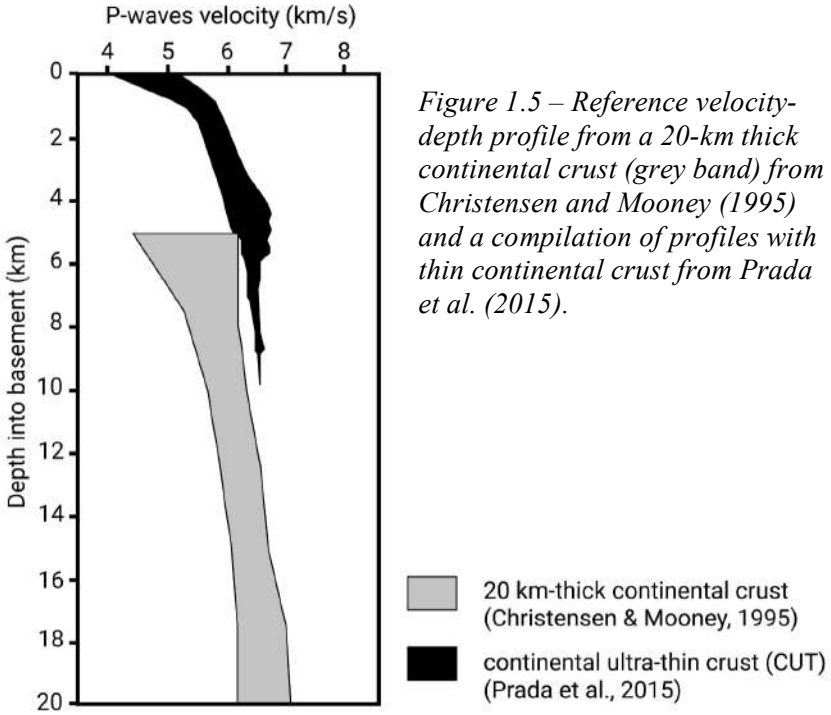

Figure 1.5 – Reference velocity-depth profile from a 20-km thick continental crust (grey band) from Christensen and Mooney (1995) and a compilation of profiles with thin continental crust from Prada et al. (2015).

crust is modified by rifting processes and thinned due to extensional processes. Prada et al. (2015) inferred Vp-depth reference models for the thinnest crustal domains by a compilation of continental crust found in the 5-10-km-wide edge of continental margins near the crustal breakup region (Fig. 1.5). Velocity-depth profiles used for this new reference are from Nova Scotia rifted margin (Funck et al. 2003, 2004; Wu et al. 2006), the Grand Banks of Newfoundland (Lau et al. 2006; Van Avendonk et al. 2006), and the Moroccan margin (Nova Scotia Department of Energy 2011).

It is noteworthy that all of these features, seismic velocity, density, and thickness, may vary considerably depending on the geological setting that governed the formation and evolution of particular regions of continental crust. Lowermost crustal velocities of 7.0-7.5 km/s observed in several settings such are arcs, rifts or rifted margins affected by particular magmatic processes and are velocities considerably higher than that of continental crust away from those setting. These high velocities are typically associated with basic-ultrabasic magmatic rocks, suggesting that thinned continental crust might be affected by intense magmatism (e.g. intrusions, underplating) that does not strictly fit into the lithological classification referred to above (Prada, 2014).

1.3.2. Oceanic crust

Oceanic crust is formed at seafloor spreading centres. Numerous reviews of seismic experiments reviewed the structure derived by and show that the velocity-depth profiles obtained at intermediate- and fast-spreading crust from the Pacific and Indian Oceans, despite local differences, the seismic velocity depth distribution is fairly uniform within for similar age crust (White et al., 1992; Grevemeyer et al., 2018a). This large amount of geological and geophysical data has allowed identifying a standard structure for oceanic crust generally known as Penrose-type ocean crust. Its structure includes two layers' characteristic of the igneous part of the crust (Fig. 1.6):

Layer 2, which is also called "the volcanic layer", may be subdivided into two sublayers named Layers 2A and 2B. Layer 2A has an average thickness of ~0.5 km and is formed by extrusive basaltic pillow and sheeted lavas. Layer 2B is thicker than 2A. It has an average thickness of 1.5 km and is constituted by basaltic dikes (Kennett, 1982). Both layers define a region of the oceanic crust in which

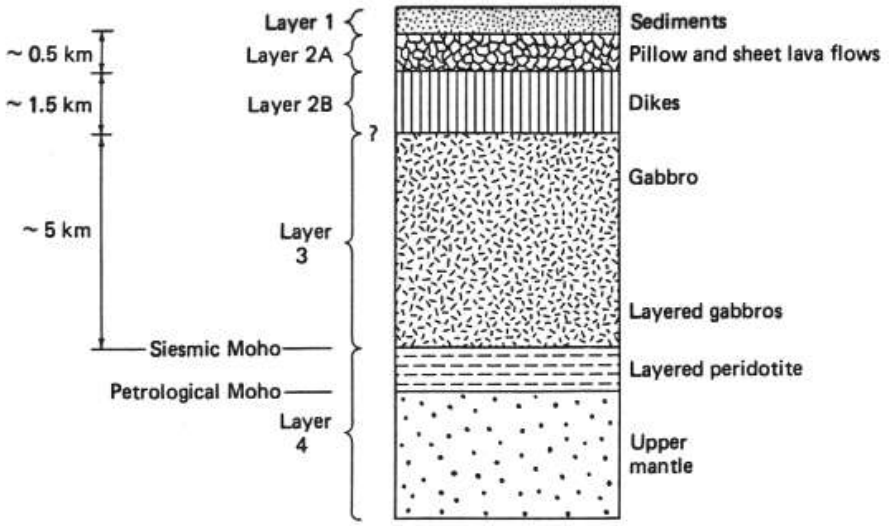

Figure 1.6 – Sketch of the standard layered structure of oceanic crust (Kennet, 1982).

seismic velocity increases rapidly with depth, from ~3.5 km/s to ~6.2 km/s in ~ 2 km of crust (gradients of 1-2 s^{-1}) (Fig. 1.7) (White et al., 1992; Grevemeyer et al., 2018a). The rapid increase of seismic velocity is mainly attributed to: (1) lithological changes as a function of depth, and (2) the decrease on the degree of fracturing/porosity, and the related alteration of the rocks (Fowler, 2005). Based on measured physical properties of core samples from the seafloor and ophiolites, the average density of Layer 2 is estimated between 2.6-2.7 $g \cdot cm^{-3}$ (Carlson and Herrick, 1990).

Layer 3 is the deepest and thickest oceanic layer. It has an average thickness of 5 km (Allaby, 2008), although it is highly variable. Based on its physical properties and onshore observations (i.e. ophiolites), it is assumed that Layer 3 is gab broic in composition (e.g. Kennett, 1982; Fowler, 2005). Seismic velocities in Layer 3 range from ~6.5 km/s on top to ~7.2 km/s just above the crust-mantle boundary (Grevemeyer et al., 2018a) (Fig. 1.7). This corresponds to a vertical Vp gradient of 0.1-0.2 s^{-1}, 10 times lower than the gradient in Layer 2. The average density of this layer is 2.9-3.0 $g \cdot cm^{-3}$ (Carlson and Herrick, 1990). In the last ~20 years as the quality of field data and modelling methods has increased, the range of variability of velocity-depth profiles has decreased. This observation supports a remarkably similar mineralogical and structural similarity of oceanic crust formed at comparable spreading rates and age (Grevemeyer et al., 2018a). Thus, the seismic structure obtained from geophysical profiles is a remarkably reliable proxy to define the oceanic crust nature of the basement (Fig. 1.5).

Based on compilations of models obtained with seismic data, it has been shown that oceanic crust is much thinner than continental crust, with a crustal thickness varying from 5.0 km and 8.5 km (White et al., 1992; Grevemeyer et al., 2018a). In some cases, such as oceanic plateaus, originated under the influence of active mantle melting anomalies commonly identified as "hotspots", oceanic crust can

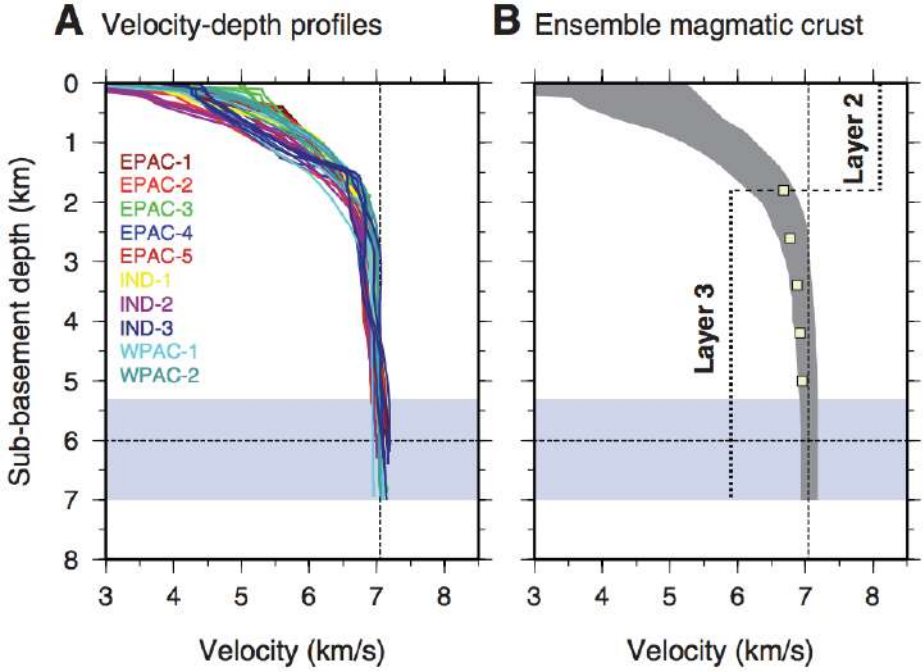

Figure 1.7 - (a) Velocity-depth profiles of magmatic crust derived from intermediate- and fast-spreading crust from the Pacific and Indian Oceans. (b) Ensemble derived from the velocity-depth profiles, providing a magmatic crust ensemble. From Grevemeyer et al. (2018a).

be much thicker, up to 20-30 km in some extreme cases such as Iceland, Galapagos Volcanic Province, or Ontong-Java (e.g. Gladczenko et al., 1997; Maclennan et al., 2001; Sallarès and Charvis, 2003).

1.3.3. Exhumed mantle

Seismic data show that, as thinning progress in rifted margins, the highly stretched continental crust may break up which leads to the so-called COT zone. In some of these transition zones, ODP drillings have found that the basement in the COT is made of serpentinized mantle rocks (e.g. Boillot et al., 1980; 1987a; Whitmarsh and Wallace, 2001).

Serpentinization of mantle rocks occurs when seawater interacts directly with the mantle at a temperature close to 400°C. This interaction results in a metamorphic process that involves hydration of the ferromagnesian minerals of mantle rocks, mostly olivine. This process destroys the structure of this mineral by adding large amounts of water into the crystalline structure, resulting in its transformation into serpentinite (Allaby, 2008).

Concerning the physical properties, serpentinization lowers both seismic velocity and density of peridotite, which originally display Vp of 8.1-8.2 km/s and density of ~3.3 $g \cdot cm^{-3}$ (Birch, 1961; Allaby, 2008). Substantial deviations from these values allow identifying the presence of exhumed mantle rocks from seismic and density models (e.g. Dean et al., 2000; Van Avendonk et al., 2006;

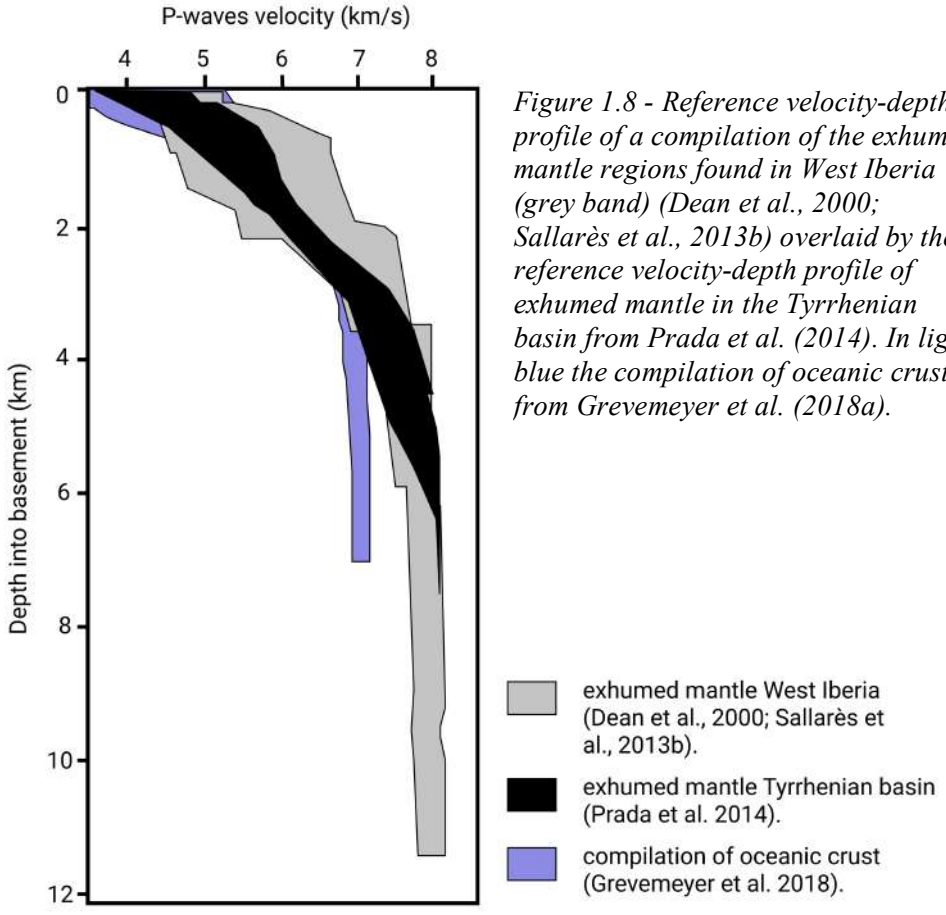

Figure 1.8 - Reference velocity-depth profile of a compilation of the exhumed mantle regions found in West Iberia (grey band) (Dean et al., 2000; Sallarès et al., 2013b) overlaid by the reference velocity-depth profile of exhumed mantle in the Tyrrhenian basin from Prada et al. (2014). In light blue the compilation of oceanic crust from Grevemeyer et al. (2018a).

Sibuet et al., 2007). The most relevant features concerning the seismic velocity structure of exhumed mantle regions are the following ones:

In the uppermost 2-4 km of the basement, Vp increases rapidly, with gradients that can be twice stronger than those observed in oceanic *Layer 2*. This rapid increase is mostly attributed to a concomitant decrease in peridotite serpentinization degree with depth due to the significant reduction of rock fracturing, and fluid percolation (Chian et al., 1999; Dean et al., 2000; Sallarès et al., 2013a; Prada et al., 2014) (Fig. 1.8).

Then, a moderate increment of seismic velocities underlies this fast transition zone (Fig. 1.8), reflecting a less intense, more homogeneous serpentinization degree that leads progressively to unaltered mantle rock velocities (8.1-8.2 km/s) (Chian et al., 1999; Dean et al., 2000). Finally, no Moho discontinuity is observed, since there is no lithological discontinuity defining the crust-mantle boundary (e.g. Dean et al., 2000).

All those characteristics make geophysical measurements particularly well suited to differentiate exhumed mantle basement from oceanic o continental domains and thus a powerful tool to characterize the complex transitions of rock domains at deep-water sedimented rifted margins.

Chapter 2

Presentation of this thesis

2.1. Interest of the study

The nature and spatial distribution of geological domains across rifted continental margins are used to infer the processes that governed the formation of those systems. Current conventional wisdom states that continental rifted margins formed away from the influence of hot-spots are systematically characterized by a spatial distribution of domains that entails a common temporal sequence of geological events. The current paradigm of the evolutionary model proposes that extension of continental lithosphere causes thinning and breakup of the crust leading to exhumation of the underlying mantle, followed by a phase of decompression melting of the asthenosphere that results in the establishment of an active spreading centre. This widely accepted conceptual model is greatly influenced by past work in the West Iberia Margin, that is considered to be a book example of magma-poor rifted margins (e.g. Péron-Pinvidic and Manatschal, 2008; Sutra and Manatschal, 2012; Péron-Pinvidic et al., 2013). However, the interpretation of the characteristics of the geological domains of the West Iberia Margin, including their nature, spatial distribution and geometrical relationships are for most of the region constrained by a few profiles of old-vintage, comparatively low-resolution geophysical data, and scarce locally restricted ground-truthing information.

Despite the large amount of work and improvements regarding this conceptual model, there is still a significant gap of knowledge on key questions concerning the structure, formation processes and evolution of rifted margins. Some of the most relevant open questions are related to the timing and kinematics of the extension and with the petrological nature and processes involved in the formation of the continent-ocean transition (COT) zone which appears to vary depending on the geological setting in a range not fully encapsulated in conceptual models (e.g. Taylor et al., 1995; Benes et al., 1997; Dean et al., 2000; Pérez-Gussinyé and Reston, 2001; Ranero and Pérez-Gusinyé, 2010) (Fig. 2.1).

Our working hypothesis is that a considerable body of knowledge of the structure in the continental margin needs to be revisited and updated with the help of modern comparatively higher-resolution geophysical data, processed and modelled with state-of-art methodologies that provide a novel more accurate and quantifiable observational data sets. Using improved observations, we aim at defining the characteristics of the geological domains of the rifted margin with higher accuracy and resolution and revising, in turn, the existing conceptual models, based on objective criteria.

The work presented in this thesis consists of the analysis, processing, modelling and interpretation of both already available and newly acquired, by our group, geophysical data in two regions that constitute previously intensively studied examples of rifted margins. The two selected sites were formed in different geodynamic settings. One is the Tagus Abyssal Plain, located in southern part of the Western Iberia margin, and the other is the Gulf of Lions, located in the Western Mediterranean.

On one hand, the Gulf of Lions is a continental margin located in the north-western Mediterranean that forms part of the Ligurian-Provençal Basin. The comparatively small segmented basins in the Western Mediterranean were formed partially or fully as back-arc basins due to the eastward retreating of the west-directed Apenninic subduction zone in a localise geodynamic context with near-field forces (Cohen, 1980; Le Douaran et al., 1984; Rehault et al., 1984; Gueguen et al., 1998; Jolivet et al., 2000; 2006; 2015). In our study, the Multi-Channel streamer (MCS) data, and the Wide-Angle Seismic (WAS) data were acquired during the SARDINIA-2006 survey, on board the French R/V L'Atalante by the Institut Français de Recherche pour l'Exploitation de la Mer, Ifremer (France). The main objective of this experiment was to study the impact of lithospheric stretching on the crustal structure (Gailler et al. 2009; Moulin et al. 2015). In particular, we use seismic records along three spatially consecutive MCS segments and a WAS seismic profile that form a coincident continuous profile.

On the other hand, the Tagus Abyssal Plain occurs at the southern segment of the West Iberia margin, which was formed by the effect of far-field forces or continental drift apart that led to the opening of the North Atlantic Ocean and contributed to the breakup of Pangea. Since this is the least studied segment with geophysical methods of the West Iberian margin, the FRAME cruise was performed in July and September 2018 to improve the knowledge of the petrological and tectonic processes in the area. To accomplish this goal, our group and collaborators used modern MCS and WAS equipment of the RV "Sarmiento de Gamboa" to acquire the seismic data. The work presented in this thesis consists on the analysis processing, modelling, and interpretation of the coincident WAS, MCS and gravity data corresponding to a transect acquired across the Tagus Abyssal Plain.

The main motivation of this PhD work is thus to contribute new observations of leading-edge quality, and to discuss and interpret them to help answering open questions regarding the formation of the magma-poor rifted margins. To answer the breadth of open questions concerning fundamental issues regarding the formation of rifted margins we need to determine the nature of the geological domains and their boundaries. Furthermore, by comparing the results of these two margins, we want to challenge the currently dominant conceptual models often based on partial or vintage geophysical data sets, where the amount of thinning is poorly constrained and often the nature of the basement has not been determined due to scant data quality or methodological limitations. Our new results

allow to better understand the architecture and structural features of the margins and compare them with predictions stated in the current conceptual models.

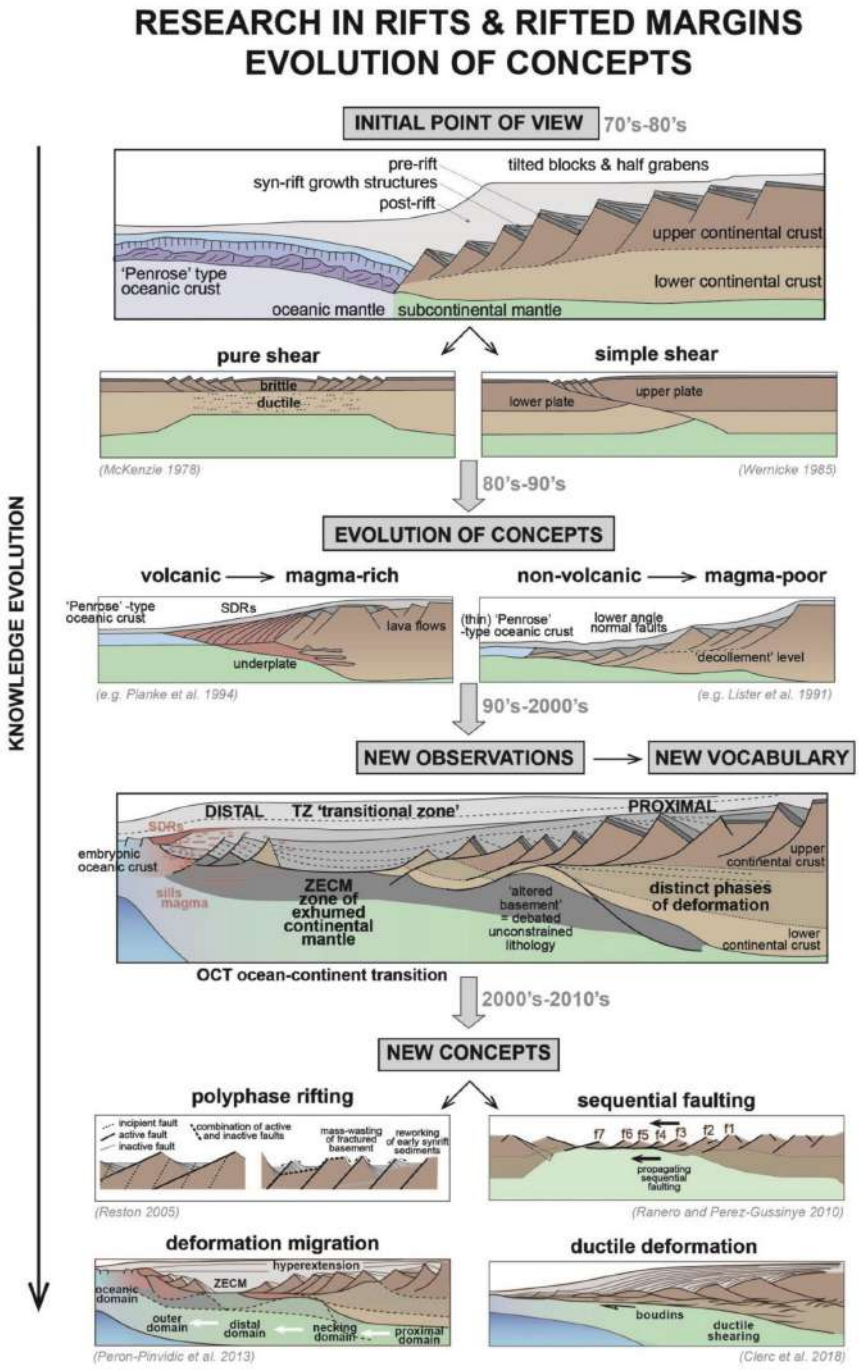

Figure 2.1 - Schematic representation of the significant progress of knowledge operated by the rifted margin community these last decades, from top (initial point of view from the 70's) to bottom (new concepts with illustration of recent models) The initial models attempting to represent rifted margins envisaged a continental crust gradually thinned oceanward and juxtaposed to a normal three-layers -type oceanic crust. Thanks to improvements in offshore imaging and modelling techniques, rifted margins are not examined within an end-member classification (volcanic/non-volcanic) anymore, but in light of a gradual change in processes (new observations – new vocabulary). From Péron-Pinvidic et al. (2019).

2.2. Objectives

This work aims to determine the properties and petrological nature of the basement in the different domains of the Gulf of Lions and the Tagus Abyssal Plain and their genetic process. To do this, we define the location, extension and deep geometry of these domains and their boundaries, throughout the processing, modelling and interpretation of MCS and WAS seismic profiles.

This information is used to investigate the processes involved during rifting including the tectonic structure as well as the changes in extensional and magmatic processes. In the case of the Tagus Abyssal Plain, the final objective is to integrate all the observations in an updated geodynamic evolution model. In summary, the goal of the study is to better understand fundamental questions concerning the mechanisms of the formation of rifted margins. To achieve this overarching goal, the following specific objectives have been defined:

1) To obtain the seismic velocity distribution of the crust and uppermost mantle and to define the geological domains and its boundaries

At present day, the basement affinity distribution along the Gulf of Lions and the Tagus Abyssal Plain is based on data acquired along regional profiles in each basin, which include sparse data modelled with old-fashioned methodologies. We combine collocated WAS and MCS data strategically located across the main structures to better constrain the nature of the basement based on objective criteria and to delineate the boundaries across both margins, as well as their lateral continuity and deep geometry.

i. Processing, interpretation and modelling of the WAS+MCS seismic data corresponding to Profile A-B in the Gulf of Lions and FRAME-2 in the Tagus Abyssal Plain to obtain 2D seismic velocity models of the crust and uppermost mantle, the geometry of the boundaries between domains and the main tectonic features.

ii. Quantifying the uncertainty of the model parameters; that is, seismic velocity, and geometry/depth of the different horizons.

2) To classify the petrological nature of the main geological domains across the margins

In order to improve the characterization, it is necessary to provide information on the physical properties of the basement and to prove the affinity of the different geological domains and their boundaries.

iii. Defining the most likely lithological affinities along the two profiles by comparing 1D velocity-depth structure in the different parts of the models with existing 1D velocity-depth reference profiles for continental crust, oceanic crust, and exhumed mantle regions.

iv. In the case of the Tagus Abyssal Plain, performing a gravity modelling of the velocity-derived density distribution to check the consistency with the velocity-based interpretation (iv).

3) To characterize the crustal structure along the basin

The geophysical models and seismic images allow understanding whether the structures formed during extension determine the location of tectonic lithological-domain boundaries (e.g. largest faults) that we observe today.

v. Analysing, processing and interpreting the MCS data to provide a time-migrated seismic image of both margins.

vi. Combining the information provided by the seismic velocity models (i) with that provided by the MCS time-migrated sections (vi).

4) Understanding the rifting opening phase and its evolution that led to the formation of the observed basement domains

Some aspects to address specifically are the nature and location of continental-ocean transition (COT), geometry of extensional fault systems, and the identification of the different crustal domains (continental, oceanic and exhumed mantle).

Models of rifting for the cases under study -and thus used in conceptual models in the literature- are based on incomplete, outdated, comparatively low-resolution information. The new information should permit redefining the mechanisms of extension in the margin.

vii. Integrating all the results obtained from the analysis, processing and modelling of WAS, MCS and gravity data for the two profiles to define the distribution of the main geological domains.

viii. Investigating the mechanisms involved in the formation of the main geological domains in the Tagus Abyssal Plain and presenting a conceptual model to explain their formation during the opening of the basin as well as their present layout.

2.3. Organization of this volume

To achieve the above objectives and to present the results in a clear structure, we organized this volume into five parts. Each of these parts is subdivided into chapters, and each of the chapters focuses on a different topic. The volume organization is as follows:

Part I: Introduction	*Chapter 1*: Basic concepts *Chapter 2*: Presentation of this thesis
Part II: Methodology	*Chapter 3*: Multi-Channel reflection Seismic data *Chapter 4*: Refraction and Wide-Angle reflection Seismic data *Chapter 5*: Travel-time tomography *Chapter 6*: Gravity anomaly data
Part III: Results	*Chapter 7*: The structure of the continent-ocean transition in the Gulf of Lions from joint refraction and reflection travel-time tomography *Chapter 8*: The rift and continent-ocean transition structure under the Tagus Abyssal Plain West of the Iberia *Chapter 9*: Rifting model and seafloor spreading of the Tagus Abyssal Plain
Part IV: Discussion	*Chapter 10*: Discussion
Part V: Conclusions and Forward look	*Chapter 11*: Conclusions *Chapter 12*: Forward look
Appendix	

Part I is the introductory section. It is composed of two chapters. Chapter 1 includes basic concepts of plate tectonics, a brief summary of the rifted margins and the different nature of the basement. Chapter 2 is this chapter, which focuses on the motivation and the explanation of the main objectives of the thesis.

Part II describes the data and methodology used. It includes four chapters, one for each type of data used in this thesis and their specific methodology to process and model them. Chapter 3 presents the multi-channel seismic reflection data and the corresponding processing sequence. Chapter 4 presents wide-angle seismic data and Chapter 5 explains the related modelling by travel-time tomography. Finally, Chapter 6 explains the basics of gravity data modelling.

Part III presents the results. This is the main part of this volume, in which processed data and models are presented, analysed and interpreted. Chapter 7 and Chapter 8 focus on the characterization of the main basement domains along the Gulf of Lions and the Tagus Abyssal Plain, respectively. Chapter 9 studies the deep tectonic structure of the Tagus Abyssal Plain, focusing on the crustal-scale features and characteristics.

Part IV has a single chapter (Chapter 10), which focuses on the discussion of all finding of the PhD work and common implications, which have not been analysed in the margin-based chapters. This

includes the discussion of the geodynamic models for the formation of rifted margins and their critical analysis in the light of new recent studies, data and models, including those presented in this thesis.

Part V comprises conclusions (Chapter 11) and a forward look (Chapter 12).

Finally, we have included in the Appendix the supplementary material related to the Chapter 7, 8 and 9.

References

Allaby, M. (2008). Oxford Dictionary of Earth Science, Oxford University Press Inc., New York, pp. 654.

Benes, V., Bocharova, N., Popov, E., Scott, S.D. and Zonenshain, L. (1997). Geophysical and morpho-tectonic study of the transition between seafloor spreading and continental rifting, western Woodlark Basin, Papua New Guinea. Marine geology, 142(1-4), pp.85-98.

Beslier, M.O., Ask, M. and Boillot, G. (1993). Ocean-continent boundary in the Iberia Abyssal Plain from multichannel seismic data. Tectonophysics, 218(4), pp.383-393.

Birch, F. (1961). The velocity of compressional waves in rocks to 10 kilobars, part 2, J. Geophys. Res., 66, 2199–2224.

Boillot, G., Grimaud, S., Mauffret, A., Mougenot, D., Kornprobst, J., Mergoil-Daniel, J. and Torrent, G. (1980). Ocean-continent boundary off the Iberian margin: a serpentinite diapir west of the Galicia Bank. Earth and Planetary Science Letters, 48(1), pp.23-34.

Boillot, G., Winterer, E.L., Meyer, A.W. (1987a). Introduction, objectives, and principal results: Ocean Drilling Program Leg 103, west Galicia Margin. Proc. ODP, Init. Repts., 103: College Station, TX (Ocean Drilling Program), doi: 10.2973/odp.proc.ir.103.

Carlson, R.L., and Herrick, C.N. (1990). Densities and Porosities in the Oceanic Crust and Their Variations With Depht and Age, J. Geophys. Res., 95 (B6), 9153-9170.

Carlson, R.L., and Miller, D.J. (2003). Mantle wedge water contents estimated from seismic velocities in partially serpentinized peridotites, Geophys. Res. Let., 30 (No. 5), doi: 10.1029/2002GL016600.

Chian, D., Louden, K.E., Minshull, T.A. and Whitmarsh, R.B. (1999). Deep structure of the ocean-continent transition in the southern Iberia Abyssal Plain from seismic refraction profiles: Ocean Drilling Program (Legs 149 and 173) transect. Journal of Geophysical Research: Solid Earth, 104(B4), pp.7443-7462.

Christensen, N., and Mooney, W. (1995). Seismic velocity structure and composition of the continental crust: a global view, J. Geophys. Res, 100 (B7), doi: 10.1029/95JB00259.

Cohen, C.R. (1980). Plate tectonic model for the Oligo-Miocene evolution of the Western Mediterranean. Tectonophysics 68, 283–311.

Cox, A., and Hart, R.B. (1986). Plate Tectonics: How it works: Wiley-Blackwell.

Dean, S.M., Minshull, T.A., Whitmarsh, R.B. and Louden, K.E. (2000). Deep structure of the ocean-continent transition in the southern Iberia Abyssal Plain from seismic refraction profiles: The IAM-9 transect at 40 20′ N. Journal of Geophysical Research: Solid Earth, 105(B3), pp.5859-5885.

Dietz, R.S. (1961). Continent and Ocean Basin Evolution by Spreading of the Sea Floor: Nature, v. 190, p. 372–373, doi: 10.1038/190854a0.

Fowler, C.M.R. (2005). The Solid Earth: An introduction to global geophysics: Eos, Transactions American Geophysical Union, v. 72, no. 40, p. 427–427, doi: 10.1029/90EO00309.

Franke, D. (2013). Rifting, lithosphere breakup and volcanism: Comparison of magma- poor and volcanic rifted margins. Mar. Pet. Geol. 43, 63T87, doi: 10.1016/j.marpetgeo.2012.11.003.

Funck, T., Hopper, J.R., Larsen, H.C., Louden, K.E., Tucholke, B.E. and Holbrook, W.S. (2003). Crustal structure of the

ocean-continent transition at Flemish Cap: Seismic refraction results, J. geophys. Res., 108 (B11), 2531, doi: 10.1029/2003JB002434.

Funck, T., Jackson, H.R., Louden, K.E., Dehler, S.A. and Wu, Y. (2004). Crustal structure of the northern Nova Scotia rifted continental margin (eastern Canada), J. geophys. Res., 109, B09102, doi:10.1029/2004JB003008.

Gueguen, E., Doglioni, C., Fernandez, M. (1998). On the post-25 Ma geodynamic evolution of the western Mediterranean. T ectonophysics 298, 259–269. doi: 10.1016/S0040-1951(98)00189-9.

Gladczenko, T.P., Coffin, M.F. and Eldholm, O. (1997). Crustal structure of the Ontong Java Plateau: modeling of new gravity and existing seismic data. Journal of Geophysical Research: Solid Earth, 102(B10), pp.22711-22729.

Grevemeyer, I., Ranero, C.R., Ivandic M. (2018a). Structure of oceanic crust and serpentinization at subduction trenches. Geosphere, v. 14, no. 2, doi: 10.1130/GES01537.1.

Hamblin, W.K. (1992). Earth's dynamic systems: Mcmillan publishing company.

Harkin, C., Kusznir, N., Tugend, J., Manatschal, G., McDermott, K. (2019). Evaluating magmatic additions at a magma-poor rifted margin: An East Indian case study. Geophys. J. Int. 217, 25T40, doi: 10.1093/gji/ggz007.

Hess, H.H. (1962). History of Ocean Basins: Pretrologic studies: A volume to honor A.F. Buddington, v. November, p. 599–620.

Heezen, B.C. (1960). The Rift in the Ocean Floor: Scientific American, v. 203, no. 4, p. 98–110, doi: 10.1038/scientificamerican1060-98.

Isacks, B., Oliver, J., and Sykes, L.R. (1968). Seismology and the new global tectonics: Journal of Geophysical Research, v. 73, no. 18, p. 5855–5899, doi: 10.1029/JB073i018p05855.

Jolivet, L., and Faccenna, C. (2000). Meditterranean extension and the Africa-Eurasia collision. Tectonics 19, 1095–1106. doi:10.1029/2000TC900018

Jolivet, L., Augier, R., Robin, C., Suc, J.P., Rouchy, J.M. (2006). Lithospheric-scale geodynamic context of the Messinian salinity crisis. Sediment. Geol. 188–189, 9–33. doi:10.1016/j.sedgeo.2006.02.004

Jolivet, L., Gorini, C., Smit, J., Leroy, S. (2015). Continental Break-up and the dynamics of rifting in back-arc basins: the Gulf of Lion margin. T ectonics 34, 662–679. doi:10.1002/2014TC003570

Kearey, P., Klepeis, K.A., and Vine, F.J. (2009). Global tectonics (Wiley-Blackwell, Ed.).

Kennett, J.P. (1982). Marine Geology, Prentice-Hall, Englewood Cliffs, New Jersey, 813 pp.

King, S.D., and Anderson, D.L. (1995). An alternative mechanism of flood basalt formation. Earth Planet. Sci. Lett., 136:269 279.

Korenaga, J., and Kelemen, P.B. (2000). Major element heterogeneity in the mantle source of the North Atlantic igneous province, Earth and Planet. Sci. Lat., 184, 251-268.

Korenaga, J., (2004). Mantle mixing and continental breakup magmatism. Earth Planet. Sci. Lett., 218:463 473, doi: 10.1016/ S0012-821X(03)00674-5.

Lau, K.W.H., Louden, K.E., Funck, T., Tucholke, B.E., Hobrook, W.S., Hopper, J.R. and Larsen, H.C. (2006). Crustal structure across the Grand Banks-Newfoundland basin continental margin – I. Results from a seismic refraction profile, Geophys. J. Int., 167, 127–156.

Le Douaran, S., Burrus, J. and Avedik, F. (1984). Deep structure of the north-western Mediterranean Basin: Results of a two-ship seismic survey. Marine Geology, 55(3-4), pp.325-345.

Le Pichon, X. (1968). Sea-floor spreading and continental drift: Journal of Geophysical Research, v. 73, no. 12, p. 3661–3697, doi: 10.1029/JB073i012p03661.

McKenzie, D. P. (1978). Some remarks on the development of sedimentary basins. Earth Planet.Sci. Lett. 40, 25-32.

Maclennan, J., McKenzie, D., Gronvold, K. (2001). Plume-driven upwelling under central Iceland, Earth Planet. Sci. Lett., 194, 67-82.

Morgan, W.J. (1968). Rises, trenches, great faults, and crustal blocks: Journal of Geophysical Research, v. 73, no. 6, p. 1959–1982.

Mutter, J. C., Buck, W. R., and Zehnder, C. M. (1988). Convective partial melting: 1. A model for the formation of thick basaltic sequences during the initiation of spreading. Journal of Geophysical Research, 93(B2), 1031. doi: 10.1029/jb093ib02p01031.

Nova Scotia Department of Energy (2011). Play Fairway Analysis – Offshore Nova Scotia, Chapter 2 - Plate tectonics offshore Nova Scotia, 17 pp., Canada, http://energy.novascotia.ca/oil-and-gas/ offshore/play-fairway-analysis/analysis.

Pérez-Gussinyé, M. and Reston, T.J., 2001. Rheological evolution during extension at nonvolcanic rifted margins: Onset of serpentinization and development of detachments leading to continental breakup. Journal of Geophysical Research: Solid Earth, 106(B3), pp.3961-3975.

Péron-Pinvidic, G., and Manatschal, G. (2008). The final rifting evolution at deep magma-poor passive margins from Iberia-Newfoundland: a new point of view. International Journal of Earth Sciences, 98(7), 1581–1597. doi:10.1007/s00531-008-0337-9.

Péron-Pinvidic, G., Manatschal, G., Osmundsen, P.T. (2013). Structural comparison of archetypal Atlantic rifted margins: A review of observations and concepts. Mar. Pet. Geol. 43, 21T47, doi: 10.1016/j.marpetgeo.2013.02.002.

Peron-Pinvidic, G. and Manatschal, G. (2019). Rifted margins: State of the art and future challenges. Frontiers in Earth Science, 7, p.218.

Pluijm, B. A. V. der, and Marshak, S. (2004). Earth Structure: An Introduction to Structural Geology and Tectonics, 2nd Edition, W.W. Norton an Company, New York, US.

Prada, M, (2014). The structure and formation of the Tyrrhenian basin in the Western Mediterranean back- arc setting. Doctoral Thesis, Barcelona University, 294 p.

Prada, M., Sallarès, V., Ranero, C.R., Vendrell, M.G., Grevemeyer, I., Zitellini, N. and de Franco, R., 2014. Seismic structure of the Central Tyrrhenian basin: Geophysical constraints on the nature of the main crustal domains. Journal of Geophysical Research: Solid Earth, 119(1), pp.52-70.

Prada, M., Sallarès, V., Ranero, C.R., Vendrell, M.G., Grevemeyer, I., Zitellini, N. and de Franco, R. (2015). The complex 3-D transition from continental crust to back-arc magmatism and exhumed mantle in the Central Tyrrhenian Basin. Geophys. J. Int., 203(1), 63–78.

Ranero, C.R., Pérez-Gussinyé, M. (2010). Sequential faulting explains the asymmetry and extension discrepancy of conjugate margins. Nature 468, 294–9. doi:10.1038/nature09520.

Rehault, J.-P., Boillot, G., Mauffret, A. (1984). The western mediterranean basin geological evolution. Mar. Geol. 55, 447–477.

Reston, T.J. (2009). The structure, evolution and symmetry of the magma-poor rifted margins of the North and Central Atlantic: A synthesis. Tectonophysics 468, 6T 27, doi: 10.1016/j.tecto.2008.09.002.

Ryan, W. B. R., K. J. Hsü, M. B. Cita, P. Dumitrica, J. Lort, W. Maync, W.D. Nesteroff, G. Pautot, H. Stradner, and F. C. Wezel (1973). Site 120, in Initial Reports of the Deep Sea Drilling Project, JOIDES, vol. 13, edited by A.G. Kaneps, pp. 19-41, Washington (U.S. Government Printing Office).

Sallarès, V., and Charvis, P., (2003). Crustal thickness constraints on the geodynamics evolution of the Galapagos Volcanic Province, Earth and Planet. Sci. Let., 214, 545-559, doi: 10.1016/S0012-821X(03)00373-X.

Sallarès, V., Martínez-Loriente, S., Prada, M., Gràcia, E., Ranero, C., Gutscher, M.A., Bartolome, R., Gailler, A., Dañobeitia, J.J. and Zitellini, N. (2013). Seismic evidence of exhumed mantle rock basement at the Gorringe Bank and the adjacent Horseshoe and Tagus abyssal plains (SW Iberia). Earth and Planetary Science Letters, 365, pp.120-131.

Sallarès, V., Meléndez, A., Prada, M., Ranero, C.R., McIntosh, K. and Grevemeyer, I. (2013b). Overriding plate of the Nicaragua convergent margin: relationship to the seismogenic zone of the 1992 tsunami earthquake, Geochem. Geophys. Geosyst., 14, 3436–3461.

Sawyer, D., Whitmarsh, R., and Klaus A. (1994). Iberia Abyssal Plain Sites 897-901, paper presented at Proceedings of the Ocean Drilling Program Initial Rep.

Sibuet, J.C., Srivastava, S. and Manatschal, G. (2007). Exhumed mantle-forming transitional crust in the Newfoundland-Iberia rift and associated magnetic anomalies. Journal of Geophysical Research: Solid Earth, 112(B6).

Smith, P.J. (1973). Topics in geophysics: The Open University Press.

Sutra, E., Manatschal, G. (2012). How does the continental crust thin in a hyperextended rifted margin? Insights from the iberia margin. Geology 40, 139T 142. doi: 10.1130/G32786.1.

Taylor, B. (1995). Backarc Basins: Tectonics and Magmatism, Plenum Press, New York, 524 pp.

Van Avendonk, H.J., Holbrook, W.S., Nunes, G.T., Shillington, D.J., Tucholke, B.E., Louden, K.E., Larsen, H.C. and Hopper, J.R. (2006). Seismic velocity structure of the rifted margin of the eastern Grand Banks of Newfoundland, Canada. Journal of Geophysical Research: Solid Earth, 111(B11).

Vine, F.J., and Matthews, D.H. (1963). Magnetic Anomalies over Oceanic Ridges: Nature, v. 201, no. 4897, p. 947–949, doi: 10.1038/201591a0.

White, R., and McKenzie, D. (1989). Magma at Rift Zones: The Generation of Volcanic Continental Margins and Flood Basalts, J. Geophys. Res., Vol. 94, No. B6, pp 7685- 7729.

White, R.S., McKenzie, D., and O'Nions, R.K. (1992). Oceanic crustal thickness from seismic measurements and rare earth element inversions. J. Geophys. Res. 97, 19683–19715.

White, R.S., Smith L.K., Roberts A.W., Christie P.A.F., Kusznir N.J., and the rest of the iSIMM Team (2008). Lower-crustal intrusion on the North Atlantic continental margin, Nature, Vol. 452, doi:10.1038/nature06687460.

Whitsmarsh, R.B., Bull, J.M., Rothwell, R.G., and Thomson, J. (1996). The evolution and structure of ocean basins, in Summerhayes, C. and Thorpe, S.A. eds., Oceanography: An illustrated guide, Manson Publishing Ltd, p. 113–135.

Whitmarsh, R. B., M.-O. Beslier, P. J. Wallace, and Shipboard Scientific Party (1998). Sites 1065–1070, Proc. Ocean Drill. Prog. Initial Rep.,173, 65–294.

Whitmarsh, R. B., and Wallace, P. J. (2001). The rift-to-drift development ofthe west Iberia nonvolcanic continental margin: A summary and reviewof the contribution of Ocean Drilling Program leg 173, Proc. Ocean Drill.Prog. Sci.

Results, 173. doi: 10.2973/odp.proc.sr.173.017.2001.

Wegener, A. (1915). The origin of continents and oceans: Courier Corporation.

Wilson, J.T. (1963). Hypothesis of Earth's Behaviour: Nature, v. 198, no. 4884, p. 925–929, doi: 10.1038/198925a0.

Wilson, J.T. (1965). A new class of faults and their bearing on continental drift.: Nature, v. 207, no. 4995, p. 343–347, doi: 10.1038/207343a0.

Wu, Y., Louden, K.E., Funck, T., Jackson, H.R. and Dehler, S.A. (2006). Crustal structure of the central Nova Scotia margin off Eastern Canada, Geophys. J. Int., 166, 878–906.

Part II
METHODOLOGY

Chapter 3

Multi-Channel reflection Seismic data

3.1. Data acquisition

A marine Multi-Channel Seismic (MCS) reflection system is formed by a source and an array of receivers (Fig. 3.2). The source generates a controlled acoustic energy signal through a compressed air release from airgun chambers. The energy is released systematically in points with recorded spatial and temporal coordinates. The acoustic waves generated by the airgun travel through the water layer and penetrate within the subsurface, being partially reflected at internal physical boundaries having a contrast of acoustic impedance. Aside from internal reflections, the acoustic wavefield also suffers other wave-transforming effects (Lowrie, 2007). Acoustic impedance (Z) is a physical property that results from the contrast in two juxtaposed layers of the product of the material density (ρ) and propagation velocity (v) of the seismic waves through them:

$$Z = \rho v \tag{3.1}$$

The variability of this physical property across neighbouring rock bodies or layers is the one that allow us to image changes in lithology or different structures at depth. Variations in the acoustic impedance give rise to reflections according to the reflection coefficient defined by:

$$R = \frac{Z_2 - Z_1}{Z_2 - Z_1} \tag{3.2}$$

The goal of this system is to record these acoustic reflections at the internal boundaries for a later processing and analysis. The repetition of this process in every shot and the combination of the different recordings provides a “seismic image” of the subsurface (Yilmaz, 1987).

The energy originated by a shot and recorded as a time series by a receiver is called a seismic trace. Seismic traces are function of the amplitude and the time of the reflection (Yilmaz, 1987). The MCS reflection method is based on redundancy by recording of the same information in neighbouring

receivers, so that we enhance the signal-to-noise ratio. To produce redundancy, each reflector surface points are recorded in more than one seismic trace using multiple shots. Consequently, by recording the same subsurface information from multiple shots in multiple receivers random noise can be easily attenuated, and the real signal amplified (Yilmaz, 1987).

In particular, in marine MCS experiments the data are acquired with instruments that are towed at several meters depth behind a vessel. The most common energy source is the airgun (Fig. 3.1a,b), which releases bursts of compressed air. A combination of airguns is used to attenuate the bubble effect produced by the repeated collapse of the air bubble released from the source so that the source signal is as similar to a spike as possible. The source is towed at the depth designed to minimize the loss of desired frequency content by destructive interference of the signal ghost, produced by the energy reflection of the sea surface. Recording elements are distributed along a cable, which we refer to as the streamer (Fig. 3.1a). The recording units inside the cable are commonly hydrophones that record the pressure perturbations produced by the generated acoustic signal together with the ambient noise. The signal received at different groups of hydrophones of the streamer are typically summed before recording the combined signal into a "channel". The course of the streamer is monitored with compasses, which provide information of the lateral deviations (feathering angle) of the streamer along all its length (Fig. 3.1d). The streamer depth is controlled by "birds", (Fig. 3.1c), which are attached all along the streamer. Birds measure and move the streamer to a depth designed to minimize the effect of the streamer ghost. The last element is the tail-buoy, equipped with a differential GPS, allowing to continuously monitoring the position of the end of the streamer (Fig. 3.1e).

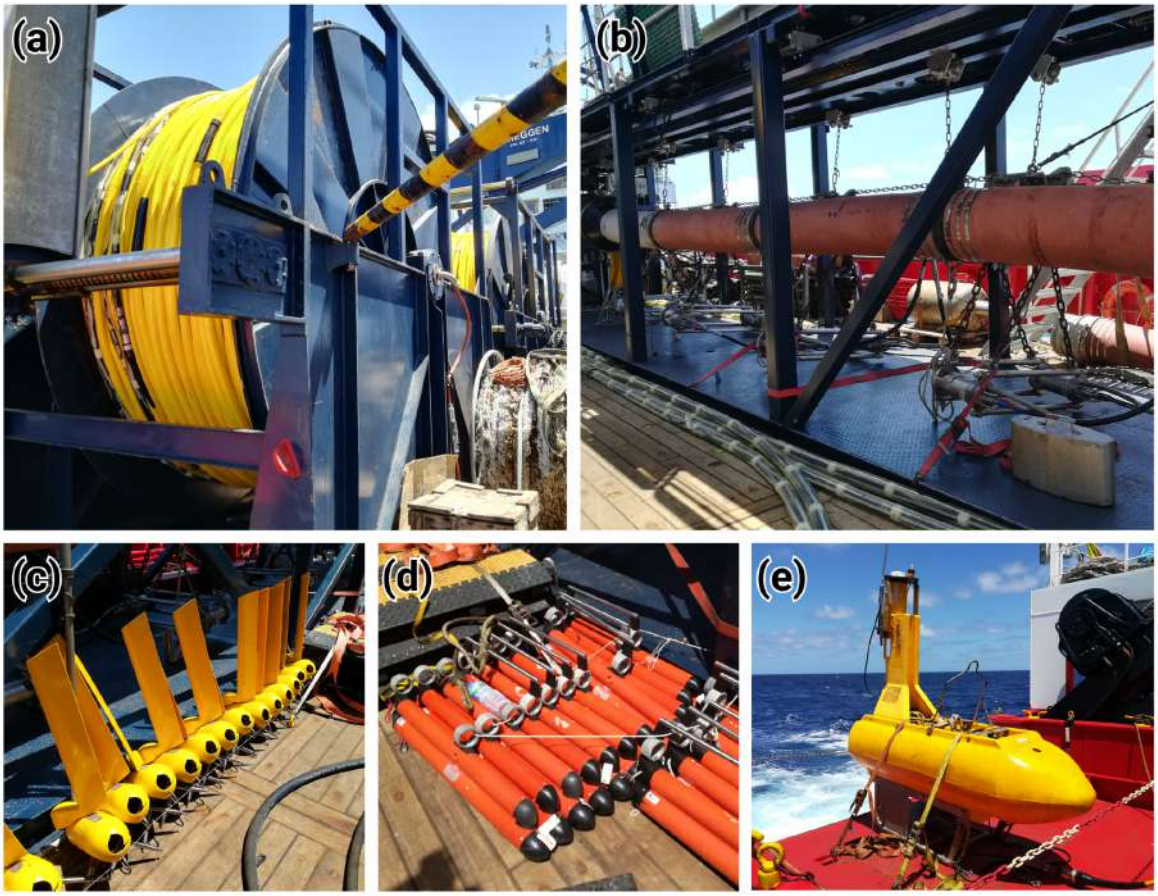

Figure 3.1 - Detail of the MCS acquisition system used during the FRAME survey (2018). It includes (a) the ~6.0 km long streamer with 480 channels, which record the signal received by the hydrophones, (b) an array of air guns used as seismic source, (c) the birds, (d) the compasses and (e) the tail buoy.

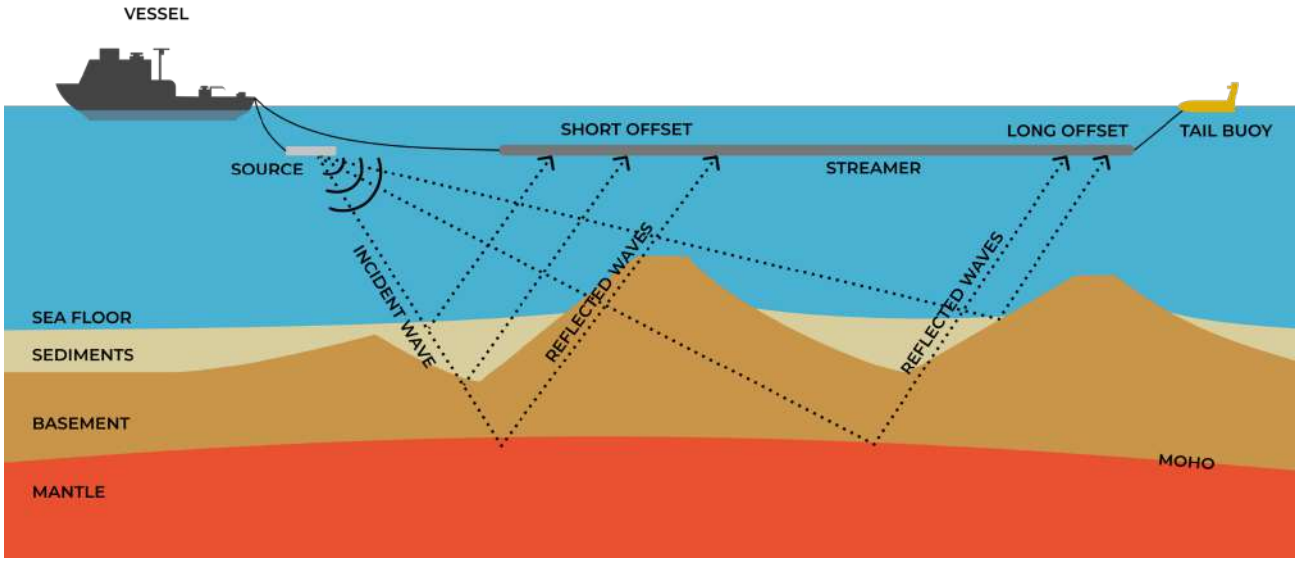

Figure 3.2 - Schematic representation of the MCS experiment and the propagation of the reflected waves at each interface of the subsurface.

3.1.1. Acquisition parameters

In my Ph.D. thesis, I processed and interpreted two profiles acquired in two different marine seismic surveys. One was acquired during the FRAME cruise in July 2018 (Leg-1) across the Tagus Abyssal Plain. I participated in this cruise, which was leaded by the Barcelona-CSI group. The second was acquired during the SARDINIA cruise in July 2006 across the Gulf of Lions, leaded by Ifremer (France). The acquisition parameters of each survey as well as my contribution to produce the final seismic image used for this work are detailed below:

➢ FRAME cruise (2018)

The profile across the Tagus Abyssal Plain was acquired in the framework of the FRAME project, funded by the Plan Nacional I+D+I with reference number CTM2015-71766-R (PIs: C.R. Ranero and V. Sallarès). The acquisition was done with the MCS system of the Spanish Research Vessel (R/V) "Sarmiento de Gamboa". During the Leg-1, deep-penetration seismic data were acquired allowing to image the basin at a crustal scale. Two G-II gun sub-arrays with a total volume of 3920 c.i. and air pressure of 2000 p.s.i. and a 6 km-long Sercel Sentinel solid state multi-channel digital streamer with 480 active channels were towed behind the vessel. The result is a comprehensive dataset of MCS profiles of unprecedented quality for academic cruises in the region. This dataset allowed us to use modern processing and imaging techniques to retrieve high quality images of crustal-scale tectonic structures, and a good resolution of the sedimentary infill of the basin.

➢ SARDINIA cruise (2006)

The profile across the Gulf of Lions was acquired by Ifremer (France) during the SARDINIA survey, which took place in July of 2006 on board the French R/V "L'Atalante". The vessel was equipped with a tuned airgun array with a total capacity of 8260 c.i. and a 4.5 km long streamer with 360 active channels. The shot interval was 60 s, giving a trace spacing of about 140-150 m because the streamer

data were collected at the same time of the wide-angle data on ocean bottom seismometers. The acquisition parameters are detailed in table 3.1.

The acquisition parameters of both MCS profiles are described in the following table (Table 3.1).

	FRAME – Leg 1	**SARDINIA**
Number of active channels	480	360
Distance between channels (m)	12.5	12.5
Total streamer length (m)	6000	4500
Streamer depth (m)	19-20	NA
CMP distance (m)	6.25	6.25
Sample rate (ms)	2	2
Trace length (s)	14.5	12
Shot distance (m)	37.5	150
Air-guns depth (m)	10	NA

Table 3.1 - Acquisition parameters of the MCS profiles during the FRAME and SARDINIA cruises.

3.2. Data processing

We should take into account that a seismic image is not exactly an image of the sub-surface. It is a representation of the wave field produced by energy travelling across the sub-surface (Stein and Wyssession, 2003). As stated above, a seismic study focuses on the record and analysis of the reflections generated by a contrast in acoustic impedance (Z) at the interfaces of the medium. Changes of the value of Z producing reflections are associated with changes in lithology or fluid content, either related to stratigraphic changes or to tectonic structure. Unfortunately, data contains background and ambient noise that deteriorates the signal expression and obscures primary reflections, which are the seismic processing target.

Examples of coherent noise (i.e. it occurs always at the same location when shooting) in marine reflection experiments are the water-layer multiples, and refracted waves. Furthermore, it is necessary to take into account that our signal is not a perfect spike due to source bubbles, and also that acoustic signal loses energy with depth, which is particularly acute at high frequencies. All these problems affect the quality of the seismic image, although it can be largely mitigated with an adequate processing of the data.

The three main steps in a processing flow are the following: (i) Deconvolution, which increases the vertical resolution by compressing the generated signal (wavelet) close to a spike while suppressing reverberations, (ii) Common Mid-Point (CMP) stack to increase the signal-to-noise ratio, and (iii) Migration, which removes the diffractions and moves dipping reflections closer to their real position in the sub-surface, and increases horizontal resolution (Yilmaz, 1987). Most other processing techniques can be considered secondary, in the sense that they help to the effectiveness of these three primary steps.

The processing flow in the time domain (Table 3.2) has been designed to put special emphasis in frequency preservation, amplitude preservation and velocity determination. The processing software is the commercial package *GLOBE Claritas*.

3.2.1. Pre-processing

In this step, we describe the first analysis of data to design the proper time processing sequence. It consists on a first data quality control, a broad band-pass filter, a time resample of data, addition of the geometry information, and an amplitude recovery to balance amplitudes that is convenient for subsequent processing steps. During the acquisition of MCS data several factors like the malfunction of channels or the interference of signal due to marine traffic may occur, causing incoherent noise on the registered signal. It is important, then, to control the quality of the data before starting with a more exhaustive processing. Hence, during quality control, checks was carried out for missing traces, and bad or noisy shots. A delay between trigger and the air-guns shot time, applying a positive time shift correction of 50 ms was applied.

The **band-pass filter** is designed to partially attenuate high-amplitudes and to remove the lowest frequencies related to sea swell and instrument noise, and a high cut to prevent time aliasing of the signal. The values applied are 1-3-100-120 Hz.

Data were **resampled** from 2 millisecond (ms) to 4ms to reduce data volume without losing information in the frequency bandwidth of interest given the seismic source designed for the goal to study entire crustal-scale structure.

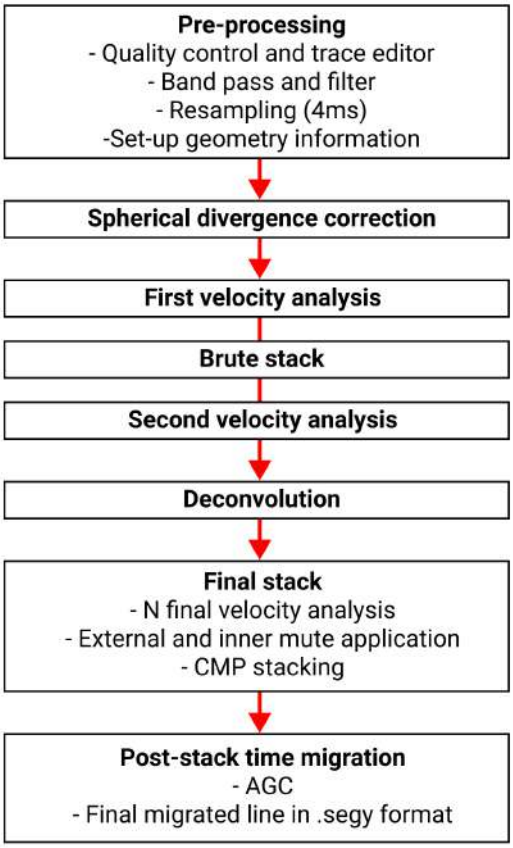

Table 3.2 - Processing flow applied to process the FRAME-2018 dataset.

Finally, **we integrated the shot and receiver (channels) acquisition geometry** information in the *seismic trace* headers (i.e. the standard seismic data recording format). This is one of the most important points in a processing sequence, and an essential step to optimize the seismic image. The correct geometry information will place the traces, and therefore, the recorded reflections on their correct positions, increasing the horizontal and vertical resolution. This is fundamental for a later re-organization of the data in Common Mid Points (CMP, Fig. 3.3). Knowing for each shot the position of the source, and channels (receivers) from the navigation information of the streamer allows to insert X, Y coordinates for each trace, and to make the CMP distribution based on that positioning.

Based on the field geometry information, each trace is assigned to a middle point between the shot and the receiver associated to that trace. Traces with the same middle point are grouped together, forming a CMP gather. This term is often used indistinctly with Common Depth Point (CDP) gather, but it must be noted that they are the same only when the reflector is horizontal (Fig. 3.3) and layer velocities are constant, due to the ray path propagation geometry. The CMP groups all the traces with the same shot-receiver middle point, while the CDP refers to the traces that have been reflected in the same point at depth (Fig. 3.3) (Yilmaz, 1987).

3.2.2. Spherical divergence

A **spherical divergence amplitude** correction based on a geological velocity layers' model has been applied. The aim is to recover amplitude decay at depth, especially visible on the high frequencies, due to the geometrical spreading of the wave front propagating through the medium as it interacts with the different layers of the subsurface. Hence, it is necessary to compensate this loss and recover the best resolution of the seismic trace in time before applying further processing.

Therefore, to apply a spherical divergence correction is necessary to have a first estimation of the velocity propagation of the medium. To apply a spherical divergence, we digitized a set of layers following geological criteria, and the velocities of these layers were assigned. The correction of amplitude decay, then, is done by multiplying the samples of the trace by a time variant scalar function that enhances the signal of the trace, increasing its temporal resolution.

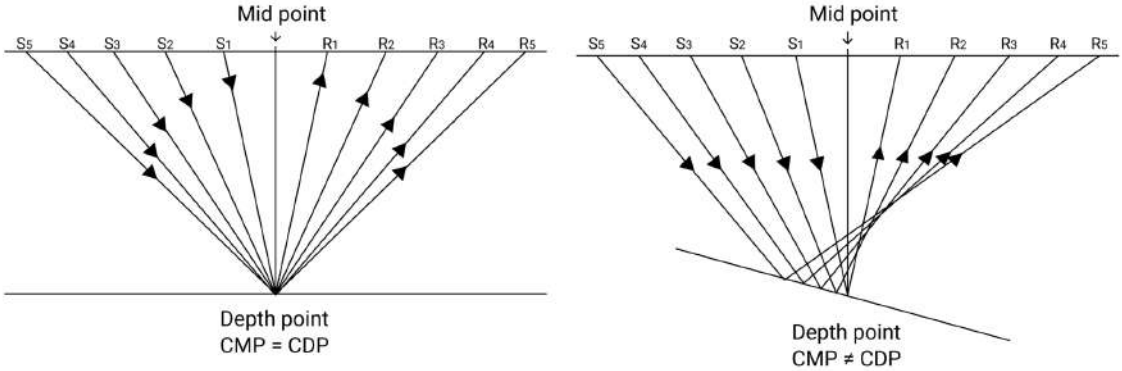

Figure 3.3 - a) CMP gather. When the reflector is a horizontal surface, the depth point for all the traces in the same, thus CMP is coincident (Yilmaz, 1987). b) CMP is used when the reflector is dipping. Although the traces are in the same CMP because the mid-point between source and receiver is the same, they do not come from the same point at depth (Stein and Wyssession, 2003). S: shot; R: receiver.

3.2.3. Deconvolution

Deconvolution tries to recover the reflectivity series, or in other words, the earth impulse response, removing the record of the source wavelet from the seismic trace. The main aim of this process is to bring the wavelet as close to a spike as possible, increasing the vertical resolution Sorry, no English. no es tus datos, es en general para aguas someras (Yilmaz, 1987; Stein and Wysession, 2003).

To understand how does deconvolution works, it is necessary to understand how the record of a seismic trace is done. Earth is composed by layers of different lithologies and physical properties. From a seismic point of view, these materials are defined by their density and by the seismic velocity of the waves traveling across them. The seismic trace is the convolution between the earth impulse response and our wavelet. In an ideal case, the generated wavelet would be a unique spike, and we will record just the impulse response. As the generated signal is not a perfect spike, we carried out a deconvolution processes. The deconvolution tries to approximate the generated wavelet as close as possible to a spike, leaving in our record section just the earth impulse response (Yilmaz, 1987).

To perform deconvolution, we need to design a filter, which will modify the wavelet recorded in our data. A fundament assumption of this filter is that the geology is random, so the impulse response is also random. This implies that if there is a pattern replicated along the seismic trace, it must be induced by the source wavelet (Yilmaz, 1987).

In our case, we applied a Wiener Predictive deconvolution. The main advantage of performing a Wiener deconvolution is that preserves relative amplitudes and primary reflection energy. It is used to attenuate short period reverberations, such as source bubble signature. It is more effective in deep waters, although it also improves the seismic profiles in the shallower parts. Wiener filters are used to compress the seismic wavelet, increasing in that way temporal resolution. In the limit, it can be used to spike the seismic wavelet and to obtain an estimate for the earth reflectivity series (Yilmaz, 1987).

This deconvolution process has been performed with a spatial variant filter, designed in the shots. In this work, two design windows were used to account for the different geological structures with depth and for the loss of energy and frequency content of the seismic wavelet with depth. Hence, a first window was designed for the shallow sediments and a second one for the basement. We compared the results for a same operator length of 400 ms with different values of the gap length (Fig. 3.4) and finally we chose the 24 ms gap length for processing.

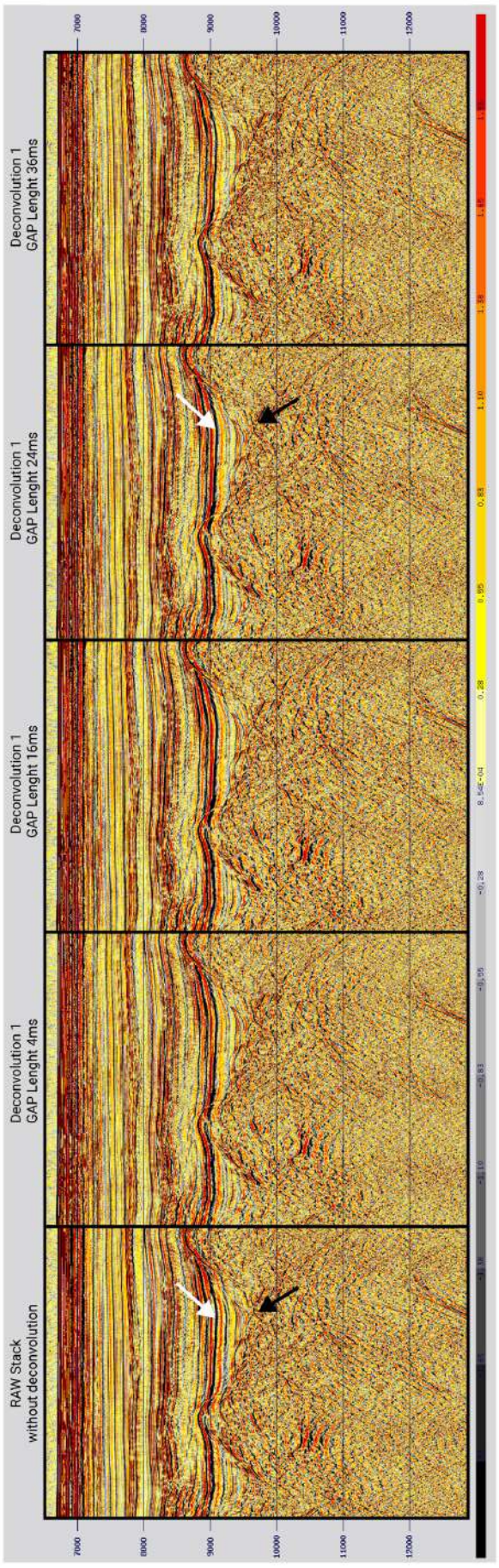

Figure 3.4 - (a) Zoom of a stack without and (b, c, d, e) with deconvolution. The deconvolution process is highly efficient removing the bubble noise and other short peg reverberations, which is important to obtain a clearly image of the sedimentary layer. White arrows in (a) and (d) show that with the deconvolution, reflections gain in continuity and amplitudes of low energy reflections are enhanced over the surrounding noise. Dark arrows in (a) and (d) show that with the deconvolution the reflections (e.g. the top of the basement) are also more continuous.

3.2.4. Velocity analysis

To create a first velocity model and a brute stack, we made a first approach on the basis of an interval velocity model, taking into account the geology of the area. After a water-velocity stack, we digitized a set of layers following geological criteria, and the velocities of these layers were asigned based on known average velocities in the region from literature (Afilhado et al., 2008; Dean et al., 2000). This procedure can be used in regions where there is a pre-existing considerable knowledge of the geology.

Once we had this first "coarse" regional velocity model, we started with the velocity analysis to achieve an accurate velocity model. The NMO is the difference between the travel-time at some offset and at zero offset. The velocity needed to correct the NMO effect is the NMO velocity, which is equivalent to the velocity of the medium above the target reflection (r.m.s velocity). This is the velocity which best flatten the hyperbolas (Fig. 3.5a,c) (Yilmaz, 1987; Stein and Wyssession, 2003). In order to determine this NMO velocity, we performed the velocity spectrum analysis through the analysis of semblance panels. In this method, different NMO velocities are applied to the same CMP for all the travel times, and the result is stacked for each velocity. The resulting panels are function of the velocity used for the NMO correction (X axis) and the travel time (TWT, Y axis). In the points where the chosen velocity is the correct one, reflection hyperboles are horizontal, given a maximum of amplitude in the semblance panel (Fig. 3.5b). Using the correct NMO velocity, the primary reflection will be aligned in phase on all traces, summing in a constructive way and giving strongly arrivals. On the other hand, other arrivals as incoherent noise or multiples will be shifted and out of phase, summing in a destructive way and so, losing amplitude (e.g. Stein and Wyssession, 2003).

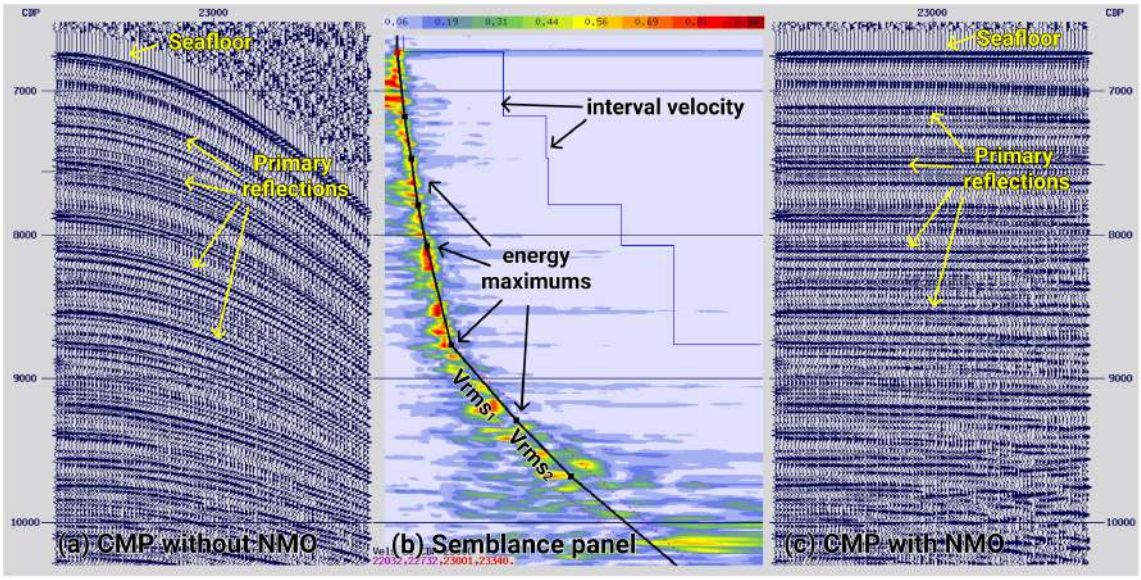

Figure 3.5 - a) CMP 23000 of the profile acquired in the FRAME survey without NMO correction. Seafloor and other primary reflections are identified and present a hyperbolic shape due to the different travel times in function of the offset (X axis: offset increasing toward the right, Y axis: TWTT in ms). b) Semblance spectrum calculated for CMP 23000. Velocities (X axis) vary from 1475 m/s to 3000 m/s. Red colours correspond to energy maximums, which are associated with a proper r.m.s velocity (Vrms). This Vrms can be converted to interval velocity. With the Vrms, the NMO correction is applied. c) Same CMP with the NMO correction applied. Vrms has been found through the semblance analysis. It is noticed how this velocity removes the difference in travel time due to the offset, and the primary reflections are now horizontal, making possible the stacking of the signal energy.

3.2.5. Final stack

At this point, the pre-stack processing sequence is almost finished. To obtain the final stack section, we performed the two main following steps: final velocity analysis, trace muting, CMP stacking and band-pass filter.

To obtain the final stack section, we performed several velocity analyses, following the same basic principles as in the initial one (see section 3.2.3). This task was done by systematically analysing the semblance panels closer in areas of local complex geology. The aim of this analysis is to estimate an accurate NMO velocity model. NMO correction has an associated a stretching deformation, especially clear in far offset shallow reflections (Yilmaz, 1987; Liner, 1999). It is necessary to remove this deformation, as it can hide the primary reflections. In our case, we have designed an external mute, picked in our NMO corrected CMP (Fig. 3.6). With the aim of removing the remaining multiple energy, we picked an inner mute that helps removing remnants of multiple energy in very near offset were, despite the NMO correction, multiple energy remains horizontal in the CMP corrected gathers (Fig. 3.6).

After the final NMO velocity analysis and the muting, data are ready for the final stack. During stacking, all reflections coming for the same point are summed up, so that the signal to noise (SNR) ratio is enhanced. The longer is the streamer (i.e. the more channels are stacked) the better is the SNR of the stacked image. The result is a final section showing an improved image of the crustal-scale basin structure. Stratigraphic relations between the different sedimentary layers are well imaged in the basin, but deeper structures corresponding to intra-basement discontinuities and even to the Mohorovicic (crust – mantle boundary) discontinuity can also be detected. Before applying the migration to the seismic stack section, we applied a post-stack filtering to attenuate those undesired frequencies from the stack. The frequencies of the filter applied are 1-3-45-60 Hz.

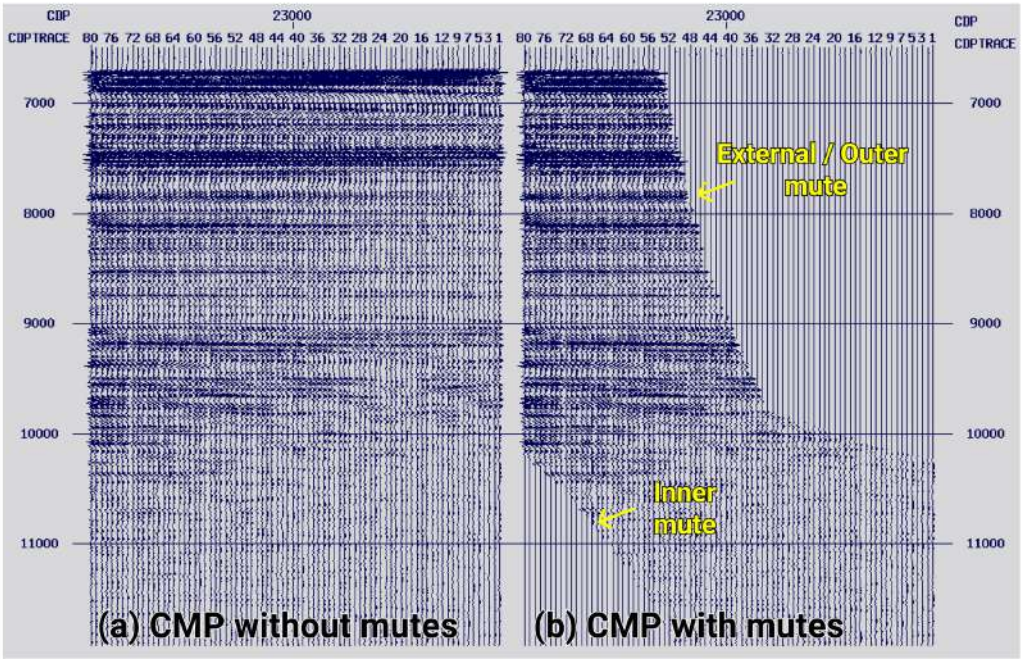

Figure 3.6 - a) CMP 23000 with the final NMO correction applied (X axis: offset increasing toward the right, Y axis: TWT in ms). b) Same CMP with the outer and inner mute applied.

3.2.6. Post-Stack Time Migration

Migration moves dipping reflections to their true position at the subsurface and collapse diffractions. This process allows us to increase the horizontal resolution and the obtaining a seismic image of the subsurface (Yilmaz, 1987).

The migration process assumes that the recorded section is zero offset or, in other words, that source and receivers are at different depths but at the same horizontal coordinate. This is not true, but it can be solved by the so-called "exploding reflectors propagation model", in which every point at the reflector surface acts as a new source, generating a new wave field (Fig. 3.7) (Yilmaz, 1987; Stein and Wysession, 2003).

The aim of the migration is removing the effects of the propagation and distortions in the reflection positions caused by the ray-path trajectory, and also to undo the effects of diffraction, obtaining a realistic image of the subsurface (Stein and Wyssession, 2003).

The velocity model used to perform the time migration has to be designed carefully since low velocities do not entirely collapse reflectors, and high velocities may create overcorrected artifacts or smiles. The velocity model used in this work was designed following the geometry of the main reflections, which were interpreted to correspond to the main geological boundaries, which in turn limit layers with different seismic velocity. In this work, the migration step has been performed by applying a post-stack time migration based on a finite difference algorithm that works on the T-X domain and allows migration of 45°-60° dipping events. In our case, a window for the time slices of 20 ms and a dip filter factor equal to the cosine of 65°.

Finally, we applied a seafloor mute and a final amplitude balance. This balance is a time-variant scaling in which the scaling function follows a predefined criterion (Yilmaz, 1987). In our case, we choose an Automatic Gain Control (AGC) criterion, designed to bring up weak signals.

The final result is a crustal scale section displaying a number of crustal features and tectonic structures at the whole crust scale. It also has a reasonably good resolution in the sedimentary infill of the basin.

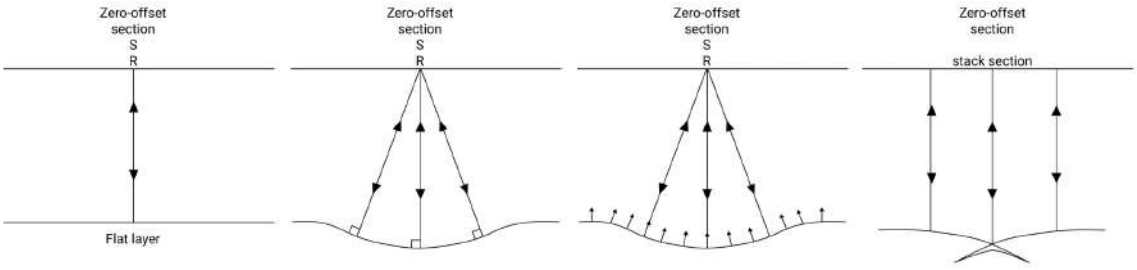

Figure 3.7 - SR: Source-Receiver pair. a) Zero offset seismic section from a horizontal reflector. Reflectors points are located directly below the SR. b) When the reflector is not horizontal, reflections paths can travel along different paths with the same longitude. c) When the energy arrives to the reflector, explode giving a wave field with the geometry of the reflector (exploding reflector model). d) Stacked section of this structure assuming zero-offset reflections, migration tries to reverse this process and find the initial wave field and the correct reflector geometry (Stein and Wyssession, 2003).

Chapter 4

Refraction and Wide-Angle reflection Seismic data

4.1. Data acquisition

Refraction and Wide-Angle reflection Seismic (WAS) profiling is also a controlled-source seismic method using both reflected and refracted waves recorded at considerably larger offsets than Multi-Channel Seismic (MCS) data, typically distances of several tens of km (although shorter offsets are used for shallow targets). In marine studies, the signal is produced by a seismic source (typically airguns), as for MCS, that generates a seismo-acoustic wavefield that propagates through the media and reflects and interfaces or travels along seismic boundaries to return back to the surface, where it is recorded by a set of receivers. The fact that the signal is recorded at longer offsets makes that the system allows recording not only reflected but also refracted waves travelling at high depths that map

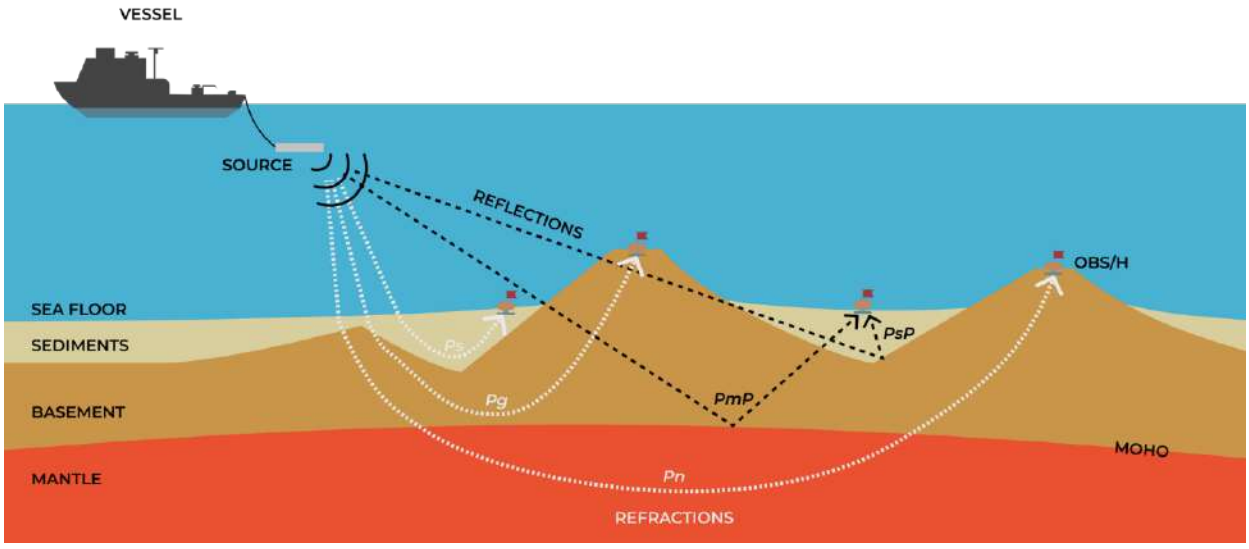

Figure 4.1 - Schematic representation of the WAS experiment and the propagation of the different P-waves seismic phases refracted through the sediments (PsP), crust (Pg), and mantle (Pn); and reflected at the sediment-basement boundary (PsP), and at the crust-mantle boundary (PmP).

for longer times the structure of the medium. Modelling of WAS refractions provides direct information of the medium's velocity field and, when it is combined with reflections, it provides information on the geometry of the geological discontinuities, too.

In a marine setting, the acquisition system consists of a source of an airgun array and a set of receivers commonly deployed at the seafloor (Fig. 4.1). Receivers can be either Ocean Bottom Seismometers (OBS) and/or Ocean Bottom Hydrophones (OBH), as shown in Figure 4.2 respectively. The difference is that OBSs measure the three components of motion with a seismometer located at the seafloor, while OBHs measure only pressure variations within the water column. After the survey, OBH/S are released from their anchors and rise up to the sea surface, where they are recovered from the vessel. The airgun source towed behind the vessel is similar to that of MCS systems but, as the objective is to map longer travel times in the deep subsurface, the source is typically more powerful than that of MCS and is towed a few meters deeper to generate lower frequencies. The low frequencies suffer less attenuation as they propagate so they can reach longer distances and in cases comparatively deeper depths. Firing interval is also larger than in MCS experiments to avoid the background noise produced by the noise from the previous shots trapped in the water layer, the so-called "wrap around" noise. The typical shooting interval is 60-120s or 150-300m in distance. Receiver spacing is much larger than the distance between channels in MCS systems, of several kms

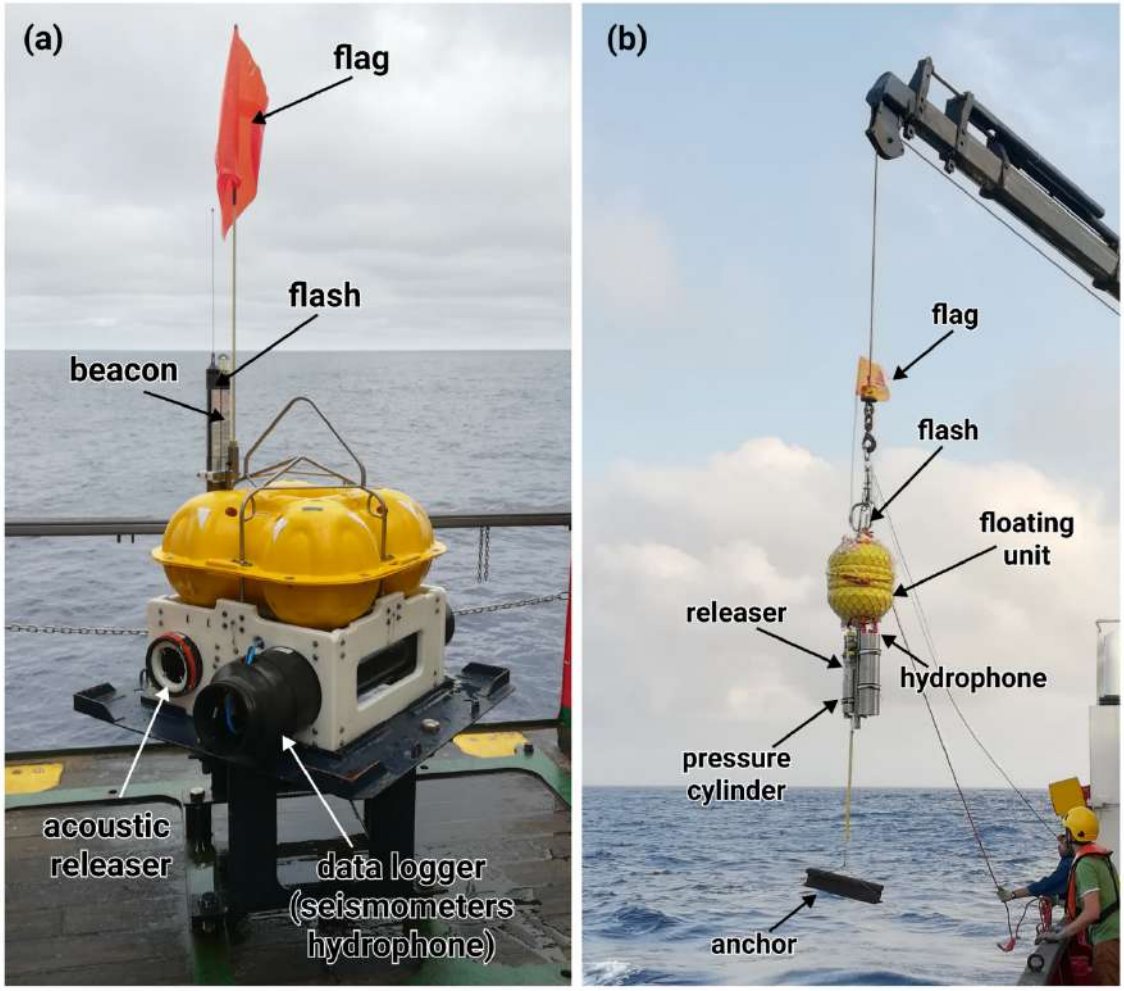

Figure 4.2 - (a) Ocean Bottom Seismometer just after being recovered and (b) Ocean Bottom Hydrophone ready for deployment during the FRAME (2018) WAS survey.

typically. Denser spacing helps improving the accuracy of the final velocity model although this depends on the method used to retrieve the velocity model. In general, the smaller the receiver spacing, the higher the redundancy of data, and hence the information provided by the data set in the modelling process is better constrained. The interval between receivers depends on many factors, such as the bathymetry or the number of available receivers, but for modern crustal-scale experiments it is typically set at 5-15 km spacing.

From the different phases recorded in the OBS/H, those that are used for velocity modelling are the body waves (i.e. in general primary or P-waves, and less frequently, also secondary or S-waves). In general, the ones that are more visible in WAS experiments are the P-waves because they arrive earlier in the recordings, hence their name (Fig. 4.1). As in the case of MCS recordings, at short offsets OBS/Hs mainly record near-vertical reflections at acoustic impedance contrasts across sharp geological interfaces, whereas at larger offsets they record both reflections and transmitted or refracted waves through the medium following Snell's law:

$$\frac{\sin\theta_1}{sin\ \theta_2} = \frac{v_1}{v_2} \tag{4.1}$$

The ray path (red line in Fig. 4.3) incides with angle θ_1 from a medium with velocity v_1, and refractive index n_1 to a lower medium with velocity v_2, and refractive index n_2; $v_1 < v_2$. As a result, the ray path is refracted with an angle θ_2 through the lower medium.

As the angle of incidence increases due to the increase of the source- receiver distance, the refracted rays experience a change of direction according to Snell's law (Fig. 4.3). When the source – receiver distance reaches the critical distance, the ray is critically refracted, and travels parallel to the boundary between the two layers along the one with faster velocity (Fig. 4.3), following the equation of the critical angle:

$$\sin i_c = \frac{V_1}{V_2} \tag{4.2}$$

where i_c is the angle of incidence, and V_1 and V_2 are the velocities in the two-different media.

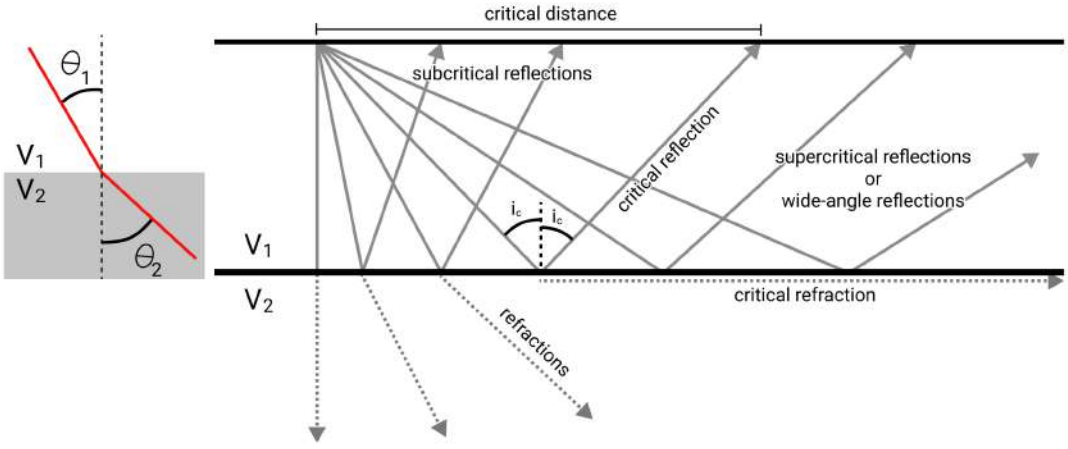

Figure 4.3 - Schematic representation of the evolution of reflections and refractions as the source – receiver distance increases, following the Snell's law. i_c= critical angle, v_1=velocity of layer 1, v_2=velocity of layer 2, $v_1 < v_2$.

At angles greater than the critical angle refraction is no longer possible. The energy from seismic rays that are incident more obliquely than the critical angle is entirely reflected. These reflections are known as *supercritical reflections*, or simply *wide-angle reflections*. They lose little energy to refractions and travel large distances providing information of boundaries like the sediment-basement boundary or the Moho (Lowrie, 2007).

The data recorded consist of a continuous temporal trace than includes, at different offsets, the seismic events produced by the arrivals of the recorded waves corresponding to the different seismic phases. This traces are sorted by source - receiver offset, providing the so-called "common receiver gather" or "record section", where each trace corresponds to a shot and that are commonly represented in an offset-time corrected diagram as shown in Figure 5.2a. This representation makes easier the phase identification and interpretation.

4.1.1. Acquisition parameters

For my Ph.D. thesis, I used WAS data acquired during two surveys, as with the MCS data. I participated in the second leg of the FRAME cruise in September 2018 (Leg-2) across the Tagus Abyssal Plain, which was leaded by the Barcelona-CSI group. I also used WAS data acquired during the SARDINIA cruise in July 2006 across the Gulf of Lions, which was leaded by IFREMER (Gailler et al., 2009).

➢ FRAME cruise (2018)

During the FRAME cruise, a total of 35 instruments, including 17 LC2000 4x4 Ocean Bottom Seismometers (OBS) from the Spanish CSIC pool, and 18 Ocean Bottom Hydrophones (OBH) from Geomar-KUM (Germany), were deployed along a 450km-long profile, so the average distance between instruments was of 10 km. The seismic source consisted of a total of 16 airguns of the G-II model, organized in 2 arrays and towed behind the vessel at a depth of 15 m to enhance the low frequency content in the source signal. The released total volume was 5200 c.i (2600 c.i. for each array). Out of the 35 instruments, the data from OBS59 and OBH52 and 75 were corrupted, and OBS70 was not retrieved from the seafloor, so there were 32 usable record sections.

➢ SARDINIA cruise (2006)

Three different OBS models were used during the SARDINIA experiment: 9 micrObs and 1 OldOBS from the IFREMER pool and 4 OBS/H from Geomar-KUM (Germany), totalizing 14 instruments. They were deployed along a 375 km-long profile, so the average distance between instruments was of ~13km. The seismic source was an array of 16 airguns with individual volumes between 61 and 100 c.i., providing a total volume of 8260 c.i. Data from instruments OSB45, OBS49, OBS52 and OBS55 had problems and they were unusable for processing and modelling.

The acquisition parameters for both profiles are detailed in Table 4.1.

	FRAME – Leg 2	SARDINIA
Number of receivers	35	14
Distance between receivers (km)	10	13
Total profile length (m)	490	375
Shot distance (m)	150	150
Number air-gun arrays	16	16
Air-gun capacity (c.i.)	5200	8260
Air-guns depth (m)	15	--

Table 4.1 - Acquisition parameters of the WAS data during the FRAME and SARDINIA cruises.

4.2. Data processing

WAS data processing is simpler than that of MCS data. The WAS processing sequence includes:

4.2.1. Relocation of the instruments

Oceanic currents may drift the OBS/H on its way to the seafloor, causing a variation of the seafloor location with respect to the position of the deployment that can be in cases be as much as hundreds of meters. The relocation allows to define exactly where was the final deployment location of the OBS/OBH before to continue with the next steps. In our case, we relocated the instruments using the arrival times of the direct water-wave from the airgun shots and applying the Metropolis-Hastings algorithm, that minimizes the misfit function between the observed and synthetic first arrival travel-times of the water wave to find the most likely location of the OBS. We relocated all OBSs using an in-house Metropolis-Hastings algorithm that minimizes the misfit function between the observed and synthetic first arrival travel-times of the water wave to find the most likely location of the OBS (Prada et al., 2020).

4.2.2. Processing sequence

The processing sequence used is that generally applied within the group based on previous experience and that includes a predictive deconvolution (see section 3.2.3), a time- and offset-variant Butterworth (or an equivalent) bandpass filter and an amplitude balancing like an Automatic Gain Control (AGC) (e.g. Sallarès and Ranero, 2005; Moeller et al., 2013). In this work the WAS data processing consisted of a Butterworth band-pass filter (5-18Hz) and an AGC for the OBSs of both lines, and a predictive deconvolution, a Butterworth band-pass filtering (2-11Hz) and an AGC for the OBHs.

Chapter 5

Travel-time tomography

There are different ways to model WAS data. Here I focus on the most common methods, which are those that make use of the travel times (or arrival times) of some selected seismic phases, which are known as travel-time modelling methods. Since the information to be fit are the arrival times, the wave propagation equations are commonly simplified to the ray approximation, in which only trajectories and travel times of individual phases for each shot-receiver pair are calculated. These methods can be organized in two categories depending on the way of extracting the spatial distribution of wave propagation velocity from the travel time data: either forward modelling or inversion.

Forward modelling implies that the velocity model and the geometry of the geological boundaries are manually built by an interpreter, and the model is progressively improved by trial- and-error until an acceptable fit between the observed and simulated data is obtained. The fundamental tool to construct the velocity and reflector geometry model is thus a ray-tracing algorithm (e.g. Zelt and Smith, 1992). This method was the most common until the 90's and it is still widely used today, particularly in land experiments where the number of sources is comparatively limited. However, this approach has many limitations, the final solution is strongly subjective, and it does not allow performing formal parameter uncertainty analysis (Loureiro et al., 2016). In addition, it becomes impracticable when there is a large number of sources and receivers as is the case of modern 2D marine WAS experiments, let alone the 3D ones.

In contrast, inverse methods, also known as "tomographic" methods, aim at determining the velocity field in an automatized manner. In addition, the geometry of reflecting boundaries can also be inverted and used to help further constrain the velocity (e.g. Toomey et al., 1994; Korenaga et al., 2000). The tomographic problem is divided in two parts. The first one corresponds to the forward problem, so is the same that must be solved in the forward modelling techniques. It consists on the ray tracing and on the calculation of the synthetic travel-times. The second one is the inverse problem. In this case the actual problem of travel-time calculation is approximated by a linear inversion, in which the travel

time residuals for an initial (i.e. reference) model are related to the model changes by means of the gradient matrix of partial derivatives (i.e. the Jacobian), also known as the sensitivity kernel or Fréchet matrix. The inverse problem, which is solved iteratively, consists on inverting this matrix to retrieve the model changes in the direction of the gradient out from the travel time residuals in each iteration.

5.1. Datasets used for travel-time tomography

The tomographic approach applied in this study combine travel-time picks from MCS and WAS data into a joint inversion, using a modified version of the joint refraction and reflection travel-time tomography code *tomo2d* (Korenaga et al., 2000; Melendez et al., 2015). This tomographic approach is a technical innovation by the Barcelona-CSI group (Begović, 2020), and my PhD is the first application of the new code to field data. Almost all previous joint refraction and reflection travel-time tomography studies use only WAS data, and the MCS information is qualitatively incorporated during the interpretation (e.g. Wu et al., 2006; Klingelhoefer et al., 2014). In contrast, I have jointly inverted travel-times of WAS refractions (first arrivals), near-vertical reflections of MCS and OBS records, and wide-angle WAS reflections. The first step is identifying and picking data from both seismic datasets, for which it is necessary to apply different methodologies that are detailed in the next sections.

5.1.1. Picking of the main horizons in the MCS data

After processing the MCS data, I picked the arrival times of the reflected P-waves at different structural boundaries, particularly the regional, most continuous ones that determined clear vertical changes in P-waves velocities (Vp) observed during processing along the profiles. In particular, I identified and included in the inversion the following MCS horizons: the top and bottom of the salt layer and the top of the basement (TOB) for the Gulf of Lions profile, and those of a regional unconformity and the TOB in the Tagus Abyssal Plain profile. I picked travel-times of each of those interfaces at CMP gathers using the *Globe Claritas* software package (Fig. 5.1b). During picking, I used the final image section as a guide to ensure that the travel-time of each selected hyperbolic event in the CMP gather corresponded to the seismic interface of interest (Fig. 5.1a). I then resorted the data set from CMP gathers to shot gathers, and used the picked travel-times every other shot gather. This means that I used data from one every 6-8 shots in the inversion, which provides a spatial sampling of one shot every 250-300m. This is important because the resolution of travel-time tomography methods is considered to be the size of the Fresnel zone (5.1), where ν dominant frequency of the source, V the velocity of the media and h_0 the depth/distance of the target.

$$R_1 = \sqrt{\frac{V h_0}{2\nu}} \tag{5.1}$$

Note that the spatial sampling is smaller than 400 m, which is the width of the Fresnel zone at the depth of the first sedimentary interface (~5 km of depth), considering a dominant frequency of 40 Hz. Therefore, the travel-time dataset decimation should not downgrade the tomographic resolution of the model. In total, we inverted 795 reflected picks from the top and 593 from the bottom of the salt layer, and 889 from the top of the basement for the profile in Gulf of Lions and we inverted 924

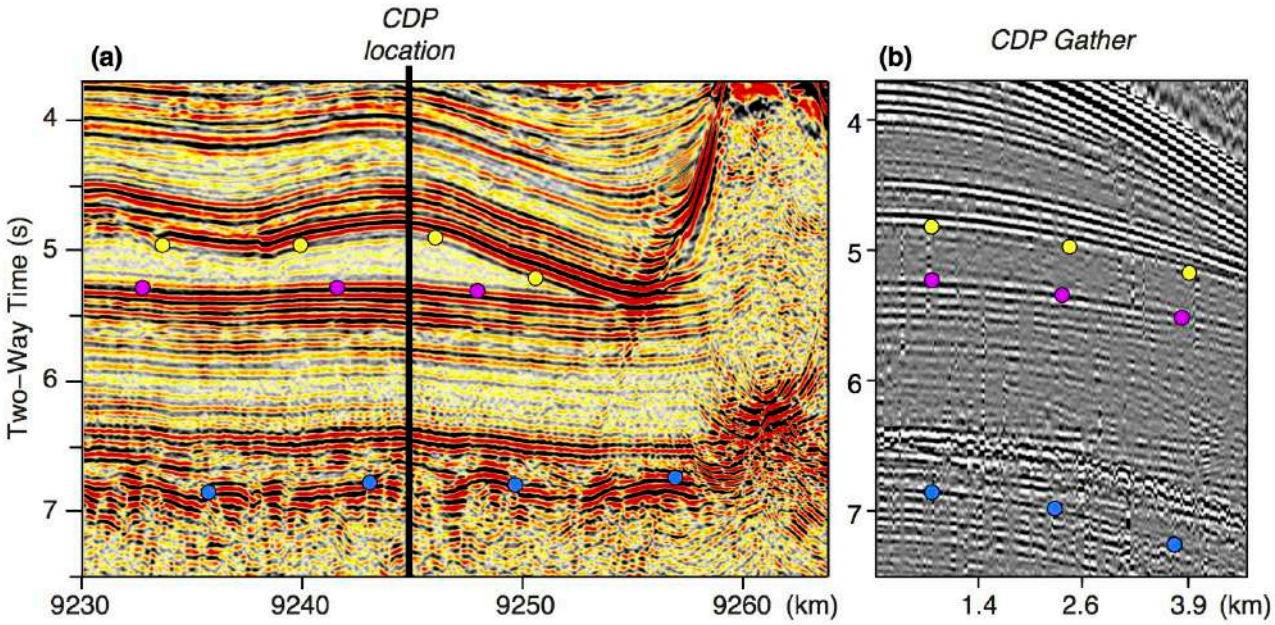

Figure 5.1 - (a) Zoom from the time-migrated section of Gulf of Lions profile. The black line display the CDP location. (b) Display of the CDP gather at the location of Fig. 5.1(a). The yellow dots display the picking for the top of the layer of salt, pink dots for the base of the layer of salt and blue dots for the top of the basement.

reflected picks for the unconformity and 1243 for the TOB for the Tagus Abyssal Plain profile. Based on the amplitude ratio between the signal within a 250ms window before and after the selected pick (Zelt and Forsyth, 1994), the picking time uncertainty is estimated to be between 20ms and 40ms for the MCS picks.

5.1.2. Picking of seismic phases in the WAS data

For the WAS data, once data are processed the first step for phase identification is to determine the type of information that is available in the record section (Fig. 5.2a). In the case of refractions, the first arrivals are displayed as short segments of straight lines whose slope is proportional to the seismic velocity of the layer at which they turn out (e.g. Pg and Pn in Fig. 5.2b). In this case, phases displaying slopes that are smaller than the so-called "reduction velocity" Vr (see figure caption of Fig. 5.2b) must correspond to waves propagating at velocity lower than Vr (e.g. Pg in Fig. 5.2b), whereas phases displaying slopes larger than the correction velocity must correspond to a propagation velocity higher than Vr (e.g. Pn in Fig. 5.2b).

In contrast, reflections are secondary arrivals represented by deformed hyperbolic functions that are asymptotic to the corresponding refracted wave in the record sections. For example, PmP is asymptotic to Pg/Pn in the record section of Figure 5.2b.

The analysis of WAS data consist in the identification of these seismic phases and the manual or selection (picking) of their arrival times.

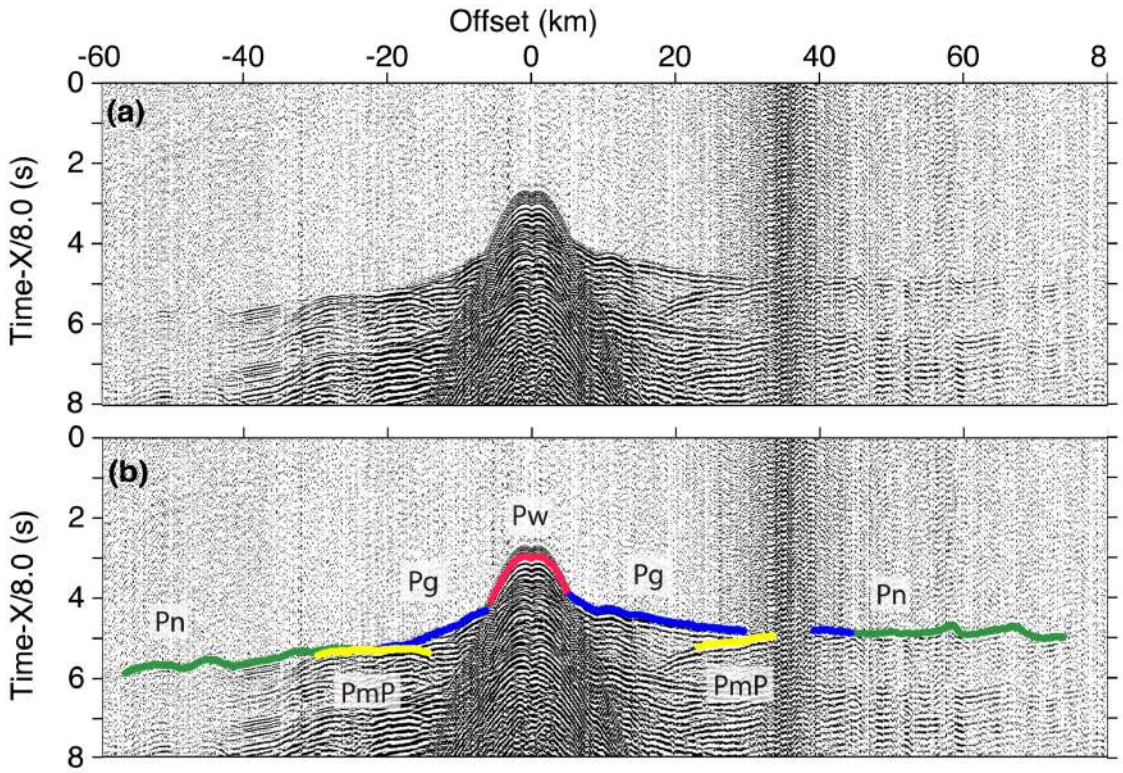

Figure 5.2 - (a) Seismic record section corresponding to OBS60 in the FRAME experiment. It is obtained after sorting by offset the recorded seismic traces. The vertical axis commonly represents a "reduced time", this is T-offset/Vr, where Vr is a reference velocity known as reduction velocity. This way, the slope of the different phases indicates if the propagation velocity is higher or lower than, or equal to, Vr. In the diagram above Vr= 8 km/s. (b) Record section including three seismic phases of P-waves refracted through the crust (Pg) and mantle (Pn), and reflected at the Moho (PmP). Approximation of the hodochrone or travel time curves of the same seismic phases identified. Note that the relation between the refracted Pg and the reflected PmP is asymptotic.

5.2. Joint travel-time tomography

The modified version of the joint refraction and reflection travel-time tomography code *tomo2d* (Korenaga et al., 2000; Melendez et al., 2015) also enables to have both source and receivers at any point of the model, including the water layer (Begović, 2020). This allows the user to include MCS data, in which both source and receivers in the inversion are located close to the sea surface. The MCS data offset is restricted to the streamer length, so it is much shorter than for WAS data, but in contrast the coverage of reflectors is much denser so data redundancy is much higher than for WAS data in the shallow region. WAS data recordings provide travel-time information up to offsets of >100 km, so they record refracted waves travelling deep into the crust and uppermost mantle, although they have low data redundancy and a poor coverage in the shallow crust. The denser spatial sampling of MCS data as compared to WAS data provides a two orders of magnitude larger number of rays in the sediments and upper crust, yielding a better ray coverage and thus helping to resolve the Vp distribution and the geometry of reflectors with greater accuracy and resolution. Combining WAS and MCS travel-times not only allows to better constrain the velocity structure, but also retrieving complex geometries of the seismic interfaces, especially the shallow ones, that cannot be resolved by inverting travel-times from sparse WAS acquisition settings alone (Begović, 2020).

In contrast to the most common first arrival (i.e. refraction) travel-time tomography approaches (e.g. Van Avendonk et al., 2006), the joint refraction and reflection travel-time tomography code developed by our group and applied here allows inverting not just the two-dimensional velocity distribution but also the geometry of a floating reflector. The velocity model is represented as a sheared mesh of velocity nodes hanging from the seafloor and/or land surface. The floating reflector is represented by an array of linear segments, whose nodal spacing is independent of that used in the velocity mesh (Korenaga et al., 2000). The flow diagram of *tomo2d* is shown in Table 5.1 and explained below.

Tomo2d uses ray theory to compute synthetic travel-times and a linearized and regularized least-squared inversion scheme to update the initial model by minimizing the root mean squared (r.m.s.) residuals between the observed and synthetic travel-times (Korenaga et al., 2000). This is done iteratively until the final residuals are of the order of the picking uncertainty (i.e. chi-squared, χ^2~1). Regularization parameters are introduced by fixing horizontal and vertical correlation lengths that control the smoothing of the model at each iteration step.

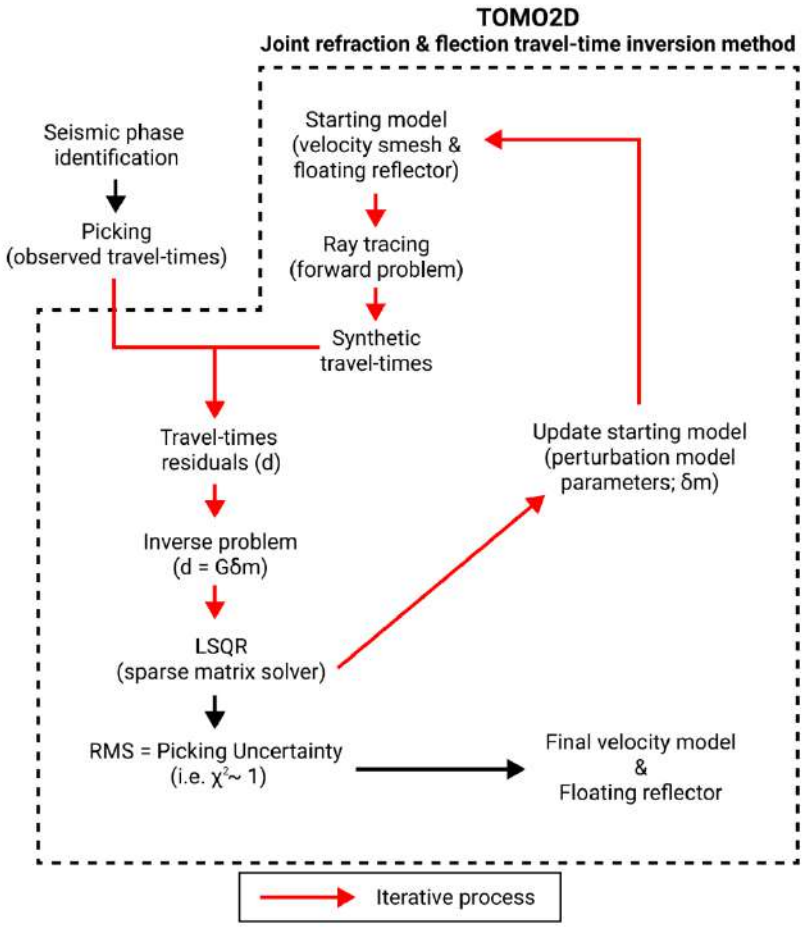

Table 5.1 - Flow diagram of the joint refraction and reflection travel time inversion method applied in this work with a version of TOMO2D (Korenaga et al., 2000) modified by Begović (2020) to combine both WAS and MCS data.

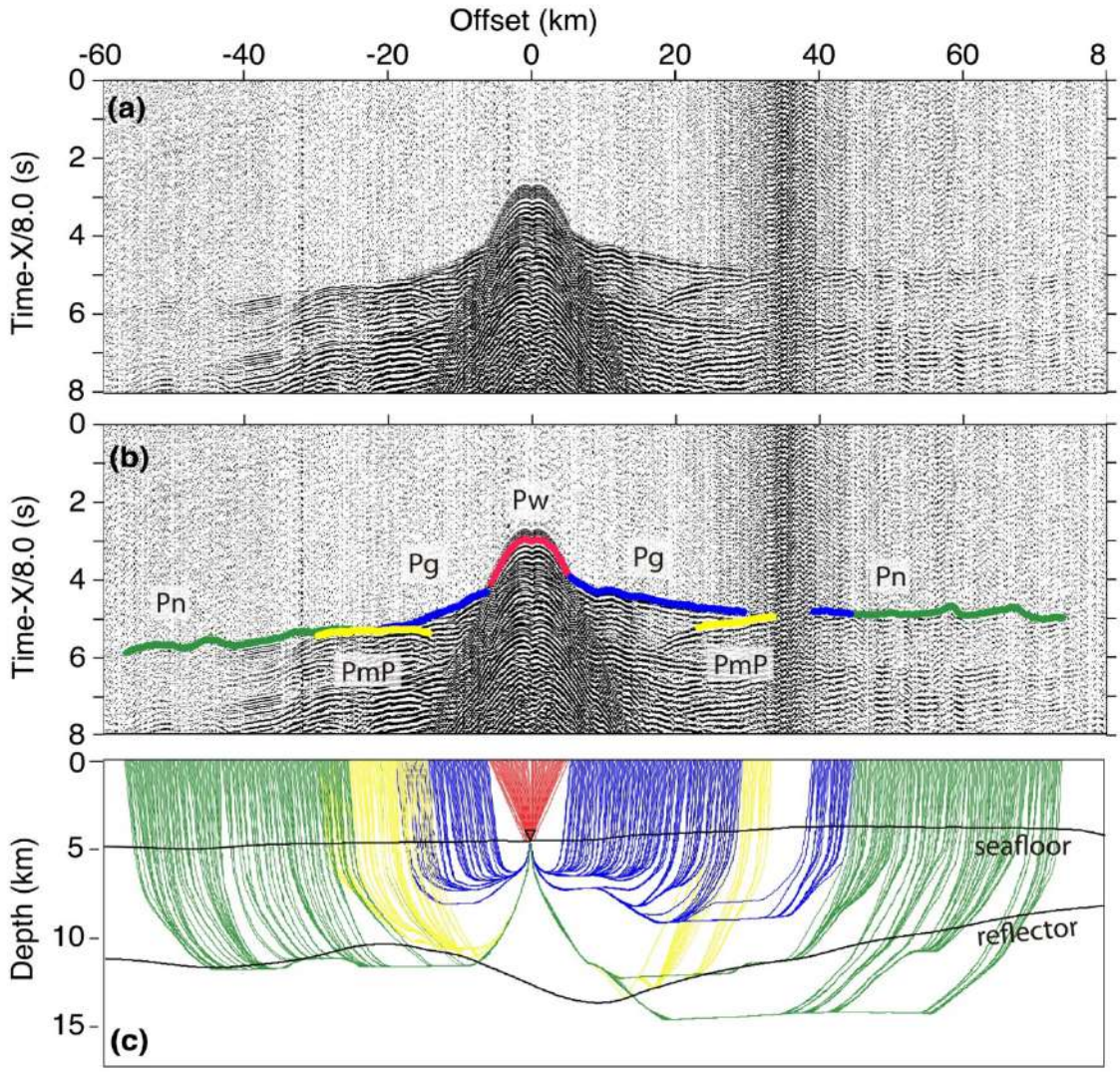

Figure 5.3 - (a) and (b) as in Figure 5.2. (c) Ray-tracing resulting from the combination of the graph and ray-bending methods for both refracted and reflected waves (Moser et al., 1992).

To solve the forward problem (Table 5.1), this method uses a hybrid ray-tracing strategy that first calculates a polygonal ray trajectory using the graph method (Moser, 1991) that is subsequently refined by applying a ray-bending technique (Moser et al., 1992). The optimal parameters for bending are calculated using the conjugate gradients method (Fig. 5.3c).

Then, an inverse problem is set to solve equation 5.2, which represents the linear approximation of the forward problem around a reference model:

$$\mathrm{d} = \mathrm{G}\delta\mathrm{m} \qquad (5.2)$$

In this case, ***d*** is the travel time residual vector, obtained from the difference between observed and synthetic data, ***G*** is the Fréchet matrix of partial derivatives of the travel-time residuals with respect to the model parameters (velocity and reflector depth in our case) and ***δm*** is the array of unknown model perturbations. The matrix to be resolved is commonly sparse and underdetermined, so it cannot be inverted in its simplest form. A regularization of the linear system is needed in order to stabilize the inversion. Additionally, smoothing constraints are applied to both velocity and reflector geometry

by defining a set of laterally- and vertically-variable correlation lengths that determine the smoothing degree for each parameter and each direction. Damping constraints are also used to regularize the linear system and stabilize the inversion. Hence, with these weighting parameters added to the linear system, equation 5.3 is expressed as:

$$\begin{bmatrix} d \\ 0 \\ 0 \\ 0 \\ 0 \\ 0 \end{bmatrix} = \begin{bmatrix} G_v & wG_d \\ \lambda_v L_{H_v} & 0 \\ \lambda_v L_{V_v} & 0 \\ 0 & w\lambda_d L_d \\ \alpha_v D_v & 0 \\ 0 & w\alpha_v D_d \end{bmatrix} \begin{bmatrix} \delta m_v \\ \frac{1}{w}\delta m_d \end{bmatrix} \tag{5.3}$$

where, *v* and *d* subscripts denote the velocity and depth components. $\boldsymbol{L_{Hv}}$ and $\boldsymbol{L_{Vv}}$, correspond to the horizontal and vertical correlation length matrices for velocity, respectively, and $\boldsymbol{L_d}$ is the correlation length matrix for depth. λ_v and λ_d are control parameters of the smoothing constraints. The depth kernel weighting is represented by *w*, which adjust the depth sensitivity in the Fréchet matrix. Damping matrices for velocity and depth are represented by $\boldsymbol{D_v}$ and $\boldsymbol{D_d}$, respectively, and**,** α_v and α_d control the strength of the damping constraints.

As stated above, equation 5.2 is a sparse system, so it can be efficiently solved using a sparse matrix solver. In the case of *tomo2d* the Fréchet matrix is inverted applying the LSQR solver (Paige and Saunders, 1982). Given that the problem solved is a linear approximation of the real one, equation 5.2 must be applied iteratively using as input of each iteration the model parameters issued in the previous iteration. This scheme is repeated until convergence is achieved (Table 5.1). For that reason, the reference model is modified successively by $\boldsymbol{\delta m}$ until the root mean square (r.m.s) value of travel time equals approximately the uncertainty of the observed data (i.e. ~70-60ms), or, what is the same, when the chi-squared (χ^2) value becomes ~1 (Table 5.1). The linear sensitivity of the inversion, which is also a measure of the ray coverage throughout the model, is estimated by calculating the Derivative Weight Sum (DWS) on each node of the model (Toomey and Foulger, 1989).

$$DWS(\alpha_n) = N \sum_i \sum_j \{ \int_{P_{ij}} \omega_n (X) ds \} \tag{5.4}$$

where i and j are the event and station indices, ω is the weight used in the linear interpolation and depends on coordinate position, P_{ij} is the ray path between i and j, and N is a normalization factor that takes into account the volume influenced by α_n. The magnitude of the DWS depends on the step size of the incremental arc length ds utilized in the numerical evaluation of equation 5.4.

In this work, the size of the models is 350 km for the Gulf of Lions and 460 km for the Tagus Abyssal plain, and 30 km deep for both of them. Node spacing varies in the vertical direction from 90 m at the seafloor to 500 m at the bottom, while it is of 90 m in the horizontal component. The reflector is set as a floating interface with a constant node spacing of 90 m. In order to select the most appropriate set of regularization constraints, several combinations of correlation lengths, damping and smoothing parameters were tested. Regularization parameters are set as horizontal and vertical correlation lengths for the mesh and the reflector components and are summarize in Table 5.2 for the Gulf of

Lions modelling and Table 5.3 for the Tagus Abyssal Plain modelling.

Inversion step	**Horizontal** (km)		**Vertical** (km)		**Reflector**
	Top of the model	Bottom of the model	Top of the model	Bottom of the model	
Top Salt	5	10	1	2	1
Base Salt	5	10	1	2	1
TOB	5	10	1	2	1
Top HVL	2	8	0.5	2	3
Moho	2	8	0.5	2	3
Mantle	2	8	0.5	2	3

Table 5.2 - Correlation length for each inversion step from the Gulf of Lions Vp model.

Inversion steps	**Horizontal** (km)		**Vertical** (km)		**Reflector**
	Top of the model	Bottom of the model	Top of the model	Bottom of the model	
Unconformity	5	10	1	2	1
TOB	5	10	1	2	1
Moho	2	10	1	6	4
Mantle	1	8	0.5	6	4

Table 5.3 - Correlation length for each inversion step from the Tagus Abyssal Plain Vp model.

The final velocity model of Gulf of Lions profile (see Fig. 7.4a) was obtained after 6 layer-stripping steps with a r.m.s of 65ms, and a χ^2 of 1.4. In case of Tagus Abyssal Plain profile (see Fig. 8.3a), the final model was obtained after 4 layer-stripping steps with a r.m.s misfit of 55ms, and a χ^2 of 1.3. The basics of the layer-stripping strategy are described in the next section.

5.3. Layer-stripping strategy

The codes *tomo2d/3d* allow inverting a single reflector at a time. Although other codes allow simultaneous inversion of multiple reflection, it is strategically meaningful to constraint the velocity above a single horizon before mapping the Vp underneath. Thus, it is convenient to define an iterative strategy that will allow to constrain the Vp for successively deeper boundaries, or layers, which have to be inverted in a layer stripping strategy. To solve this issue, I followed a top-to-bottom layer-stripping strategy similar to that described in Sallarès et al. (2013a) and Prada et al. (2014).

This strategy permits to account for sharp geological contacts such as those occurring across the sediment/basement interface or the Moho (e.g. Sallarès et al., 2011, Prada et al. 2014) by adding the data sequentially to the inversion, starting with the shortest offsets (e.g. sediment phases) and finishing with the longest offset ones (e.g. mantle phases). The data of this work show clear sediment, basement and inter-crustal boundary phases, so that, I built the Vp models layer by layer. The first step is to resolve the velocity and reflector of the shallowest layer (see Step 1, Fig. 5.4, ones the this is solved, to concentrate changes in those regions that are unresolved, the velocity nodes above the resolved reflector were damped by a factor of 100:1 and it is used as the initial model for the next

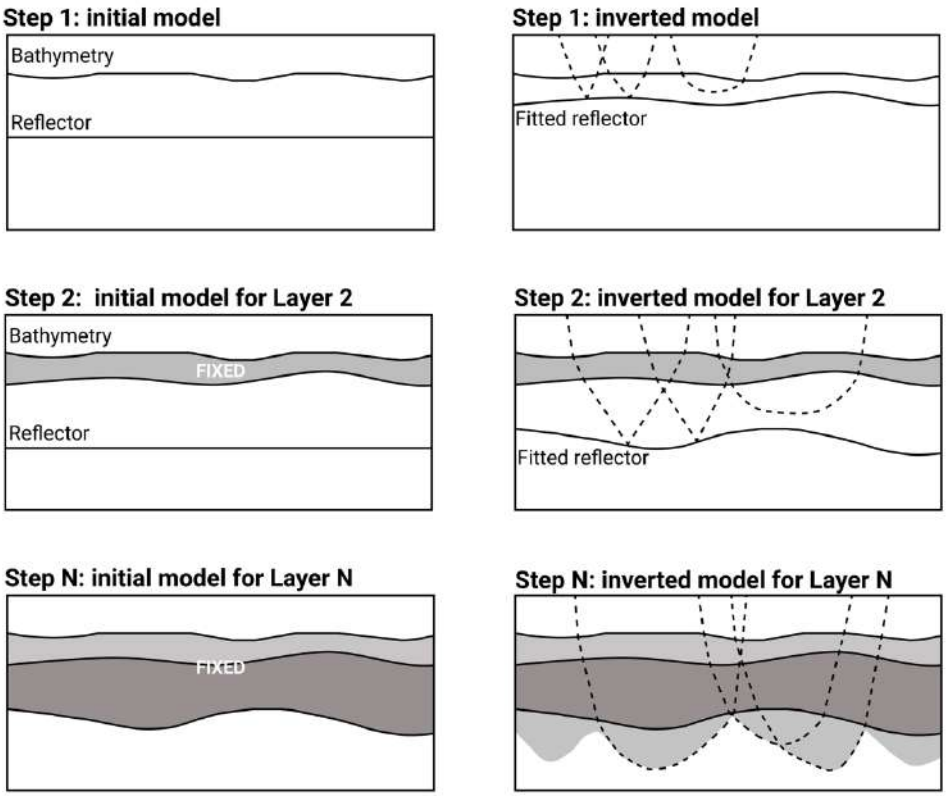

Figure 5.4 - Schematic representation of the layer-stripping procedure. Step 1: the model is initialized with a constant velocity gradient and a constant depth reflector. The velocity of layer 1 and the geometry of the reflector are inverted using refracted phases inside and above this layer and reflections at its base. Step 2: the velocity field for the layer 1 is fixed. Below the inverted reflector in step 1the model is initialized with a constant velocity gradient. A deeper reflector is set at constant depth and the refracted phases inside this layer and reflections at the new reflector are incorporated. The process is repeated for as many layer-reflector pairs as necessary. The last step (Step N) involves fitting the velocity model above the last fitted reflector (typically Pn).

layer (see Step 2, Fig. 5.4). This procedure is repeated as for as many reflectors are identified in the seismic data. The last step Pn phases were incorporated to the data set (see Step N, Fig. 5.4). As a result, the obtained velocity model displays a sharp velocity contact that coincides with the location of the major reflector, such as: main unconformities, the top of the basement, Moho reflector, etc.

The specific details of the procedure followed on each profile is detailed in the Chapter 7 and Chapter 8, respectively for the Gulf of Lions and the Tagus Abyssal Plain.

5.4. Uncertainty analysis

Calculating the uncertainty of the seismic velocity, reflector depth, and other velocity-derived parameters is fundamental for a reliable interpretation of the rock composition, which is especially relevant to estimate the nature of the basement in the different domains. Several deterministic techniques have been proposed to estimate the parameter uncertainty based on the covariance matrix, but most of them only take into account the mathematical indetermination that is intrinsic to the approach and do not consider other sources of indetermination such as for example the dependence

of the solution on the initial model used for the inversion. In practical terms, the only methods to estimate the model uncertainty for a large-scale, non-linear inversions such as this one, are based on stochastic, Monte Carlo-type approaches (e.g., Tarantola and Valette, 1982; Tarantola, 1987).

In this work, we performed a Monte Carlo-type statistical analysis based on that proposed by Korenaga et al. (2000). As in Prada et al. (2017), we modified the procedure to perform the analysis layer by layer, following the layer-stripping strategy described in the previous section. The flow diagram of the analysis made is shown in Table 5.4.

This approach consists of randomly perturbing the velocity values of the initial model and the depth of the resolved reflectors for each layer, using a Gaussian distribution with a variance (σ_V for the velocity values and σ_Z for the reflector depth) that takes into account *a priori* information. A Gaussian filter is applied to the perturbed velocity mesh to avoid abrupt changes of velocity within the model caused by the perturbation step. Also, the errors in the travel times follow a normal distribution, and the variance is assigned based on Zhang and Toksöz (1998) approach, which suggest combining picking errors arising from common shot (or receiver), common phase, and individual picking errors.

This way, we performed 100 inversions for each layer (1000 realizations). On each realization a randomly selected pair of perturbed reference models and reflectors, and a set of noisy data are inverted. The process is repeated for each layer. Each realization included a travel-time dataset adding Gaussian random picking errors with a variance corresponding to the picking uncertainty, a starting 1D Vp model for each layer with a random velocity-depth distribution, and a flat reflector randomly

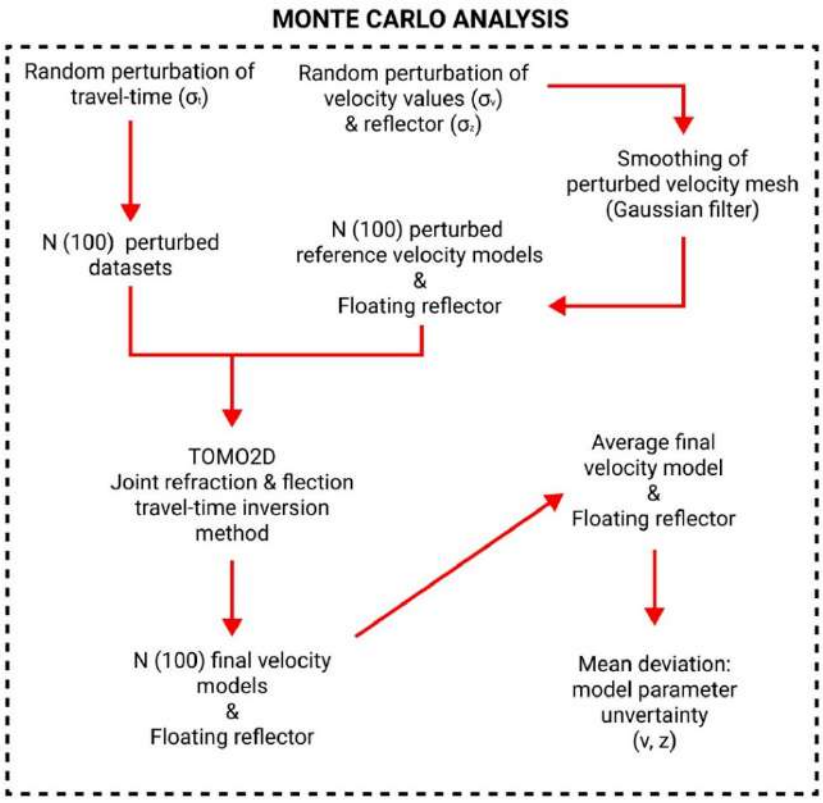

Table 5.4 - Flow diagram of the Monte Carlo Uncertainty approach applied to travel time inversion.

generated within certain bounds depending on each layer (see Table 5.5). To include the effect of the regularization constraints (e.g. Korenaga and Sager, 2012), we also varied correlation lengths within a certain range in the different inversions (see Table 5.5).

The standard deviation of all the inverted Vp models and reflector geometry is taken as an estimation of the model parameter uncertainty (Tarantola et al., 1987).

Details of the results obtained with this analysis are given in Chapter 7 for the Gulf of Lions. In the case of the Tagus Abyssal Plain, we have followed a slightly different approach due to the geological characteristics of the profile. In this region, we decided to focus the uncertainty analysis on the crystalline crust. The method is described in detail in section 8.3.2., Chapter 7.

Inversion step	**Vp initial** (km/s)	**Vp final** (km/s)	**Variability** (%)	**Layer thickness** (km)	**Variability** (km)
Top Salt	1.8	4.0	±10	6.5	±2
Base Salt	2.5	6.0	±10	7	±2
Top Basement	2.5	6.0	±2	8	±1
Top HVL	2.5	7.5	±5	10	±2
Moho	5.0	7.5	±5	20	±2
Mantle	5.0	7.5	±5	20	±2
Correlation length (km)					
Horizontal		**Vertical**		**Reflector**	
Top of the model	Bottom of the model	Top of the model	Bottom of the model		
2 ± 1	6 ± 2	0.75 ± 0.25	1.5 ± 0.5	0.75 ± 0.25	

Table 5.5 - Ranges of values used for the model parameterization in the Monte-Carlo analysis for the Gulf of Lions profile.

Chapter 6

Gravity anomaly data

6.1. Gravity data acquisition

Gravitational attraction measurements and hence gravity anomalies are routinely used in many crustal-scale studies to complement WAS-derived information such as crustal thickness and velocity, and hence to further constrain the petrological nature of the rocks (e.g. Todd and Reid, 1989; Reid and Jackson, 1997).

Gravity is directly proportional to the distribution of the masses inside the Earth, so it is directly related with density (ρ). Additionally, there is also empirical evidence showing that in most cases approximately linear relationships exist between the density of rocks and their P-wave velocity (Vp) (e.g. Christensen and Mooney, 1995; Carlson and Miller, 2003). Thus, it is possible to convert modelled Vp values to ρ using the existing Vp-ρ empirical relationships for different rock types and model the density distribution to test whether it is compatible with the observed gravity data. This section explains the fundamentals of the acquisition and modelling of gravity data, and presents the Vp- relationships used in this work.

Gravity data are acquired with a gravimeter, which measures variations of the downward gravity acceleration. The units of these measurements are *milligals* (mGal) (10^{-3} mgal = 10^{-5} m s^{-2}). Since these instruments are extremely sensitive to vibrations, gravimeters in marine experiments are habitually stabilized on a platform that isolates the sensor from the influence of the movements of the ship.

Marine gravity measurements are affected by sea level changes, and variations on heading, speed and gyro of vessel. Besides, neither the shape of Earth nor its density distribution are uniform, there are deviations in the direction and magnitude of the gravity across its surface. Therefore, data must be corrected by sea level, Eötvös effect (Moritz, 2000), which is the change in perceived gravitational force caused by the eastbound or westbound velocity, and drift corrections to obtain the Free Air Gravity Anomaly, which according with the Geodetic Reference System of 1980 (Moritz, 2000), is

calculated with equation 6.1.

$$Free\ Air\ Anomaly = Gm + Eot - drift - Gt \quad (6.1)$$

$$Eot = 7.508 * v * \sin(\alpha) * \cos(\lambda) + 0.0416 * v2 \quad (6.2)$$

$$Gt = 978031.846(1 + 0.005278895 * \sin(\lambda)^2 + 0.000023462 * \sin(\lambda)^4 \quad (6.3)$$

Where, *Gm* is the measured gravity data, and *Eot* the Eötvös correction (Equation 6.2), which depends on the velocity (***v***) and the gyro (α) of the vessel, and on the latitude (λ). ***Gt*** is the theoretical gravity value, which depends exclusively on (Equation 6.3) (Nagy, 1978). Once these corrections are applied, the observed gravity data can be used as a reference value during the gravity modelling.

6.2. Empirical relationships between P-wave velocity (Vp) and density (ρ)

In this work, gravity modelling has been used to complement the information provided by WAS data along profile FRAME-2. To do this, I have converted the WAS-derived Vp models to density models using different empirical Vp-ρ relationships assuming a given lithological composition for each geological layer and domain. The idea behind this approach is to see whether it is possible to discern between interpretations of the nature of basement rocks based on seismic velocity exclusively (as in Korenaga et al., 2001; Sallarès et al., 2001; Sallarès and Ranero, 2005).

The selection of the "appropriate" Vp-ρ relationships is based on our geological interpretations of the velocity model and the MCS image. This, in turn, allows the definition of the regions or domains where the selected Vp-ρ relationships will be applied (Fig. 6.1). Vp-ρ relationships of interest in this work include the Hamilton's (1978) conversion law for sediments (Fig. 6.1), which is a result of a compilation of large amount of DSDP data, and reflection and refraction measurements of sound velocity in marine sediments. For the crustal basement, I have tested Vp- relationships for three different rock compositions, including continental, oceanic and exhumed mantle rocks. For continental igneous and metamorphic rocks I applied the relationship from Christensen and Mooney's (1995) (Fig. 6.1). For basalts and gabbros of the oceanic Layers 2 and 3 I applied the Carlson and Herrick's (1990) conversion law (Fig. 6.1). Finally, for partially serpentinized peridotites I used Carlson and Miller's (2003) relationship (Fig. 6.1). All these relationships have been widely used in similar studies.

6.3. Gravity modelling

The 2D gravity modelling is performed using Parker's (1972) spectral method as modified by Korenaga et al. (2001). It calculates the free air gravity anomaly produced by a density distribution. In this approach, the 2-D gravity anomaly caused by a 1-D density variation bounded by two limits is expressed in the Fourier domain as a function of the density distribution between these two limits (Parker, 1972). This formulation is used to derive an iterative inversion formula for the density variation and then for the gravity anomaly in the Fourier space. An inverse transformation gives the final gravity anomalies. This method is implemented in the code grav2d from Korenaga et al. (2001), which we use to calculate the gravity anomaly of the different density models tested in this work.

It is worth to mention that the measured gravity anomaly is affected by surrounding bodies that may be out of the modelled structure, like deeper mantle, lateral density variations or distant large crustal bodies that usually results in long-wavelength variations of the gravity field. This influence is not included in the velocity-derived density model, and hence in the synthetic gravity anomaly. Consequently, the synthetic anomaly is habitually affected by a systematic shift respect the observed anomaly that must be corrected to properly compare both anomalies.

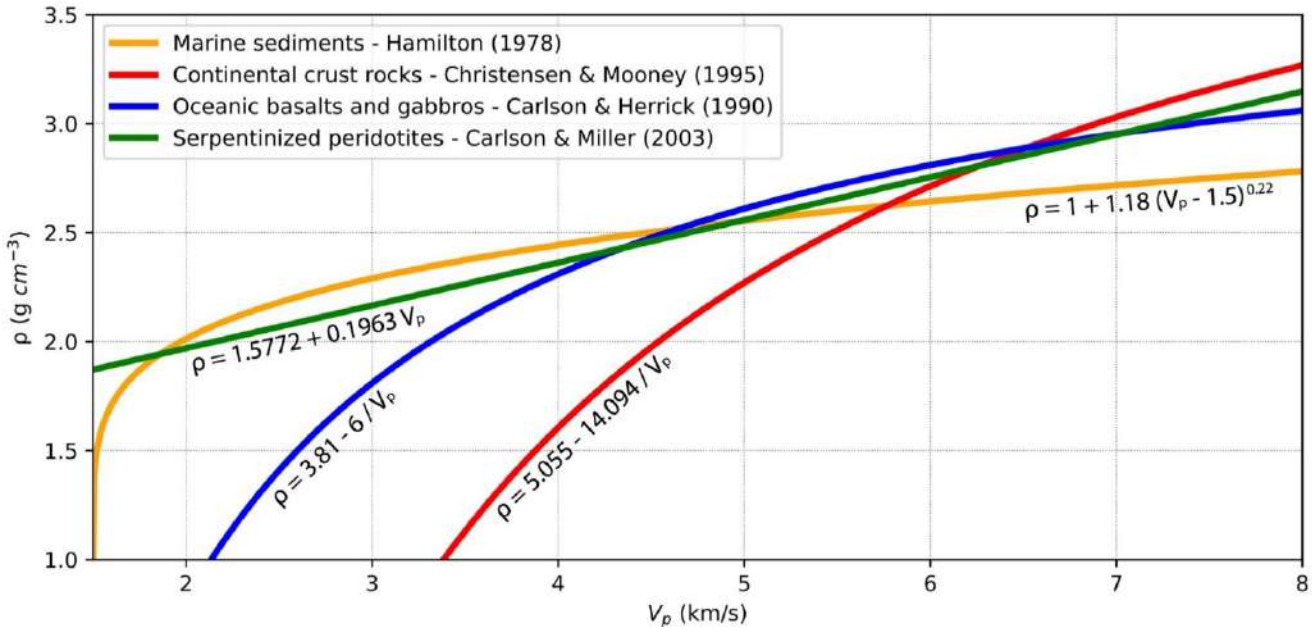

Figure 6.1 - Graphical representation of all the Vp- relationships used in this work. Empirical formulas and corresponding references are shown above and below each relationship, respectively.

References

Begović, S. (2020). Structure and physical properties of the subduction plate boundary. Universitat de Barcelona. PhD Thesis.

Carlson, R.L., and Herrick C.N. (1990). Densities and Porosities in the Oceanic Crust and Their Variations With Depht and Age, J. Geophys. Res., 95 (B6), 9153-9170.

Carlson, R.L., and Miller D.J. (2003). Mantle wedge water contents estimated from seismic velocities in partially serpentinized peridotites, Geophys. Res. Let., 30 (No. 5), doi: 10.1029/2002GL016600.

Christensen, N., and Mooney, W. (1995). Seismic velocity structure and composition of the continental crust: a global view, J. Geophys. Res, 100 (B7), doi:10.1029/95JB00259.

Hamilton, E.L. (1978). Sound velocity-density relations in sea-floor sediments and rocks, J. Acoust. Soc. Am., 63, 366-377.

Klingelhoefer, F., Evain, M., Afilhado, A., Rigoti, C., Loureiro, A., Alves, D., Leprêtre, A., Moulin, M., Schnurle, P., Benabdellouahed, M. and Baltzer, A. (2014). Imaging proto-oceanic crust off the Brazilian Continental Margin. Geophysical Journal International, 200(1), pp.471-488.

Korenaga, J., Holbrook, W. S., Kent, G. M., Kelemen, P. B., Detrick, R. S., Larsen, H.-C., Hopper, J. R. and Dahl-Jensen, T. (2000). Crustal structure of the southeast Greenland margin from joint refraction and reflection seismic tomography, J. Geophys. Res., 105(B9), 21, 591–21, 614, doi:10.1029/2000JB900188.

Korenaga, J., Holbrook, W.S., Detrick, R.S. and Kelemen, P.B. (2001). Gravity anomalies and crustal structure at the southeast Greenland margin, J. Gophys. Res., 106 (B5), 8853- 8870.

Loureiro, A., Afilhado, A., Matias, L., Moulin, M., and Aslanian, D. (2016). Monte Carlo approach to assess the uncertainty of wide-angle layered models: Application to the Santos Basin, Brazil. Tectonophysics, 683, 286-307.

Lowrie, W. (2007). Fundamental of Geophysics, Cambridge University Press, New York, pp. 374.

Meléndez, A., Korenaga, J., Sallarès, V., Miniussi, A. and Ranero, C.R. (2015). TOMO3D: 3-D joint refraction and reflection traveltime tomography parallel code for active-source seismic data—synthetic test. Geophysical Journal International, 203(1), pp.158-174.

Moeller, S., Grevemeyer, I., Ranero, C.R., Berndt, C., Klaeschen, D., Sallarès, V., Zitellini, N. and de Franco, R. (2013). Rifted structure in the northern Tyrrhenian Sea Basin: Results from a combined wide-angle and multichannel seismic study. Geochem. Geophys. Geosyst.

Moser, T.J. (1991). Shortest path calculation of seismic rays, Geophysics, 56, 59-67.

Moser, T.J., Nolet, G. and Snieder, R. (1992). Ray bending revisted, Bull. Seismol. Soc. Am., 82, 259-288.

Moritz, H. (2000) Geodetic Reference System 1980, J. Geod., 74(1), pp. 128-162, doi:10.1007/S001900050278.

Nagy, D. (1978). Direct gravity formula for the geodetic reference system 1967. Bulletin géodésique, 52(2), 159-164.

Paige, C.C., and Saunders, M.A. (1982). LSQR: An algorithm for sparse linear equation and sparse least squares, Trans. Math. Software, 8, 43-71.

Parker, R.L. (1972). The rapid calculation of potential anomalies, Geophys. J. R. Astron. Soc., 31, 447-455.

Prada, M., Sallarès, V., Ranero, C.R., Vendrell, M.G., Grevemeyer, I., Zitellini, N. and de Franco, R. (2014). Seismic structure of the Central Tyrrhenian Basin: geophysical constraints on the nature of the main crustal domains. J. Geophys. Res. Solid Earth, 119. doi:10.1002/2013JB010527.

Prada, M., Watremez, L., Chen, C., O'Reilly, B.M., Minshull, T.A., Reston, T.J., Shannon, P.M., Klaeschen, D., Wagner, G. and Gaw, V. (2017). Crustal strain-dependent serpentinisation in the Porcupine Basin, offshore Ireland. Earth and Planetary Science Letters, 474, pp.148-159.

Prada, M., Ranero, C. R., Sallares, V., Grevemeyer, I., de Franco, R., Gervasi, A. and Zitellini, N. (2020). The structure of Mediterranean arcs: New insights from the Calabrian Arc subduction system. Earth and Planetary Science Letters, 548, 116480, doi:10.1016/j.epsl.2020.116480.

Reid, I., and Jackson, H. R., (1997). Crustal structure of the northern Baffin Bay: Seismic refraction and tectonic implications, J. Geophys. Res., Vol 102; No B1, 523-542.

Sallarès, V., Dañobeitia, J.J. and Flueh, E.R. (2001). Lithospheric structure of the Costa Rican Isthmus: Effects of subduction zone magmatism on an oceanic plateau. Journal of Geophysical Research: Solid Earth, 106(B1), pp.621-643.

Sallarès, V., and Ranero, C. R. (2005). Structure and tectonics of the erosional convergent margin off Antofagasta, north Chile (23_300S), J. Geophys. Res., 110, B06101, doi:10.1029/2004JB003418.

Sallarès, V., Gailler, A., Gutscher, M.A., Graindorge, D., Bartolomé, R., Gracia, E., Diaz, J., Dañobeitia, J.J. and Zitellini, N. (2011). Seismic evidence for the presence of Jurassic oceanic crust in the central Gulf of Cadiz (SW Iberian margin). Earth and Planetary Science Letters, 311(1-2), pp.112-123.

Sallarès, V., Martínez-Loriente, S., Prada, M., Gràcia, E., Ranero, C., Gutscher, M.A., Bartolome, R., Gailler, A., Dañobeitia, J.J. and Zitellini, N. (2013). Seismic evidence of exhumed mantle rock basement at the Gorringe Bank and the adjacent Horseshoe and Tagus abyssal plains (SW Iberia). Earth and Planetary Science Letters, 365, pp.120-131.

Stein, S., and Wysession, M. (2009). An introduction to seismology, earthquakes, and earth structure. John Wiley and Sons.

Tarantola, A., and Valette, B., (1982). Inverse Problems=Quest for Information, J. Geophys., 50, 159-170

Tarantola, A. (1987). Inverse Problem Theory: Methods for Data Fitting and Model Parameter Estimation, Elsevier Science, New York. 613 pp.

Todd, B. J., and Reid, I., (1989). The continent–ocean boundary south of Flemish Cap: constraints from seismic refraction and gravity, Canadian Journal of Earth Sciences, Vol. 26, No. 7 : pp. 1392-1407 (doi: 10.1139/e89-119).

Toomey, D.R., and Foulger, G.R. (1989). Tomographic inversion of local earthquake data from Hengill-Grensdalur central volcano complex, Iceland, J. Geophys. Res., 94, 17497- 17510.

Toomey, D.R., Solomon, S.C. and Purdy, G.M. (1994). Tomographic imaging of the shallow crustal structure of the East Pacific Rise at 9° 30′ N. Journal of Geophysical Research: Solid Earth, 99(B12), pp.24135-24157.

Van Avendonk, H.J., Holbrook, W.S., Nunes, G.T., Shillington, D.J., Tucholke, B.E., Louden, K.E., Larsen, H.C. and Hopper, J.R. (2006). Seismic velocity structure of the rifted margin of the eastern Grand Banks of Newfoundland, Canada. Journal of Geophysical Research: Solid Earth, 111(B11).

Wu, Y., Louden, K.E., Funck, T., Jackson, H.R. and Dehler, S.A. (2006). Crustal structure of the central Nova Scotia margin off Eastern Canada. Geophysical Journal International, 166(2), pp.878-906.

Yilmaz, O., (2001). Seismic data processing. Society of exploration geophysicists, ed.: Doherty, S., Tulsa, US, 522 pp.

Zhang, J., and Toksöz, M.N, (1998). Nonlinear refraction traveltime tomography, Geophysics, 63, 1726-1737.

Zelt, C.A., and Smith, R.B., (1992). Seismic traveltime inversion for 2-D crustal velocity structure, Geophys. J. Int., 108, 16-34.

Zelt, C. A. and Forsyth D. A. (1994). Modeling wide-angle seismic data for crustal structure: Southeastern Grenville Province. Journal of Geophysical Research: Solid Earth 99. B6, 11687- 11704.

Part III
RESULTS

Chapter 7

The structure of the continent-ocean transition in the Gulf of Lions from joint refraction and reflection travel-time tomography

Most Western Mediterranean basins have formed since Oligocene times by back-arc extension associated to rollback of oceanic slabs during the retreat of subduction fronts (Dewey et al., 1989; Schettino and Turco, 2011). Over the last decade, studies using modern geophysical data, particularly wide-angle seismic (WAS) and multichannel seismic (MCS) data and tomographic techniques, provide constraints on the petrological nature of the crystalline crust and its structure in this region. This has allowed to define the structure and spatial extent of crustal domains in the Alboran sea (Booth-Rea et al., 2018; Gómez de la Peña et al., 2020), as well as to constrain the location of the continent-ocean transition (COT) in different sectors of the Algerian margin (e.g. Badji et al., 2015). In the Tyrrhenian, this type of geophysical studies has revealed that the configuration of basement domains is more complex than previously assumed, implying spatially rapid changes between magmatic and amagmatic processes during back-arc formation (Moeller et al., 2013, 2014; Prada et al., 2014; 2015; 2016).

In the Western Mediterranean, the crustal nature of the Gulf of Lions - Ligurian basin is still debated, in particular along the COT (Fig. 7.1). The structure and petrological nature of the COT in this margin has been studied along the same geophysical transect by different authors using wide-angle seismic data modelling (Gailler et al., 2009; Moulin et al., 2015). Yet, these studies present contrasting results along the same transect showing a complex and atypical crustal Vp structure across the COT. Gailler et al. (2009) define three domains of different petrological characteristics and proposed that the COT zone is made of lower continental crust or a mixture of serpentinized mantle and lower crust. Alternatively, Moulin (2015) interpreted a two-layer COT basement made of lower continental crust overlying intruded rocks. The different interpretations are due to differences in the Vp models, which may be partially attributed to differences in the modelling techniques and the seismic phases used in each case. Gailler et al. (2009), simultaneously inverted wide-angle refracted and Moho reflected

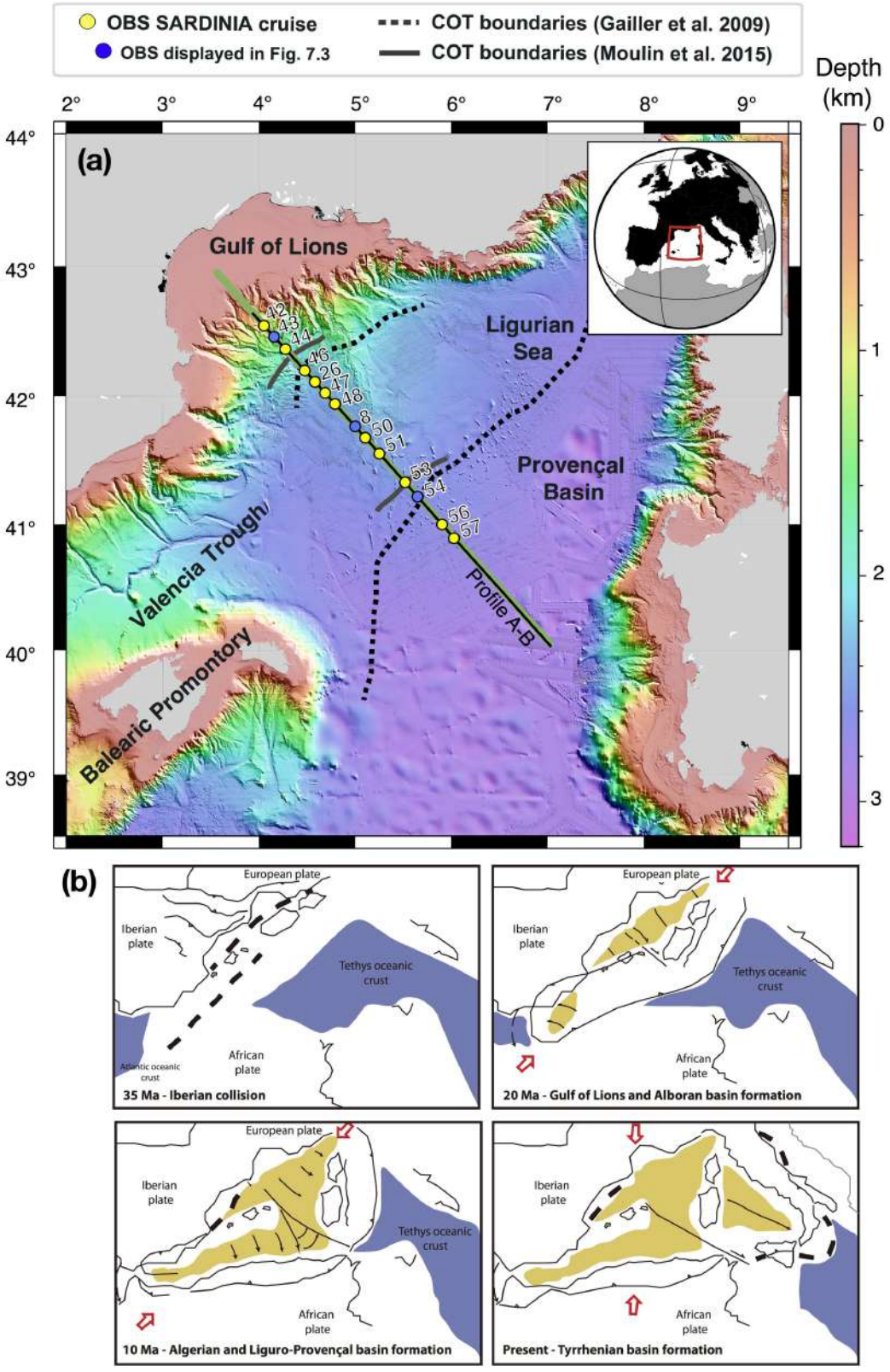

Figure 7.1 - (a) Bathymetric map of the study area. Green line is the wide-angle seismic profile A-B, while collocated black line is the multi-channel seismic profile. Yellow and blue dots correspond to the position of ocean bottom seismometers used in this study. (b) Geodynamic evolution of the Western and Central Mediterranean back-arc basins. Light yellow regions depict newly formed back-arc basins, while dashed black lines show the onset of formation of each basin. Red arrows depict Eurasia-Africa convergence at each step. (Modified from Gelabert et al., 2002).

travel-times to obtain the Vp structure of the crust and mantle and the Moho geometry. Their approach does not provide velocity contrasts across the Moho and does not constrain the top of the basement, yielding to a smooth vertical velocity structure that may influence the interpretation of the petrological nature of the basement. In contrast, Moulin et al. (2015) used forward modelling of wide-angle refracted and reflected phases, which involved a visual inspection of the structures inferred from the co-located MCS images. Forward modelling has a user-dependent ingredient that increases the inherent non-uniqueness of crustal-scale velocity models, i.e. a range of models can explain the travel-times, which is difficult to assess without a concomitant uncertainty analysis.

In this study, we use a different tomographic approach aimed at further decreasing the Vp uncertainty of the model, and consequently the uncertainty on the interpretation of the petrological nature of the crystalline crust and geological domains. We applied a novel approach that inverts not only all wide-angle reflections and refractions used by Gailler et al. (2009) and Moulin et al. (2015) but also reflections recorded in the streamer. Overall, the approach involves two key ingredients: (1) joint refraction and reflection travel-time tomography of P-wave velocity (Vp) and the geometry of bounding reflections following a layer-stripping approach; and (2) joint inversion of travel-times from MCS reflections and WAS phases so that the illumination of subsurface structures is significantly improved, particularly on the sediment section and top of the basement. We demonstrate the improved quality of the Vp model performing a Monte Carlo-type uncertainty analysis. The final model shows three basement domains, in agreement with previous results, but their dimension, geometry and Vp-depth distribution differ. The new Vp-depth distribution is used to discuss a new interpretation of the petrological nature of geological domains in the area.

7.1. Geological setting

The opening of most Western Mediterranean basins was driven by the interaction between subduction processes and extensional tectonics (Fig. 7.1b). The region includes the Ligurian-Provençal basin, Algero-Balearic basin, Alboran basin, and Tyrrhenian basin, formed since Oligocene times as back-arc basins associated to retreating subduction slabs (Auzende et al., 1973; Dewey et al., 1973; Cohen et al., 1980; Rehault et al., 1984; Gueguen et al., 1998; Jolivet et al., 2000) (Fig. 7.1b). The Gulf of Lions margin is part of the Ligurian-Provençal basin (Fig. 7.1). The age of the deep water syn-rift is not calibrated but it is believed that the Ligurian-Provençal basin opened during Oligocene-Miocene times (Rehault et al., 1984). Most authors interpret that the basin formed as a back-arc system, related to the eastward roll-back of the west-directed Apenninic subduction zone (Cohen, C.R., 1980; Le Douran et al., 1984; Rehault et al., 1984; Gueguen et al., 1998; Jolivet et al., 2000) (Fig. 7.1b), although Ziegler (1992) proposed the opening to be related to the southward propagation of the Saône Graben.

The conjugate margin to the Gulf of Lions is the NW Sardinia margin. The Variscan lithosphere of Corsica and Sardinia rifted from Europe during the late Oligocene time, (Burrus, 1984). The tectonic activity possibly ceased in the Aquitanian/Early Burdigalian (20-19 Ma), perhaps due to the collision of Corsica and Sardinia with the Apennines and to the cessation of extension in the Ligurian-Provençal basin (Burrus, 1984; Rehault et al., 1984; Bache et al., 2010), or by the steepening of the

slab in the upper mantle (Faccenna et al., 2001), changing the locus of extension further east to start the opening of the Tyrrhenian basin (Fig. 7.1b).

7.2. Data Sets

The MCS and WAS data used in this study were acquired during the SARDINIA-2006 survey, which was conducted on board the French R/V L'Atalante. The main objective of this experiment was to study the impact of lithospheric stretching on the crustal structure (Gailler et al. 2009; Moulin et al. 2015). In particular, we use seismic records along three spatially consecutive MCS lines and a WAS profile acquired along these same lines (Fig. 7.1). The transect with good seismic coverage is 300 km long running NW-SE from the Gulf of Lions to the central part of the Liguro-Provençal basin (Fig. 7.1).

7.2.1. Multi-channel Seismic data

The MCS lines were acquired using a 360 channel, 4.5 km-long streamer and a tuned airgun array with a total capacity of 8,260 c.i., towed at a depth of 18-28 m depending on the profile (Moulin et al. 2015). The shot interval was 60 s, giving a shot spacing of about 140-150 m. These data were reprocessed using Globe Claritas software to obtain the section in Fig. 7.2. The main steps during the processing included shot interpolation every 50 m, spherical divergence correction, normal move out, near- and far-offset mute. We also applied a pre-stack multiple removal with parabolic radon filtering using super-gathers of 4 CMPs, which yield a common-mid point (CMP) fold of 25 with parabolic radon filtering, and a distance between channels of 12.5 m. This was followed by stack and post-stack finite difference time migration using a velocity model that follows the geology and is based on the tomographic results in this work. After stack, we applied a time- and space-variant band-pass frequency filter that was designed on the basis of the geological structure. We finally applied a two-window time-variant automatic gain control for amplitude balancing.

After processing, we picked the arrival times of P-waves reflected at three different seismic interfaces, corresponding to the top and bottom of the salt layer where visible and the top of the basement (Fig. 7.2). The main purpose of using MCS travel-times was to provide improved constraints on the overlying sedimentary structure, in order to diminish the uncertainty of the vertical velocity structure of the underlying crystalline crust. Deep near-vertical Moho reflections on the MCS shot gathers were not included in the inversion because the 4.5 km-long streamer provides negligible information of the internal Vp distribution in the crystalline crust, and the Moho is generally well determined from wide-angle PmP reflections. Further, near-vertical reflections might be affected by crustal velocity anisotropy (e.g. Sallares et al., 2013b). We first picked travel-times of each interface reflection at CMP gathers. During picking, we used the seismic image as a guide to ensure that the travel-time of each selected hyperbolic event in the CMP gather corresponded to the seismic interface of interest (see Fig. 5.1 in the Chapter 5: *Travel-time Tomography*). We picked every ~100 CMP gathers where the seismic interface was continuous and clear across the stack section. For the salt layer, we picked only those regions where both the top and bottom of the unit are clearly visible and do not display complex steep boundaries related to diapirism (e.g. km 160 along the profile; Fig. 7.2). Despite of these local discontinuities the three seismic interfaces are rather continuous along the region of

interest, particularly across the COT (Fig. 7.1). We then resorted the data set from CMP gathers to shot gathers, and used the picked travel-times every two shot gathers providing travel-time picks from each interface every 250-300 m along the profile. This spatial sampling is smaller than 400 m, which is the width of the first Fresnel zone at the depth of the first interface (~5 km of depth) considering a dominant frequency of 40 Hz. Therefore, decimating the travel-time dataset should not downgrade the tomographic resolution of the model. In total, we selected 795 reflected picks from the top and 593 from the bottom of the salt layer, and 889 from the top of the basement.

The estimated picking uncertainty is between 20 ms and 40 ms for MCS picks. These values are based on the signal-to-noise (S/N) ratio of the trace 250 ms before and after the selected travel pick as proposed by Zelt and Forsyth (1994).

7.2.2. Wide-Angle Seismic data

The WAS profile extends from the Gulf of Lions to the Liguro-Provençal basin (Fig. 7.1). This line was recorded by a total of 25 ocean bottom seismometers (OBS) spaced ~13 km from each other. For the purpose of this work we use OBS42 to OBS57 and OBS 8 deployed across the COT zone, excluding OBS 45, 49 and 52 that did not work properly. The wide-angle seismic source was an airgun array of 16 guns with single bubble configuration that released a total volume of 8,260 c.i. with main frequencies centred around 10-15 Hz. A total of 3,032 shots were fired along the profile. The OBS records were filtered between 1-3-15-30 Hz to enhance the signal.

The configuration of seismic phases identified in each OBS allows us to divide the seismic records in three groups. The first group, from OBS 42, to 44, is located across the continental slope in the first 110 km of the profile, and displays 4 phases (Fig. 7.3a). From 5 km to ~10 km offset we identify a seismic phase with an apparent velocity of ~4.0 km/s, and interpreted it as a P-wave refracted through the post-rift sediment (Ps in Fig. 7.3a). From 10 km to 50 km, we identify a second seismic phase with an apparent velocity of ~6.0 km/s, which we interpret as a P-wave arrival refracted through the crystalline crust (Pb in Fig. 7.3a). Finally, from 50 km to 80 km, OBS records show a prominent arrival with an apparent velocity of ~8 km/s that we interpreted as a P-wave refraction in the uppermost mantle (Pn). The crossover distance between Pb and Pn is marked by a secondary arrival that we interpret as a P-wave reflected at the crust-mantle boundary (PmP in Fig. 7.3a). The crossover distance between Pb and Pn varies from ~50 km in OBS 42 to ~30 km in OBS 44 (Fig. 7.3a), indicating crustal thinning oceanwards.

The second group includes OBS 46 to 51 and OBS 8 (Fig. 7.1 and 7.2). These receivers, which are located between 125 km and 225 km in the abyssal plain, display 5 different seismic phases (Fig. 7.3b). From 5 km to ~30 km offset they show a clear seismic phase with apparent velocity of ~4.0 km/s that we interpreted as the Ps (Fig. 7.3b). Between 25 km and 35 km offset, we identify a second seismic phase that we interpret as the Pb. This refracted arrival has an apparent velocity of ~7.0 km/s, which is higher than the apparent velocity of the Pb phase identified in the first group of OBSs. For this second group, we also picked the reflected phase that is identified at the crossover distance between the Ps and the Pb (PbP in Fig. 7.3b) to define the geometry of the top of this comparatively faster layer. From 35 km to 40-50 km of offset OBS records show a prominent arrival with apparent

velocity of ~8 km/s that we interpret as a Pn. In all the record sections, we observe wide-angle reflections at the crossover distance between the Pb and the Pn that we interpret as a PmP (Fig. 7.3b). The crossover distance between Pb and Pn is similar for all OBS records (~35 km of offset, Fig. 7.3b), which indicates little crustal thickness variations.

Finally, the third group of receivers includes OBSs 53 to 57. Although the quality of these receivers is poor at far offsets (> 40-50 km), possibly because of the presence of widespread diapirism in the post-rift sequence distorting the seismic signal (Fig. 7.2), we identify 4 seismic phases (Fig. 7.3c). First, a Ps phase with an apparent velocity of ~4.0 km/s identified between 5 km and 25 km of offset. Then a Pb phase between 25 km and 35 km, with an apparent velocity of ~6.0 km/s. This velocity is similar to that found in the first group of OBS but slower than that of the second group, indicating the existence of petrological variations in the crust along the profile. From 35 km to 45-50 km, the OBS records show a prominent arrival with apparent velocity of ~8 km/s that we interpret as a Pn. PmP phases cannot be identified in OBS number 53, 54 and 56 due to the decreasing signal-to-noise ratio at far offsets (Fig. 7.3c).

In total, we picked 3 refracted seismic phases with the following number of travel-time picks: 988 Ps; 1238 Pb; 6518 Pn. Also, 2 reflected seismic phases with this number of picks: 1172 PbP; 2554 PmP. OBS records present lower signal-to-noise ratio than MCS shot gathers. WAS picking uncertainty is estimated to be between 40 and 100 ms applying the same criterion as with MCS picks (i.e. Zelt and Forsyth, 1994).

◄ *Figure 7.2 - Reprocessed time-migrated seismic reflection from the profile A-B (see Figure 7.1 for location). The yellow dots are the OBS/OBHs location. The reflections in the seismic images show three main geological units: a sedimentary cover above and below layer of salt, a crystalline crust bounded by a strong reflector interpreted as the TOB (white dots) and finally, the reflections at ~8 s TWT that are interpreted as the Moho (blue dots).*

◄ *Figure 7.3 - Record sections corresponding to the vertical component of (a) OBS43 from Domain I, (b) OBS8 from Domain II and (c) OBS54 from Domain III. The interpretation of each seismic phases picked for the inversion is shown in the top panels, while the same record with the synthetic (red circles) and observed travel times (coloured vertical bars) is shown in the lower panel. Blue bars correspond to picked refracted phases (Pw, Ps, Pb and Pn), while yellow and orange correspond to reflected phases PbP and PmP, respectively. Pw are travel-times of the water wave; Ps are travel-times of refracted P-waves through the sedimentary unit; Pb are travel-times of refracted P-waves through the crystalline crust, Pn are travel-times of refracted P-waves through the uppermost mantle; and PbP and PmP are travel-times of reflected P-waves at the top of the basement and at the Moho, respectively. Record sections from the rest of receivers can be found in Fig. A7 in Appendix.*

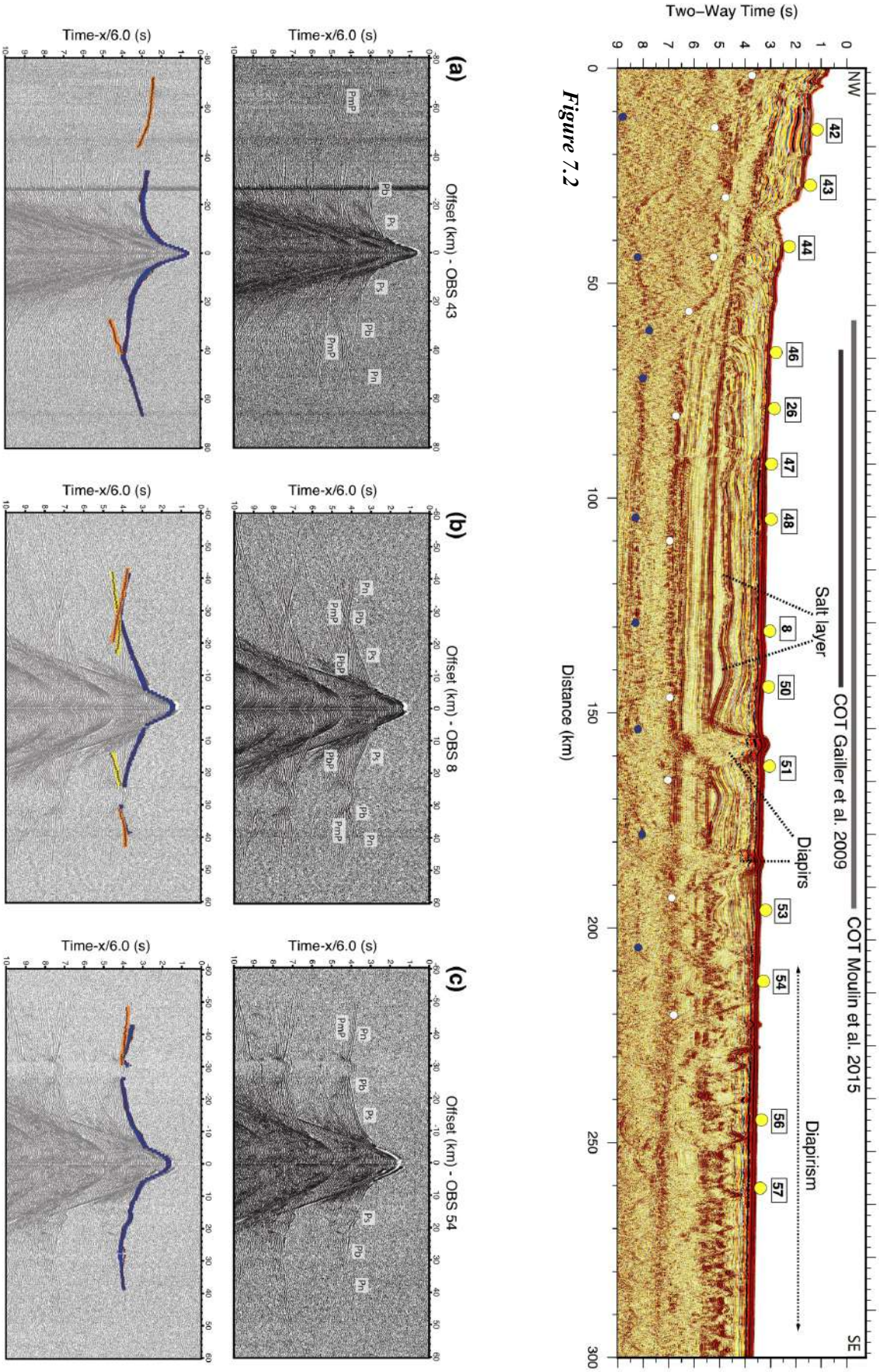

Figure 7.2

Figure 7.3

7.3. Methods

The tomographic approach applied in this study was aimed at decreasing the uncertainty in the Vp model and thus to facilitate the interpretation of the petrological nature of the crystalline crust by using additional travel-time information compared to previous modelling efforts. While WAS data recordings provide travel-time information up to ~100 km offset, it has a low data redundancy and a poor coverage within the sediment layer. In contrast, the MCS data offset is restricted to the streamer length (4.5 km in this experiment) but coverage and redundancy are much higher in the shallow region. The denser spatial sampling of MCS data as compared to WAS data provides a two orders of magnitude larger number of reflected travel-times, yielding a better ray coverage and thus helping to resolve the Vp distribution and the geometry of reflectors with greater accuracy and resolution. Combining WAS and MCS travel-times not only allows to better constrain the velocity structure, but also to retrieve complex geometries of the seismic interfaces that cannot be resolved by inverting WAS travel-times alone (Begović, 2020).

In addition, applying a tomographic method (i.e. *tomo2d;* Korenaga et al., 2000; Melendez et al., 2015) also allows to assess the velocity and depth uncertainty of each layer by means of statistical analysis with greater accuracy than techniques commonly applied to estimate model parameter uncertainty in forward modelling approaches. Tomographic methods fit the data in a series of linearized iterations yielding lower travel-time residuals than forward modelling. Consequently, results have a lower degree of uncertainty typically <± 0.2 km/s (e.g. Prada et al. 2015) as compared to forward modelling uncertainty analysis that are typically of ~0.5-1 km/s or even larger (Loureiro et al., 2016), as a result of the inherent subjectivity of the method. In addition, tomography provides a higher resolution Vp model in which each of the (thousands of) grid nodes is inverted to minimize the travel-time residuals, compared to the gentle ad hoc modifications of a few pre-defined Vp nodes in forward modelling approaches.

7.3.1. Joint refraction and reflection travel-time inversion of MCS and WAS data

To combine travel-time picks from MCS and WAS data into a joint inversion, we used a modified version of the joint refraction and reflection travel-time tomography code *tomo2d* (Korenaga et al., 2000; Melendez et al., 2015). This new version of the code enables to have both source and receivers at any point of the model, including the water layer (Begović, 2020). This allows the user to use MCS travel-times, in which both source and receivers are located close to the sea surface.

Tomo2d computes synthetic travel-times and ray paths using the graph method followed by the ray-bending method, and a linearized and regularized least-squared inversion scheme to update the initial model by minimizing the root mean squared (r.ms.) residuals between the observed and synthetic travel-times (Korenaga et al., 2000). This is done iteratively until the final residuals are of the order of the picking uncertainty (i.e. chi-squared, χ^2~1). Regularization parameters are introduced by fixing horizontal and vertical correlation lengths that control the smoothing of the model at each iteration step. The set of correlation lengths used in this study is shown in Table 5.2 in the Chapter 5: *Travel-time Tomography*. The inverted velocity model is 350 km-long and 20 km-deep (Fig. 7.4a). The node spacing in the vertical direction varies from 90 m at the seafloor to 500 m at the bottom, while it is

90 m in the horizontal component. Node spacing for the floating reflector used in each inversion step is also 90 m.

To construct the Vp model, we followed a layer-stripping strategy as in Sallarès et al. (2013a) and Prada et al. (2014). The final model in Fig. 7.4a was obtained after 6 layer-stripping steps (see Section A.1.1. in Appendix). In the first step, we inverted for the geometry of the top of the salt layer and the overlying Vp structure using only reflected MCS travel-time picks. The output of the first inversion step is then used as input for the second step, the area covered by the rays during the first step is overdamped to favour changes in the second layer, and we impose a velocity jump across the reflector. This process is repeated at each inversion step to account for vertical velocity contrasts between consecutive layers.

In the second step, we inverted the geometry of the bottom of the salt layer and its Vp structure using reflection travel-times from MCS data (Fig. A.2 in Appendix), whereas in the third step, we inverted the top of the basement and the velocity structure of the rest of the post-rift sedimentary unit. In this third step, we combine travel-times of reflected P-waves at the top of the basement from MCS data and Ps refractions from WAS data to constrain sediment velocity of the entire layer (Fig. A.3 in Appendix).

We used exclusively WAS travel-times for the velocity and interface geometry inversion of the underlying layers (i.e. crystalline crust and uppermost mantle). Thus, in the fourth step we inverted the top of the high velocity layer (HVL) observed in the second group of OBSs using Ps first arrival travel-times and PbP reflection travel-times from OBS 46 and 51 (Fig. A.4 in Appendix). In addition to the overdamping of the overlying layer, the inclusion of Ps phases in the inversion allows to preserve the overlying velocity structure.

In the fifth step, we used Ps, Pb, and PmP travel-times to invert for the Vp structure of the crystalline crust and the geometry of the Moho (Fig. A.5 in Appendix). Finally, in the sixth and last step we inverted for the uppermost mantle velocity using all the first arrival travel-times (i.e. Ps, Pb, Pn) together with the PmP reflections (Fig. A.6 in Appendix). The preferred final model, which is shown in Fig. 7.4, has a r.m.s travel-time residual of ~65 ms (see Table A.3.1 in Appendix for the r.m.s values at each inversion step). The averaged derivative weight sum from all the layer-stripping steps, which is a measure of the ray coverage throughout the model, is shown in Fig. 7.4b, while the ray coverage corresponding to MCS and WAS travel-times is shown separately in Fig. A.7 in Appendix, respectively.

7.3.2. Uncertainty analysis

To estimate the uncertainty of the model parameters due to combinations of the picking errors and of the selected starting velocity model, we performed a Monte Carlo-type statistical analysis. As in Prada et al. (2017), we performed the analysis layer by layer, following the layer-stripping strategy described in the previous section.

In this case, we performed 100 inversions for each layer. Each realization included a travel-time dataset adding Gaussian random picking errors with a variance corresponding to the picking uncertainty, a starting 1D Vp model for each layer with a random velocity-depth distribution (±5%, ±5% and ±6% for sediments, crustal and mantle velocities, respectively), and a flat reflector randomly generated within certain bounds depending on each layer (see Table S3 for the initial values of Vp and reflector depth of each layer, as well as the given range of variation). To include the effect of the regularization constraints, we also varied correlation lengths within a certain range in the different inversions (see Table 5.5 in Chapter 5: *Travel-time Tomography*).

The standard deviation of all the inverted Vp models and reflector geometry is taken as a proxy of the model parameter uncertainty (Tarantola et al., 1987). The outcomes of this analysis show that the Vp of most of the post-rift sequence is well constrained, with uncertainty of <0.2 km/s (Fig. 7.4c), except for areas with a high vertical velocity gradient (i.e. top and bottom of salt), and for regions with limited ray coverage (i.e. beneath OBS 51 in Fig. 7.4c), where uncertainty is 0.3-0.5 km/s. Depth uncertainty for the reflectors inverted with MCS travel-times is 0.05-0.2 km for the top of the salt, 0.02-0.3 km for the bottom of the salt, and 0.1-0.6 km for the top of the basement. The small variations indicate that the overall vertical velocity structure is well constrained throughout most of the model.

Uncertainty is higher in the crust and in the uppermost mantle layers, due to the fact that it is only sampled by WAS data. Thus, Vp uncertainty is 0.1-0.2 km/s in the basement, with localized regions showing higher values (up to 0.5 km/s at 180-200 km) due to a poorer ray coverage. Uppermost mantle velocity is also well constrained with Vp uncertainty <0.2 km/s. The HVL reflector and the Moho are constrained within 0.32-1.5 km and 0.25-1.6 km, respectively. The highest uncertainty, of >1 km, correspond to the edges of both reflectors which have limited ray coverage and are subject to strong Vp-depth trade-offs.

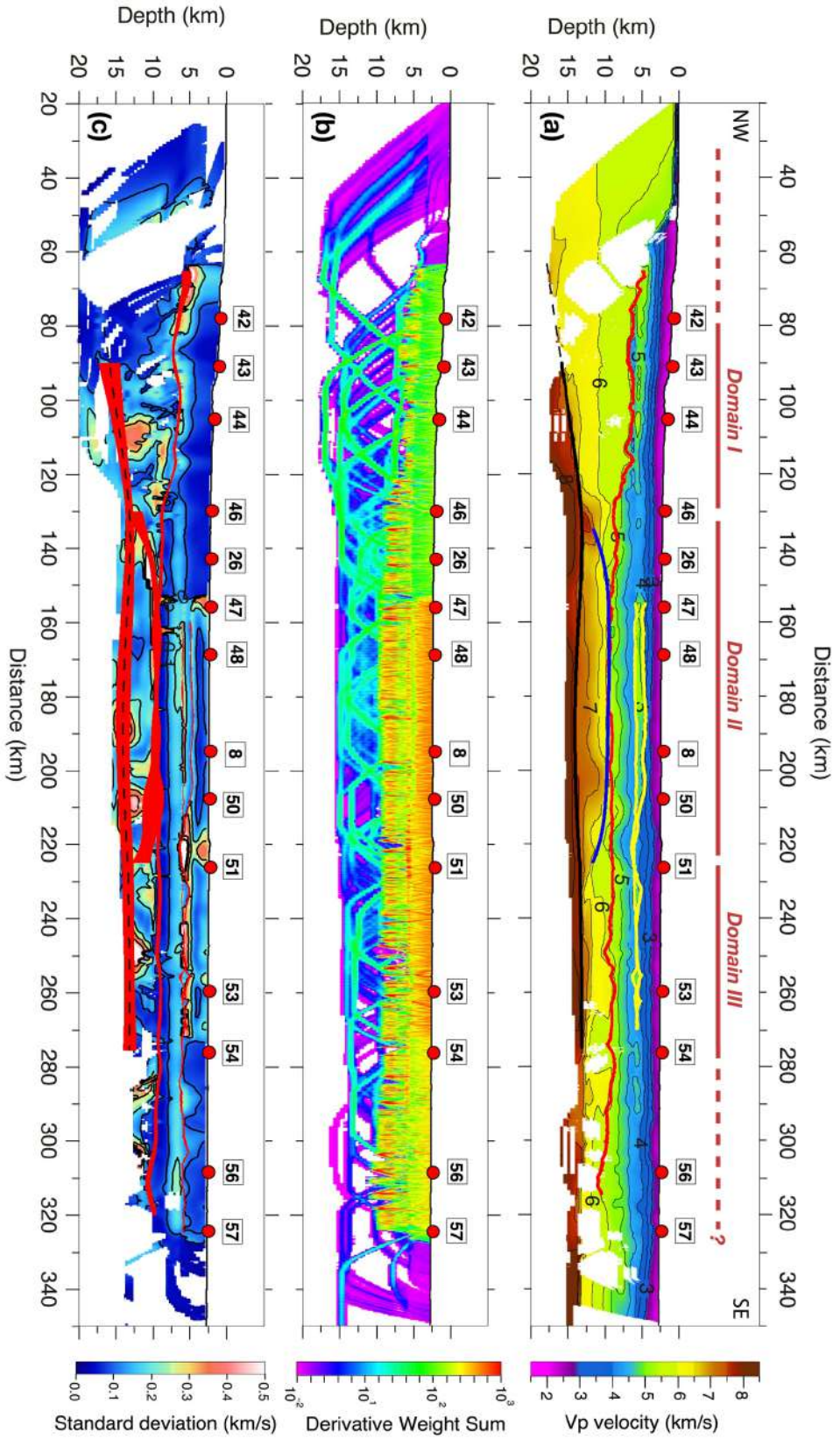

Figure 7.4 - (a) Preferred 2-D P-wave model and geometry of the reflectors obtained from the tomography along transect A-B. The different horizons are in yellow the base and the top of the salt layer, red is the top of the basement, in blue the high velocity layer (HVL), and in black the Moho geometry. (b) Derivative weight sum (DWS) of tomographic model in (a). (c) Standard deviation of Vp values of the average solution of the Monte-Carlo analysis for profile A-B. The width of the red band shows the standard deviation of the depth of the inverted horizons in (a). Red circles are OBS locations.

7.4. Results

7.4.1. P-wave velocity structure

Our preferred model (Fig. 7.4) includes the sediment cover, the crystalline crust and the uppermost mantle. Post-rift sediment displays a smooth vertical velocity gradient with Vp of 1.7 km/s at the top and ~5.0 km/s at the bottom. The salt body inserted within the sediments has Vp of 4.5-5.0 km/s. The top of the basement deepens from 5 km depth at km 60 along the profile to ~10 km at km 150. From 150 km to 275 km, the basement top is rather flat and located at ~10 km depth. At further offsets, this interface gently deepens towards the southeast (Fig. 7.4).

The Vp and thickness variations of the crystalline crust allows us to identify three different domains (Domains I, II, III in Fig. 7.4):

Domain I, which extends from 80 km to ~135 km along the model (Fig. 7.4), is the area where crustal thinning concentrates. Crustal velocities range between ~5.5 km/s at the top to 6.5-6.7 km/s at the bottom. The Moho in this domain is constrained oceanwards from 90 km of profile distance, and shallows towards the SE from 15 km depth at 90 km along the profile to ~12.5 km depth at ~130-135 km.

Domain II extends from ~135 km to 225 km (Fig. 7.4). The geometry of the Moho and the reflector inverted from PbP phases along this domain define a well-delimited lens-shaped high-velocity body (~7.0-7.2 km/s). This HVL narrows between 135 km and 225 km along the profile, having a maximum thickness of 4-5 km over ~50 km of profile distance. Interestingly, the top of the HVL layer coincides with the top of the basement independently inverted from MCS travel-times in the central ~50 km of the HVL.

Domain III extends towards southeast from 225 km to at least 275 km of profile distance (Fig. 7.4). At further offsets, the sparse OBS spacing, and the low S/N of the OBS records, potentially caused by widespread diapirism, increases the uncertainty of the tomographic results for Domain III. Along this domain, crustal Vp ranges between 5.5-6.0 km/s at the top to ~6.7-6.9 at the bottom, similar to Domain I and considerably slower than in Domain II. The discontinuously imaged Moho displays a sub-horizontal geometry at ~12.5 km depth.

The limited ray coverage of the uppermost mantle shows relatively low velocities beneath Domain I profile, increasing from ~7.6 km/s right under the Moho to 7.8-8.0 km/s 2-4 km deeper (Fig. 7.4).

7.4.2. Tectonic Structure

The reprocessed and post-stack time-migrated MCS data display the sediment cover, the top of basement along most of the profile, and groups of deep reflections in the lower crust, some of them possibly delineating the Moho (Fig. 7.5a). We converted the Vp model to two-way-time (TWT) and superimposed it on the MCS seismic image to directly compare the information obtained with the two methods (Fig. 7.5b). Numerous structures in the seismic image have a good correspondence with

the domains defined by Vp changes, providing links between tectonic features and the nature of the basement rocks. Thus, we used the time migrated MCS section and the Vp model superimposed on the MCS image to interpret the tectonic evolution of the different domains (Fig. 7.6).

The thickness of the sedimentary sequence resting on top the basement ranges from 3-4 km under the slope to 7-8 km under the deep basin. The oldest post-rift layers downlap on the basement top, syn-rift deposits, or previous downlapping deposits as the younger layering progresses into the deep basin. Just beneath the salt layer there is a unit that overlays these deposits and laps on them, filling the basin upslope. The salt layer has slid downslope into the deep basin causing abundant diapirism and extension with listric faulting in the overriding sediment (Fig. 7.6).

Domain I displays a ~10-km thick crust under OBS 43 that thins to 4-5 km at km 100, under the base of the slope. The tectonic structure of the basement is dominated by faults with vertical offset of up to ~2 km. Although fault planes are not imaged, block tilting and the top basement geometry indicate that they dip towards SE. The main half-grabens infill, of up ~0.8 s TWT-thick, are chaotic sediment packages probably representing syn-tectonic deposits. Normal faults become smaller towards the edge of Domain I, where the crystalline crust is ~5 km thick. These faults seem to cut most of the crust in this region of Domain I.

The HVL in Domain II is observed in the MCS data as a high-amplitude smooth top basement reflection and a base reflection representing the Moho (Fig. 7.6). The centre of this domain displays little evidence of normal faulting and has smooth basement relief. The seismic image does not show intra-basement reflectivity, but two dipping reflections delineate the boundaries with the other two domains. A reflection dipping at shallow angle towards the continent delineates the boundary between Domains I and II. A similar reflection identified as T-reflector (de Voogd et al., 1991) has been observed in other MCS lines in the area at about the same structural location (Jolivet et al., 2015, Granado et al., 2016). This new reprocessed section allows to identify a SE-dipping reflection that coincides with the inverted boundary between Domain II and III, and that was not reported in earlier studies (e.g. Moulin et al., 2015). The Moho is delineated by high-amplitude low-continuity reflections at 12.5 km depth.

In Domain III, salt halokinesis results in numerous narrow and steep salt diapirs that obscure the seismic image, so that the structure below cannot be clearly interpreted because of 3D energy scattering and abrupt lateral velocity changes. We can infer that the structure of the basement is relatively constant with a thin crust (4-5 km thick). The basement displays a few discontinuous reflections that may indicate minor normal faults dipping NW (Fig. 7.6).

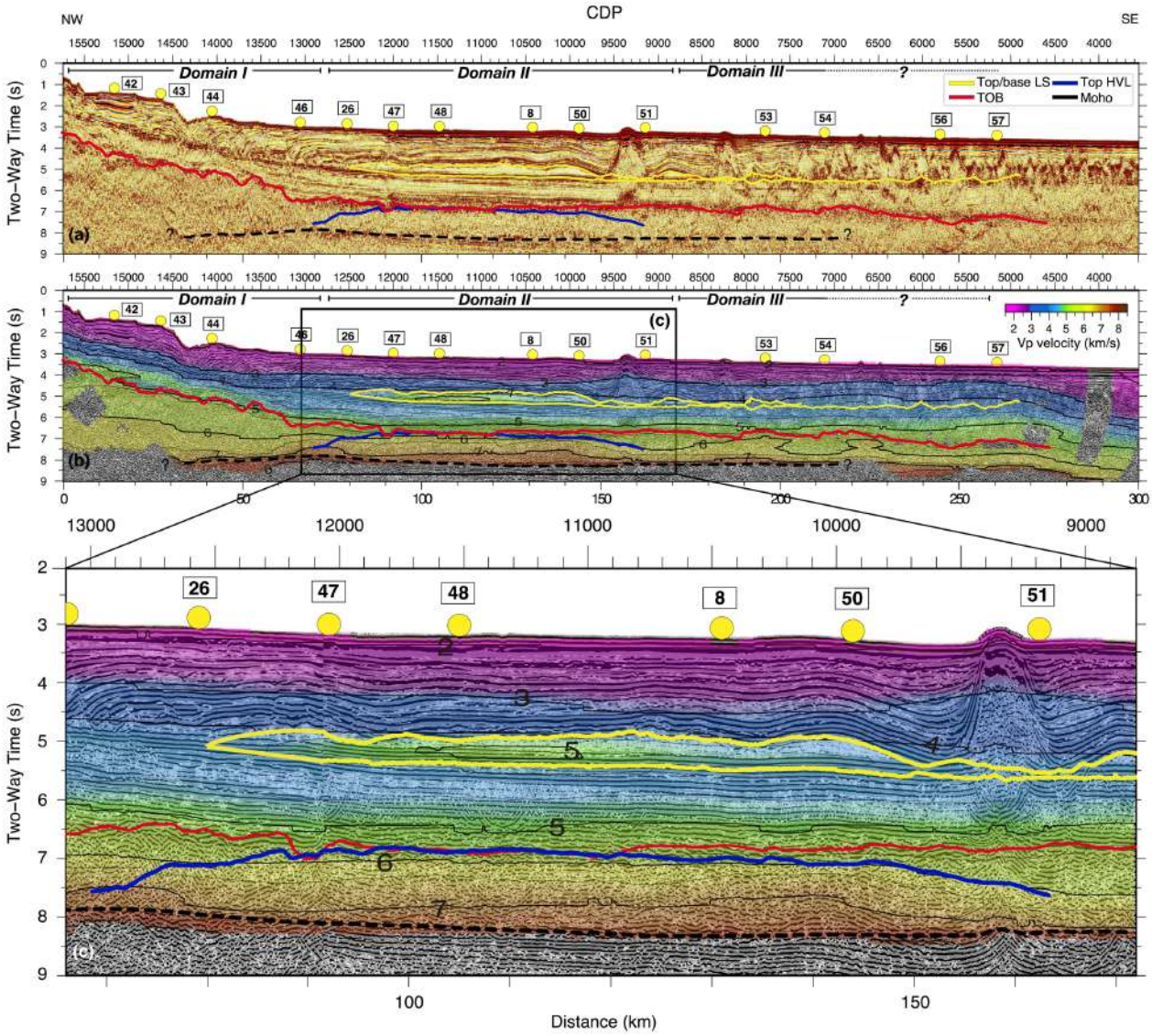

Figure 7.5 - (a) Time-migrated seismic reflection of profile A-B overlaid with geometry of the inverted horizons (yellow lines for the top and base of the layer of salt, red line for the top of the basement, blue line for the top of the layer with high velocities and black for the Moho boundary). (b) MCS image of profile A-B overlaid by the P-wave velocities of the tomographic model in Fig. 7.4a converted to TWT. The inverted horizons from Fig. 7.4a are also display in this figure. Yellow circles represent the OBS location. (c) Close-up of Domain II (location at Fig.7.5b).

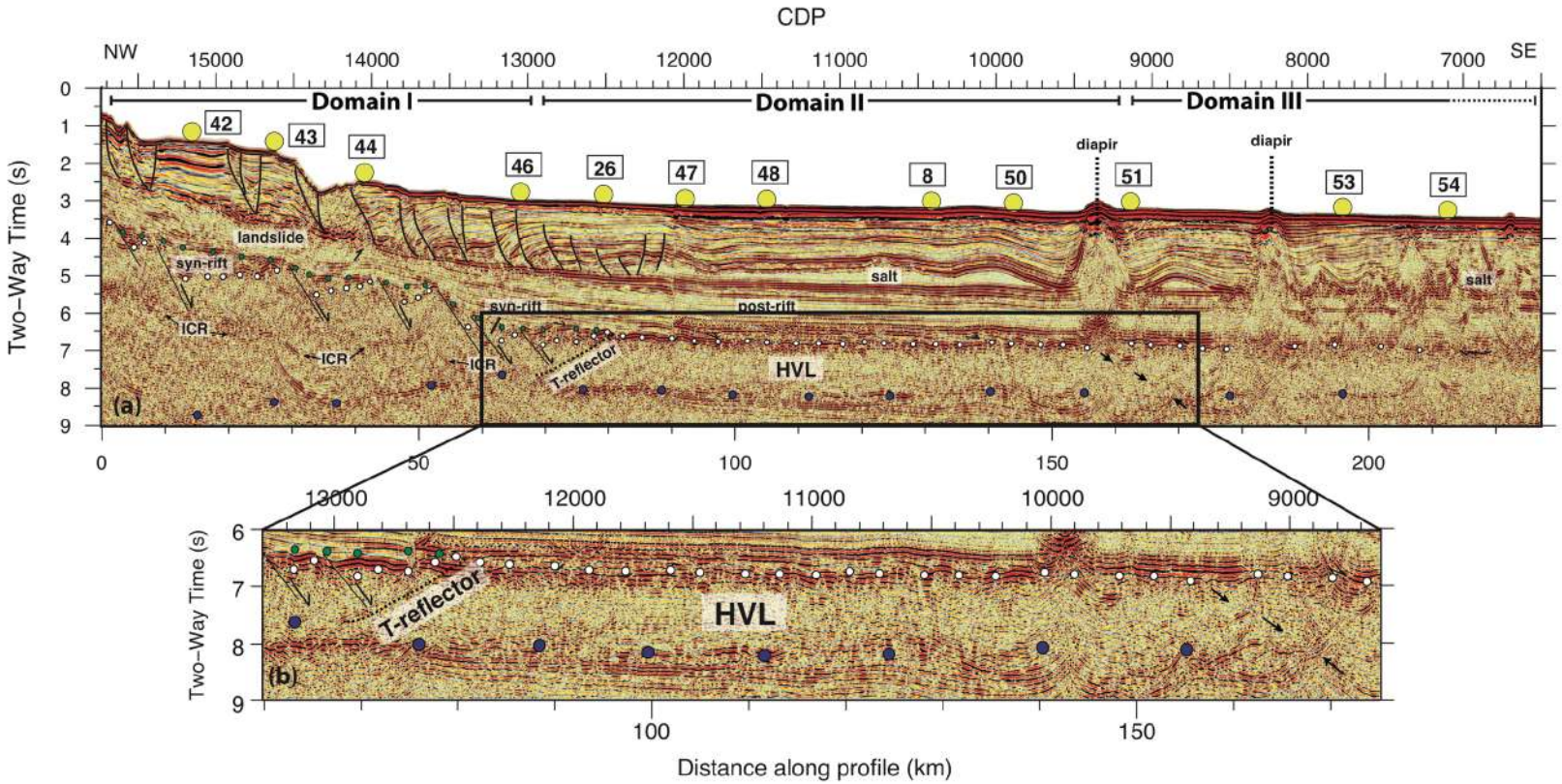

Figure 7.6 - Time-migrated seismic reflection of profile A-B. Yellow circles represent the OBS/OBH location. The reflections in the seismic images show a strong reflector interpreted as the TOB (white dots) cut by normal faults. The top of the syn-rift sediments is delimited by green dots. The reflections at ~7-8 s TWT are interpreted as the Moho (blue dots). HVL: high velocity layer, ICR: intra-crustal reflections.

7.5. Discussion

7.5.1. The nature of the basement

The Vp model displays three domains defined by a combination of differences in Vp ranges (Fig. 7.7), vertical Vp gradient, and crustal thickness (Fig. 7.8). Overall, the lateral Vp variations and the juxtaposition of crustal domains are comparable to those observed in previous studies (Gailler et al., 2009; Moulin et al., 2015), but our results locally differ in Moho location and on the 1D vertical velocity structure (Fig. 7.9b), requiring a re-evaluation of the petrological nature of the geological domains.

We infer the petrological nature of the crust from the Vp range and vertical Vp gradient (Fig. 7.7 and 7.8), as well as gravity modelling (Fig. 7.10). To infer rock type for the crystalline crust we compared the vertical Vp structure with 1D Vp-depth reference models for continental crust (Christensen and Mooney, 1995), ultra-thin continental crust (Prada et al., 2015), exhumed mantle from the Tyrrhenian basin (Prada et al., 2014) and the Gulf of Cadiz (Sallarès et al., 2013a), and for oceanic crust (Grevemeyer et al., 2018) (Fig. 7.7). We extracted 1D Vp-depth profiles from each domain in our model, avoiding regions with high uncertainty (Fig. 7.4c). We focused on regions with Vp uncertainty < 0.1 km/s, corresponding to km 95-105 in Domain I, km 150-175 in Domain II, and km 260-270 in Domain III (Fig. 7.7d).

- ***Domain I***

Previous studies with 1D models from expanded spread profiles (ESP) mapped one basement layer of ~6.2 km/s velocity in Domain I, interpreted as continental crust (Pascal et al., 1993), although that velocity also is an average of oceanic crust (e.g. Grevemeyer et al., 2018). Our Domain I model presents a Vp-depth distribution that corresponds to continental crust (Christensen and Mooney, 1995) (Fig. 7.7a). Domain I Vp-depth structure and Moho geometry slightly differ from previous models (Fig. 9c). The Vp structure from all studies indicates continental crust, but our model is up to 0.5-km/s slower in the upper crust, which may be due to the improved definition of the top of the basement and a higher Vp of the lowest strata (Fig. 9c). We constrained top of the basement geometry with MCS travel-times, providing higher spatial resolution of relief than with WAS travel-times (Begović, 2020). The joint inversion of WAS and MCS travel-time defines the relief of tilted fault blocks of Domain I in the Vp model (Fig. 7.6), whereas the boundary was either not inverted (Gailler et al., 2009), or manually built (Moulin et al., 2015) as a comparatively smooth interface (Fig. 9b). Comparison of the Vp model with the MCS image shows a detailed match of top of basement image and inverted reflection (Fig. 7.5). Our layer stripping approach defines generally slower velocities above the TOB than previous studies (Fig. 7.9a), along Domain I.

The different Vp-depth structure of the crust of Domain I and transition to II respect previous studies causes differences of ≤4-5 km in Moho depths between our results and previous models (Fig. 7.8b). Overall, our model shows a sharper crustal thinning along Domain I, partially caused by a deeper TOB (Fig. 7.9b).

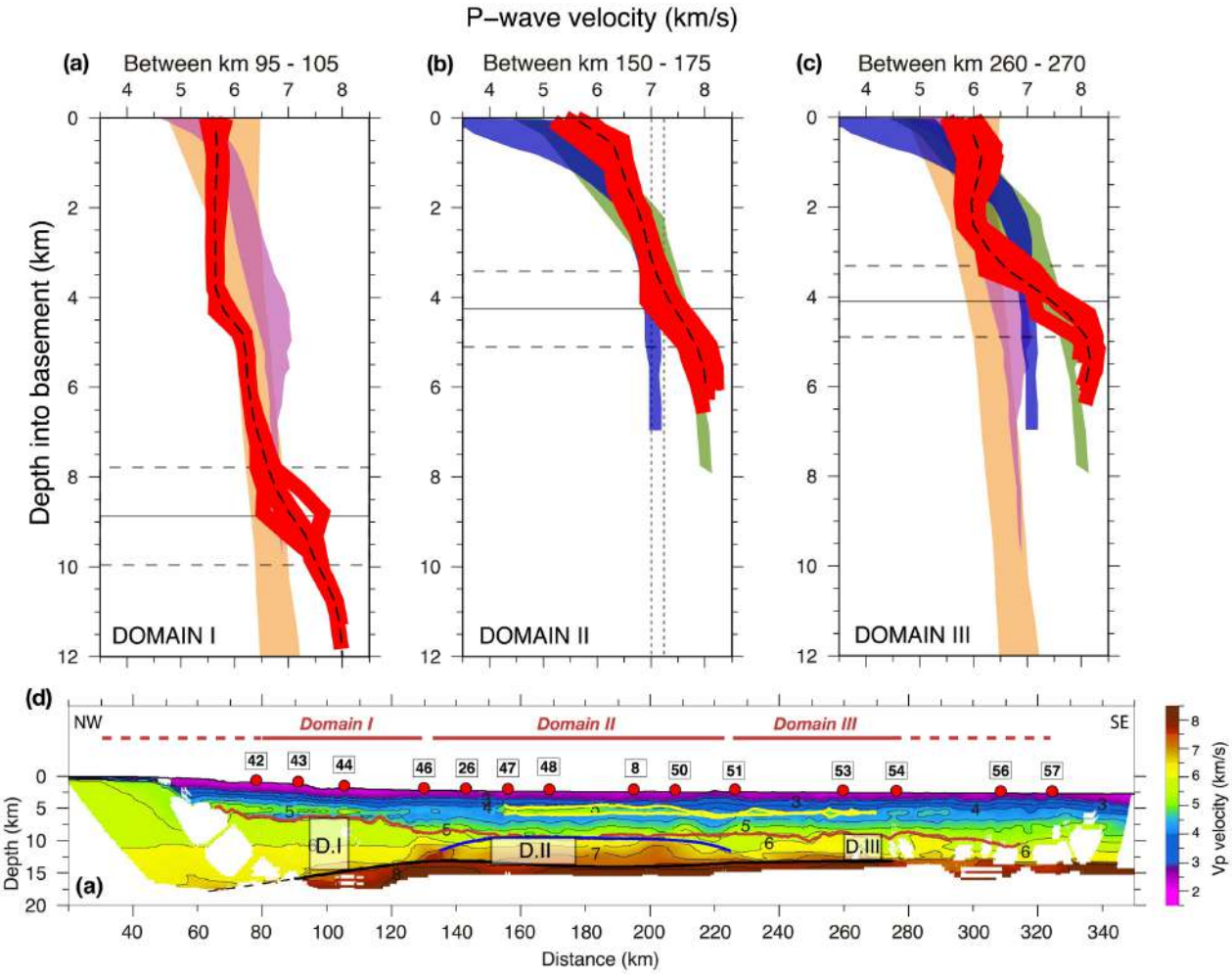

Figure 7.7 - Comparison of the vertical velocity structure of the crystalline crust along Domain I (a), II (b) and III(c) with seismic velocity reference models. The red profiles represent 1D profiles from each domain, while the black dashed line correspond to the average profile for each domain. Dashed horizontal lines represent the uncertainty in Moho depth, while the solid black line is the average depth. The 1D P-wave velocity depth references are displayed in different colors: oceanic crust (after Grevemeyer et al. 2018) in blue, continental ultra-thin (CUT) crust in violet (after Prada et al., 2015), and tan color for continental crust (from Christensen and Mooney, 1995). The exhumed mantle reference model is from modern seismic data in the Gulf of Cadiz (Sallarès et al. 2013a) and the Tyrrhenian (Prada et al. 2014). (d) Tomographic model showing the region from which 1D velocity-depth profiles are extracted in each domain.

- ***Domain II***

The vertical crustal Vp structure of Domain II has a two-layer gradient (Fig. 7.7b). The first layer is characterized by a strong vertical Vp gradient (~1 s^{-1}) with Vp increasing from 5.5 to 6.5 km/s in < 1 km. The second layer exhibits a gentler gradient (~0.2s^{-1}) with Vp gradually increasing from 6.5 to 7.2 km/s in 3-4 km (Fig. 7.7b). The two-layer gradient is typical of oceanic crust seismic structure; however, the upper layer is somewhat faster than typical layer 2 oceanic Vp, but the second layer agrees well with oceanic layer 3 (Grevemeyer et al. 2018). The sediment cover at mid ocean ridges is 0.1-1 km thick (Grevemeyer et al., 2018; Christeson et al., 2019). However, overlying sediment units of 18 km-thick can be found in oceanic crust older than 7.5 Ma (Christeson et al., 2019). In these regions, increasing sediment overburden results in higher Vp at the top of layer 2. In our study, the sediment unit above Domain II is 7-8 km thick, and the velocity at the top of this domain is ~6 km/s (Fig. 7.8b). These values are consistent with the trend of sediment thickness and Vp at the top of layer 2 observed in oceanic crust worldwide (Christeson et al., 2019) (Fig. 7.8b), thus supporting the presence of highly-compacted oceanic Layer 2 rocks in this domain.

Previous interpretations along this domain include lower continental crust (Gailler et al., 2009; Moulin et al., 2015) or a mixture of serpentinized mantle and lower crust (Gailler et al. (2009). The abrupt Moho boundary mapped with clear PmP arrivals and visible in MCS images is at odds with the presence exhumed serpentinized mantle (Prada et al., 2015; 2016). A well-constrained 6.5-6.6 km/s Vp across much of Domain I lower crust (i.e. 90-100 km in Fig. 7.7) is somewhat lower than average lower crust of Domain II. The two basement layers of Moulin et al. (2015) differ from our inversion results, which locate the top of the HVL at a shallower depth (Fig. 7.8c). Further, our model has higher Vp, which is constrained by wide-angle refractions and bounded by the TOB that is inverted by MCS travel-times and the Moho along Domain II (Fig. 7.7). This makes the Vp distribution of the crystalline crust to be remarkably well constrained. WAS data along Domain II lack reflections between PbP (top of HVL) and PmP (bottom of HVL) phases, so no abrupt intermediate interface occurs. Based on analysis of typical forward modelling uncertainty, the intra-basement reflector in Moulin et al. (2015) may have uncertainties of ±1-2km (Fig. 8 in Loureiro et al., 2016), which are large enough to match the top of the HVL in our model.

Thus, although the average Vp of the HVL is similar in all existing models, the detailed internal Vp-depth profile, which has been refined with our modelling strategy, displays key characteristics of back-arc oceanic crust. Although the HVL in Domain II shows lower average Vp and is thinner than the average oceanic crust created by pressure release melting of a pyrolytic mantle source (Fig. 7.8a), both Vp and thickness agree with those observed in other back-arc settings. In these settings, the mantle source composition and the melting release process are thought to be more complex than Atlantic-type oceanic spreading because of the interaction between the slab and the back-arc mantle (Fig. 7.8) (Grevemeyer et al., 2020). Our results show that the average vertical Vp of the HVL is 6.8-7.0 km/s, while its thickness is 4-5 km. These values coincide with those observed in the Parece Vela Basin and the western Parece Vela Basin (Grevemeyer et al., 2020) (Fig. 7.8a). The average vertical Vp structure along the HVL is also similar to those found in the Algerian-Balearic oceanic Basin, although crustal thickness along the HVL is 0.5-1 km thinner (Fig. 7.8b). These observations further support the presence of back-arc oceanic crust in Domain I.

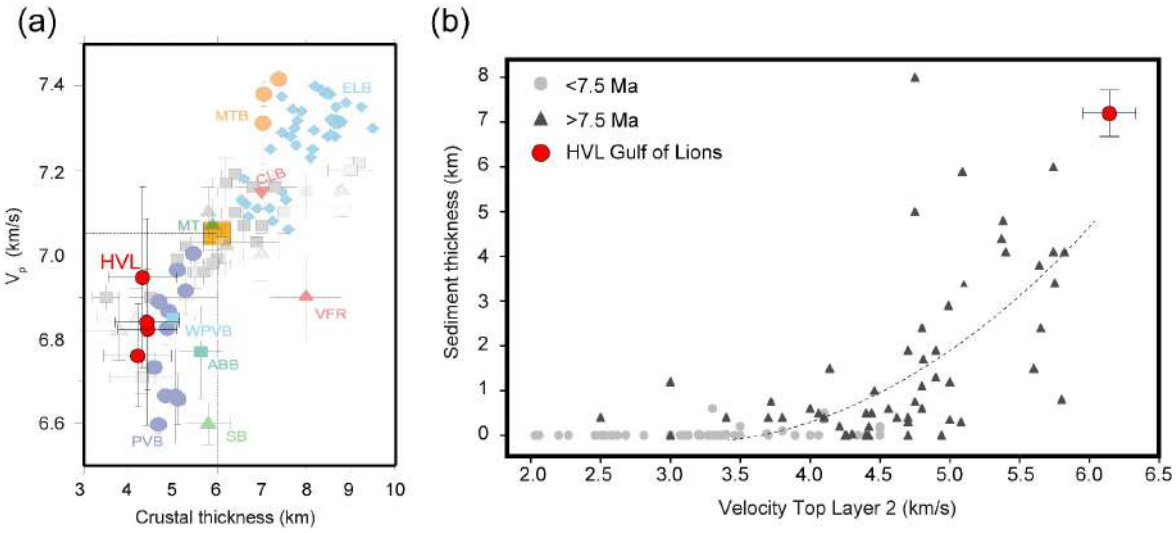

Figure 7.8 - (a) Comparison of crustal Vp and crustal thickness values from this studies (red circles) and other oceanic crusts of the world (after Grevemeyer et al., 2020). The orange square indicates a 6 km-thick crust expected for a pyrolytic mantle source and normal mantle temperature. Values for oceanic crust at slow and ultraslow spreading ridges (light grey), and fast spreading ridges (dark grey) are included in the figure, as well as values from oceanic back-arcs (coloured symbols). Red dots correspond to average values of vertical velocity and crustal thickness extracted from 10 km-wide bins along the HVL in this study. Back-arc basins included in this figure are PVB: Parece Vela Basin; WPVB: Western Prece Vela Basin; ABB: Algerian-Balearic Basin; VFR: Valu Fa ridge; MTB: Mariana Trough Basin; MT: Marian Trough spreading center; ELB: Eastern Lau Basin (references to each back-arc location can be found in Fig. 3 of Grevemeyer et al., 2020). (b) Diagram showing the variation of Vp at the top of layer 2 (L2) with increasing overlying sediment thickness for oceanic crust older and younger than 7.5 Ma (after Christeson et al., 2019). The red dot is the average value from the top of the HVL region in this study.

- ***Domain III***

The vertical Vp structure of the crystalline crust in Domain III has two layers. The upper layer Vp ranges between 5.0-5.5 km/s, whereas the lower layer Vp increases from 5.5-7.0 km/s, although the large Moho location uncertainty makes the Vp gradient unreliable (Fig. 7.7c). The range and Vp-depth gradient in Domain III fits better with that of ultra-thin continental crust (Fig. 7.7c). This also agrees with the weaker velocity contrast at the TOB, indicating the lack of highly reflective magmatic rocks at the top of the basement. A similar interpretation was proposed further north in the Ligurian Basin from a nearby WAS profile (Dannowski et al., 2020). Our model suffers from limited ray coverage south-eastwards of km 275 along this domain, so that the petrological interpretation of the basement in this region has large uncertainty bounds.

Previous interpretations of Domain III support oceanic crust (Pascal et al., 1993; Contrucci et al., 2001; Gailler et al., 2009) or atypical oceanic crust (Moulin et al., 2015). The different interpretations for the nature of Domain III arise from the lower Vp (~0.5-1 km/s) that we retrieve along this domain and the lack of low-crustal velocities exceeding 7.0 km/s (Fig. 7.9c). In addition, the average vertical velocity structure (6.0-6.5 km/s) and the thin crust (4-5 km-thick) along this domain resembles that of continental rifted crust reported in the Ligurian Basin (i.e. between 70 km and 120 km of profile distance in Fig. 4a in Dannowski et al., 2020). Altogether, these observations support the continental nature of Domain III.

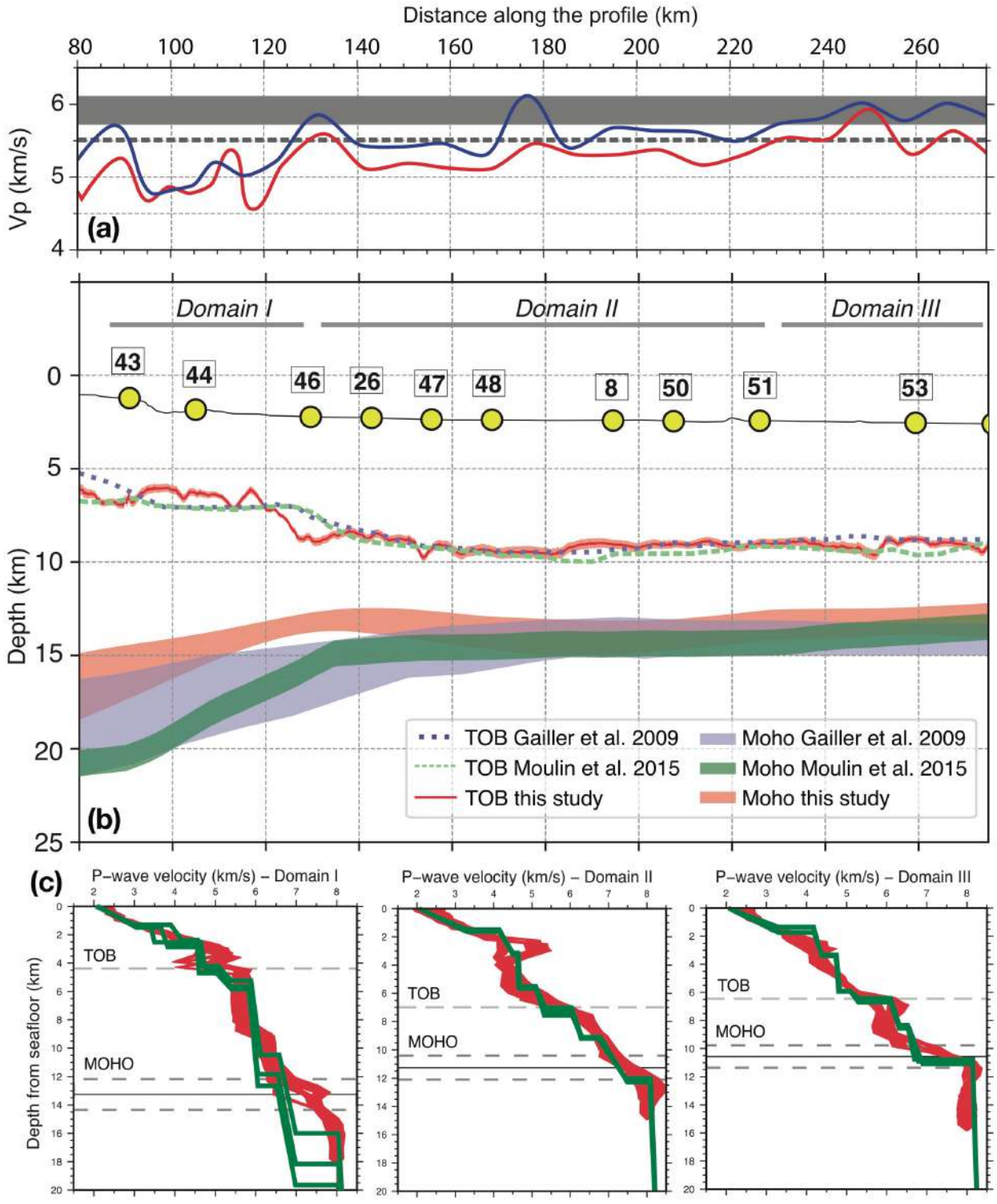

Figure 7.9 - (a) Velocity at 0.5 km above the TOB (line in red) and velocity at 0.5 km below the TOB (line in blue) in this study. The TOB velocity from Gailler et al. (2009) is represented by the dashed line and the velocity from the TOB velocity from Moulin et al. (2015) is represented by a shaded area in grey. (b) Comparison between TOB and Moho reflectors from Gailler et al. (2009), from Moulin et al. (2015) and this study. Uncertainties on reflectors depth are reported as shaded areas. Yellow circles represent the OBS location. (c) Vertical velocity structure comparison from the seafloor between Moulin et al. (2015) Vp model (green) and this study (red). The black dashed line corresponds to the Moho depth uncertainty, and the solid line is the average Moho depth in this study. The dashed grey line shows the location of the top of the basement in this study.

7.5.2. Gravity modelling

We tested our petrological interpretation of the crystalline crust with gravity modelling (Fig. 7.10). We converted mmodel Vp using Vp-density (ρ) relationships for each rock-type interpreted in this study. We used Hamilon's (1978) relationship to convert Vp of sediments to density, and decreased densities within the salt layer to 2.2 g/cc based on empirical observations (Samperi et al., 2020). We applied Christensen and Mooney (1995) relationship for continental crust to convert Vp of the crystalline crust along Domain I and III, and Carlson and Herrick (1990) relationship for oceanic crust to convert velocities along Domain II. We assumed a constant mantle density of 3.3 g/cc in this case. The synthetic gravity response of the resulting model has an RMS of ~16 mGal respect the satellite anomaly (Sandwell et al., 2014), with the largest misfit concentrated along Domain I (Fig. 7.10a), where the deep crustal structure is poorly constrained by the WAS data.

To improve the fit between both anomalies, we build a second model in which we take into account the low uppermost mantle velocities retrieved beneath Domain I (Fig. 7.10b). We use Carlson and Miller (2003) Vp-ρ relationship for serpentinized peridotites to convert Vp of the mantle in this region. This new model results in a better fit of ~5 mGal indicating that lower densities are required to explain the gravity anomaly in this region. Due to the limited ray coverage in this domain, we cannot fully resolve if the gravity anomaly is related to partially serpeninized uppermost mantle or continental crust somewhat thicker than our model. However, this second scenario would imply a high-density lower crustal material, which is unlikely based on lower-crustal Vp of ~6.5 km/s retrieved by earlier modelling results with more OBSs along the shelf and better ray coverage underneath (Gailler et al., 2009; Moulin et al., 2015). Regardless Domain I, gravity modelling supports the presence of oceanic crust along Domain II between continental crust of Domains I and III.

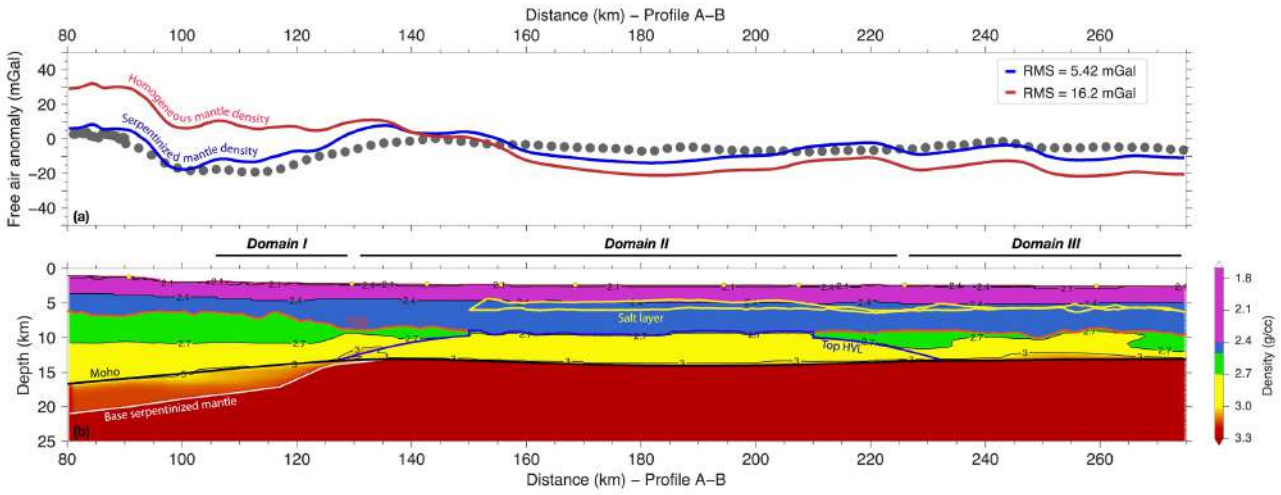

Figure 7.10 - (a) Satellite free air gravity anomaly along the profile in this study (Sandwell et al., 2014) compared with the synthetic gravity anomalies derived from a density model with serpentinized mantle beneath Domain I (b) (blue line), and with a homogeneous mantle density of 3.3 g/cc beneath the Moho along the entire model (red). Details of the Vp-ρ conversion can be found in the text.

7.5.3. Crustal thinning and narrow oceanic crust in the Gulf of Lions

In our model, the continental crust displays a rather asymmetric structure, with progressive crustal thinning until break up in ~70 km along Domain I. Faulting is limited to a < 40-km-wide region where the crust thins from 12.5 km to 4-5 km. In contrast, Domain III accommodates no further thinning within 60-80 km, where it displays a 4-5 km thick crust. This type of asymmetry is typical of most rifted margins and may arise from gradual migration and focusing of the area of faulting (Ranero and Pérez-Gussinyé, 2010).

In our study, MCS data image the top of the basement, which is well delineated in the sector where it corresponds to the top of the HVL, and it also images the edge of the HVL as it pinches out to either side abutted by continental crust domains (Fig. 7.6), with the T-reflector at the NW limit as it had been previously observed (de Voogd, 1991). This means that we have an excellent control on the dimensions and properties of the HVL body, its geometrical relationship to the continental domains, and the geometry and nature of the corresponding COT (Fig. 7.11). Other authors, who inferred the basement nature on the basis of the MCS images, propose that Domain II is a 100 km-wide segment of exhumed lower crust with a fairly constant thickness of 5 km (Jolivet et al., 2015; Granado et al., 2016). This lower crustal body would have been exhumed by a large detachment structure. In these models, the basement in Domain III is interpreted to be made of exhumed mantle rocks (e.g. Jolivet et al., 2015). Our interpretation of the Vp tomographic model and the MCS images is that the crust thins from ~12.5 km under the continental shelf to 4-5 km in ~70 km of profile distance (Fig. 7.11a). Assuming an initial crustal thickness of 30 km (e.g. Moulin et al., 2015) this values result in a stretching factor (β) of 6-7 before break up and seafloor spreading. Considering a potential temperature of 1350°C for the asthenosphere and a rift duration of 8-12 m.yr. (Gattecceca et al. 2007), melt production for this β should produce a 4-5 km-thick oceanic crust (Bown and White, 1995). It is possible that part of the melt did not reach the crust, and some 20% may have remained in the mantle (White et al. 1992). We assume that melt production was gradual and that emplacement in the crust initiated by underplating the continental crust at the locus of thinning. This scenario is compatible with the thickness of the HVL, which gradually increases for ~10-15 km under the thinned continental crust at either side of the HVL. This ~40-km-wide transition region is reasonably well constrained in the Vp model. First, the location of its top is resolved by a wide-angle reflection (PbP in Fig. 7.3c and Fig. 7.4a) and, second, the upper boundary is also marked by a reflection in the MCS data that supports the presence of an abrupt boundary between the continental crust and the underlying magmatic body (Fig. 7.6). Assuming that the opening rate remained constant, the crustal thickness (4-5 km) agrees with the melt production predictions (Fig 7.11a). Thus, the COT on either side of Domain II extends for ~10-15 km, but locally it is an abrupt petrological contact visible at the scale of the MCS resolution, with a 6 km/s Vp and ~10 Hz peak frequency at that depth (Fig. 7.6).

Therefore, the HVL is ~75 km-wide and extends ~10-15 km more as underplating of continental Domains I and III (Fig. 7.10b). The confinement of oceanic crust in such a narrow domain may relate to back-arc extension jump eastwards to form the Tyrrhenian, ceasing the oceanization in this region of the Liguro-Provençal basin. The confined oceanic domain agrees with recent tomographic results further north in the Ligurian Basin that support continental crust and failed rifting (Dannowski et al., 2020).

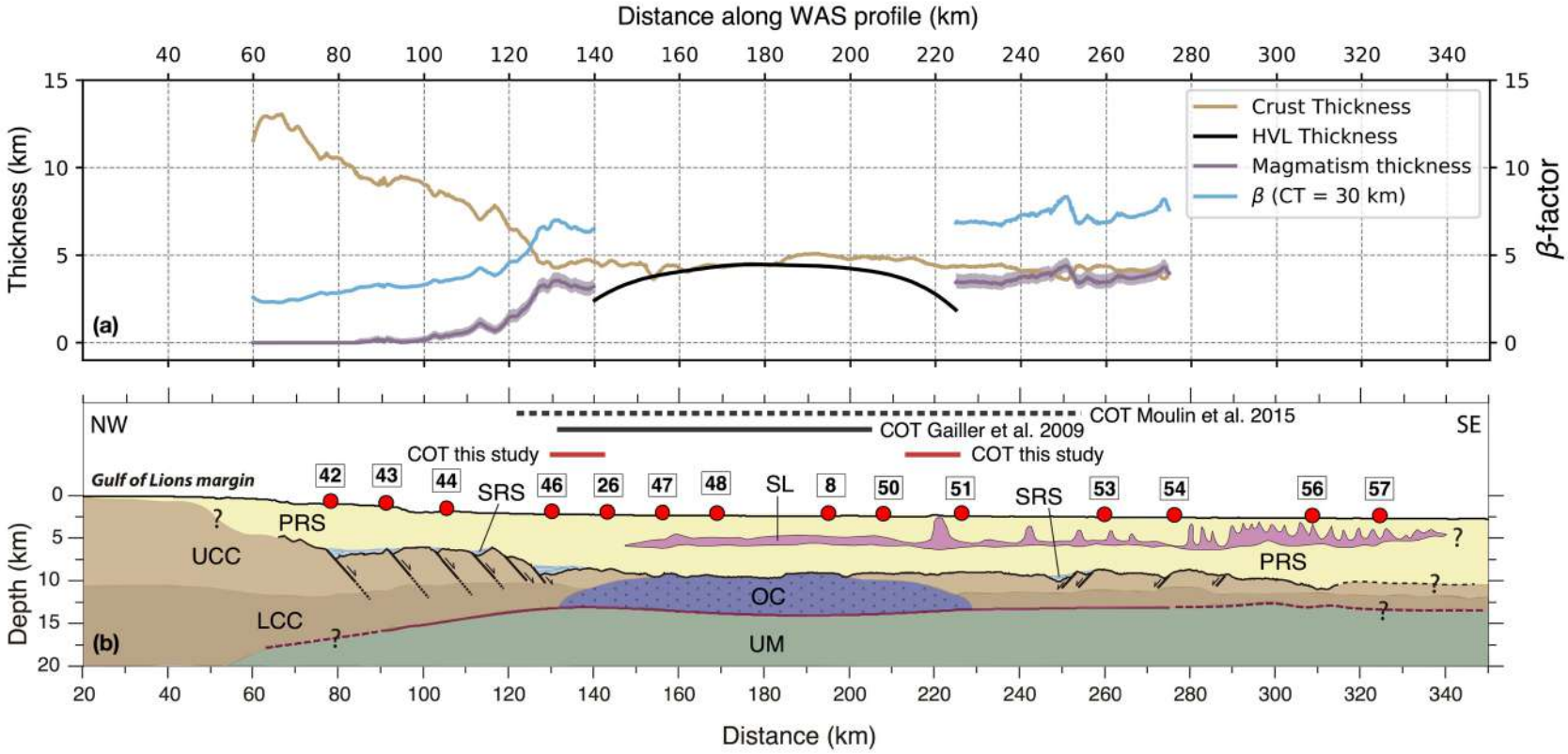

Figure 7.11 - (a) Relation between continental crustal thickness (brown line), β-factor (light blue line estimated from a Continent Thickness CT=30 km) and magmatic thickness (violet line) expected for a rift duration of 10 m.y. and an asthenosphere with a temperature of 1350°C (Bown and White, 1995). The variation of magmatism is represented by a violet shaded area, and the variation is a rift age between 8 to 12 Ma (Gattecceca et al. 2007). The black line is the thickness of the HVL. (b) Interpretative cross section corresponding to the profile A-B. The interpretation is based on the 2-D P-wave tomographic model (Fig. 7.4ab) and the interpretation of the MCS seismic line (Fig. 7.6). UCC: upper continental crust, LCC: lower continental crust, OC: oceanic crust, PRS: post-rift sediments, SRS: syn-rift sediments and SL: salt layer. Red circles represent the OBS location.

7.6. In summary

With the overall objective of better constraining the nature of the COT of the Gulf of Lions-Ligurian Basin, we have applied a novel travel-time inversion technique that reduces Vp model uncertainty as compared to previous modelling approaches. In particular, we have applied a joint refraction and reflection travel-time tomography to a combined set of travel-times of WAS refractions and reflections and MCS reflections. This new tomographic approach allows retrieving the sediment velocity structure and the top of basement geometry with unprecedented accuracy, which helps to better constrain the Vp of the crystalline crust particularly relevant across the COT zone.

The crystalline crust along the profile can be divided in three different domains based on crustal geometry and on the vertical velocity structure. Domain I is interpreted as a rifted continental crust, thinning from ~30 km under the coastline to ~15 km under the continental shelf edge to ~4-5 km oceanwards near the COT, implying a stretching factor (β) of 6-7. Domain II, was previously interpreted as a broad COT made of either exhumed mantle rocks or lower crustal continental rocks, but our results support a 4-5 km-thick lens of oceanic crust. Based on models of partial decompression melting generation, we show that the presence of a 4-5 km-thick oceanic crust is consistent with the amount of lithospheric stretching observed. Oceanwards, Domain III displays a Vp structure that coincides with that of ultra-thin (4-5 km) continental crust rather than the previously inferred oceanic crust or exhumed mantle.

In summary, the joint refraction and reflection tomography of WAS and MCS travel-times allows to constrain the Vp structure across the deep-water region of the Gulf of Lions better than previous modelling approaches, revealing the presence of an abrupt COT (< 10 km-wide) on either side of a ~100 km-wide segment of thin (4-5 km) oceanic crust.

References

Auzende, J.M., Bonnin, J., Olivet, J.L. (1973). The origin of the Western Mediterranean basin. J. Geol. Soc. London 19, 607–620.

Bache, F., Olivet J. L., Gorini C., Aslanian D., Labails C. and Rabineau M. (2010). Evolution of rifted continental margins: The case of the Gulf of Lions (western Mediterranean Basin). Earth Planet. Sci. Lett., 292(3–4), 345–356.

Badji, R., Charvis, P., Bracene, R., Galve, A., Badsi, M., Ribodetti, A., ... and Beslier, M. O. (2015). Geophysical evidence for a transform margin offshore Western Algeria: a witness of a subduction-transform edge propagator? Geophysical Journal International, 200(2), 1029-1045.

Begović, S. (2020). Structure and physical properties of the subduction plate boundary. Universitat de Barcelona. PhD Thesis.

Boillot, G., Winterer, E.L., Meyer, A.W. (1987a). Introduction, objectives, and principal results: Ocean Drilling Program Leg 103, west Galicia Margin. Proc. ODP, Init. Repts., 103: College Station, TX (Ocean Drilling Program), doi:10.2973/odp.proc.ir.103.

Bown, J.W. and White, R.S. (1995). Effect of finite extension rate on melt generation at rifted continental margins. Journal of Geophysical Research100, B9, 18 011–18 027.

Burrus, J., (1984). Contribution to a geodynamic synthesis of the Provencal Basin (North- Western Mediterranean). Bull. Soc. Géol. Fr. 8, 377–393.

Christeson, G. L., Goff, J. A., and Reece, R. S. (2019). Synthesis of oceanic crustal structure from two-dimensional seismic profiles. Reviews of Geophysics, 57, doi:10.1029/2019RG000641.

Christensen, N., and Mooney, W. (1995). Seismic velocity structure and composition of the continental crust: A global view. J. Geophys. Res., 100(B7), 9761–9788, doi:10.1029/95JB00259.

Cohen, C.R. (1980). Plate tectonic model for the Oligo-Miocene evolution of the Western Mediterranean. Tectonophysics 68, 283–311.

Contrucci, I., Nercessian, A., Béthoux, N., Mauffret, A. and Pascal, G. (2001). A Ligurian (western Mediterranean Sea) geophysical transect revisited. Geophysical Journal International, 146(1), pp.74-97.

Dannowski, A., Kopp, H., Grevemeyer, I., Lange, D., Thorwart, M., Bialas, J., and Wollatz-Vogt, M. (2020). Seismic evidence for failed rifting in the Ligurian Basin, Western Alpine domain. Solid Earth, 11(3), 873–887, doi:10.5194/se-11-873-2020.

Dewey, J. F., Helman, M. L., Turco, E., Hutton, D. H. W., and Knott, S. D. (1989). Kinematics of the western Mediterranean. Alpine Tectonics, vol. 45, edited by P. Cowardm, D. Dietrich, and G. Park, pp. 265–283, Geological Society Special Publication, London.

Dewet, J.F. (1988). Extensional collapse of orogens. Tectonics, 7, 1123 1139.

Faccenna, C., Becker, T.W., Lucente, F.P., Jolivet, L. and Rossetti, F. (2001). History of subduction and back-arc extension in the Central Mediterranean. Geophys. J. Int., 145, 809–820.

Gailler, A., Klingelhoefer, F., Olivet, J. L., Aslanian, D. (2009). The Sardinia scientific party, and Technical OBS team. Crustal structure of a Young margin pair: New results across the Liguro-Provençal Basin from wide-angle seismic tomography. Earth Planet. Sci. Lett., 286, 333–345, doi:10.1016/j.epsl.2009.1007.1001.

Gomez de la Peña, L., Grevemeyer, I., Kopp, H., Díaz, J., Gallart, J., Booth-Rea, G., ... and R. Ranero, C. (2020). The lithospheric structure of the Gibraltar Arc System from wide-angle seismic data. Journal of Geophysical Research: Solid Earth, 125(9), e2020JB019854, doi:10.1029/2020JB019854.

Granado P., Urgeles R., Sàbat F., Albert-Villanueva E., Roca E., Muñoz J. A., Mazzuca N., Gambini R. (2016). Geodynamical framework and hydrocarbon plays of a salt giant: the NW Mediterranean Basin. Petroleum Geoscience, 22, 309-321, doi:10.1144/petgeo2015-084.

Grevemeyer, I., Ranero, C.R., Ivandic M. (2018a). Structure of oceanic crust and serpentinization at subduction trenches. Geosphere, v. 14, no. 2, doi:10.1130/GES01537.1.

Gueguen, E., Doglioni, C., Fernandez, M. (1998). On the post-25 Ma geodynamic evolution of the western Mediterranean. Tectonophysics 298, 259–269, doi:10.1016/S0040-1951(98)00189-9

Jolivet, L., Gorini, C., Smit, J. and Leroy, S. (2015). Continental breakup and the dynamics of rifting in back-arc basins: the Gulf of Lion margin. Tectonics, 34, 662–679, doi:10.1002/2014TC003570.

Jolivet, L., and Faccenna, C. (2000). Mediterranean extension and the Africa-Eurasia collision. Tectonics, 19(6), 1095–1106, doi:10.1029/2000TC900018.

Korenaga, J., Holbrook, W.S., Kent, G.M., Kelemen, P.B., Detrick, R.S., Larsen, H.C., Hopper, J.R. and Dahl-Jensen, T., (2000). Crustal structure of the southeast Greenland margin from joint refraction and reflection seismic tomography. Journal of Geophysical Research: Solid Earth, 105(B9), pp.21591-21614.

Le Douaran, S., Burrus, J., Avedik, F. (1984). Deep structure of the North-Western Mediterranean Basin: results of a two-ship seismic survey. Mar. Geol. 55, 325–345.

Loureiro, A., Afilhado, A., Matias, L., Moulin, M., and Aslanian, D. (2016). Monte Carlo approach to assess the uncertainty of wide-angle layered models: Application to the Santos Basin, Brazil. Tectonophysics, 683, 286-307.

Meléndez, A., Korenaga, J., Sallarès, V., Miniussi, A., and Ranero, C. R. (2015). TOMO3D: 3-D joint refraction and reflection traveltime tomography parallel code for active-source seismic data—synthetic test. Geophysical Journal International, 203(1), 158-174.

Minshull, T. A. (2009). Geophysical characterisation of the ocean–continent transition at magma-poor rifted margins. Comptes Rendus Geoscience,341(5), 382-393.

Moulin, M., Klingelhoefer, F., Afilhado, A., Schnurle, P., Rabineau, M., Beslier, M.O. and Feld, A. (2015). Deep crustal structure across a young passive margin from wide-angle and reflection seismic data (The SARDINIA Experiment) – I. Gulf of Lion's margin. Bulletin Société Géologique de France, 186, 309–330.

Prada, M., Sallarès, V., Ranero, C.R., Vendrell, M.G., Grevemeyer, I., Zitellini, N. and de Franco, R. (2014). Seismic structure of the Central Tyrrhenian Basin: geophysical constraints on the nature of the main crustal domains. J. Geophys. Res. Solid Earth, 119, doi:10.1002/2013JB010527.

Prada, M., Sallarès, V., Ranero, C.R., Vendrell, M.G., Grevemeyer, I., Zitellini, N. and de Franco, R. (2015). The complex 3-D transition from continental crust to back-arc magmatism and exhumed mantle in the Central Tyrrhenian Basin. Geophys. J. Int., 203(1), 63–78.

Prada, M., Ranero, C.R., Sallarès, V., Zitellini, N., Grevemeyer, I. (2016). Mantle exhumation and sequence of magmatic events in the Magnaghi–Vavilov Basin (Central Tyrrhenian, Italy): New constraints from geological and geophysical observations. Tectonophysics 689, 133-142, doi:10.1016/j.tecto.2016.01.041.

Prada, M., Watremez, L., Chen, C., O'Reilly, B. M., Minshull, T. A., Reston, T. J., ... and Gaw, V. (2017). Crustal strain-dependent serpentinisation in the Porcupine Basin, offshore Ireland. Earth and Planetary Science Letters, 474, 148-159.

Pascal, G.P., Mauffret, A., Patriat, P. (1993). The ocean–continent boundary in the Gulf of Lion from analysis of expanding spread profiles and gravity modelling. Geophys. J. Int. 113, 701–726.

Ranero, C.R., Pérez-Gussinyé, M. (2010). Sequential faulting explains the asymmetry and extension discrepancy of conjugate margins. Nature 468, 294–9, doi:10.1038/nature09520.

Rehault, J., Boillot, G., Mauffret, A. (1984). The Western Mediterranean Basin: geological evolution. Mar. Geol. 55, 447–477.

Ryan, W. B. R., K. J. Hsü, M. B. Cita, P. Dumitrica, J. Lort, W. Maync, W.D. Nesteroff, G. Pautot, H. Stradner, and F. C. Wezel (1973). Site 120, in Initial Reports of the Deep Sea Drilling Project, JOIDES, vol. 13, edited by A.G. Kaneps, pp. 19-41, Washington (U.S. Government Printing Office).

Sallarès, V., Martínez-Loriente, S., Prada, M., Gràcia, E., Ranero, C., Gutscher, M.A., Bartolome, R., Gailler, A., Dañobeitia, J.J. and Zitellini, N. (2013). Seismic evidence of exhumed mantle rock basement at the Gorringe Bank and the adjacent Horseshoe and Tagus abyssal plains (SW Iberia). Earth and Planetary Science Letters, 365, pp.120-131.

Sawyer, D., Whitmarsh, R., and Klaus, A. (1994), Iberia Abyssal Plain Sites 897-901, paper presented at Proceedings of the Ocean Drilling Program Initial Rep.

Schettino, A., and Turco, E. (2011). Tectonic history of the western Tethys since the Late Triassic, Geol. Soc. Am. Bull., 123(1/2), 89–105, doi:10.1130/B30064.1.

Séranne, M. (1999). The Gulf of Lions continental margin (NW Mediterranean) revisited by IBS: An overview, in The Mediterranean Basins: Tertiary Extension Within the Alpine Orogen, edited by B. Durand et al., pp. 15–36, Geol. Soc., London.

Tarantola, A. (1987). Inverse Problem Theory: Methods for Data Fitting and Model Parameter Estimation, Elsevier Science, New York. 613 pp.

White, R.S., McKenzie, D. and O'Nions, R.K. (1992). Oceanic crustal thickness from seismic measurements and rare earth element inversions. Journal of Geophysical Research: Solid Earth, 97(B13), pp.19683-19715.

Whitmarsh, R., Beslier, M.O. and Wallace, P. (1998). Leg 173, paper presented at Proc. ODP, Init. Rep.

Zelt, C. A. and Forsyth D. A. (1994). Modeling wide-angle seismic data for crustal structure: Southeastern Grenville Province. Journal of Geophysical Research: Solid Earth 99. B6, 11687-11704.

Ziegler, P.A. (1992). European Cenozoic rift system. Tectonophysics 208, 91–111, doi:10.1016/0040-1951(92)90338-7.

Chapter 8

The rift and continent-ocean transition structure under the Tagus Abyssal Plain West of the Iberia

Rifted continental margins are regions where extension processes led to continental extension, breakup and seafloor spreading with the formation of oceanic crust. However, off Iberia continental breakup is not characterized by a sharp boundary but by a broad often rather complex transition zone, called the continent-ocean transition or COT. Ground truthing with deep drilling revealed that the COT is made of mantle exhumed by extensional processes along the entire West Iberia margin (Ryan et al., 1973; Boillot et al., 1987; Sawyer et al., 1994). In addition, geophysical efforts determined heterogeneity of the structure, rock physical properties and tectonic style of the basement at a regional scale, defining the location and nature of the COT and the oldest oceanic crust (Whitmarsh et al., 1998). As a result, the West Iberia continental margin and COT became the type example of magma-poor systems that has been used as a template to interpret the structure of many other rifted systems where less information of the nature of the basement is available.

However, most experiments studied the Galicia Segment of the northern West Iberia margin, in (Whitmarsh et al., 1996, Pérez-Gussinyé et al., 2003; Dean et al., 2015) or the Iberia Abyssal Plain (IAP) in the central region of the margin (Dean et al., 2000; Minshull et al., 2014). The most accepted models of the COT in this area involve mantle unroofing, typically postulating a continuum from continental crust extension, continental mantle exhumation over wide areas and the subsequent formation of oceanic crust by the gradual instauration of a decompression melt system in a mid-ocean ridge (e.g. Pérez-Gussinyé et al., 2006). Zones of mantle exhumation have also been postulated within the COT on its conjugate margins, landward of unequivocal oceanic crust (e.g., Dean et al., 2000; Van Avendonk et al., 2006). In spite of the number of geophysical experiments, the typical seismic structure of normal oceanic crust has not yet been clearly detected along the margin and its conjugate sibling off Newfoundland. Yet, a major part of the Iberia margin has not been studied in detail, namely the Tagus Abyssal Plain (TAP) to the south of IAP and previous studies provided only a low-resolution characterization on the extent and structure of the continental crust and COT in the TAP.

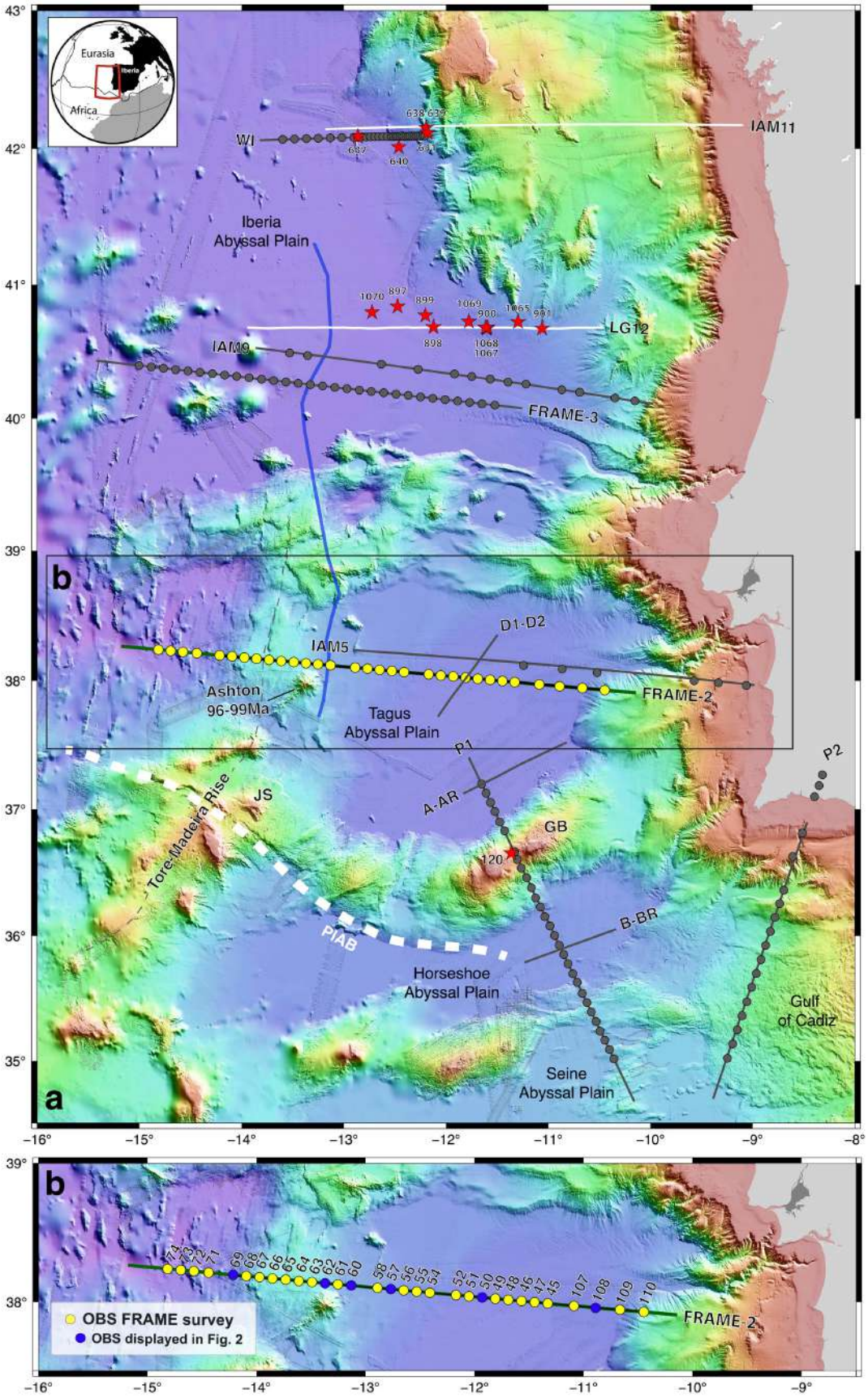
Eurasia
Iberia
Africa
WI
IAM11
LG12
IAM9
FRAME-3
Iberia
Abyssal Plain
b
IAM5
D1-D2
FRAME-2
Ashton
96-99Ma
Tagus
Abyssal Plain
P1
P2
A-AR
JS
Tore-Madeira Rise
GB
B-BR
PIAB
Horseshoe
Abyssal Plain
Gulf
of Cadiz
Seine
Abyssal Plain
a
OBS FRAME survey
OBS displayed in Fig. 2
FRAME-2

◄ *Figure 8.1 - (a) Bathymetric map of the West Iberia margin including regional seismic profiles. Black lines correspond to WAS profiles previously acquired in the area and referred to in the text, from S to N: P2 and P1 (NEAREST survey; Sallarès et al. 2011 and 2013), A-AR and B-BR (Purdy, 1975), D1–D2 (Discovery Cruise 161; Pinheiro et al., 1992). The IAM project lines (Banda, E. et al., 1995): IAM5 (Afilhado et al., 2008), IAM9 (Dean et al., 2000), and IAM 11 (Ranero and Pérez-Gussinyé, 2010), and WI (Davy et al. 2016), Lusigal-12 (LG12) (Beslier, 1996), FRAME-3 (FRAME survey; Grevemeyer et al. in prep.). Red stars indicate ODP and DSDP sites locations. Blue line indicates the location of the J-anomaly along the margin (Srivastava, et al., 2000). Green line displays the location of FRAME-2 WAS profile, and the coincident black line is the coincident MCS profile. Abbreviations: GO: Gorringe bank, JS: Josephine Seamount, PIAB: Paleo Iberia-Africa boundary. (b) Map showing the location of the FRAME-2 profile. Green line corresponds to the WAS profiles acquired during the Leg-2 and the coincident thin black line correspond to the MCS profile acquired during the Leg-1. All these profiles were acquired during the FRAME-2018 survey. Yellow and blue circles display the position of OBS and OBH along the FRAME-2 profile presented in this chapter.*

This work aims at defining the petrological affinity, i.e. the nature, of the transitions between the different basement domains across the TAP, showing for the first time the structure of the first oceanic crust formed in the north Atlantic. Here, we use high-resolution structural models obtained from jointly interpreting seismic Wide-Angle Seismic data (WAS) and gravity data combined with Multi-Channel Seismic (MCS) images. Specifically, we present results from a ~450 km long WAS and gravity profile and a coincident MCS line acquired across the TAP, at ~38°N (Fig. 8.1b). We obtained a 2-D P-waves velocity (Vp) tomography model along the FRAME-2 line by jointly inverting refraction and reflection travel-times from the WAS and MCS data (Fig. 8.3a), which is then validated with gravity modelling. The MCS image is subsequently used to help defining the crustal structure and boundaries between interpreted petrological domains.

8.1. Geological setting

The Iberia-Newfoundland rift system initiated the opening of the North Atlantic Ocean. The age of continental breakup and the onset of seafloor spreading between the two conjugated margins is inferred to decrease northward along the margin but the details are widely debated.

In the SW segment, a WAS profile (P1 in Fig. 8.1) provides strong evidence for the presence of serpentinized mantle of Early Cretaceous age extending from the Gorringe Bank (Ryan et al., 1973) under the southern TAP and northern Horseshoe Abyssal Plain (HAP) (Sallarès et al., 2013). In the central Gulf of Cadiz and Seine Abyssal Plain lines P1 and P2 found oceanic crust (Fig. 8.1; Sallarès et al., 2011; Martinez-Loriente et al. 2014).

However, the information on the configuration, nature and limits between the crustal domains in the TAP is scarce and mostly based on the modelling of a collection of vintage geophysical data (Purdy, 1975; Pinheiro et al., 1992; see Fig. 8.1) and of a WAS profile from the nineties with three OBS coincident with MCS line IAM-5 (Afilhado et al., 2008, see Fig. 8.1).

The results of seismic refraction line A–AR (Purdy, 1975, see Fig. 8.1) in the south segment of the Iberia margin indicated major changes of velocity and thickness of crustal layers within the deep basin. In particular, those data were interpreted as corresponding to oceanic crust in the external part of the Gulf of Cadiz. Farther SW of the TAP, across the Madeira-Tore Rise, the presence of the J-

anomaly magnetic lineation (Tucholke and Ludwig, 1982) support the presence of oceanic crust. The Vp model from Peirce and Barton (1991) of the Josephine Seamount and the Madeira-Tore Rise, show a crust having a total thickness of ~14-16 km and Vp values of 7.4 km/s in the lowest part. They suggest that it consists of anomalous oceanic crust. To explain the anomaly in thickness and velocity, they propose the addition of igneous material at the base of the crust with an anomalously low MgO abundance. Furthermore, they suggest that this oceanic crust formed as part of an aseismic ridge at or adjacent to the Mid-Atlantic Ridge.

Pinheiro et al. (1992) modelled WAS data of profile D1-D2 (Fig. 8.1) and document evidence of a high-velocity basement with Vp of 7.6-7.9 km/s showing a strong vertical velocity gradient that is consistent with the possible presence of exhumed and serpentinized mantle under the TAP, from 11.5°–12°W, which they interpreted to correspond to the COT. Based on a grid of seismic images, Mauffret et al. (1989) proposes a Mesozoic–Cenozoic seismic stratigraphy. They interpreted that the whole TAP is underlain by oceanic crust, and proposed an ocean–continent boundary at ~11°W, near the foot of the continental slope. They interpret that the deep basement beneath the eastern TAP was created in Late Jurassic time followed by a Cretaceous ridge jump that left oceanic crust adjacent to the continental Iberian margin.

For long time the most modern geophysical transect across the TAP was the Iberian Atlantic Margins line 5 (IAM-5) that was shot and recorded on streamer by an industry ship and had 6 OBS deployed during acquisitions. Only 3 of the OBS were located in the floor of the abyssal plain, with a lateral spacing of 30-40 km, and the other 3 across the uppermost slope and shelf (Fig. 8.1). The arrivals in the OBS records and selected horizons from the seismic boundaries were forward modelled and interpreted together with magnetic data (Afilhado et al., 2008). They interpret a ~40 km-wide segment of highly reflective and slightly magnetized "transitional crust" extending under the continental slope and eastern sector of the TAP, and proposed that it corresponds to the COT. They inferred the presence of oceanic crust further to the west under the TAP. Further west, they identified magnetic anomalies suggesting seafloor spreading. WAS data acquired in 1963 along the Tagus and Horseshoe abyssal plains using sonobuoys (lines A-AR and B-BR in Fig. 8.1; Purdy, 1975) had previously been interpreted as showing oceanic crust in the Horseshoe and TAP.

8.2. Data Sets

The MCS and WAS data used in this work were acquired during the FRAME (*FoRmAtion of geological domains in the Western Iberian Margin and tectonic rEactivation of their limits*) experiment in 2018, conducted on board the Spanish R/V Sarmiento de Gamboa. The FRAME experiment aimed at providing new insights into the spatial distribution of geological domains to characterize the COT offshore Iberia, and improve our understanding of the processes that have shaped the margin. Here, we use data acquired along the FRAME-2 transect, which runs E-W from 10º to 15º of longitude across the TAP and the J-anomaly ridge (Fig. 8.1). The experiment combines a ~330-km-long MCS line and a ~490-km-long WAS profile along the same transect.

8.2.1. Multi-Channel Seismic data

The MCS data were recorded with a seismic source composed of two airgun arrays with a total volume of 3920 c.i. and air pressure of 2000 p.s.i. deployed at 10 m depth and fired every ~37.5 m. The seismic signal was recorded in a 6-km-long streamer with 480 channels 12.5m long. This configuration provides a nominal 80-fold common-mid-point (CMP) gather data. Raw data were recorded in SEG-D format at a 2 ms sample interval. The streamer was deployed at 19-20 m depth to favour low frequency content (e.g., Williams and Pollatos, 2012). The trace length was 14.5 seconds for the line.

The MCS data were processed using the Globe Claritas processing software to obtain the section in Fig. 8.5a. The processing sequence includes defining the streamer navigation and source position for the CMP binning, velocity analysis, spherical divergence correction, two-window statistical deconvolution, normal move out, near and far offset mute, stack, and post-stack finite differences time migration with a smooth velocity model based on geology. After stack, we applied an automatic gain control for amplitude balancing.

After processing, we identified key horizons and picked travel-times of P-waves reflected at two different geological interfaces, namely the major intra-sedimentary unconformity and the top of the basement (TOB). We picked travel-times of phases reflected at each of these interfaces CMP gather images simultaneously compared to stack images for horizon visual tracking. Travel time picks were input in shot gather geometry for the inversion. We inverted every 6-8 shots, which provides a spatial sampling of 250-300m. This sampling is lower than 400 m, which is the width of the first Fresnel zone at the depth of the first sedimentary interface (~5 km of depth), considering a dominant frequency of 25-30 Hz. Thus, tomographic resolution is not downgraded by the decimation.

In total, we inverted 924 reflected picks for the unconformity and 1243 for the TOB. Errors are derived from travel time uncertainty that is estimated using Zelt and Forsyth's (1994) approach. The picking uncertainty is estimated at 20-40 ms for MCS picks, based on the amplitude S/N ration between the signal within a 250 ms window before and after the selected travel time.

8.2.2. Wide-Angle Seismic data

The WAS data were recorded by 35 instruments, including 17 LC2000 4x4 Ocean Bottom Seismometers (OBS) from the Spanish pool, and 18 Geomar Ocean Bottom Hydrophones (OBH). In this case, the seismic source consisted of a total of 16 airguns of the G-II model, organized in 2 symmetrical arrays with 5200 c.i. total volume, towed behind the vessel at a depth of 15 m to enhance the low frequency content in the source signal. The data from OBS59, OBH52 and OBH75 were corrupted, and OBS70 was not retrieved from the seafloor. The records of the other receivers have good quality, displaying seismic phases up to 100-120 km of offset after a basic data processing consisting of predictive deconvolution, 5-18 Hz bandpass filtering, and automatic gain control (Fig. 8.2).

From East to West, the line crosses the low continental slope of the Iberian margin, the TAP and the J-anomaly ridge (Fig. 8.1). The configuration of seismic phases identified in each receiver display changing characteristics along the line that occur in five groups that we have named domains.

The record sections of OBS/H 47-110 define the first domain containing three clear seismic phases. From ~10 km to ~30 km of offset, a phase with apparent velocity of ~4.0-6.0 km/s is observed. We have interpreted this phase as a refraction through the post-rift sedimentary sequence and basement (Pg) (Fig. 8.2a). From 30 to 80 km of offset OBSs records show a prominent arrival with apparent velocity of near 8.0 km/s that we interpret as a refraction within the uppermost mantle (Pn). The crossover distance between Pg and Pn is marked by a secondary arrival that we interpret as a reflection at the crust-mantle boundary (i.e. Moho), or PmP (Fig. 8.2). This distance is similar in all receivers of this domain, indicating that crustal thickness is rather uniform there.

The OBS/H 48-54 map a second domain (Fig. 8.1). These records display a prominent seismic phase that extends to up to 100 km of offset and have an apparent velocity of near 8.0 km/s, so we interpret it as a Pn. At near offset (< 10 km), some receivers display a slower seismic phase with apparent velocity of ~3.0-4.0 km/s that we interpret as refractions within the sedimentary cover (Ps) (Fig. 8.2). The seismic phase configuration of these set of receivers closely resembles that observed in exhumed mantle regions (Sallarès et al., 2013; Prada et al., 2014).

The OBS/H 55-58 records form the third group (Fig. 8.1). These instruments show a first seismic phase with lower velocity than the second group (~5.0 km/s) from 5 km to 15-20 km offset, which we identify as a Pg. Between 30 and 90 km of offset, a prominent phase with apparent velocity of 8.0 km/s is observed and interpreted as Pn. Finally, PmP phases are observed at a crossover distance between Pg and Pn of 3-5 km.

The OBS/H 60 to 64 are the fourth group. Here, Pg phases are faster than in the previous domain, with apparent exceeding 6.0 km/s between 5 and 30-40 km of offset, indicating a thicker and faster crust than in the previous domain. At offsets larger than 40 km, seismic records show a prominent Pn phase with apparent velocity of ~8 km/s (Fig. 8.2c). PmP reflections are also identified at the crossover distance between the two refracted phases.

The OBS/H from 65-74 group in the fifth domain. After the direct wave, we interpreted Pg phases from ~5 to 20 km offset, with apparent velocities of 6.0-6.5 km/s. Pn phases were identified in most receivers up to 70-80 km, with apparent velocity of ~7.5-8.0 km/s. In some receivers, Pn phases were better observed and picked at the seafloor multiple than at the primary arrivals, possibly indicating the lack of thick water-saturated sediments and a shallow basement (Meléndez et al., 2014) (Fig. 8.2). PmP phases are interpreted at the crossover distance between Pg and Pn. The amplitude of this secondary phase is fainter than in the rest of domains, hampering their identification. This indicates a weaker impedance contrast between the crust and mantle than in the rest of crustal domains.

In total, we manually picked 3363 Pg, 9171 Pn and 1782 PmPs arrival times. In some cases, where the signal-to-noise ratio is higher, we picked travel-times from the multiple instead of the primary phase (e.g., OBS60 in Fig. 8.2). This allowed to substantially increase the number of picks at far

offsets. OBS records present a smaller signal-to-noise ratio than the MCS shot gathers. The corresponding WAS picking uncertainty is therefore larger, of 40 ms to 100 ms following the same criterion as for the MCS picks (i.e. Zelt and Forsyth, 1994).

◄ *Figure 8.2 - Examples of wide-angle seismic data recorded at OBS/H during the FRAME survey. Record sections correspond to (a) OBS108 from Domain I, (b) OBS50 from Domain II, (c) OBS57 from Domain III, (d) OBS69 from Domain V and (e) and (f) OBS60-OBS62 from Domain IV. The interpretation of the seismic phases picked for the inversion is shown in the top panels. The same record with the synthetic (red circles) and observed travel times (coloured vertical bars) is shown in the lower panel. Blue bars correspond to picked refracted phases (Pg and Pn), while orange and yellow correspond to continental and oceanic Moho reflections (PmP), respectively.*

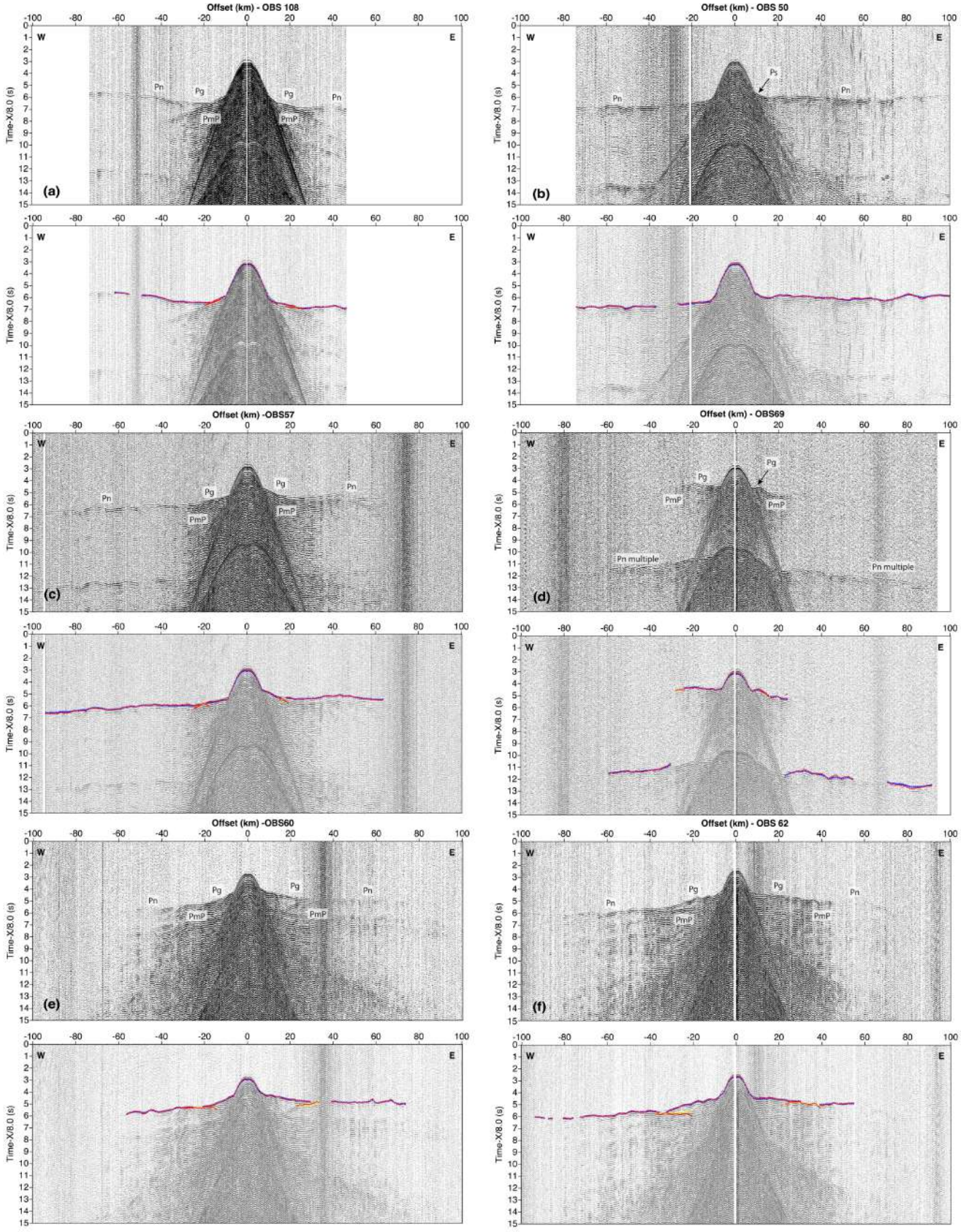
Offset (km) - OBS 108
Offset (km) - OBS 50
Offset (km) -OBS57
Offset (km) - OBS69
Offset (km) -OBS60
Offset (km) - OBS 62
Time-X/8.0 (s)
W
E
Pn
Pg
PmP
Ps
Pn multiple
(a)
(b)
(c)
(d)
(e)
(f)

8.3. Methods

8.3.1. Joint refraction and reflection travel-time inversion of WAS and MCS data

To invert for Vp as well as the depth of the different interfaces, we used a modified version of the joint refraction and reflection travel-time inversion code *tomo2d* (Korenaga et al., 2000; Meléndez et al., 2015; Begović, 2020), which allows combining MCS and WAS travel-times in the inversion. The initial velocity model is parametrized as a 460 km-wide mesh hanging from the seafloor, with constant node spacing of 90m in the horizontal direction, and increasing node distance with depth, from 90 m at the surface to 500m at the bottom of the model. The reflector is set as a floating interface with a constant node spacing of 90m. Regularization parameters including smoothing constrains are set as horizontal and vertical correlation lengths (see Table 5.3 in the Chapter 5: *Travel-time Tomography*).

We followed a layer-stripping strategy to build our model layer by layer by inversion but allowing to incorporate Vp steps between the different seismic interfaces. In this case, the inversion process included four layer-stripping steps (Section A.1.2. in Appendix).

In the first step, we inverted for the geometry of the unconformity inside the sediment layer and the overlying Vp structure using travel-times from MCS reflections alone (Fig. A.7 in Appendix). The output of this first inversion is set as input for the following step, and the area covered by the rays during the first step is overdamped to prevent the following step to excessively modify these velocities. In addition, we impose a velocity jump beneath the resolved reflector to force the inversion to resolve the velocity contrast between both layers. This process is repeated at each step to account also for the vertical Vp contrasts. Hence, in the second step, we inverted for the geometry of the top of the basement and the Vp of the rest of the post-rift sedimentary unit. During this second step, we use travel-times of MCS reflections at the TOB (Fig. A.8 in Appendix).

We used exclusively travel-times from WAS data to invert for the Vp and geometry of the underlying layers (i.e. basement and uppermost mantle). Thus, in the third step included Pg, Pn phases and PmP phases to resolve the velocity structure of the crust, mantle and the geometry of the Moho (Fig. A.9 in Appendix). Including Pn phases in this step allows increasing the ray coverage, and thus, the amount of information at crustal levels. In addition, we have refined the Moho geometry between OBS 58 and 60 as important misfits in PmP arrivals was observed. Lowering the reflector correlation length from 4 to 2 km allowed to better fit PmP travel-times from these receivers and retrieving finer details of the Moho relief. We used the output of the third step as input for this Moho refinement (Fig. A.10 in Appendix).

Finally, in the last step, we inverted for Pg, PmP and Pn phases using the velocity model obtained in the previous step but imposing a velocity step across the Moho to account for the velocity contrast of this interface and invert for mantle Vp (Fig. A.11 in Appendix) (Fig. 8.3).

The final preferred model in Figure 8.3a has an overall root mean square (r.m.s) residual of 55 ms (see Table A.3.1. in Appendix for the r.m.s values at each layer-stripping step). The Vp and horizons

uncertainty is shown in Figure 8.3d. The average Vp values and the averaged derivative weight sum (DWS) from all the inversions from the Monte-Carlo analysis are shown in Figure 8.3b and Figure 8.3c, respectively. The DWS is a measure of the ray coverage throughout the average Vp model, in Figure 8.3b.

8.3.2. Uncertainty analysis

The range of uncertainty of crustal Vp and the depth of the inverted Moho was assessed by performing a Monte Carlo-like analysis. Unlike the Monte-Carlo from the previous chapter, we have modified the strategy of this analysis. The good agreement between the location of the inverted TOB and the observed TOB along the MCS section indicates that the sedimentary structure is well constrained. Thus, we considered this section of the model resolved and fixed during each Monte-Carlo realization in the TAP. To evaluate the Vp uncertainty of the crystalline crust, the upper mantle and the Moho interface we have created 500 realizations each of them consisting of a 1D velocity model, a Moho interface and a set of travel-times with added random noise. The 1D velocity model was created by randomly varying velocities of the reference model within a ±10% (Fig. A.14 in Appendix). The Moho interface was generated by randomly applying a ± 3 km static shift to the final Moho in the preferred model in Fig. 8.3a. The random Gaussian noise added to each travel time is based on the picking uncertainty, which ranges between 30 ms and 90 ms.

From the 500 realizations, only 336 converged below 70ms. Those realizations that did not converge beneath this threshold correspond to models in which the Moho interface was randomly generated shallower than the average (i.e. the final preferred Moho) (Fig. 8.3d). Based on Tarantola et al. (1987), when the initial models (i.e. Vp and reflector depth ranges) cover all the region of non-null probability within the space of possible parameters, and the datasets (i.e. picking times) cover that of the actual picking errors, the average of all the realizations corresponds to the most probable solution so that the final standard deviation is a statistical measure of the model parameters uncertainty.

We consider well resolved areas with the following values:

$$DWS \geq \overline{DWS} - \sigma_{DWS} \tag{5.2}$$

where DWS is derivative weight sum, $\overline{DWS}$ is the average value of the derivative weight sum and σ_{DWS} the standard deviation of the DWS. Thus, taking the final standard deviation as a proxy for parameters uncertainty and those areas of the model with an acceptable ray coverage, the model shows Vp uncertainties between ±0.1 km/s and ±0.2 km/s, and Moho depth uncertainties between ± 0.1 and ±1 km. Localized high Vp uncertainties (i.e. > ±0.3 km/s) are associated with sharp velocity contrast at the Moho interface.

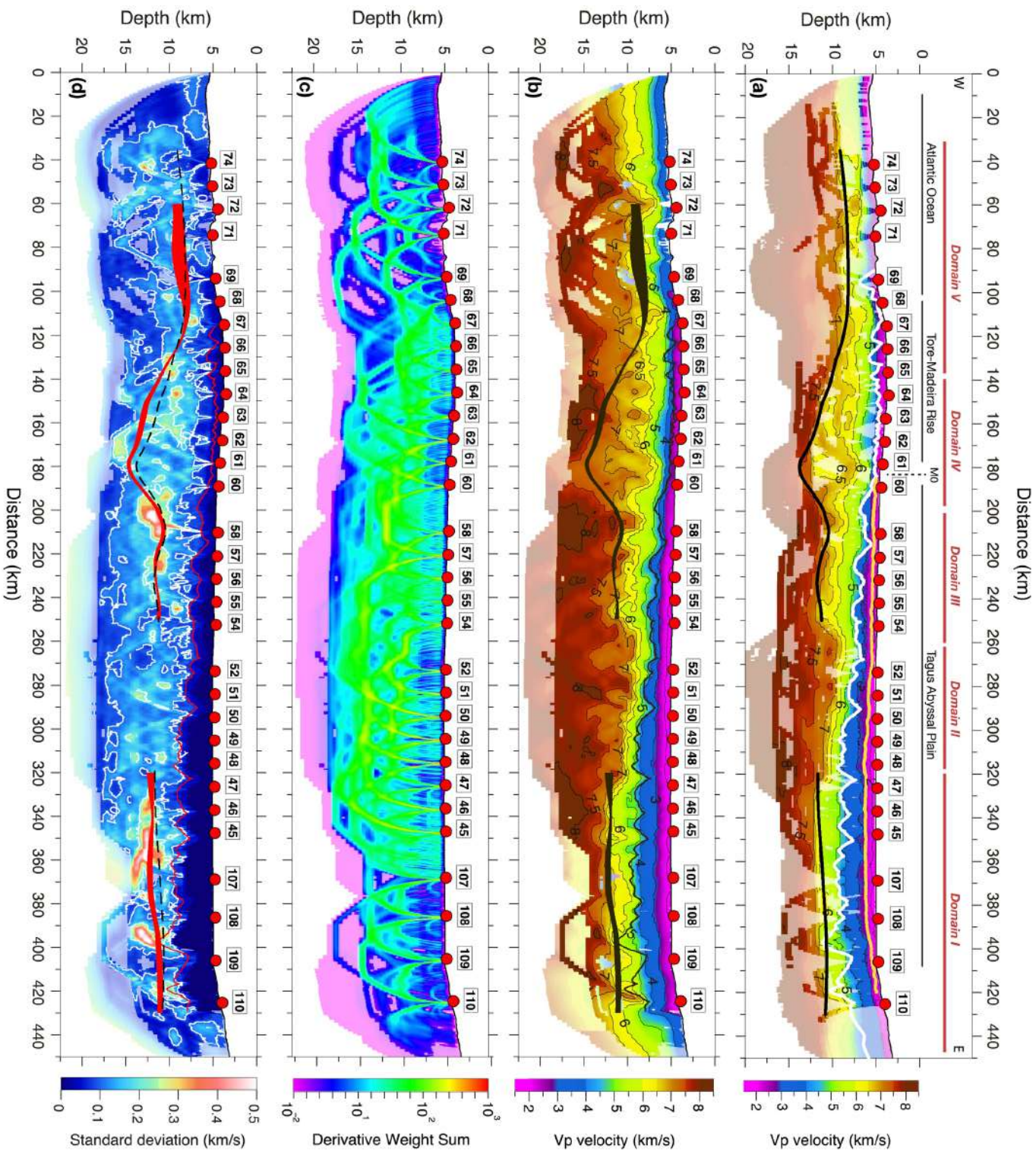

Figure 8.3 - (a) Preferred 2-D P-wave tomography model of the sediments, crust, uppermost mantle and geometry of the inverted horizons, classified following a colour code: in yellow the unconformity, white is the top of the basement and in black the Moho geometry. (b) Average Vp values from the Monte-Carlo analysis for FRAME-2 (d). The width of the dark band shows the standard deviation of the depth of the inverted horizons: unconformity, top of the basement and for the Moho. (c) Average derivative weight sum (DWS) of all the inversions of tomographic model in (b). (d) Standard deviation of Vp values of the average solution of the Monte-Carlo analysis for profile FRAME-2. The width of the red band shows the standard deviation of the depth of the inverted horizons: unconformity, top of the basement and for the Moho. In dashed black line the preferred Moho from (a). Red circles display the receiver location, OBS/OBH.

8.3.3. Gravity modelling

To test our interpretation concerning the petrological nature of the basement, we have performed a gravity modelling using the Vp model in Figure 8.3a as a reference. To do so, we have converted Vp into density (ρ) using Vp-ρ relationships corresponding to the suit of possible petrological affinities found along rifted margins (i.e. continental, exhumed mantle, oceanic). For the post-rift unit, we used Hamilton's (1978) Vp-ρ relationship, whereas for the basement we used three different relationships. We applied Christensen and Mooney's (1995) Vp-ρ relationship for rocks interpreted as continental (Domain I and III), Carlson and Herrick's (1990) conversion law for oceanic crustal rocks (Domains IV and V), and Carlson and Miller (2003)'s for partially serpentinized peridotites in Domain II. For Vp > 8.0 km/s we assumed a constant mantle density of 3.3 g cm^3. Since FRAME-2 profile is ~450 km long across from continental to oceanic lithosphere it contains long wavelength information from density contrasts deeper than the crust. We assumed an oceanic age 120 Ma old with a 120-km thick lithosphere along Domains IV and V (Fernàndez et al., 2004) and 100 km-thick continental lithosphere eastwards for Domains I-III.

The resulting gravity response of the density model shows a good fit with the observed gravity anomaly, with an r.m.s misfit of 8.3 mGal (Fig. 8.4). The largest misfits occur at the limits of the model due to edge effects. The larger misfit occurs in Domain III, between 200 and 220 km of the profile. Here, we increased density by 3% to take into account the influence and higher density of potential magmatic intrusions.

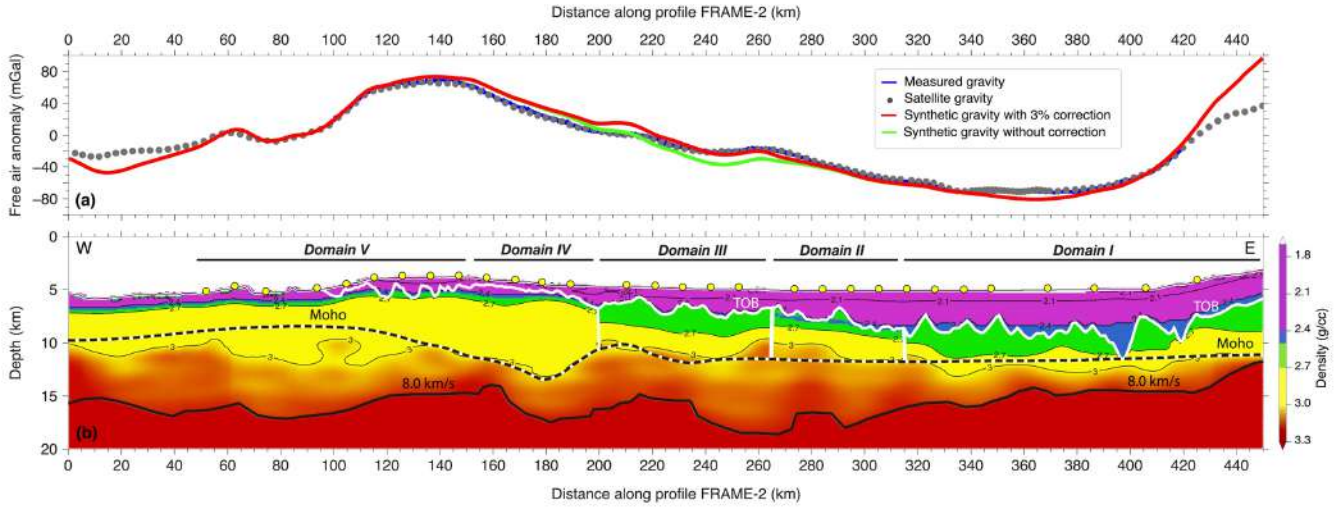

Figure 8.4 - (a) Observed free-air gravity anomaly (blue line) recorded during the FRAME survey and gravity anomaly measured from satellite (Sandwell et al., 2014). Red line corresponds to the gravity anomaly calculated from the density model obtained by using Hamilton's (1978) relationship for the sediment layer, Christensen and Mooney's (1995) relationship for continental crust in Domains I and III, Carlson and Herrick's (1990) relationship for oceanic crust in Domains IV and V, and Carlson and Miller's (2003) conversion law for partially serpentinized peridotites in Domain II. Vp-derived density in Domain III is increased by 3% to reflect magmatic intrusions. The r.m.s residual is 8.39 mGal. (b) Velocity-derived density model corresponding to the best fit (red band). Yellow circles show the location of the OBS and OBH.

8.4. Results

The tomographic model in Figure 8.3a shows the Vp structure of the post-rift sedimentary sequence, the basement and the uppermost mantle together with the geometry of an intra-sediment unconformity, the TOB, and the Moho, under the TAP and the Madeira-Tore rise. We jointly interpret the tectonic structure and the Vp distribution by overlaying the two-way time-converted Vp model on the MCS section (Fig. 8.5).

The sediment infill has a Vp varying from ~1.8 km/s at the seafloor to ~4.0-4.5 km/s above the TOB, and it can be divided between km 180 and 450 along the model in two units separated by a regional unconformity. From east to west, the upper unit thickens towards the TAP, where it is thickest (1.5 km thick in Fig. 8.3), and thins oceanwards, merging with the TOB at ~180 km of profile distance (Fig. 8.5). The lower sedimentary unit seismic velocity increases from ~2.5 km/s beneath the unconformity to 4.5 km/s at the TOB (Fig. 8.5). Both units display dominantly sub-horizontal layering, indicating post-rift deposition, although locally fan-like shape infill resting on the TOB occurs indicating syn-rift deposition (Fig. 8.5a). The lower unit is tilted oceanwards under the lower continental slope. Similar deformation in other parts of the margin is attributed to early Tertiary contractional deformation (Afilhado et al. 2008). From km 180 to 155 the TOB shallows and is covered by the thinnest sediment along the profile. Localized thick sedimentary packages are confined inside 1-2 km-deep, 5 km-wide grabens (e.g. beneath OBS 67-66 in Fig. 8.5). The reflectivity of this sediment unit is brighter than that along the TAP (Fig. 8.5), possibly indicating the presence of sediment-interbedded igneous material. Overall, the inverted geometry of the TOB agrees with the observed morphology of the TOB imaged on the MCS section (Fig. 8.5a). This supports that the overlying velocity structure is well resolved.

Lateral and vertical changes of Vp in the basement, and in particular the location of abrupt lateral velocity variations and crustal thickness variations support the definition of five different domains, which were already indicated above by the distinctly different character of seismic arrivals in record sections (I, II, III, IV, V; Fig. 8.3a).

Domain I extends from km ~320 to 450 along the profile (Fig. 8.3a). In this segment, Vp increases with depth from ~5.0 km/s to 6.0 km/s just above the Moho, which is sub-horizontal along ~100 km at ~10 km depth. The inverted topography of the TOB is highly irregular, with relief ranging from a few hundred meters to ~4 km, implying that there is extremely thin to no crustal basement in portions of the profile (i.e. ~400 km of profile distance Fig. 8.3a and Fig. 8.5). The velocity contrast at the Moho is with ≤1.5 km/s rather small, because the uppermost mantle Vp is only ~7 km/s at the Moho, increasing to 8 km/s ~5 km underneath. The WAS Moho coincides with discontinuous sub-horizontal high-amplitude low-frequency reflections in the MCS section at 9-10 s TWT (Fig. 8.5).

Domain II extends from km 250 to 320 of the model (Fig. 8.3a). Here, Vp increases abruptly from ~4.5-5.0 km/s at the TOB to ~7.0 km/s ~2 km underneath, and more gradually to 8 km/s at ~8-9 km into the basement (Fig. 8.3a and 8.5). Thus, the vertical Vp gradient in the upper ~2 km of the basement is $>1 s^{-1}$, two time larger than in Domain I. Domain II is also characterized by the lack of a Moho-like reflection in the OBS recordings. Similarly, the MCS section does not display laterally

continuous high-amplitude reflections where Vp <~7 km/s that might indicate a base-of-the-crust boundary. The MCS image contains several contains several gentle dipping discontinuous bright reflections at 2 s TWT into the basement where Vp is 7.5-8.0 km/s (Fig. 8.5).

Domain III extends from km ~200 to 250 (Fig. 8.3a). Its base is defined by clear PmP reflections and clearly imaged reflections coinciding with the inverted Moho (Fig 8.5). Vp increases from 5.0 km/s at the TOB, to 6.5-7.2 km/s in the lowermost crust, where is slightly higher than in Domain I. The Vp gradient is ~0.5 s^{-1}, which is half of that of Domain II. The crustal thickness along this domain is of only 4.5-5.0 km. The upper mantle Vp increases from 7.5 km/s at the Moho to 8.0 km/s ~7 km underneath. The uppermost mantle Vp of this domain is faster and laterally more homogeneous than in Domain I.

Domain IV extends from km 130-140 to 200, displaying the largest lateral crustal thickness variations and the smoothest TOB (Fig. 8.3 and 8.5). The inverted Moho delineates a basement thickening, reaching ~8-9 km, near the domain centre. The basement has a 2-gradient vertical Vp structure. The Vp increases with depth from ~4.5 to 6.5 km/s in the upper 3 km with 0.6 s-1 gradient, and from 6.0 km/s to 7.0 km/s in lower crust. However, the thickest basement sector has lower crustal Vp 6.5-7.2 km/s. The Moho is well defined by PmP arrivals, but coincident near-vertical reflections at are visible at few locations (e.g. beneath OBS62 at 9 s TWT in Fig. 8.5). The mantle Vp is 7.5-8 km/s, similar to Domain III but higher than Domain I.

Domain V extends from km ~30 to 130-140 (Fig. 8.3a). From km 0 to ~30, the Vp is poorly constrained and cannot be unequivocally considered as part of Domain V. Moho is constrained by PmP phases (Fig. 8.3), which coincide with scattered short reflections in seismic images (Fig. 8.5). Domain V basement thins oceanward from 5 km thickness at km 140 to 3 km thickness at km ~50. Basement thinning is accompanied by comparatively large tilted-fault blocks (Fig. 8.5). The vertical basement Vp gradient is laterally heterogeneous. Low Vp gradient varies between 5.0-6.0 km/s from TOB to mower crust (i.e. under OBS69), while strong gradient occurs at localized shallow high Vp of 7.0-7.2 km/s (i.e. under OBS 72). The uppermost 5-6 km of the mantle displays the slowest Vp along the model, ranging between 6.5-7.5 km/s, increasing progressively to 8.0 km/s at ~10 km into the mantle.

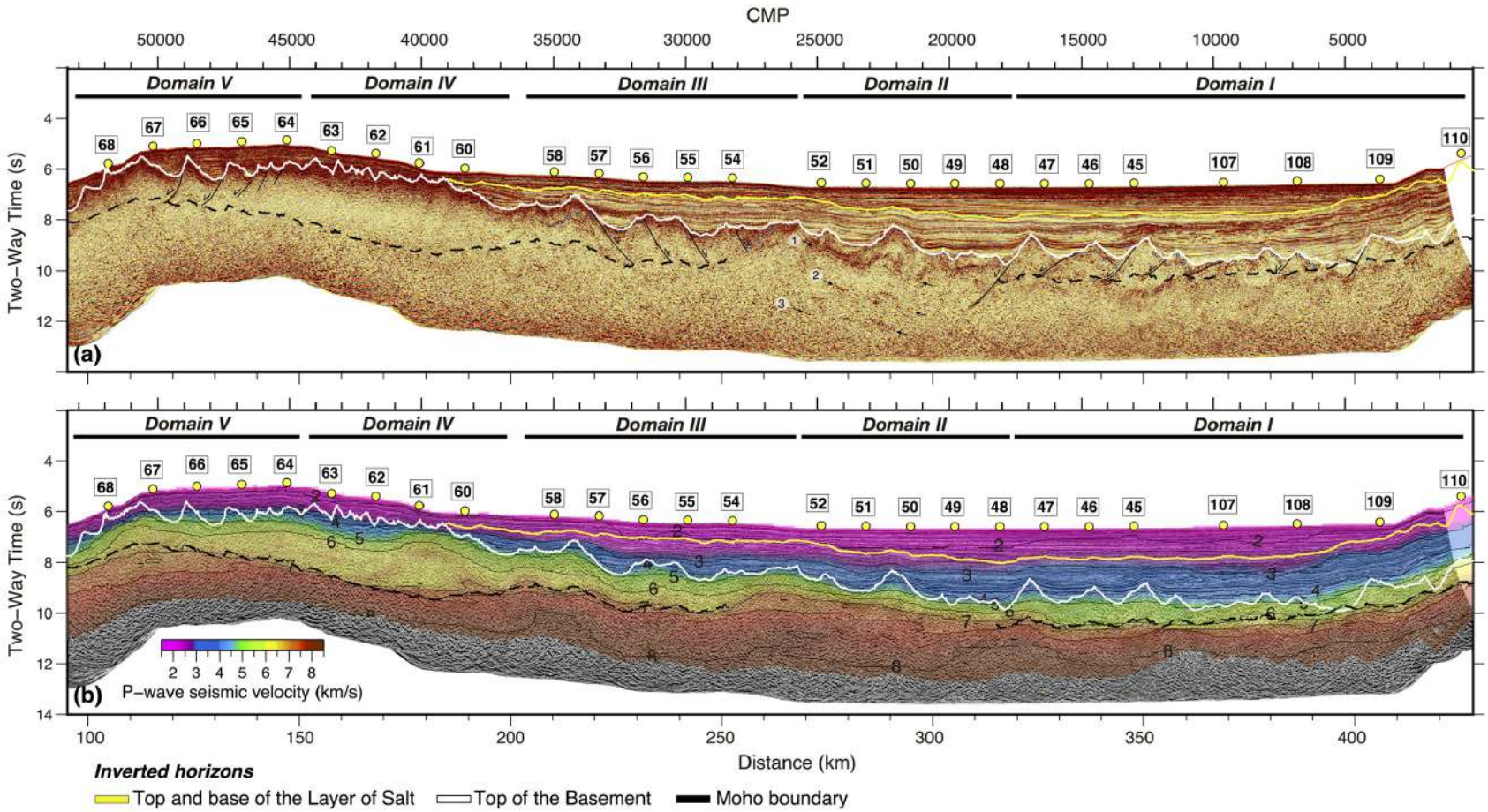

Figure 8.5 - (a) Time-migrated MCS line overlaid with geometry of the inverted horizons by travel-time tomography (yellow lines for the unconformity, white line for the top of the basement and dashed black line for the Moho boundary). The main faults are also represented. (b) MCS image of the profile overlaid by the 2D P-wave Vp model in (a) converted to TWT. The inverted horizons from Figure 8.3(a) are also displayed in this figure. Yellow circles show the OBS/OBH location.

8.5. Discussion

8.5.1. Basement affinity of the geological domains

We interpret the petrological affinity of basement domains based on their Vp structure and imaged structures. We compared the Vp-depth structure of each domain with compilations of Vp-depth profiles for continental crust (Christensen and Mooney, 1995), thinned continental crust (Prada et al., 2015), exhumed mantle (Sallarès et al., 2013a; Prada et al., 2014), oceanic crust (Grevemeyer et al., 2018a), and oceanic crust in regions with ultra-slow spreading rates (Grevemeyer et al., 2018b). We selected our Vp-depth profiles starting at the 4.5 km/s contour, which along most of the transect is close to the TOB. We chose 4.5 km/s to try to avoid Vp uncertainty associated to locations with the roughest TOB where Vp may locally be higher due to low model resolution or lower perhaps related to high rock fracturing. The comparison supports the presence of five petrological domains along the model (Fig. 8.6). The petrological interpretation has been used to calculate density from empirical Vp-ρ relationships that explain shipborne gravity data (Fig. 8.4) and further supports our definition of domains.

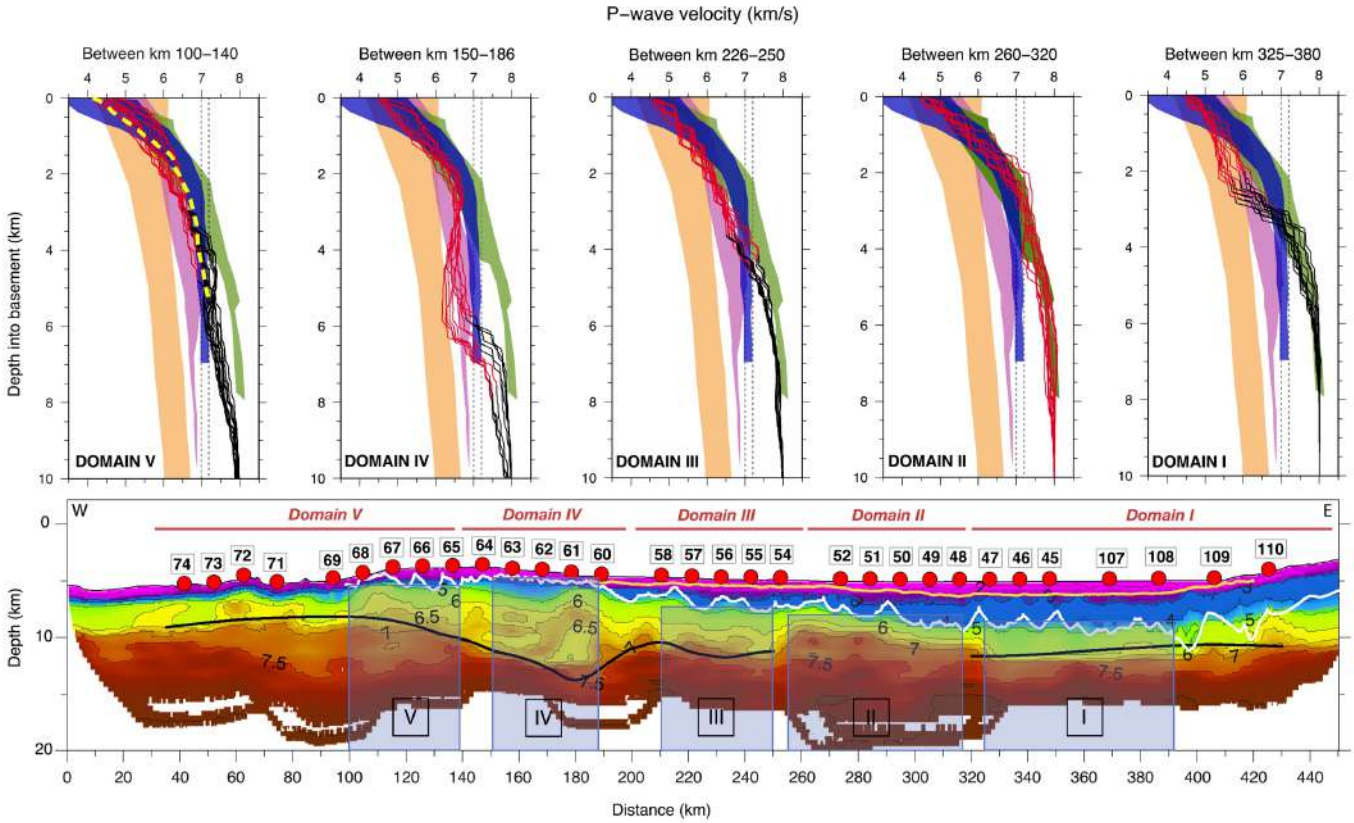

Figure 8.6 - Visual comparison between five reference models and the average vertical velocity structure of the 5 regions identified in the tomographic model (see model below). The red and black profiles represent 1D profiles from each domain along the FRAME-2 profile. The red stretch represents the velocity up to the Moho and the black stretch below the Moho. The 1D P-wave velocity depth references are displayed following the next colour code: oceanic crust (from Grevemeyer et al. 2018a) in blue, continental ultrathin crust or CUT (from Prada et al., 2015) in violet, continental crust (modified from Christensen and Mooney, 1995) in orange, and dashed yellow line for ultra-slow spreading magmatic domains (Grevemeyer et al., 2018b). The exhumed mantle reference includes 1D P-wave velocity depth profiles from the Gulf of Cadiz (Sallarès et al. 2013a) and from the Tyrrhenian basin (Prada et al. 2014) in green.

- ***Domain I of continental crust***

The Vp-depth distribution in Domain I with maximum values of ~6.5 km/s at the lower crust overlap with the reference of ultra-thin continental crust (Fig. 8.6). The comparatively rough TOB is underlain by a smooth Moho geometry so that the basement displays large lateral changes in thickness that we interpret as fault blocks (Fig. 8.7). Fault blocks were cut and tilted by seaward-dipping normal faults forming their west flanks (Fig. 8.5). The continental nature of this domain is also supported by Vp-ρ relationship explaining the gravity anomaly (Fig 8.4).

The uppermost ~4-5 km of mantle have Vp < 7.5 km/s which is anomalously low. In the SW and West Iberian margin, mantle Vp < 8.0 km/s has been found in areas of exhumed mantle, including the TAP (Sallarès et al., 2013a; Pinheiro et al., 1992). Under domain I, the low mantle Vp up supports mantle serpentinization under the continental crust, with lateral variations possibly indicating heterogeneous distribution of alteration. Low upper mantle Vp under continental fault blocks has also been described in the Deep Galicia Margin and the Porcupine Basin, where lateral changes in Vp appear related to deep faulting causing locally enhanced alteration (Bayrakci et al., 2016; Prada et al., 2017).

- ***Domain II of exhumed mantle***

Domain II steep Vp-depth profiles overlap the envelop of serpentinized mantle Vp, which together with the lack of Moho boundary in both MCS and WAS records, support that the basement is made of exhumed mantle rocks. The presence of exhumed mantle along this domain is further supported by gravity modelling (Fig. 8.4). Although low resolution WAS data along the parallel IAM-5 line did not constrain exhumed mantle (Afilhado et al., 2008), previous low-resolution data and a modern WAS line in Tagus and Horseshoe abyssal plains (Pinheiro et al., 1992; Rovere et al., 2004; Sallarès et al., 2013a) determined exhumed-mantle Vp structure (Fig. 8.1).

Domain II contains numerous internal basement reflections in the near-vertical images (Fig. 8.5). There are three sets of sub-horizontal reflections underneath the TOB, one at 0.5 s TWT, a second at ~2 s TWT and a third set at ~3 s TWT (Fig. 8.5a). Their interpretation without a detailed Vp model is speculative. The TOB of the Vp model maps well the corresponding boundary in the reflection image (Fig. 8.5a). Thus, the shallowest reflections occur in the sector of the steepest Vp vertical gradient, from 4.5 to 6.5-7.0 km/s. Their structure and lateral inter-relations are complex, and they are roughly sub-parallel to the TOB. They might represent serpentinization fronts, as interpreted for similar reflections on line IAM-9 in the Iberia Abyssal Plain (Dean et al., 2000). Alternatively, they could be ~1.5-2.0 km thick slivers of continental rocks resting on exhumed mantle, representing rafted tectonic blocks. The second and third sets at ~2 s and 3 s TWT underneath the TOB respectively, occur in a broad region with 7 > Vp < 8 km/s, supporting that they are within partially serpentinized mantle.

In the absence of detail Vp information, which is the case for the majority of seismic lines published from rifted margins, any of the two sets could speculatively be interpreted as Moho or lower crust reflections. Unless there is low-uncertainty Vp-depth information, there is no quantitative approach

to test either the nature of the domains or the origin of the seismic boundaries. Although potential field data are often analyzed in an attempt to overcame this problem, they are particularly unsuited to study deep-water margins where the basement is covered in most areas by several km of sediment, so that it is too far away from shipborne sensors to provide a clear signal. Especially constraints from gravity data alone are very tenuous, because without the Vp-depth information uncertainty would be too high to discern the nature of any of these domains. This is the reason why their presence, clearly defined in the Vp-depth distribution along the model, has not being previously detected with low-resolution WAS and/or MCS data combined with potential field data modelling.

- ***Domain III of continental crust***

Domain III extends from km 200-260, and in contrast to Domain II, there crust base is defined by clear PmP reflections. Basement thickness ranges from ~4-5 km with a Vp-depth structure ranging between 4.5 km/s near the TOB to ~6.5-7.2 km/s above Moho, and a fairly constant gradient (Fig. 8.3 and 8.5). Therefore, the basement does not show the layer2-layer3-type structure of oceanic crust. This is in stark contrast with conceptual models of magma-poor margins and in particular of models for West of Iberia that assume that continental breakup is followed by mantle exhumation and subsequent well-established seafloor spreading (e.g. Sutra and Manatschal, 2012).

Domain III Vp-depth structure appears to overlap with the Vp envelop of ultra-thin continental crust (Fig. 8.6). The exception is the deepest ~0.5 km of the lower crust that have Vp of 7.0-7.2 km/s, which is slightly high compared to the ultra-thin crust of other magma-poor margins (Prada et al., 2015) and to Domain I. The 7.0-7.2 km/s Vp range is typical of the gabbro of the lowermost part of oceanic Layer 3 (Grevemeyer et al., 2018a), which may indicate that Domain III is stretched continental crust that was intruded by mafic melts at low crustal levels. A 3% increase of the velocity-derived density of Domain II (estimated from empirical relationships; Christensen and Mooney, 1995), fits better the observed gravity anomaly, further supporting a rock composition somewhat more mafic than average continental.

- ***Domain IV of the first oceanic crust***

Domain IV extends from km ~140 to 200 across the eastern flank of the Madeira Tore Rise and includes the structure causing the J-magnetic anomaly (Fig. 8.3). The J-magnetic anomaly is attributed to oceanic crust (Srivastava, et al., 2000) or to syn-rift magmatism (Bronner et al., 2011; Nirrengarten et al., 2016). In TAP, the J-magnetic anomaly is centred at a ~20 km wide segment with ~8-9 thick basement (Fig. 8.3a) and hence much thinner than the J-magnetic anomaly basement in the American plate of the Central Atlantic where crust is ~12 km thick (Tucholke and Ludwig, 1982).

Domain IV has both, the most variable basement thickness, ranging from ~6-9 km, and the smoothest TOB relief along the transect. A ~20 km-wide segment is 7-9 thick, which is 1-3 km thicker than typical oceanic crust (Grevemeyer et al., 2018a). Most of Domain IV basement has a two-layer seismic structure resembling oceanic crust, i.e. a Layer 2 with a steep gradient and ~4.5 < Vp > 6.5 km/ and a Layer 3 with a gentle gradient. However, it is somewhat different from the seismic structure of Penrose-type oceanic crust, because Layer 3 ~6.0 < Vp < 6.7 km/s (Fig. 8.6). Despite those

departures from a classical oceanic seismic structure, the Vp-ρ conversion assuming oceanic composition (Carlson and Herrick, 1990) produces better fit to the gravity anomaly than using continental crust density.

The oceanic origin of Domain IV is further supported by findings of a similar seismic structure in locations within oceanic plates. Similarly, low Layer 3 Vp has been described as associated with thick oceanic crust in aseismic ridges, associated with the presence of mantle melting anomalies (Korenaga and Kelemen, 2000; Sallarès et al., 2003). Layer 3 bulk Vp and igneous crust thickness either correlate when melting is thermally controlled, or anticorrelate when controlled by mantle fertility (Korenaga et al., 2002; Sallarès et al., 2003). Domain IV thicker segment shows low Layer 3 Vp indicating an anticorrelation that supports that enhanced melting did not result from abnormally hot mantle, but rather from either an active upwelling component and/or compositional heterogeneities in the mantle source (Sallarès et al., 2003; 2005).

Therefore, Domain IV is the first ocean crust formed during the separation of Iberia and Newfoundland, and melting was not controlled by thinning of continental lithospheric leading to syn-rift magmatism. Domain IV oceanic crust did not form in the region of mantle exhumation where lithospheric thinning was possibly maximum. In contrast, Domain IV oceanic crust abuts continental Domain III, conforming a configuration of crustal domains not previously described West of Iberia.

- ***Domain V of the CMQZ oceanic crust***

The Vp-depth structure of Domain V shows an oceanic two-layer seismic structure similar to Domain IV (Figs. 8.6). The oceanic nature is supported by gravity modelling (Fig. 8.4). The oceanic crust formed during the Cretaceous Magnetic Quiet Zone, so that there is no direct information on spreading rate. The basement is ~4-4.5 km thick with a laterally heterogeneous Vp structure, particularly at middle-to-lower crustal levels. Basement Vp ranges from < 6.0 km/s (e.g. beneath OBS 69) to ~ 7.0 km/s (i.e. beneath OBS 72) (Fig. 8.6).

The TOB of Domain V is irregular compared to Domain IV, and the large blocks that appear tilted indicate normal faulting (Fig. 8.5), although the western half of the Domain is not covered by seismic images. Alternating low Vp sectors (e.g. beneath OBS 69) and high Vp might indicate petrological variations or fracturing associated to faulting. Similar heterogeneous structure with high-Vp anomalies (> 7.0 km/s) occurs in Mesozoic-age oceanic crust under Coral Patch Ridge and Seine Abyssal Plain of the northern Central Atlantic (Martinez-Loriente et al., 2014), and at recently formed ultra-slow spreading crust (Grevemeyer et al., 2018b). Such variations are interpreted to arise from alternation between amagmatic spreading and moderately magmatic segments.

8.5.2. Rifting, breakup and the COT

The joint interpretation of the Vp and density models with the tectonic structure from seismic reflection images has led to a radically new definition of the number and nature of geological domains under the TAP compared to previous studies. This new definition has important implications for

rifting processes, the location and formation of the COT and first seafloor spreading processes of the West Iberia margin during the first stages of North Atlantic opening.

Continental Domains I and III have conjugate fault structures, with overall asymmetric crustal thickness, inferred extension and fault style (Fig. 8.5a). Domain III Moho shallows as the basement thins towards the east accompanied by eastward-dipping normal faults that decrease in fault spacing and cut blocks of a decreasing size toward the basin centre (Fig. 8.5a). Domain I is characterized by westward dipping faults that appear to cut the entire crust in a series of blocks. The Moho is mostly sub-horizontal and extends over a 100 km-wide zone (Fig. 8.5a).

The asymmetric crustal thinning and conjugate tectonic structure of Domains I and III closely resembles the structure of the Deep Galicia Margin and conjugate segment of Newfoundland (Ranero and Pérez-Gussinyé, 2010). The asymmetric tectonic configuration under TAP may be interpreted to indicate that Domain III represents a sector of the Newfoundland continental margin that was cut during opening and transferred to the West Iberia margin during the early stages of North Atlantic opening.

Our results show that the structure from the TAP margin is more complex than previously assumed. Domain II basement composed of partly serpentinized mantle peridotites, is similar to sectors to the northwards in the IAP (Dean et al., 2000; Minshull et al., 2014; Grevemeyer et al. in prep.) and Deep Galicia Margin (Boillot et al., 1987; Whitmarsh et al., 1996; Bayrakci et al., 2016), and under the southern Tagus and Horseshoe Abyssal Plains (Sallarès et al., 2013). However, Domain II does not abut younger oceanic crust to the west, but limits at either side with the continental crust of Domains I and III. This structure contrasts with published interpretations of the structure along the IAP and Deep Galicia Margin, where exhumed mantle is inferred to bound oceanic lithosphere to the west (Dean et al., 2000; Dean et al., 2015). However, a two-layer oceanic seismic structure has not yet been shown with modern well-constraints Vp models in those two segments before the FRAME cruise. The IAP data did not map well the first ocean crust and the exhumed-mantle to oceanic crust boundary has been moved >20 km using the same data in successive analyses (Dean et al., 2000,

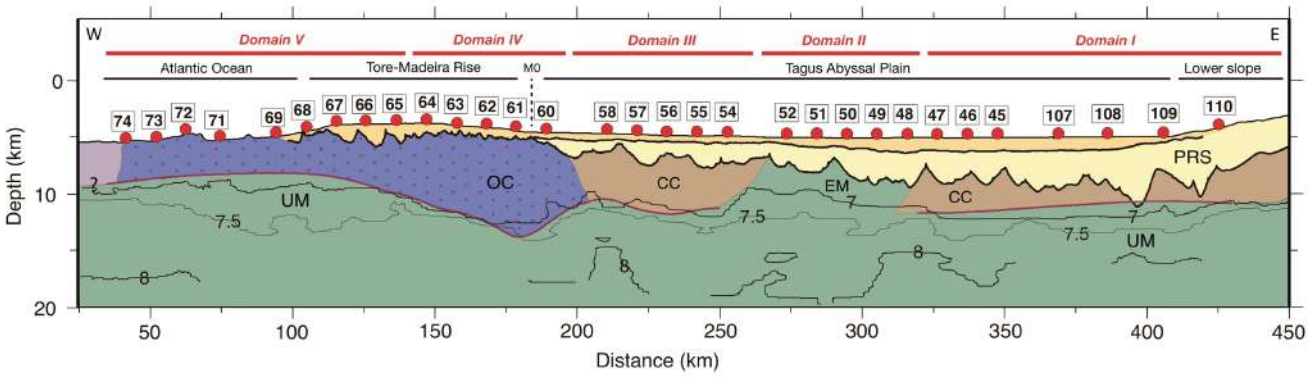

Figure 8.7 - Interpreted cross section along the FRAME-2 profile. The interpretation is based on the 2-D P-wave Vp model (Fig. 8.3a) and the corresponding basement affinity based on comparison with reference 1D Vp-depth profiles (Fig. 8.6) and the tectonic structure from the MCS image of Fig. 8.5a. Black lines showing isovelocity contours at 7.0, 7.5 and 8.0 km/s. PRS: post-rift sediments, SRS: syn-rift sediments, CC: continental crust, OC: oceanic crust, EM: exhumed mantle and UM: upper mantle. Red circles show the OBS/OBH location.

Minshull et al., 2014) indicating the uncertainty intrinsic to the resolution of sparse data. Modern seismic data from the Deep Galicia Margin COT has not found clear ocean crust west of the outcropping peridotite ridge (Dean 2015; Davy et al., 2016). However, in spite of the past paucity of data it has been traditionally assumed that lithospheric thinning during mantle exhumation led to, and directly preceded, the establishment of oceanic crustal accretion (e.g. Pérez-Gussinyé et al., 2006). This structural evolution did not occur in the TAP.

To explain the presence of exhumed mantle in Domain II, we propose a two-step process. A first phase of continental breakup, during which the formation of the exhumed mantle occurred, followed by a second phase where the rupture and the deformation jumped to the west forming Domain IV. Domain IV was formed by seafloor spreading with the J-magnetic anomaly being centred on 7-9 km-thick oceanic crust. We thus infer that the prominent north-south striking J-magnetic anomaly delineates in the western sector of the TAP the first position of oceanic crust formed by seafloor spreading centre in the north Atlantic.

8.5.3. Magmatism associated to the first oceanic crust

Given that the oceanic L3 is likely to be less altered and fractured than L2, its average seismic velocity is considered to be a good proxy of the seismic velocity of the pristine igneous crustal rocks (e.g. Kelemen and Holbrook 1995; Korenaga et al. 2000). We have calculated the long-wavelength crustal structure by averaging the L3 velocity (Vp) and crustal thickness (H) within a 20-km-wide laterally moving window along Domains IV (or J-anomaly) and V. Uncertainties of model parameters obtained from the Monte Carlo analysis (Fig. 8.3d) are used to assign error bounds to both H and Vp (Fig. 8.9).

Following Sallarès et al. (2005), we have modelled two cases taking into account a passive upwelling (X=0) and different mantle source compositions: 100% pyrolytic (square markers in Fig. 8.9) and 30% MORB and 70% pyrolytic mantle (diamond markers in Fig. 8.9). For the pure pyrolytic source, we have defined a melt productivity in the primary melting zone of 13% GPa^{-1}. Similarly, we have performed a higher melt productivity in the primary melting zone of 18% GPa^{-1} and a 60ºC lower temperature in the solidus with respect to normal pyrolytic source in order to reflect the Fe enrichment (Korenaga and Kelemen, 2002; Sallarès et al., 2005).

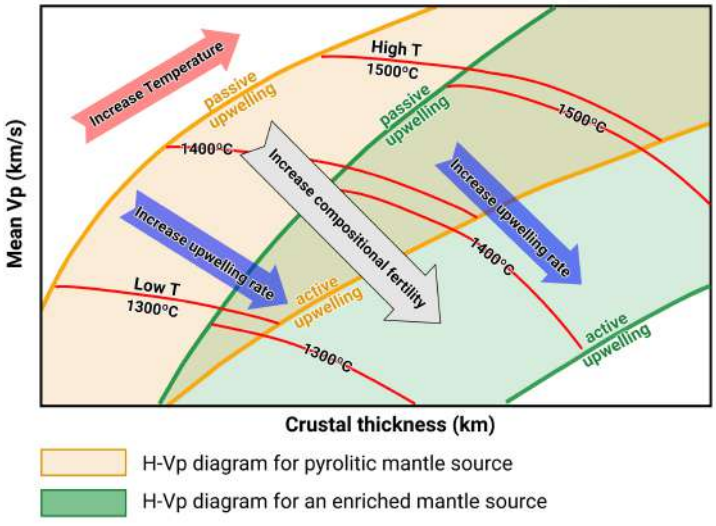

Figure 8.8 - Sketch to illustrate the relationship between crustal thickness and velocity when varying temperature, spreading rate and mantle source composition. Keeping constant the composition and the spreading rate, and varying only the temperature, thickness and mean velocity result positively correlated. Similarly, when varying only the spreading rate or the composition, they are anti-correlated. In particular, more fertile sources (in green) give thicker crusts at lower velocities compared to standard pyrolytic sources (in orange).

The results are represented in an *H–Vp* diagram including data from the Pacific (Malpelo, Cocos and Carnegie ridges from Sallarès et al. (2005); Western Mariana Ridge from Grevemeyer et al. (2020); East Pacific Rise Grevemeyer et al. (2018a)), Indian, Atlantic Oceans, and also hotspot volcanic margins from Grevemeyer et al. (2018a) (Fig. 8.9a), and in a second *H–Vp* diagram only including model samples along Domains IV and V and the Mid-Atlantic Ridge (Grevemeyer et al., 2018a) (Fig. 8.9b).

In both H–Vp diagrams the pyrolytic trend defines a "normal" oceanic crust with 7.05 km/s Vp for the L3 and 6.0 km thick (dashed lines in Fig. 8.9a,b). The samples that follow both compositions show a correlation between thickness and the average Vp for the L3. However, in the case of the Fe-Rich source, none of the samples reaches the mean Vp value for "normal" oceanic crust. We can observe that in the pyrolytic branch we need anomalous high temperature to form thick oceanic crust (e.g. hotspot volcanic margins) while in the Fe-Rich branch cooler temperatures are sufficient to generate ultra-thick oceanic crust (Fig. 8.8). For the same reason, at low temperatures (below 1200°C) the pyrolytic model cannot generate enough melting to create an oceanic crust so that we tend to have mantle exhumation with little synchronous magmatism, whereas in the Fe-Rich model there is enough melting to generate a crust like that observed in Domains IV and V. This suggests that the inception of the mid-Atlantic ridge and the creation of the first oceanic crust, as well as the J-anomaly, in this part of the Iberian margin, could have been triggered by the presence of a short-lived compositional anomaly in the mantle source.

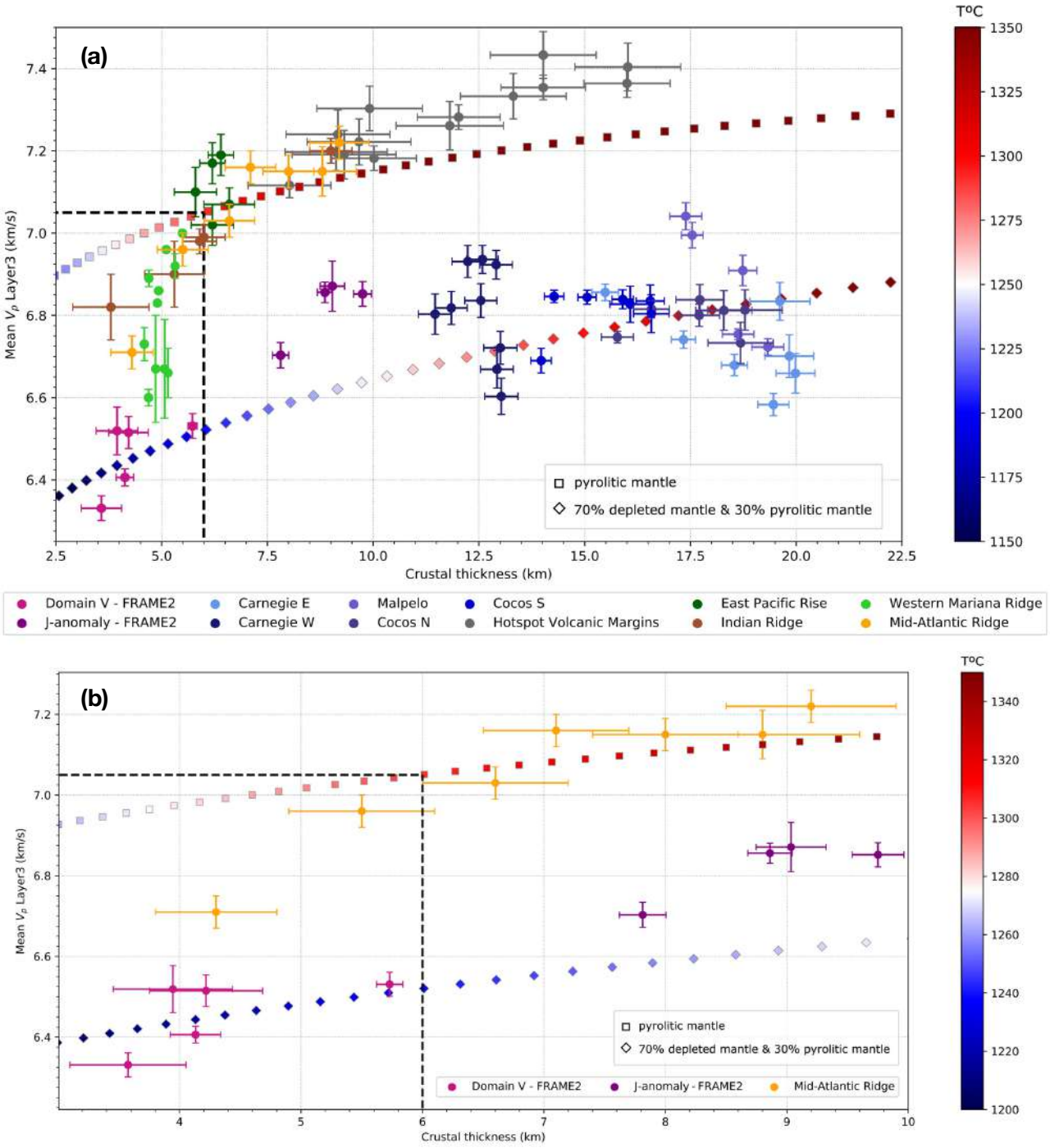

Figure 8.9 - Crustal thickness versus lower-crustal velocity (H–Vp) diagrams for the (a) Atlantic Ocean (b) and Pacific and Indian oceans. Data for Mid-Atlantic Ridge are shown in yellow (Grevemeyer et al., 2018a). Data for the Pacific (Malpelo, Cocos and Carnegie ridges) in shades of blue (Sallarès et al., 2005); Western Mariana Ridge in light green (Grevemeyer et al., 2020); East Pacific Rise in dark green (Grevemeyer et al., 2018a), and data for hotspot volcanic margins represented in grey dotes (Grevemeyer et al., 2018a). The data from Indian Ridge is represented in brown (Grevemeyer et al., 2018a). Data for J-anomaly (Domain IV) and Domain V from this work is represented in shades of violet. H-Vp values from "normal" oceanic crust is marked with thick dashed lines showing a velocity from a 6-km-thick crust (as in Sallarès et al. (2005), assuming passive upwelling) and a lower-crustal velocity of 7.05 km/s. Square markers represent the relationship between lower crustal velocity and thickness for a pyrolytic source, while diamonds markers represent the relationship for a Fe-Rich source. Markers colour hue indicates the temperature of the source.

8.5.4. Implication for early plate kinematics

The newly defined configuration of basement domains cannot be explained by the classical evolutionary model of the sequential formation of domains in magma-poor margins and requires the occurrence of different rifting episodes.

- ***Extensional phase 1: from rifting to mantle exhumation***

We propose a geodynamic scenario in which continental rifting occurs with Domains I and III as a conjugate pair, followed by mantle exhumation forming Domain II. Rifting extended continental crust until breakup that separated Domains I and III, followed by mantle exhumation across a ~70 km-wide Domain II. The exhumed mantle domain possibly extends to the south where a similar Vp model for the basement was found in the southern Tagus and Horseshoe Abyssal Plains (Sallares et al., 2013) and across the uplifted Gorrige Bank, where peridotite and gabbro were drilled (Ryan et al., 1973). However, the existence of continental crust under the TAP had not being described before, possibly due to the limited resolution of the few previous seismic studies (e.g. Mauffret et al., 1989; Afilhado et al., 2008).

We propose that the domains defined along FRAME-2 transect extend to the south to the currently Paleo Iberia–Africa Plate Boundary (PIAB in Fig. 8.1), but active during the Jurassic–Early Cretaceous. The fault system separated the Tagus-Horseshoe Abyssal Plain (the uplift of Gorringe Bank had not yet occurred) from the Seine Abyssal Plain (Rovere et al., 2004; Sallares et al., 2013; Martinez-Loriente et al., 2014). The Iberia–Africa Plate Boundary separated a magma-poor rift system with active mantle exhumation to the north from the seafloor spreading centre of the Central Atlantic to the south (Fig. 8.10).

The existence of two domains with continental basement under the TAP appears to imply that the extensional system in Figure 8.10 abruptly stopped during mantle exhumation in the Early

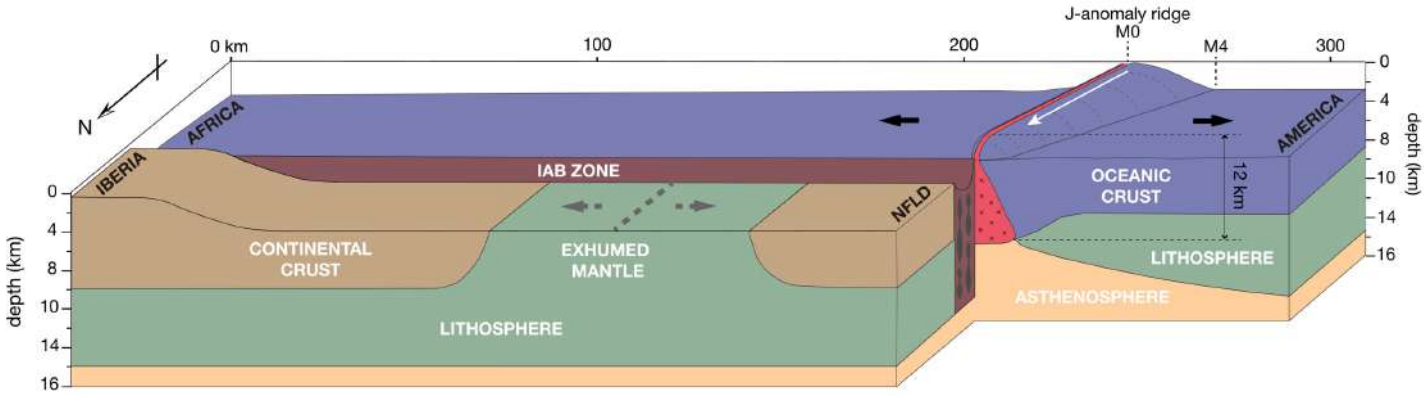

Figure 8.10 - Conceptual cartoon of the crustal and lithospheric structure Domains I-III right before the formation of oceanic Domain IV. The magma-rich J-anomaly ridge propagation (white arrow indicates the propagation direction of the spreading centre) has been blocked by the Iberia-Africa plate boundary (IAB) separating the thin spreading-centre lithosphere from the West Iberia thicker plate. The reconstruction represents the structure along FRAME-2 profile with extension axis (dashed and grey line and arrows) exhuming mantle of Domain II as Iberia and Newfoundland tectonic plates were pulled apart. Vertical exaggeration ~2.5. Abbreviations: IAB: Iberia-Africa Boundary, NFLD: Newfoundland.

Cretaceous, and that the locus of extension jumped to the west of Domain III. The jump of the centre of extension severed a sector of the conjugate Newfoundland continental margin and transferred it to the Iberia plate, forming Domain III (Fig. 8.7). Our scenario implies that extension in the exhumed mantle section was interrupted before initiation of seafloor spreading, in contrast to what is proposed by previous models of West Iberia margin formation (e.g. Bronner et al., 2011; Nirrengarten et al., 2016).

The exhumed-mantle domain under TAP is ~60 km wide, under IAP is >150 km wide, whereas under the Deep Galicia Margin it extends from the peridotite ridge at Site 637 (Boillot et al. 1987b) to the west for >50 km. However, line WI did not find a two-layer oceanic seismic structure, like in the south, and the first oceanic crust formed at the spreading centre propagating north has not yet being detected (Fig. 8.1). Thus, exhumed mantle domains do not follow the commonly assumed model where the TAP has a wider domain and the amount of mantle exhumation decreases toward the north (e.g. Nirrengarten et al., 2016).

- ***Extensional phase 2: seafloor spreading***

The second phase of extension occurs with an intense first pulse of magmatism creating Domain IV (Fig. 8.3). The Vp and gravity models of the structure support that Domain IV is made of thick oceanic crust formed at a well-established seafloor spreading centre for the first time in the North Atlantic (Fig. 8.7). The J-magnetic anomaly is centred above the thick sector of Domain IV. Thus, our data support that the J-magnetic anomaly is a lineation related to seafloor spreading volcanism. This finding is in contrast to numerous previous studies that interpreted the J-magnetic anomaly located north of the IAB boundary either as resulting from a magmatic pulse associated to continental breakup before seafloor spreading (Olivet, 1996; Sibuet et al., 2004; Bronner et al., 2011), or formed by multiple magmatic events that occurred both during and after formation of oceanic crust (Nirrengarten et al., 2016). A corollary to those previous interpretations was that the J-magnetic anomaly would either correspond to an isochron younger than M0 (Tucholke et al., 2007), or was not an isochron and its age changed in an undetermined fashion along its strike (Bronner et al., 2011).

The comparatively low resolution of the basement structure in previous studies have led to the proposition that the J-anomaly magmatic event formed the relief of the Madeira Tore Rise (Bronner et al., 2011, Afilhado et al. 2008). However, the thick oceanic crust of Domain IV does not occur under the shallowest topography of the Madeira-Tore Rise (Fig. 8.1), but under the eastern slope (Fig. 8.3). It is unclear why the ridge of the Madeira-Tore Rise is higher to the west of the thick crust, it could be due to the decrease in density of the underlaying mantle due to serpentinization as indicated by the low Vp (Fig. 8.3), or to tectonic processes from the Cenozoic contractional reactivation of different structures along the margin or both.

Therefore, we conclude that J-magnetic anomaly is a seafloor spreading lineation formed after the jump of the locus of extension that terminated mantle exhumation and that transferred continental Domain III from Newfoundland to Iberia (Fig. 8.11). The implications are that it is possible that the J-magnetic anomaly in TAP is an extension of the J-magnetic anomaly within the oceanic plate of the central Atlantic south of the PIAB.

Along the northern Central Atlantic, the high-amplitude J-magnetic anomaly is interpreted as a seafloor spreading lineation. Here, the J-magnetic lineation is a continuous feature roughly parallel to older anomalies of the Mesozoic M-series and it is interpreted to contain the M4 to M0 isochrons, at least along some of its length (Rabinowitz et al., 1979; Klitgord and Schouten, 1986, Verhoef et a., 1991). The J-magnetic anomaly occurs partly over a continuous basement ridge (Roest et al., 1992) of oceanic igneous crust ~12 km thick (Tucholke and Ludwig, 1982) that was near sea-level at least in some segments where drilling sampled reef limestone covering basalts (Tucholke and Vogt, 1979). This set of observations supports that the J-magnetic anomaly along the northern Central Atlantic corresponds to an igneous structure formed at a spreading centre sector with enhanced magmatism.

We speculate that the J-anomaly magmatism may have promoted ridge propagation, a process by which a spreading segment enlarges at the expense of neighbouring segments. The magma-rich TAMMAR segment of the Mid Atlantic Ridge opening at slow-intermediate rates, i.e. similar to the spreading rates along the J-magnetic anomaly, currently exhibits ridge propagation characteristics (Dannowski et al., 2011). The TAMMAR segment lengthening has led to the recent termination of a transform fault bounding spreading segments and the cessation of associated detachment faulting (Dannowski et al., 2018).

We propose that when the J-anomaly ridge initiated at M4, the magma-rich segment propagated north approaching the Iberia-Africa Boundary Zone (Fig. 8.10). We do not have data to determine when the magma-rich ridge arrived to the plate boundary separating the Central Atlantic oceanic plate from the north Atlantic continental plate. The shallower mid-ocean ridge migrating north may have been temporally stopped by the thicker continental lithosphere in the mantle exhumation phase or may have being able to relatively swiftly migrate further across the Iberia-Africa Boundary Zone (Fig. 8.11). The doming caused by thicker than average melt column in the asthenosphere and melt chamber in the crust created gravitational stresses to drive propagation (Mondy et al., 2017). We envision a melt-infiltrated frontal fissure propagating across the Iberia-Africa Boundary Zone from the Central Atlantic spreading centre to the north across the rifted continental lithosphere (Fig. 8.11). The melt-rich spreading centre propagating north took all deformation associated to the opening, causing cessation of mantle exhumation at Domain II, severing a sector of the continental plate of the Newfoundland margin transferred as Domain III, and terminated the differential slip across the Iberia-Africa Boundary Zone making the plate boundary inactive (PIAB, Fig. 8.11).

The propagation of a magma-rich spreading centre explains the structure of Domain IV that is the first oceanic crust of the margin with a Layer2 and Layer 3 seismic structure and 7-9 km thick, i.e. 2-3 km thicker than normal crust formed at similar spreading rates (Grevemeyer et al., 2018a). The propagation also explains the presence of the continental Domain III and may explain its slightly higher lower crust Vp perhaps associated to melt intrusions in the lower continental crust. The model implies that the first oceanic crust is not related to the gradual extension and thinning of continental lithosphere during rifting and that it is not the consequence of mantle melting processes associated to gradual mantle exhumation as proposed in conceptual models for IAP and Galicia margin (e.g. Bronner et al., 2011).

The geodynamic evolution implies that the 60 km of Domain II may represent the entire width of exhumed mantle produced during rifting and that the conjugate North American margin may not necessarily have any exhumed mantle domain as often assumed (Nirrengarten et al., 2016). The propagation of the magmatically robust ridge caused a second breakup, after the continental breakup leading to mantle exhumation. The spreading centre moved northward at unknown speed, so that the J-magnetic anomaly west of Iberia should be younger towards the north, but whether it represents the M0 isochron along its entire length or a longer time span is still unresolved. Enhanced melting source under the spreading centre stopped after M0, and the oceanic igneous crust gradually thins from 6 to ~3 km thickness from Domain IV to Domain V, in agreement with the ultra-slow spreading rates estimated for the beginning of the Cretaceous Magnetic Quiet Zone (Schettino and Turco, 2011).

8.6. In summary

A joint tomography of reflections and first arrivals in collocated streamer data and OBS records across the Tagus Abyssal Plain provides a Vp model of the crust and uppermost mantle that constrains the properties and limits of the different geological domains of the basement.

The basement has five domains differentiated in their Vp and gravity models and seismic image. Each domain has a distinct crustal geometry and Vp and density structure. From east to west, Domains I and III are made of extended continental crust. Domain II is 60 km wide made of exhumed partly serpentinized mantle. Westwards is Domain IV with a layer2-layer3 type oceanic crust seismic structure. Domain IV has a 7-9 km thick sector that correspond to the location of the J-magnetic anomaly. The igneous oceanic crust thins further west from 6 to 3 km in Domain V formed during the Cretaceous Magnetic Quiet Zone possibly formed at ultra-slow spreading rates.

The distribution of basement domains is at odds with evolutionary magma-poor models for the West Iberia margin where continental breakup is followed by mantle exhumation that promotes asthenospheric rise and the establishment of a stable spreading system.

In contrast, we propose after continental breakup of conjugate Domains I and III, when mantle exhumation was active West Iberia in Domain II, an independent event occurred in the Central Atlantic that would subsequently terminate continental rifting and start seafloor spreading in the North Atlantic. A magma-rich spreading centre formed from M4 to M0 magnetic isochron age and propagated to the north to cut the plate boundary between Iberia and African plates. The spreading centre propagation cut through a sector of the Newfoundland continental lithosphere and transferred Domain III to Iberia, and ended mantle exhumation (Domain II) as all deformation focused on the weak magma-rich system (Domain IV). The thick igneous crust sector of Domain IV generates the J-magnetic anomaly in TAP. Thus, the 3D development of the rift to drift system of West Iberia is not related to the gradual 2D evolution of the thinning of the lithosphere envision by most current conceptual models of magma-poor margins in the literature.

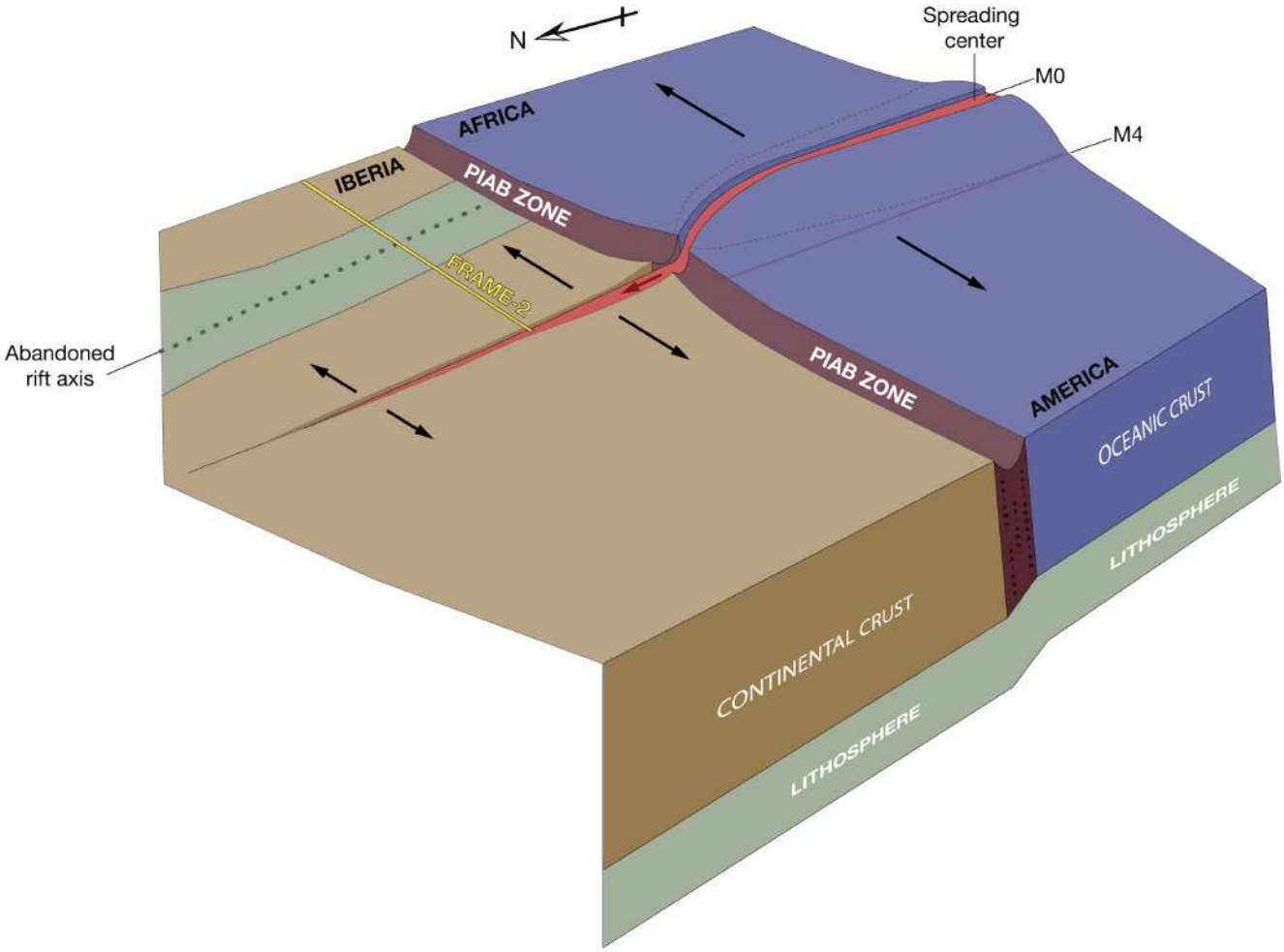

Figure 8.11 - Conceptual cartoon of the oceanic propagation event, following the model in Figure 8.9, across the PIAB zone and the Tagus Abyssal Plain. The red arrow located at the spreading centre represents the gravitational stress and the black arrows represent the extension direction of the tectonics plates: Africa, America, Iberia and Newfoundland. The yellow line represents the location of FRAME-2 profile. Abbreviations: PIAB: Paleo Iberia-Africa Boundary.

References

Afilhado, A., Matias, L., Shiobara, H., Hirn, A., Mendes-Victor, L., and Shimamura, H. (2008). From unthinned continent to ocean: The deep structure of the West Iberia passive continental margin at 38°N. Tectonophysics, 458(1–4), 9–50, doi:10.1016/ j.tecto.2008.03.002.

Banda, E., Torne, M. and Iberian Atlantic Margins Group (1995). Iberian Atlantic Margins Group investigates deep structure of ocean margins. Eos, Transactions American Geophysical Union, 76(3), pp.25-29.

Bayrakci, G., Minshull, T.A., Sawyer, D.S., Reston, T.J., Klaeschen, D., Papenberg, C., Ranero, C., Bull, J.M., Davy, R.G., Shillington, D.J., Pérez-Gussinyé, M., and Morgan, J. K. (2016). Fault-controlled hydration of the upper mantle during continental rifting. Nature Geoscience, 9(5), 384–388, doi:10.1038/ngeo2671.

Begović, S. (2020). Structure and physical properties of the subduction plate boundary. Universitat de Barcelona. PhD Thesis.

Beslier, M.O., (1996). Data report: seismic line LG12 in the Iberia Abyssal Plain. Whitmarsh, R.B., Sawyer, D.S., Klaus, A., Masson, D.G. (Eds.), Proc. Ocean Drill. Program, Sci. Results 149, 737–739.

Boillot, G., Winterer, E.L., Meyer, A.W. (1987a). Introduction, objectives, and principal results: Ocean Drilling Program Leg 103, west Galicia Margin. Proc. ODP, Init. Repts., 103: College Station, TX (Ocean Drilling Program), doi:10.2973/odp.proc.ir.103.

Bronner, A., Sauter, D., Manatschal, G., Péron-Pinvidic, G. and Munschy, M. (2011). Magmatic breakup as an explanation for magnetic anomalies at magma-poor rifted margins. Nature Geoscience, 4(8), pp.549-553.

Carlson, R.L., and Herrick, C.N. (1990). Densities and Porosities in the Oceanic Crust and Their Variations with Depht and Age, J. Geophys. Res., 95 (B6), 9153-9170.

Carlson, R.L., and Miller, D.J. (2003). Mantle wedge water contents estimated from seismic velocities in partially serpentinized peridotites, Geophys. Res. Let., 30 (No. 5), doi:10.1029/2002GL016600.

Chian, D., Louden, K.E., Minshull, T.A. and Whitmarsh, R.B. (1999). Deep structure of the ocean-continent transition in the southern Iberia Abyssal Plain from seismic refraction profiles: Ocean Drilling Program (Legs 149 and 173) transect. Journal of Geophysical Research: Solid Earth, 104(B4), pp.7443-7462.

Christensen, N., and Mooney, W. (1995). Seismic velocity structure and composition of the continental crust: A global view. J. Geophys. Res., 100(B7), 9761–9788, doi:10.1029/95JB00259.

Dannowski, A., Grevemeyer, I., Phipps Morgan, J., Ranero, C.R., Maia, M. and Klein, G. (2011). Crustal structure of the propagating TAMMAR ridge segment on the Mid-Atlantic Ridge, 21.5 N. Geochemistry, Geophysics, Geosystems, 12(7).

Dannowski, A., Morgan, J. P., Grevemeyer, I., and Ranero, C. R. (2018). Enhanced mantle upwelling/melting caused segment propagation, oceanic core complex die off, and the death of a transform fault: The Mid-Atlantic Ridge at 21.5°N. Journal of Geophysical Research: Solid Earth, 123, doi:10.1002/2017JB014273.

Davy, R.G., Minshull, T.A., Bayrakci, G., Bull, J.M., Klaeschen, D., Papenberg, C., Reston, T.J., Sawyer, D.S. and Zelt, C.A. (2016). Continental hyperextension, mantle exhumation, and thin oceanic crust at the continent-ocean transition, West Iberia: New insights from wide-angle seismic. Journal of Geophysical Research: Solid Earth, 121(5), pp.3177-3199.

Dean, S.M., Minshull, T.A., Whitmarsh, R.B. and Louden, K.E. (2000). Deep structure of the ocean-continent transition in the southern Iberia Abyssal Plain from seismic refraction profiles: The IAM-9 transect at 40 20′ N. Journal of Geophysical Research: Solid Earth, 105(B3), pp.5859-5885.

Dean, S., Sawyer, D. and Morgan, J. (2015). Galicia Bank ocean–continent transition zone: New seismic reflection constraints, Earth Planet. Sci.

Fernàndez, M., Marzán, I., Torne, M. (2004). Lithospheric transition from the Variscan Iberian Massif to the Jurassic

oceanic crust of the Central Atlantic. Tectonophysics 386, 97–115.

Grevemeyer, I., Ranero, C.R., Ivandic M. (2018a). Structure of oceanic crust and serpentinization at subduction trenches. Geosphere, v. 14, no. 2, doi:10.1130/GES01537.1.

Grevemeyer, I., Hayman, N. W., Peirce, C., Schwardt, M., Van Avendonk, H. J. A., Dannowski, A., and Papenberg, C. (2018b). Episodic magmatism and serpentinized mantle exhumation at an ultraslow-spreading centre. Nature Geoscience, 11(6), 444–448, doi:10.1038/s41561-018-0124-6.

Grevemeyer, I., Kodaira, S., and Takahashi, N. (2020). Structure of oceanic crust in back-arc basins modulated by mantle source heterogeneity. Geology. doi:10.1130/g48407.1.

Hamilton, E.L. (1978). Sound velocity-density relations in sea-floor sediments and rocks, J. Acoust. Soc. Am., 63, 366-377.

Kelemen, P.B. and Holbrook, W.S. (1995). Origin of thick, high-velocity igneous crust along the U.S. East Coast margin, J. geophys. Res., 100, 10 077–10 094.

Klitgord, K.D. and Schouten, H. (1986). Plate kinematics of the central Atlantic. Geol. N. Am., 1000, 351–378.

Korenaga, J., Holbrook, W.S., Kent, G.M., Kelemen, P.B., Detrick, R.S., Larsen, H.C., Hopper, J.R. and Dahl-Jensen, T. (2000). Crustal structure of the southeast Greenland margin from joint refraction and reflection seismic tomography. Journal of Geophysical Research: Solid Earth, 105(B9), pp.21591-21614.

Korenaga, J., Kelemen, P.B. and Holbrook, W.S. (2002). Methods for resolving the origin of large igneous provinces from crustal seismology, J. geophys. Res., 107(B9), 2178, doi:10.1029/2001JB001030.

Korenaga, J., and Kelemen, P. B. (2000) Major element heterogeneity in the mantle source of the North Atlantic igneous province, Earth Planet. Sci. Lett., 184, 251–268.

Korenaga, J., Kelemen, P.B. and Holbrook, W.S. (2002). Methods for resolving the origin of large igneous provinces from crustal seismology, J. geophys. Res., 107(B9), 2178, doi:10.1029/2001JB001030.

Martínez-Loriente, S., Sallarès, V., Gràcia, E., Bartolome, R., Dañobeitia, J. J., and Zitellini, N. (2014). Seismic and gravity constraints on the nature of the basement in the Africa-Eurasia plate boundary: New insights for the geodynamic evolution of the SW Iberian margin. Journal of Geophysical Research: Solid Earth, 119(1), 127-149.

Mauffret, A., Mougenot, D., Miles, P.R., Malod, J.A. (1989). Cenozoic deformation and Mesozoic abandoned spreading center in the Tagus Abyssal-Plain (West of Portugal) - results of a multichannel seismic survey. Canadian Journal of Earth Sciences 26 (6), 1101–1123.

Meléndez, A., Sallarès, V., Ranero, C. R., and Kormann, J. (2014). Origin of water layer multiple phases with anomalously high amplitude in near-seafloor wide-angle seismic recordings. Geophysical Journal International, 196(1), 243-252, doi:10.1093/gji/ggt391.

Meléndez, A., Korenaga, J., Sallarès, V., Miniussi, A. and Ranero, C.R. (2015). TOMO3D: 3-D joint refraction and reflection travel-time tomography parallel code for active-source seismic data - Synthetic test, Geophysical Journal International, doi:10.1093/gji/ggv292.

Minshull, T., Dean, S. and Whitmarsh, R. (2014). The Peridotite Ridge province in the southern Iberia Abyssal Plain: Seismic constraints revisited, J. Geophys. Res. Solid Earth, 119, 1580–1598, doi:10.1002/2014JB011011.

Mondy, L.S., Rey, P.F., Duclaux, G., and Moresi, L. (2018). The role of asthenospheric flow during rift propagation and breakup: Geology, v. 46, p. 103–106, doi:10.1130/G39674.1.

Nirrengarten, M., Manatschal, G., Tugend, J., Kusznir, N. J., and Sauter, D. (2016). Nature and origin of the J-magnetic anomaly offshore Iberia-Newfoundland: implications for plate reconstructions. Terra Nova, 29(1), 20–28. doi:10.1111/ter.12240.

Olivet, J.-L. (1996). La cinématique de la plaque Ibérie, Bull. Cent. Rech. Explor.-Prod. Elf Aquitaine, 20, 131– 195.

Peirce, C., Barton, P.J. (1991). Crustal structure of the Madeira-Tore Rise, Eastern North- Atlantic - results of a dobs wide-angle and normal incidence seismic experiment in the Josephine Seamount region. Geophysical Journal International 106 (2), 357–378.

Pérez-Gussinyé, M., Morgan, J. P., Reston, T. J., and Ranero, C. R. (2006). The rift to drift transition at non-volcanic margins: Insights from numerical modelling. Earth and Planetary Science Letters, 244(1–2), 458–473, doi:10.1016/j.epsl.2006.01.059.

Pérez-Gussinyé, M. (2012). A tectonic model for hyperextension at magma-poor rifted margins: an example from the West Iberia–Newfoundland conjugate margins, Geol. Soc. London Spec. Publ., 369(1), 403–427.

Pinheiro, L.M., Whitmarsh, R.B., Miles, P.R. (1992). The ocean–continent boundary off the western continental margin of Iberia—II. Crustal structure in the Tagus abyssal plain. Geophys. J. Int. 109 (1), 106–124.

Pinheiro, L.M. (1994). The crustal structure under the Tagus Abyssal Plain and the ocean-continent transition off western Iberia [Ph.D. thesis]. Univ. London.

Prada, M., Sallarès, V., Ranero, C.R., Vendrell, M.G., Grevemeyer, I., Zitellini, N. and de Franco, R. (2014). Seismic structure of the Central Tyrrhenian basin: Geophysical constraints on the nature of the main crustal domains. Journal of Geophysical Research: Solid Earth, 119(1), pp.52-70.

Prada, M., Sallarès, V., Ranero, C.R., Vendrell, M.G., Grevemeyer, I., Zitellini, N. and de Franco, R. (2015). The complex 3-D transition from continental crust to back-arc magmatism and exhumed mantle in the Central Tyrrhenian Basin. Geophys. J. Int., 203(1), 63–78.

Prada, M., Watremez, L., Chen, C., O'Reilly, B.M., Minshull, T.A., Reston, T.J., Shannon, P.M., Klaeschen, D., Wagner, G. and Gaw, V. (2017). Crustal strain-dependent serpentinisation in the Porcupine Basin, offshore Ireland. Earth and Planetary Science Letters, 474, 148–159, doi:10.1016/j.epsl.2017.06.040.

Purdy, G.M. (1975). The Eastern end of the Azores-Gibraltar plate boundary. Geophys. J. R. Astr. Soc., 43, 123–150.

Rabinowitz, P.D., Cande, S.C. and Hayes, D.E. (1979). The J-Anomaly in the Central North Atlantic Ocean. In: Initial Reports of the Deep Sea Drilling Project, Vol. 43, pp. 879–885. U.S. Government Printing Office, Washington, DC.

Ranero, C. R., and M. Pérez-Gusinyé (2010). Sequential faulting explains the asymmetry and extension discrepancy of conjugate margins, Nature, Vol. 468, pp. 294-300, doi:10.1038/nature09520.

Roest, W.R., Dañobeitia, J.J., Verhoef, J. and Collette, B.J. (1992). Magnetic Anomalies in the Canary Basin and the Mesozoic Evolution of the Central North Atlantic. Mar. Geophys. Res., 14, 1-24.

Rovere, M., Ranero, C. R., Sartori, R., Torelli, L., and Zitellini, N. (2004). Seismic images and magnetic signature of the Late Jurassic to Early Cretaceous Africa–Eurasia plate boundary off SW Iberia. Geophysical Journal International, 158, 554–568.

Ryan, W. B. R., K. J. Hsü, M. B. Cita, P. Dumitrica, J. Lort, W. Maync, W.D. Nesteroff, G. Pautot, H. Stradner, and F. C. Wezel (1973). Site 120, in Initial Reports of the Deep-Sea Drilling Project, JOIDES, vol. 13, edited by A.G. Kaneps, pp. 19-41, Washington (U.S. Government Printing Office).

Sallarès, V. (2003). Seismic structure of Cocos and Malpelo Volcanic Ridges and implications for hot spot-ridge interaction. Journal of Geophysical Research, 108(B12). doi:10.1029/2003jb002431.

Sallarès, V., Charvis, Ph., Flueh, E. R., Bialas, J., and the SALIERI Scientific Party (2005). Seismic structure of the Carnegie ridge and the nature of the Galápagos hotspot, Geophys. J. Int., 161, 763–788, doi:10.1111/j.1365-246X.2005.02592.x.

Sallarès, V., Gailler, A., Gutscher, M.A., Graindorge, D., Bartolomé, R., Gracia, E., Diaz, J., Dañobeitia, J.J. and Zitellini, N. (2011). Seismic evidence for the presence of Jurassic oceanic crust in the central Gulf of Cadiz (SW Iberian margin). Earth and Planetary Science Letters, 311(1-2), pp.112-123.

Sallarès, V., Martínez-Loriente, S., Prada, M., Gràcia, E., Ranero, C., Gutscher, M.A., Bartolome, R., Gailler, A., Dañobeitia, J.J. and Zitellini, N. (2013). Seismic evidence of exhumed mantle rock basement at the Gorringe Bank and the adjacent Horseshoe and Tagus abyssal plains (SW Iberia). Earth and Planetary Science Letters, 365, pp.120-131.

Sandwell, D. T., Muller, R. D., Smith, W. H. F., Garcia, E., and Francis, R. (2014). New global marine gravity model from CryoSat-2 and Jason-1 reveals buried tectonic structure. Science, 346(6205), 65–67, doi:10.1126/science.1258213.

Sawyer, D., Whitmarsh, R. and Klaus, A. (1994). Iberia Abyssal Plain Sites 897-901, paper presented at Proceedings of the Ocean Drilling Program Initial Rep.

Sibuet, J.-C., Srivastava, S. P., and Spakman, W. (2004). Pyrenean orogeny and plate kinematics. Journal of Geophysical Research: Solid Earth, 109(B8), doi:10.1029/2003jb002514.

Srivastava, S.P., Sibuet, J.C., Cande, S., Roest, W.R. and Reid, I.D. (2000). Magnetic evidence for slow seafloor spreading during the formation of the Newfoundland and Iberian margins. Earth and Planetary Science Letters, 182(1), pp.61-76.

Sutra, E., Manatschal, G. (2012). How does the continental crust thin in a hyperextended rifted margin? Insights from the iberia margin. Geology 40, 139T 142, doi:10.1130/G32786.1.

Tucholke, B. E., Sawyer, D. S., and Sibuet, J.-C. (2007). Breakup of the Newfoundland–Iberia rift. Geological Society, London, Special Publications, 282(1), 9–46, doi:10.1144/sp282.2.

Tucholke, B.E., Ludwig, W.J. (1982). Structure and origin of the J-Anomaly ridge, Western North-Atlantic Ocean. Journal of Geophysical Research 87 (NB11), 9389–9407.

Tucholke, B. E. and Vogt, P. R. (1979). Site 384: The Cretaceous/Tertiary boundary, Aptian reefs, and the J-Anomaly Ridge. Initial Rep. Deep Sea Drill. Proj, 43, 107-165.

Van Avendonk, H.J., Holbrook, W.S., Nunes, G.T., Shillington, D.J., Tucholke, B.E., Louden, K.E., Larsen, H.C. and Hopper, J.R. (2006). Seismic velocity structure of the rifted margin of the eastern Grand Banks of Newfoundland, Canada. Journal of Geophysical Research: Solid Earth, 111(B11).

Verhoef, J. H., Collette, B.J.; Dañobeitia, J.J., Roeser, H.A. and Roest, W.R. (1991). Magnetic Anomalies Off West-Africa (20-38˚ N). Mar. Geophys. Res., 13, 81-103.

Whitmarsh, R.B., White, R.S., Horsefield, S.J., Sibuet, J.C., Recq, M. and Louvel, V. (1996). The ocean-continent boundary off the western continental margin of Iberia: Crustal structure west of Galicia Bank. Journal of Geophysical Research: Solid Earth, 101(B12), pp.28291-28314.

Whitmarsh, R. B., M.-O. Beslier, P. J. Wallace, and Shipboard Scientific Party (1998). Sites 1065–1070, Proc. Ocean Drill. Prog. Initial Rep.,173, 65–294.

Zelt, C.A., and Forsyth, D.A. (1994). Modeling wide-angle seismic data for crustal structure - Southeastern Grenville Province. Journal of Geophysical Research-Solid Earth 99 (B6), 11687-11704.

Chapter 9

Rifting model and seafloor spreading of the Tagus Abyssal Plain

The nature of the basement in the West and Southwest Iberian margin and the geometry and location of the boundaries between the different crustal domains have been a matter of debate since the mid 70's (see Chapter 8, section 8.1). The area has been the site of multiple experiments including deep sea drilling, dredging, deep-sea submersible expeditions, as well as numerous geophysical surveys with seismic and bathymetric data (e.g. Boillot et al. 1987; Sawyer et al.1994; Whitmarsh and Sawyer, 1996; Whitmarsh et al. 1998; Tucholke et al. 2007).

However, nearly all modern geophysical surveys have focused on the Deep Galicia segment of the margin, and the existing ODP drilling sites of the Iberia Abyssal Plain (IAP) have had comparatively little associated modern seismic studies. Most of the seismic data acquired in the region correspond to Multi-Channel Seismic (MCS) reflection profiles, which provide images of the tectonic structure but is not the most appropriate to estimate rock properties and thus to constrain their nature and composition. Most of the studies done in the West Iberia margin (e.g. Reston, 2009; Ranero and Perez-Guissinyé, 2010) are based on the interpretation of two main MCS lines: the Lusigal-12 (LG) across the IAP, and the ISE-1 across the Deep Galicia Basin. The LG12 reflection line was acquired in 1990 and described by Beslier (1996) and Krawczyk et al. (1996) in combination with several ODP drill hole data. The ISE-1 line on the Deep Galicia margin was acquired in 1997 and first published and discussed by Zelt et al. (2003) and Henning et al. (2004).

Particularly significant is the lack of modern wide-angle seismic studies in West Iberia allowing to link drilling data to basement nature and structure at a large scale. Here, only two lines, one across the IAP coincident with IAM-9 was collected in the 90's with OBS (Ocean-Bottom Seismometers) spacing of 30-40 km apart (Dean et al., 2000) and in the Tagus Abyssal Plain (TAP) coincident with IAM-5 with an even sparser instrument spacing (Pinheiro et al., 1992; Afilhado et al., 2008) (Fig. 9.1). With such an instrument separation, the spatial resolution is severely compromised, and even though profiles are presented in publications as 2D velocity models, the reality is that, for crustal-

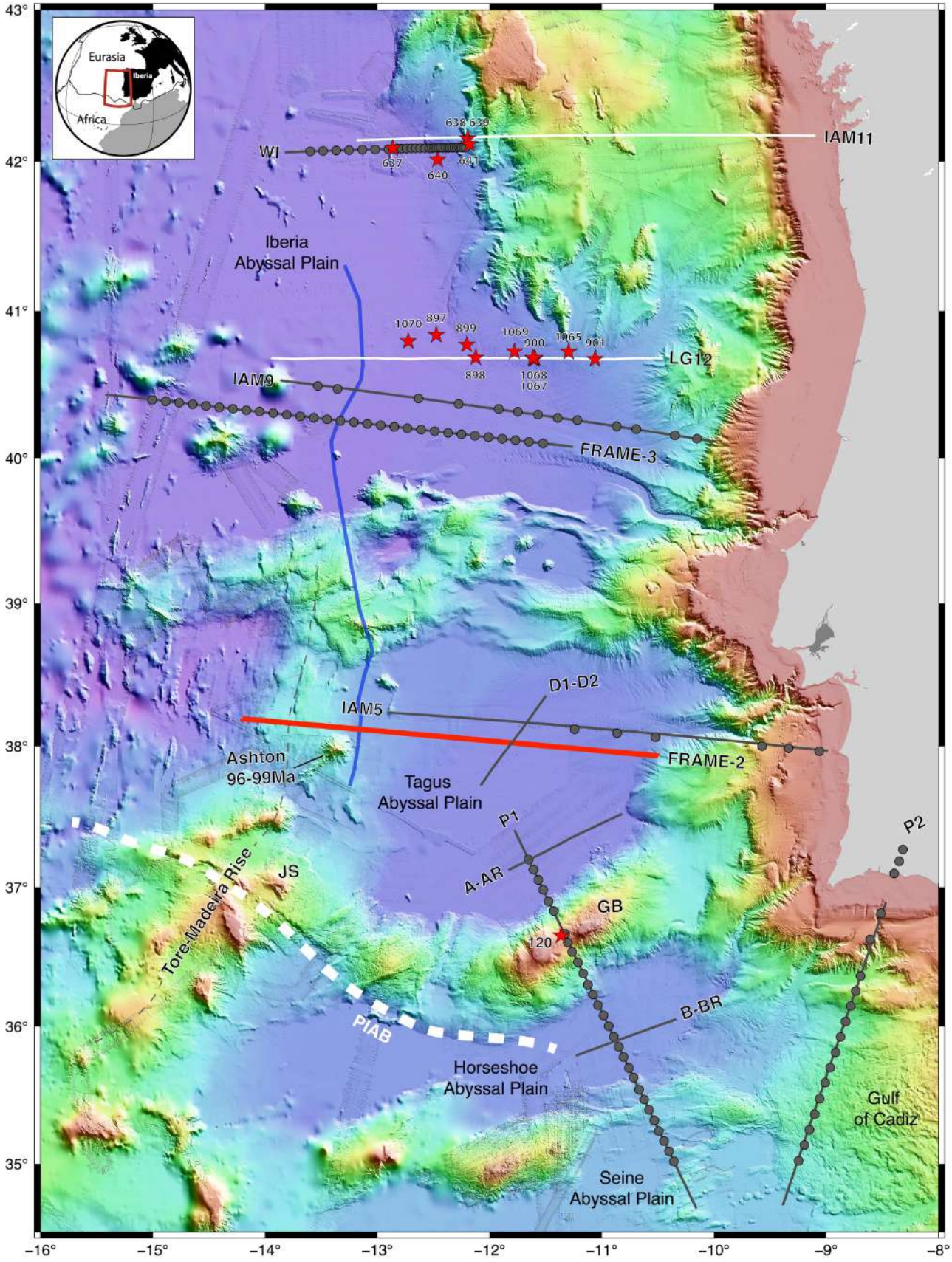
Eurasia
Iberia
Africa
WI
IAM11
638
639
637
641
640
Iberia
Abyssal Plain
1070
897
899
1069
1065
901
900
LG12
898
1068
1067
IAM9
FRAME-3
D1-D2
IAM5
FRAME-2
Ashton
96-99Ma
Tagus
Abyssal Plain
P1
P2
A-AR
JS
Tore-Madeira Rise
GB
120
B-BR
PIAB
Horseshoe
Abyssal Plain
Gulf
of Cadiz
Seine
Abyssal Plain
43°
42°
41°
40°
39°
38°
37°
36°
35°
−16°
−15°
−14°
−13°
−12°
−11°
−10°
−9°
−8°

◄ *Figure 9.1 - Bathymetric map of the West Iberia margin showing the seismic profiles acquired in the region. Red line corresponds to the MCS profile acquired during the Leg-1 (FRAME-2018 survey). Black lines correspond to WAS profiles previously acquired in the area and referred to in the text, from S to N: P2 and P1 (NEAREST survey; Sallarès et al. 2011; 2013), A-AR and B-BR (Purdy, 1975), D1–D2 (Discovery Cruise 161; Pinheiro et al., 1992), IAM5 (Iberian Atlantic Margins project; Afilhado et al., 2008), FRAME-3 (FRAME survey; Grevemeyer et al. 2020, in prep.), IAM9 (Iberian Atlantic Margins project; Dean et al., 2000) and WI (Galicia 3-D survey; Davy et al. 2016). White lines correspond to MCS profiles from the following surveys: Lusigal-12 (LG12) (Beslier, 1996) and IAM 11 (Banda, E. et al., 1995). Red stars indicate ODP and DSDP sites locations. Blue line indicates the location of the J-anomaly along the margin (Srivastava, et al., 2000). Red line displays the location of FRAME-2 MCS profile. Abbreviations: GO: Gorringe bank, JS: Josephine Seamount, PIAB: Paleo Iberia-Africa boundary.*

scale studies, they are basically a series of 1D velocity models under each OBS, that are interpolated to create 2D maps.

In this chapter, we perform a characterisation of the TAP crustal features based on the observations and tectonic analysis of the FRAME-2 (2018) MCS profile, acquired with the objective of imaging the entire crustal structure. The MCS time-migrated sections are then combined with the information provided by the seismic velocity models to interpret the seismic images. The Vp model has been converted to two-way time (TWT) (Fig. 9.2b) and overlain on the seismic image to directly compare the structure obtained by the two methods. Overall, there is a remarkably good correspondence between structures in both images, but the two methods map the structures in different ways, providing complementary information on the nature of rocks forming the domains.

The main objectives of this chapter are: (i) To characterize the different types of crust within the Tagus Abyssal Plain and (ii) To explain the basin configuration taking into account the different crustal structures identified.

9.1. Geological setting

The Tagus Abyssal Plain and its conjugate margin have not been drilled to date. In addition, they have been much less investigated by geophysical methods than the margins to the north of the West Iberia margin. Afilhado et al. (2008) modelled a wide angle and near vertical seismic data along the IAM-5 MCS and in their interpretation, they suggested that nearly the entire TAP is underlain by oceanic crust. To the east of ~10.5°W they recognised an approximately 40 km wide zone that they identified to constitute the COT, interpreted to be floored by exhumed serpentinized mantle rocks similarly to that identified further north in the Iberia Abyssal Plain. However, the COT in the TAP are here rather narrower than the exhumed serpentinized mantle zone in the Iberia Abyssal Plain.

The interpretation of the transect proposed by Afilhado et al. (2008) for the TAP, along the IAM-5 seismic line, is in contradiction with previous interpretations by other authors, who propose that the whole extent of the crust at the TAP is made of oceanic crust (Mauffret et al., 1989, Srivastava et al., 2000) or transitional crust (Rovere et al., 2004). Although indicating different locations for the COT, both Pinheiro et al. (1992) and Afilhado et al. (2008) conclude that the transitional basement extends over a narrow zone in the TAP. The interpretation of the different crustal/lithosphere domains have

important consequences on the proposed ages for the earliest ocean floor and for plate reconstruction models, as shown by the difficulties of closing the conjugate margins using only the unquestionable domains of conjugate continental crust (Klitgord and Schouten, 1986, Olivet, 1996, Srivastava et al., 2000, Sibuet et al., 2004).

Besides, based mainly upon the Mesozoic–Cenozoic seismic stratigraphy, Mauffret et al. (1989) and Mougenot (1989) interpreted the whole extent of the Tagus Abyssal Plain as oceanic crust and proposed a COT located near the foot of the continental slope, at ~ 11°W. They also suggested that the deep basement beneath the eastern Tagus Abyssal Plain was generated in the Late Jurassic, before a ridge jump that left original oceanic crust adjacent to the Iberia margin. Although not considering a ridge jump, Srivastava et al. (2000) suggested a similar nature for the Tagus Abyssal Plain crust, identifying the M20 magnetic anomaly close to the foot of the continental slope.

9.2. Data Set

The multi-channel seismic reflection profile FRAME-2 acquired during the FRAME cruise is the base of this chapter as it allows us to image the crust and the upper mantle across the whole Tagus Abyssal Plain. The processing of this seismic data has been designed to image the deeper part of the basins while keeping a relatively good resolution in the sedimentary units (see Chapter 3: *Multi-Channel reflection Seismic data)*. In addition, we have the information from the Vp velocities all along the profile from the Vp model obtained in the previous chapter, Chapter 8. We have converted the Vp model in TWT in order to directly compare the seismic structure from the MCS profile and the velocity distribution obtained in the travel-time tomography model.

The location of the seismic profiles discussed in this chapter is shown in Figure 9.1.

◄ *Figure 9.2. - (a) Time-migrated MCS line overlaid with geometry of the horizons inverted by travel-time tomography (yellow lines for the unconformity, white line for the top of the basement and dashed black line for the Moho boundary). (b) MCS image of the profile overlaid with the 2D P-wave Vp model converted to TWT. The inverted horizons are also displayed in this figure. Yellow circles show the OBS/OBH location. Scale: 1:2. (c) Interpreted cross section along the FRAME-2 profile. The interpretation is based on the 2-D P-wave Vp model (Fig. 8.3a in Chapter 8) and the corresponding basement affinity based on comparison with reference 1D Vp-depth profiles (Fig. 8.6 in Chapter 8) and the tectonic structure from the MCS image of Fig. 9.2a. Black lines showing isovelocity contours at 7.0, 7.5 and 8.0 km/s. Main faults are also represented. PRS: post-rift sediments, CC: continental crust, OC: oceanic crust, EM: exhumed mantle and UM: upper mantle. Red circles show the OBS/OBH location.*

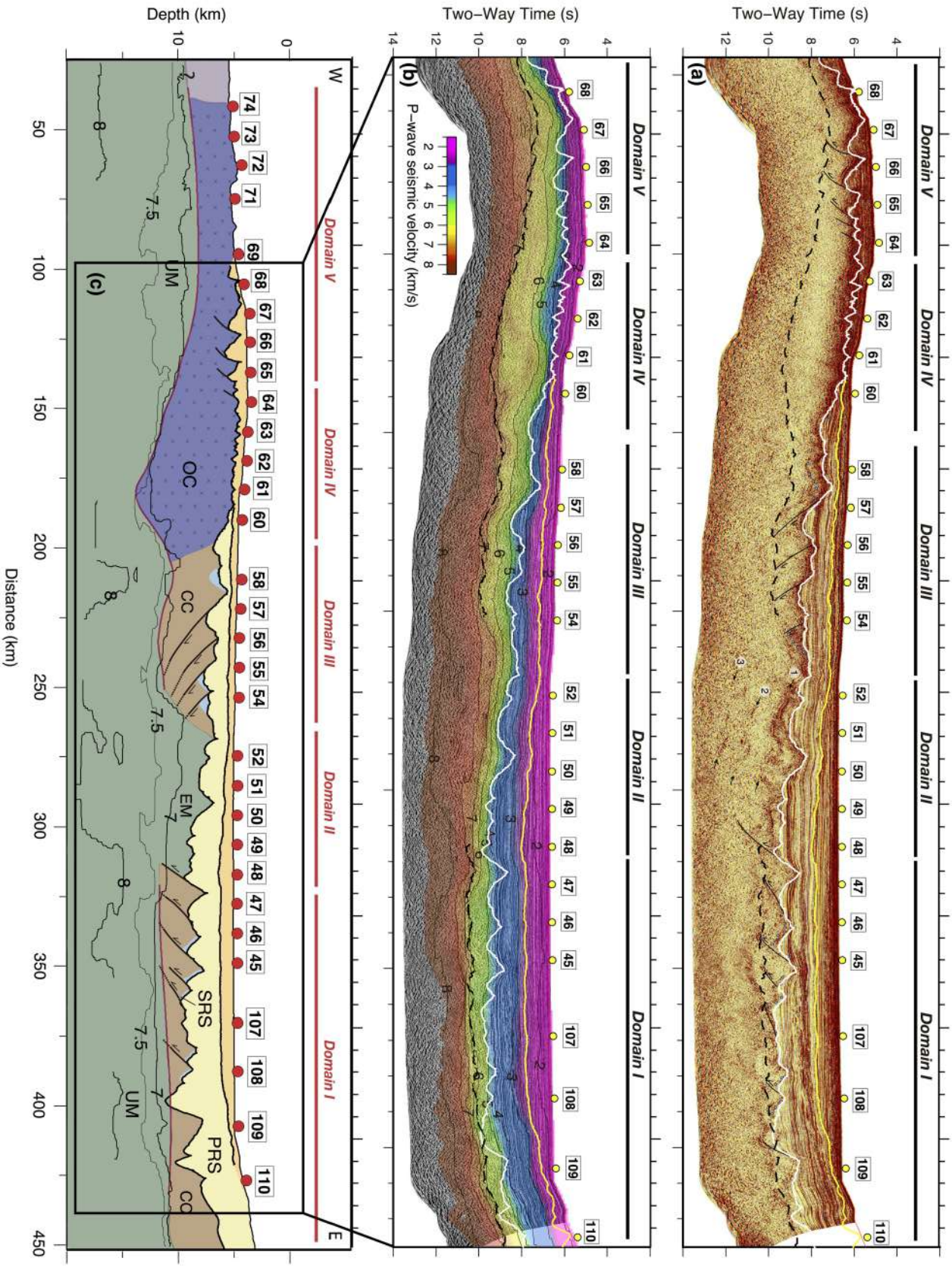
(a)
(b)
(c)
Two–Way Time (s)
CMP
Domain V
Domain IV
Domain III
Domain II
Domain I
P-wave seismic velocity (km/s)
Depth (km)
Distance (km)
W
E
OC
CC
EM
SRS
PRS
UM

9.3. Seismic character of the basement

FRAME-2 is a ~330-km-long W–E transect that crosses the Tagus Abyssal Plain and the Madeira-Tore Rise (15.2°W), and reaches the continental slope (10.2°W) at approximately 38°N (Fig. 9.1). The interpretation of the seismic images is supported by the information provided by the Vp model along the co-located wide-angle seismic profile (Chapter 8). The combination of both type of data that provide robust information to define the lithological nature of the different basement domains. The lack of clear kinematic markers prevents a detailed knowledge of the opening direction. However, the line was collected striking parallel to the assumed flow line direction, and therefore overall the seismic records should provide images of the true geometry of the crustal structure (Srivastava et al., 2000).

The post-stack time-migrated profile images the sediment cover, the tectonic fabric, and intra-basement reflectivity with dipping and sub-horizontal events in the upper and lower crust above possible Moho reflections, as well as intra-mantle reflections (Fig. 9.2a). The sediment cover contains strata that are dominantly sub-horizontal and extend for tens of km, indicating their post-rift character (Fig. 9.2). There are a few restricted packages directly overlaying basement that display tilted layers and may thus correspond to syn-rift deposits (Fig. 9.2a,c). The post-rift sediment is divided in two main units separated by a regional angular unconformity. From east to west, sediment thickness varies considerably. The sediment infill ranges from ~3 km at the eastern sector of the profile and 5-6 km under the lowermost slope, to 7-8 km above the deepest basement under central TAP, and thins towards the Madeira Tore rise to <1km thickness (Fig. 9.2c). The lower post-rift unit laps on the basement and pinches out towards the west, where the basement relief is higher. Much of the sediment cover is tilted under the lower continental slope, which occurs across the region resulting from Tertiary contractional deformation (Afilhado et al. 2008). The initial pulse deforming the margin may have caused the regional angular unconformity under the TAP (Fig. 9.2a).

Based on variations in the vertical and horizontal Vp and density structure (Chapter 8, section 8.5.1.), we interpret that the basement is divided in five different domains that have a clear correspondence in the reflective character of the seismic image.

The TWT-converted Vp model is overlaid on the MCS images to compare the structures imaged by the two methods (Fig. 9.2b). The combined seismic image gives information on the relationship between tectonics and nature of basement rocks. The basement displays different types of reflectivity and tectonic structure that also define five domains. Following the characterization based on Vp structure we distinguish: Domain I, made of thin continental crust, Domain II of exhumed mantle, Domain III of continental crust, and Domains IV and V of oceanic crust, denoted as the J-anomaly and the Cretaceous Quiet Zone, respectively. We use the time-migrated MCS section to interpret the tectonic evolution of the domains of the basin, whereas the Vp model and the Moho inverted from wide-angle PmP reflections provide a proxy to interpret the intra-basement reflections in the seismic image that would have been unconstrained otherwise.

9.3.1. Domain I: ultra-thin continental crust

Domain I extends under the lower continental slope and ~90 km to the east under the TAP (Fig. 9.2a, CMPs 100 – 18000).

The MCS image displays a continuous boundary that correspond to the top of the igneous basement (TOB), coincident with a sharp increase in seismic velocity (Fig. 9.3). The TOB delineates the change between the overlying well-stratified reflections and a body with discrete reflectivity interpreted as the upper crystalline crust. The TOB appears as a relatively low to medium amplitude reflective boundary visible along the whole domain. Its irregular relief ranges from a few hundred meters to ~4 km offset.

A set of indistinct reflections agrees with the position of the wide-angle Moho converted to TWT (Fig. 9.3). Without the support of the Vp model it would appear highly speculative to interpret the base of the crust on the seismic image. We however interpret a continuous continental Moho defined by variable amplitude, discontinuous sub-horizontal events 5-10 km-long, at ~10 s TWT about 0.7–1s TWT underneath the TOB (Fig. 9.3). The changes in TOB relief and Moho geometry define basement blocks B1 to B11, which we interpret as fault blocks (Fig. 9.3). The geometry of B1-B11is generally asymmetric with the west flank either steeper or longer than the east flank. The east flank is in most blocks defined by a thin wedge-shaped unit that possibly represents syn-tectonic sediment deposits (Fig. 9.3). The interpretation of the west flank as the exhumed fault plane produces a congruent interpretation of tilted blocks by faults f1 to f11 of different geometry and dimensions. The interpreted faults are mapped by short intra-basement dipping reflections that project up-dip to the west flanks of basement blocks (i.e. exhumed fault segment), reinforcing the interpretation.

Most faults including f1-f3, f5, f8, f9 and f11 dip ~40°-50°, have variable vertical offset that does not exceed ~1 s TWT, and ~1-5 km heave (Fig. 9.3a). The corresponding blocks are ~5-10 km wide and 3-6 km thick. Larger blocks are cut by somewhat steeper faults with larger vertical offset (e.g. B3, B5 and B9 in Fig. 9.3a).

A second group of faults f4, f6, f7 and f10 are characterized by comparatively gentler dip angles of the exhumed fault segment and heaves of ~5-7 km, which are proportionally much greater than their <0.5 s TWT vertical offsets. Their geometry implies comparatively large rotation and accumulated extension. They bound elongated basement blocks with a geometry that possibly indicates intense internal deformation, although it is unresolved in the seismic images. Faults f4, f6 and f10 stopped movement close before mantle unroofing (Fig. 9.3a).

The mantle displays an upper <~1 s TWT thick region largely featureless that is underlain by a zone of pervasive landward-dipping reflections of moderate amplitude (IMR, Intra Mantle Reflections, in Fig. 9.3). The ~1-3 km-long dipping events align to form a pervasive pattern particularly clear between CMP 7000 – 15000. The change between the upper and lower zones is not sharp but it roughly agrees with the increase to Vp > 8.0 km/s (Fig. 9.3b).

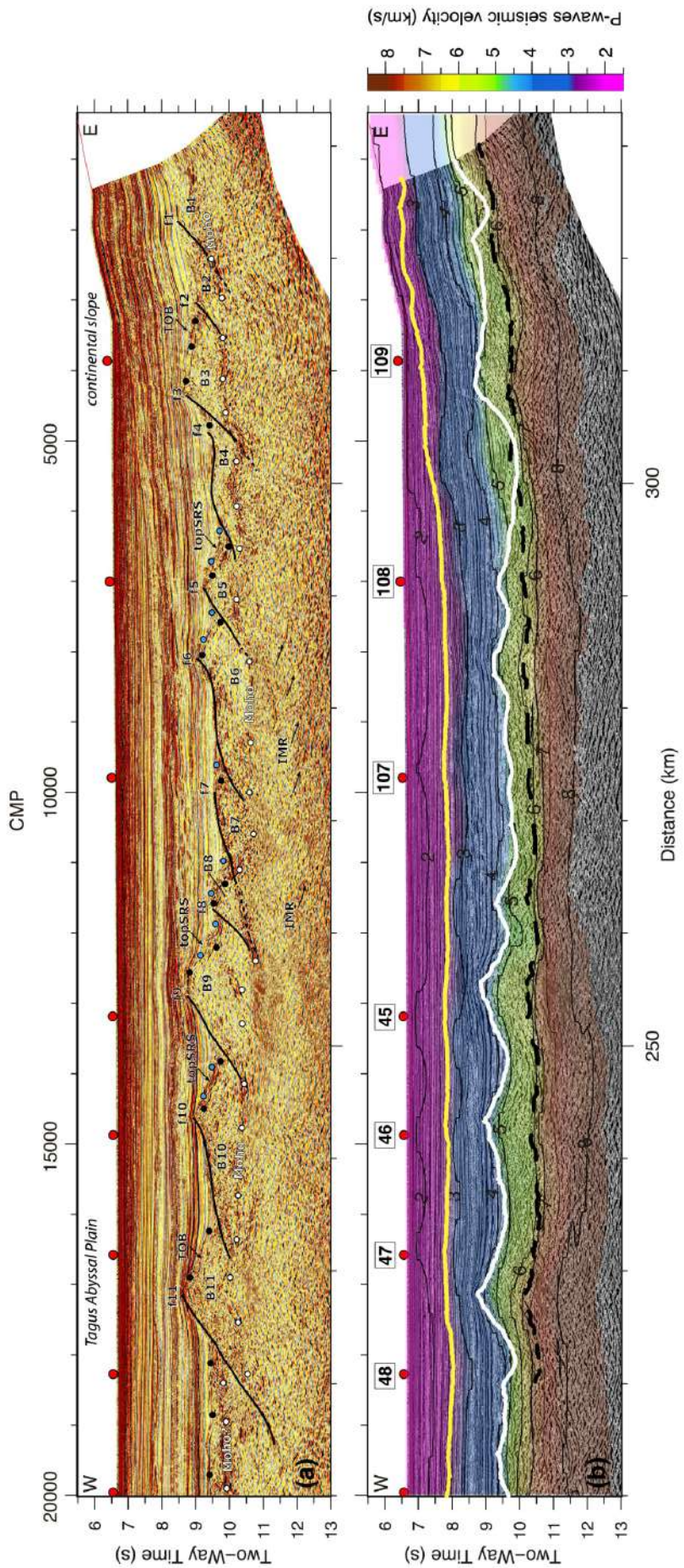

Figure 9.3 - Close-up of Domain I of post-stack time migration of profile FRAME-2. Vertical exaggeration is of ~x:1 taking into account basement velocities. Red circles display the location of the OBSs and OBHs along the domain. (a) Tectonic interpretation of the crust along this section. It is mainly represented by seaward normal faults (black lines). The top of the basement is displayed with black dots and the Moho with white dots. The top of the syn-rift sediments is displayed with blue filled dots. Abbreviations: topSRS: top syn-rift sediments; TOB: top of basement; IMR: intra-mantle reflections; B#: block; f#: faults. (b) Same seismic reflection line as (a) overlaid with the P-wave velocity model converted to TWT. Inverted horizons are also displayed (yellow line for the unconformity, white line for the top of the basement and dashed black line for the Moho boundary). Note the excellent correlation between the interpreted horizons (specially the TOB and the Moho) along the MCS profile and their counterpart obtained by travel-time tomography.

9.3.2. Domain II: exhumed mantle

The Vp-depth distribution in Domain II, characterized by a strong vertical gradient, together with the lack of clear Moho reflections, supports that this domain is fundamentally made of exhumed mantle, partially serpentinized in the upper 6-8 km (Chapter 8, section 8.5.1.). The TOB has an irregular and complex relief delineated by a high-amplitude continuous reflection (Fig. 9.4). In spite of the ~2 km relief of the central high, the rather smooth relief along this domain makes it is difficult to interpret exhumed fault planes and fault blocks across the entire domain.

The basement is characterized by a complex internal reflectivity. It displays three sets of events forming reflectivity bands at different depths (IBRs, Intra Basement Reflections, in Fig. 9.4). The shallowest reflectivity band is a complex lateral succession of events of variable amplitude ~0.3-1s TWT under TOB (Fig. 9.4a). The reflectivity occurs where Vp rapidly increases with depth from ~5 km/s near the TOB to 6.5 km/s or locally ≤7.0 km/s, roughly coincident with some of the reflections (Fig. 9.4b). Some single events can be traced for ~10 km, but mostly they are a few km long and collectively roughly mimic the TOB geometry. Some of these reflections undulate towards the TOB and appear to delineate the geometry of thin rocks slivers. The relatively low Vp and restricted dimensions of some of the uppermost rock bodies makes feasible the presence of thin laterally-restricted continental slivers overlaying this domain of exhumed mantle. However, no reflectivity patter can be easily interpreted as syn-rift sediment deposits. A second reflectivity band is located ~2s TWT below the basement top. These IBRs is formed by a group of short reflections that delineate longer features extending for ~20 km (CMPs 21000 – 25000), dipping east from ~10.2 to ~11 s TWT. This second group of laterally discontinuous events occurs at Vp ~7.8 km/s and roughly delineates the base of the basement region where Vp changes with depth. The third group of IBRs deepens eastward from 11-12 s TWT at ~3 s TWT below TOB and roughly parallel to the overlaying IBRs band. This third reflectivity level occurs near the 8.0 km/s velocity contour (Fig 9.4b). The two deepest reflectivity bands are deeper than the Moho imaged and determined in the Vp model of the adjacent Domain I and Domain III.

The correspondence of the second band of reflections and the base of the steep gradient of Vp-depth change might indicate that the reflection is related to changes in the serpentinization degree (Fig. 9.4b). The reflections at ~12 s TWT could be interpreted as the crust-mantle because they roughly coincide with the 8<Vp> 8 km/s change. However, the overlaying relatively high 7.0<Vp<8.0 km/s in the several km above the reflections do not support that the third and deepest band of reflectivity may represent the base of the petrological continental or oceanic crust, but rather the base of the serpentinized mantle layer. It is however unclear whether the serpentinized mantle stops abruptly with depth to be able to form an abrupt Vp contrast.

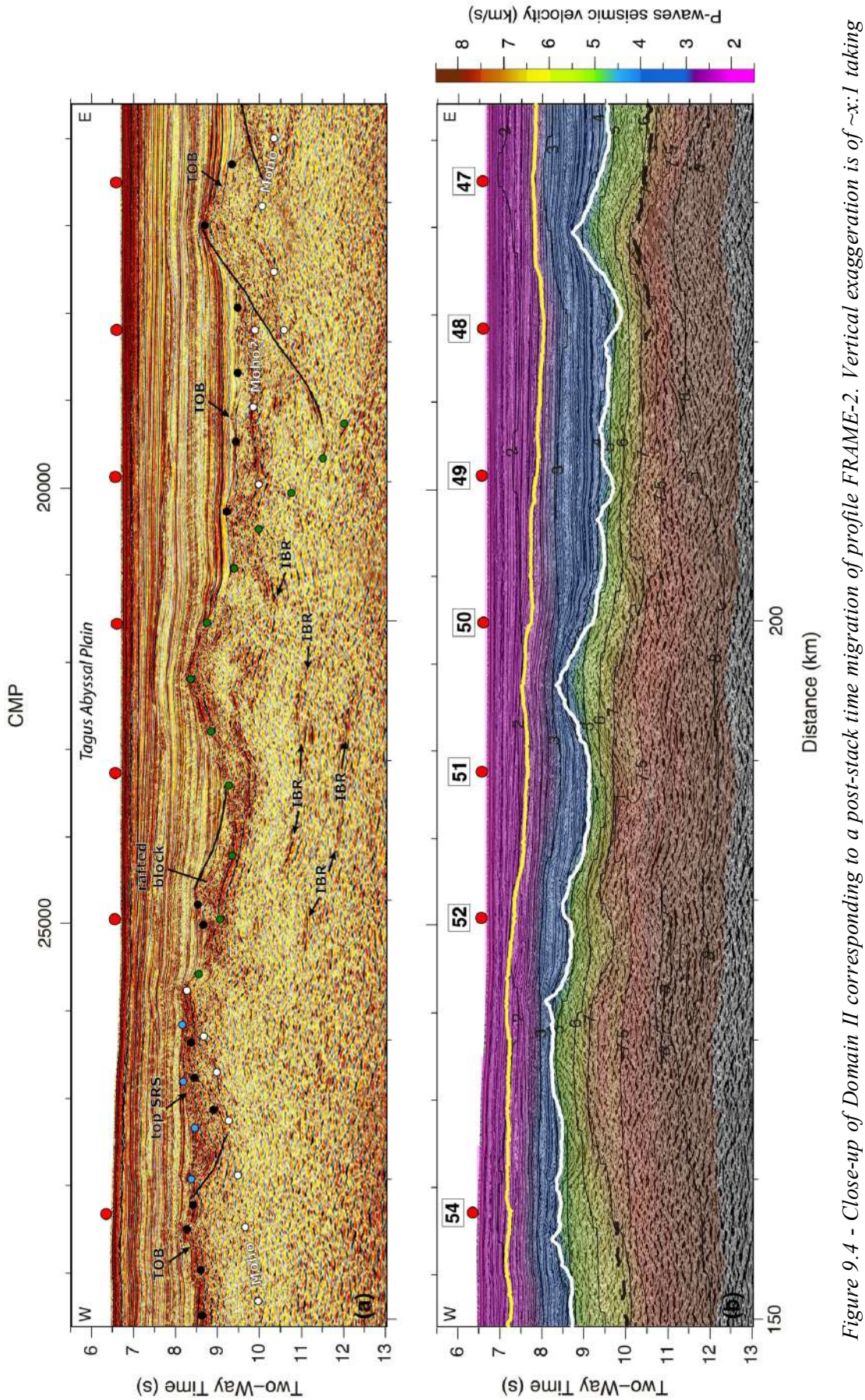

Figure 9.4 - Close-up of Domain II corresponding to a post-stack time migration of profile FRAME-2. Vertical exaggeration is of ~x:1 taking into account basement velocities. Red circles display the location of the OBSs and OBHs along the domain. (a) Tectonic interpretation of the crust along this section. The top of the basement is displayed with black dots and the Moho with white dots. The top of the syn-rift sediments is displayed with blue filled dots. Green dots represent a detachment fault. Abbreviations: topSRS: top syn-rift sediments; TOB: top of basement; IMR: intra-mantle reflections. (b) Same seismic reflection line as (a) overlaid with the P-wave velocity model converted to TWT. Inverted horizons are also displayed (yellow line for the unconformity, white line for the top of the basement and dashed black line for the Moho boundary). Note the excellent correlation between the interpreted horizons (the unconformity and the TOB) along the MCS profile and their counterpart obtained by the tomographic inversion.

9.3.3. Domain III: ribbon of continental crust

Domain III is located in between CMPs 25500 – 37000 (Fig. 9.2a) and it extends through the western most part of the TAP. The Moho has been constrained in the Vp model up to OBS54 (km ~160) and we have extended it further east based on the MCS image (Fig. 9.4a). This is supported by the high underlaying velocities that we associate to mantle rocks (7.0-8.0 km/s) between CMPs 28300 – 25800 (Fig. 9.4b) with a thin sliver of continental crust overlain by syn-rift sediment (Fig. 9.4a).

The TOB is imaged as a high-amplitude reflection at 7-8 s TWT. It has an irregular topography characterized by smooth segments offset at several locations. The images show several packages of restricted length with internal reflectivity that can be interpreted as syn-rift sediment (Fig. 9.5a) with 5<Vp<6 km/s (Fig. 9.5b) over blocks B1, B4 and B5. This unit is filling the accommodation space created by faults f1 and f4, respectively, and deposit size increases at the deepest part of fault-controlled local depocenters. Blocks are cut by normal faults dipping eastwards that can be traced ~2 s TWT into the basement (Fig. 9.4a). Assuming an average Vp of ~6 km/s the faults are mostly planar and dip ~40°-50°, but they show negligible heave and vertical offset; regardless of the large ~10 km wide rotated blocks they are bound. Block size in Domain III decreases toward the centre of the basin (from B1 to B5, Fig. 9.5a) accompanied by a decrease in fault spacing and displacement of the faults (see f1 to f4, Fig. 9.5a). The elongated and smooth shape of the rotated blocks could represent an imaging problem due to the obliquity of the line with respect to the strike of the tectonic structure. Since the seismic line is straight, the obliquity would imply a relative change in orientation of the tectonic fabric of Domain III.

Indistinct sub-horizontal reflections ~1.5 s TWT-long beneath TOB agree with the Moho inverted with the wide-angle seismic data (Fig. 9.5b). The Moho reflections constrain basement thickness to ~4.5-5.0 km. Between CMPs 34000 – 37000, the Moho is located at a depth of 9s TWT. To the east, under CMPs 33000 – 34000, it deepens to ~10s TWT by the offset along fault f1 (Fig. 9.5b). Westwards and for the next 4.000 CMPs, the Moho boundary remains mostly sub-horizontal. Although Moho is poorly constrained between CMPs 28300 – 25800, faint reflections may indicate shallowing from 10s to 9s TWT along ~20km.

To the east of the domain, several sub-horizontals to shallow dipping ~5-7-km-long reflections (IMRs) occur in the uppermost mantle, ~1s TWT beneath the calculated Moho (Fig. 9.5a).

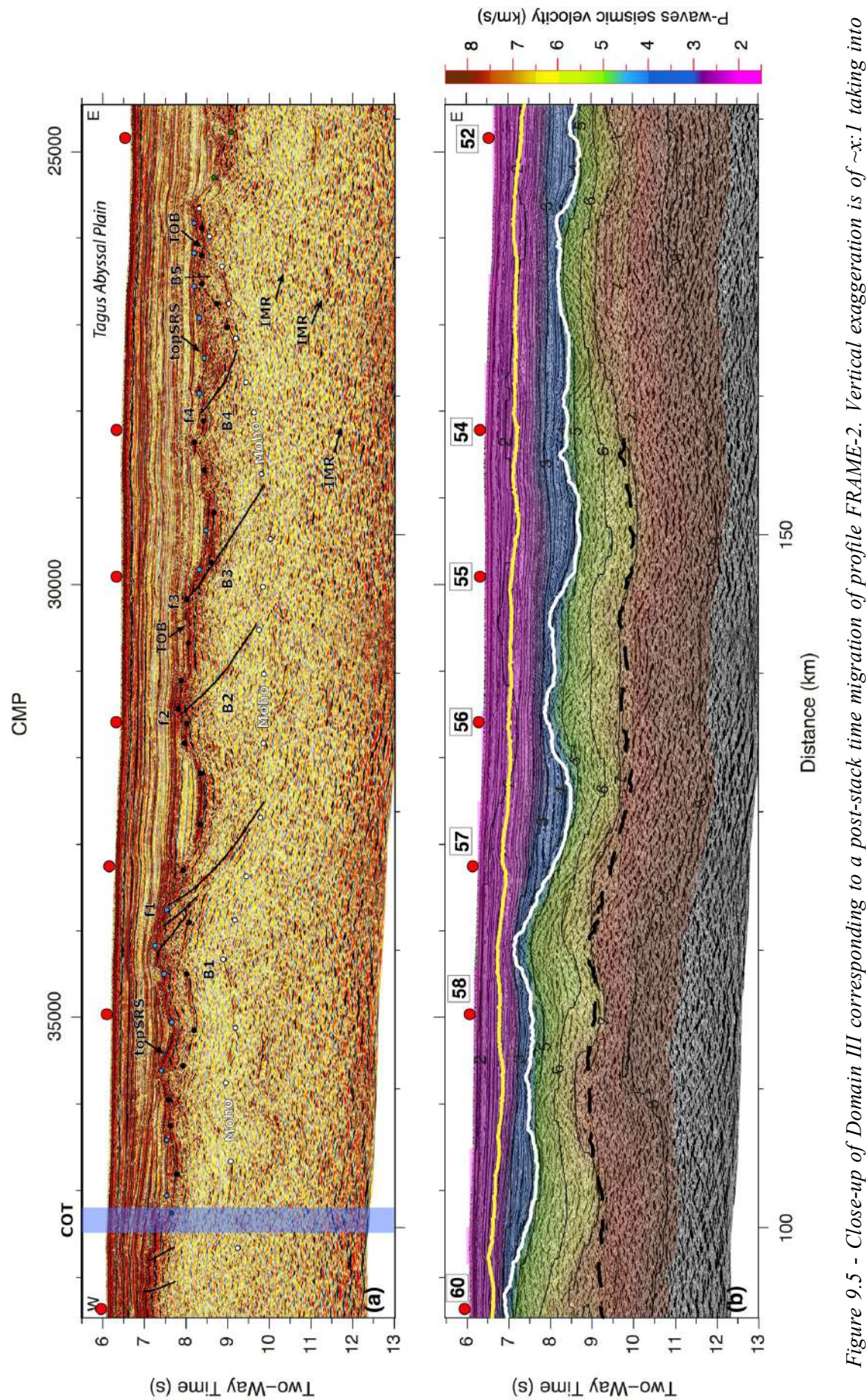

Figure 9.5 - Close-up of Domain III corresponding to a post-stack time migration of profile FRAME-2. Vertical exaggeration is of ~x:1 taking into account basement velocities. Red circles display the location of the OBSs and OBHs along the domain. (a) Tectonic interpretation of the crust along this section. It is mainly represented by landward normal faults (black lines). The top of the basement is displayed with black dots and the Moho with white dots. The top of the syn-rift sediments is displayed with blue filled dots. The COT zone is represented by a blue band. Abbreviations: topSRS: top syn-rift sediments; TOB: top of basement; IMR: intra-mantle reflections; B#: block; f#: faults. (b) Same seismic reflection line as (a) overlaid with the P-wave velocity model converted to TWT. Inverted horizons are also displayed (yellow line for the unconformity, white line for the top of the basement and dashed black line for the Moho boundary). Note the excellent correlation between the interpreted horizons (specially the TOB and the Moho) along the MCS profile and their counterpart obtained by the tomographic inversion.

9.3.4. Domain IV: J-anomaly

Domain IV is located between CMPs 38000 – 53000 across the eastern slope of the Madeira-Tore Rise, which forms the west flank bounding the TAP (Fig. 9.2a). Based on the Vp distribution, Domain IV is interpreted to be formed by oceanic crust (Chapter 8, section 8.5.1.).

Domain IV images display a different reflective character from Domains I-III. The TOB is not a sharp reflection but a band of reflectivity of variable amplitude forming a unit that is ≤~1 s TWT thick (Fig. 9.6a). This band of reflectivity is continuous along most of the domain, for about ~35 km, ranging from ~1 s TWT maximum thickness around CMP 42000 and laterally thinning towards both domain edges until it pinches out. The TOB unit in this domain displays a complex stratigraphy, but it shows a smooth and relatively continuous topography and gradual lateral changes in thickness. The TOB unit at the centre of the domain (Fig. 9.6a CMPs 39000 – 43000) shows an irregular reflectivity characterised by short segments forming a sub-horizontal pattern possibly formed by a complex succession of overlapping seafloor-spreading related volcanic units, each whit a ~0.1 s TWT thickness. Domain IV is next to a large post-spreading volcano (Fig. 9.1) and a 0.1-0.2 s TWT possibly volcanoclastic sequence covers the complex TOB stratigraphy (Fig. 9.6).

The basement image is largely featureless, devoid of clear reflections from the Moho boundary, to match the Moho boundary defined from wide-angle data (green dots in Fig. 9.6b). The Moho is located at ~9.2 s TWT between CMPs 39000 – 41200, where a ~3 s TWT basement is thickest across the region (Fig. 9.6a). Towards the west, the Moho shoals from 9.2 to 8.0 s TWT, in parallel to the shoaling of the TOB under the flank of the Madeira-Tore Rise with a roughly constant crustal thickness. There is no evidence of either significant rotation of strata or faulting or abrupt crustal thinning, and no fault blocks have been interpreted.

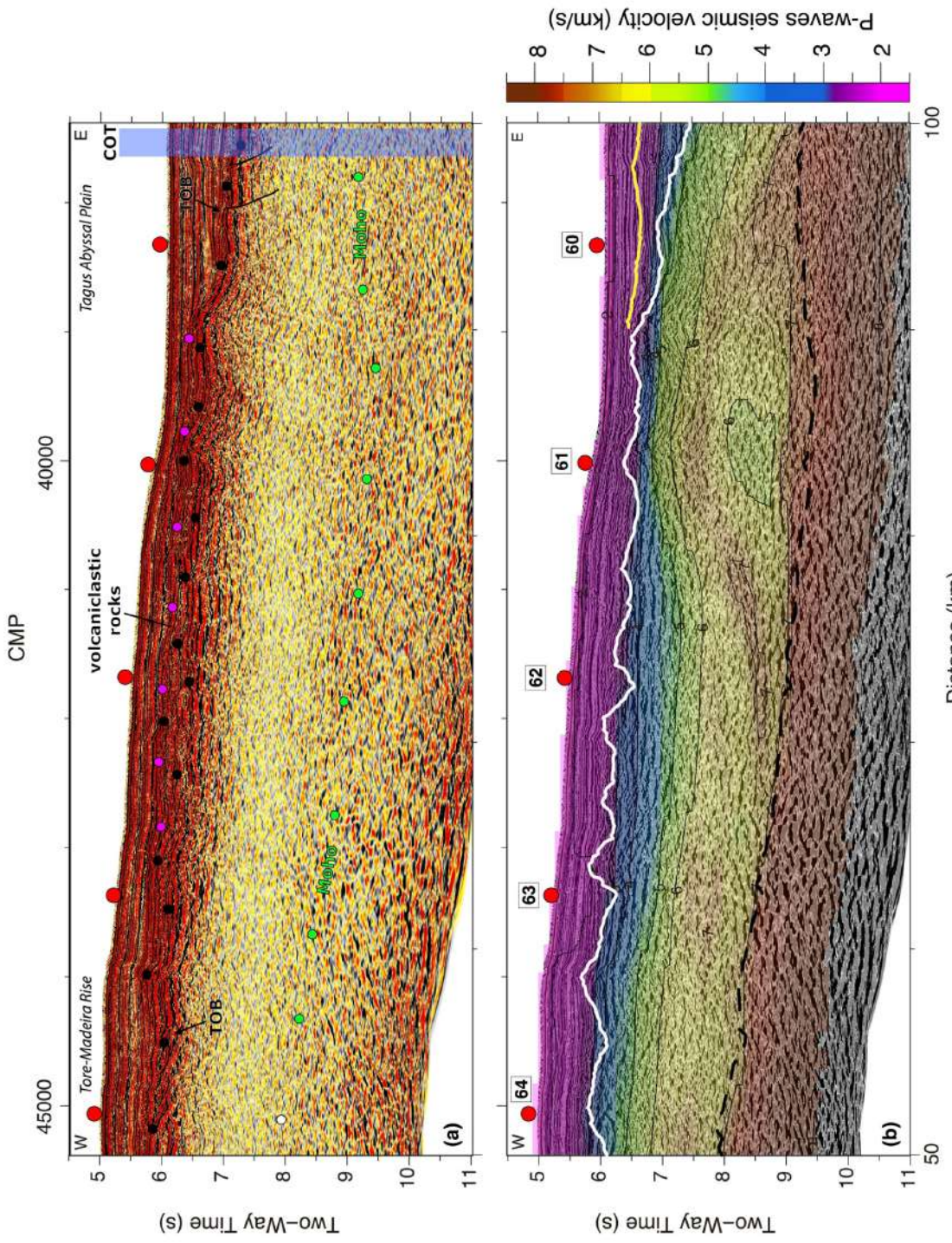

Figure 9.6 - Close-up of Domain IV corresponding to a post-stack time migration of profile FRAME-2. Vertical exaggeration is of ~x:1 taking into account basement velocities. Red circles display the location of the OBSs and OBHs along the domain. (a) Tectonic interpretation of the crust along this section. This domain doesn't show important tectonic activity. The top of the basement is displayed with black dots. The Moho is displayed with light green dots because it cannot be identified in the MCS image and its position is inferred from the inverted Moho (Chapter 8, Fig.8.3a). Pink dots display the top of volcanoclastic rocks unit. Abbreviations: TOB: top of basement. (b) Same seismic reflection line as (a) overlaid with the P-wave velocity model converted to TWT. Inverted horizons are also displayed (yellow line for the unconformity, white line for the top of the basement and dashed black line for the Moho boundary). Note the excellent correlation between the interpreted TOB along the MCS profile and its counterpart obtained by the tomographic inversion.

9.3.5. Domain V: the oceanic Cretaceous Magnetic Quiet Zone

Domain V extends from CMP 45000 to the west end of the profile and corresponds to the western flank of Madeira-Tore Rise (Fig. 9.1 and 9.7a). Wide-angle velocity supports that it is made of 2-5 km thick ocean crust (Chapter 8, section 8.5.1.).

In contrast to Domain IV, the TOB is a sharp boundary delineated by bright reflections (e.g. CMPs 45000 – 51500) forming an irregular relief with 2-9 km long segments tilted landward (Fig. 9.7a). The TOB segments define clear basement offsets that require normal faults dipping west (Fig. 9.7a). Faults f1-f5 increase westward with vertical offset from ~0.2s TWT (~0.4 km) to almost 1s TWT (~1.8 km). Faults f4-f5 appear to cut until Moho and with the laterally complex TOB relief and associated lateral Vp changes produce a locally undulating Moho geometry.

The Moho image is discontinuous and of variable amplitude laterally. It is delineated by reflections 0.5-1 km long at ~0.7-1.0 s TWT under the TOB. The Moho boundary determined from the Wide-Angle Seismic (WAS) data (Fig 9.7b) is smoother than the undulating boundary interpreted in the seismic image, possibly due to lateral resolution limitation (Fig 9.7a). 4-5 km thick oceanic crust cut by normal faulting under the flat top of the Madeira-Tore Rise gradually thins to 2-3 km under the western flank with complex short wavelength TOB relief possibly indicative of faulting (Fig. 9.7a).

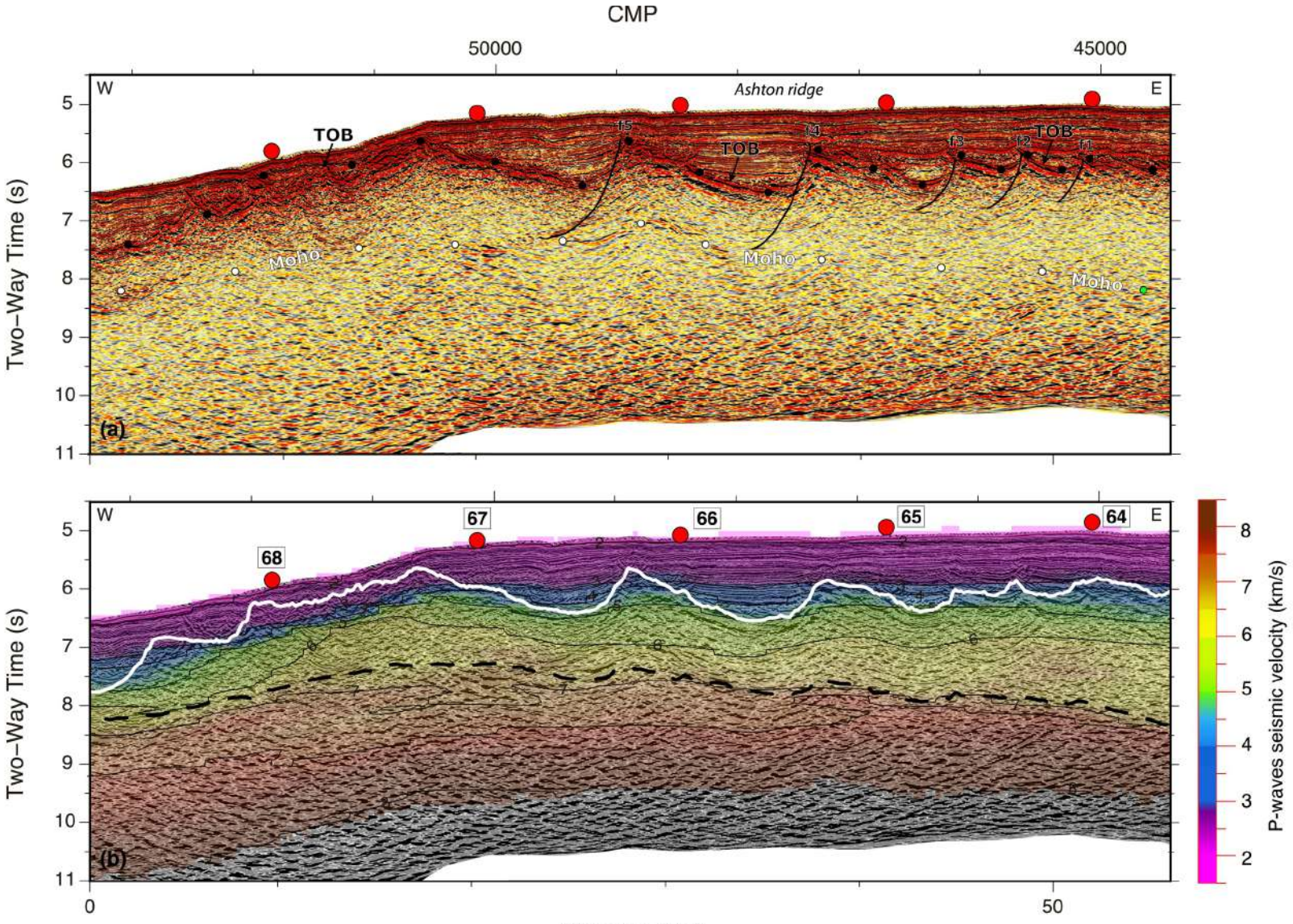

Figure 9.7 - Close-up of Domain V corresponding to a post-stack time migration of profile FRAME-2. Vertical exaggeration is of ~x:1 taking into account basement velocities. Red circles display the location of the OBSs and OBHs along the domain. (a) Tectonic interpretation of the crust along this section with normal faults dipping westwards (black lines). The top of the basement is displayed with black dots and the Moho with white. Abbreviations: TOB: top of basement. (b) Same seismic reflection line as (a) overlaid with the P-wave velocity model converted to TWT. Inverted horizons are also displayed (white line for the top of the basement and dashed black line for the Moho boundary). Note the excellent correlation between the interpreted horizons (specially the TOB and the Moho) along the MCS profile and their counterpart obtained by the tomographic inversion.

9.4. Discussion

The combination of the MCS image and WAS-based Vp model show that the tectonic structure, syn-rift deposits and basement reflectivity patterns along the FRAME-2 transect agrees well with the existence of five domains previously inferred from travel-time tomography (Chapter 8, section 8.4). These domains are the following ones: (I) 3-6 km thick continental crust under the lower continental slope extending to deep TAP; (II) exhumed mantle; (III) a ribbon of continental crust; (IV) 6-8 km thick oceanic crust coincident with the J magnetic anomaly; and (V) 2-5 km thick faulted oceanic of the Cretaceous Magnetic Quiet Zone (Fig. 9.2). In this section, we will discuss the evolution of these domains integrating the Vp model information with the seismic images to establish a general rift to seafloor spreading model for the Tagus Abyssal Plain.

9.4.1. Continental crustal thinning

The two domains of continental crust (I and III) exhibit a progressive basement thinning towards the centre of the basin and display conjugate sets of normal faults. We propose that they were part of the same rift system, with different degrees of extension. Higher extension affected Domain I basement with >100 km of rather constant ultra-thin continental crust (3-5 km thick), with basin-ward dipping normal faults (Fig 9.3), whereas Domain III displays sharper lateral changes in thickness but more subdued normal faulting with smaller apparent offset (Fig. 9.5). Syn-tectonic sediment depocenters appear related to the amount of thinning.

The relationship between block size and faulting style in Domain I suggests a causal relationship. Thicker blocks were cut by faults with the largest vertical offset and that stopped rotating at ~45º (Fig. 9.3a). Thinner but longer blocks were cut by faults with comparatively larger heaves and low-angle exhumed segments that resemble detachment fault geometries. However, neither high-angle nor detachment faults seem to be the preferred location where to encounter serpentinized mantle. Thus, we believe that the faulting style does not appear to be correlated with the formation of serpentine and consequently with the arrival of water to the upper mantle. We see this serpentinization throughout Domain I through relatively low upper mantle velocities (7.0-8.0 km/s) from 10 to 15 km depth and along ~100 km (Fig. 9.3b).

Observations off Iberia support that during the extension of continental crust, brittle deformation in <~15 km thick crust, is accommodated by sequentially active normal faults. The intense normal faulting of Domain I does not produce breakup and exhumed mantle until after extending the crust to 3-5 km for ~100 km. Most faults from f1-f11 have sufficient slip to have thinned a 3-5 km thick crust to breakup. Thus, we propose that the faults were formed successively and functioned sequentially through time, with each fault cutting a slice of crust from the conjugate margin and transferring it to the West Iberia margin, similarly to the sequential faulting model of Ranero and Perez-Gussinyé, (2010).

Therefore, the continental blocks of Domain I are blocks transported from the conjugated margin that is currently portrayed in Domain III. Assuming that a sequential faulting model cut blocks from a margin with the structural heterogeneity observed in Domain III, then each new fault must have cut a crustal block of different dimensions. The sequential faulting model proposes that short-lived,

chronologically active normal faults cause lateral rift-center migration that generates a wide area of thin crust. This is in agreement with simulations made with numerical models (Brune et al., 2014). Thus, the broad region of thin crust is not necessarily caused by concave-downward top-of-basement detachment faults (e.g. Reston et al., 1996; Manatschal, 2004.).

Conjugated Domain III presents an asymmetric structure both in terms of crustal thickness, which vary laterally more abruptly, and also in tectonic structure with faults that dip to the east and are conjugated to those of Domain I. This type of asymmetric structure, both in the thickness of the crust as in the tectonic style, is similar to that described in the conjugate pair of Iberia and Newfoundland margins (Pérez-Gussinyé et al., 2003; Funck et al. 2003; Hopper et al., 2007). The time of fault activity is unconstrained due to the lack of deep-water drill holes. We speculate that if the sequential faulting model is correct then the deformation must have focused on a single zone, creating the faults that transferred blocks of continental crust from Domain III to Domain I as deformation progressed.

Thinning of continental crust resulted in an asymmetric system normal and detachment type of faults that, in both Domains under TAP, appear to cut the entire crust. The faults reaching the mantle may have allowed water to reach the upper mantle and cause serpentinization. In conclusion, our findings in the TAP show that the embrittlement of the crust that allows faults to cut all the way through the basement until the mantle leading to its serpentinization, does not appear to control the faulting style.

9.4.2. Mantle exhumation and breakup

Following our interpretation of Domains I and III, and assuming that Domain II is composed by exhumed mantle, this domain should be younger than continental Domain I but also than the conjugate continental Domain III. The fact that Domain II is younger than both continental domains on either side could help to explain that the tectonic structures in Domain III do not appear to be perpendicular to the profile trace, as discussed above. Even though we interpret that Domain I and Domain III have been formed during the same extension system, the fault blocks in Domain III are not necessarily parallel to the fault blocks of Domain I. There could have been a change in stresses and in the direction of extension, perhaps triggering the change in the faulting that created Domain II.

Based on this hypothesis, we propose a model of mantle exhumation through a detachment fault terminating continental rifting of an asymmetric margin. The model has three stages: **(I)** an asymmetric continental crust thinning scenario followed by **(II)** extension direction change, breakup and initiation of the COT, and finally **(III)** mantle exhumation (Fig. 9.8).

Stage I took place during an advanced phase of rifting when the crust was ≤ ~10 km thick in the area of extension. The system developed an asymmetric structure by sequential normal faulting (Fig. 9.8). This process implies that a new fault forms in the most favourable position for the location of deformations in the hanging wall to the dying fault. The new fault cuts the hanging wall, which is part of the conjugate margin (Domain III), slides and further thins the crust until it locks. Subsequent faults form sequentially, following the same pattern. During this stage, the underlying mantle is covered by a 3-5 km thick carapace of crust extending for at least ~170 km. Upper mantle Vp supports partial serpentinization of the uppermost 8-10 km, facilitated by faults reaching Moho on either

conjugate side of the margin. However, despite the presence of weak serpentine in the mantle, none of the faults that cut the boundary developed to exhume the mantle. This is in disagreement with previous studies on the Iberia Abyssal Plain. Péron-Pinvidic et al. (2007) suggested that the prominent ridge made up of serpentinized peridotite observed in this margin was exhumed along a downward concave detachment fault to the seafloor (e.g. Péron-Pinvidic et al., 2007). Manatschal et al., (2001) suggested that, within the COT, sub-horizontal structures exhuming mantle at the seafloor correspond to downward concave detachment faults with large offsets (tens of kilometres). This is consistent with the rolling-hinge model of Buck (1988) suggesting that sub-horizontal sea-bed structures are formed by an active high-angle fault at depth associated with large fault offset. This leads to the exhumation of the fault footwall, becoming sub-horizontal at the sea-bed due to flexural isostatic rotation.

Stage II, leading to the formation of Domain, II may have been a trigger or associated with a change in the direction of extension that possibly caused a change in the strike of the faults. This would also rotate the strike of structures in Domain III that originally were parallel to the strike in Domain I, assuming that the sequential faulting during continental extension is correct (Fig. 9.8). This early rifting history is poorly documented in the region and does not know of processes that may have caused the change of opening direction, but we remark that there is a slight change in direction of the interpreted Paleo-Iberia Africa Boundary visible in multibeam bathymetry to the south of the TAP (Fig. 9.1). We propose that the change caused the faults of Domains I and III to stop and that a slight change in fault orientation caused the final continental breakup and initiated the exhumation of the mantle.

During **Stage III,** the fault formed in Stage II extended exhuming mantle to the surface along a ~30 km long heave that has associated a symmetric high, similar to a core complex type of detachment geometry and possibly a rafted block (Fig. 9.4 and 9.8).

In the MCS image, the detachment is associated with the basement top though most of Domain II, and between CMPs 21000 – 19000 (Fig. 9.4a) deepens into the mantle along faint reflections dipping east that penetrate relatively deeply into the mantle. The exhumed detachment is also not low angle. It has a relatively steep geometry of ~30-35º in the youngest exhumed mantle segment and steepens further as the fault extends to some depth, as indicated by east-dipping reflections.

The reflectivity within the basement has some lateral continuity and sub-horizontal dip angles. The three levels of reflectivity marked as IBR (Fig. 9.4a) have angles too low to be interpreted as faults that were active during the formation of Domain II. Furthermore, they do not project to offsets at the TOB and they rather seem to correspond to changes in velocity possibly associated with variations in the intensity of serpentinization of the mantle as the middle band occurs at the base of the steep Vp-depth gradient, and the deepest near the base of serpentinization where Vp is ~8.0 km/s.

Figure 9.8 - Formation model of the central Tagus Abyssal Plain basin in exhumed mantle setting summarised in four main stages. Stage I represents the end of the rifting resulting as an asymmetric conjugated margins configuration. Stage II display the COT initiation with the formation of a fault that will led to a detachment. Stage III represents an intermediate stage with the exhumation of mantle through the detachment fault. Finally, Stage IV represents the current configuration of the central TAP where the detachment fault has been exhuming mantle for ~30km. The brittle-ductile transition is from Grevemeyer et al. (2019).

9.4.3. Mantle exhumation models

Previous tectonic models of mantle exhumation after breakup at rifted margins have largely relied on the interpretation of the structure of the Iberia Abyssal Plain. The models proposed the evolution of detachment systems fundamentally based on the interpretation of a suite of landward-dipping reflections imaged on the IAM9 seismic line (Pickup et al., 1996). The proposal interprets those reflections as abandoned root zones of successive detachments (Reston and McDermott, 2011). Most of those reflections dip eastward across a ~100 km wide segment, and for their kinematic interpretation it has been assumed that the exhumed mantle domain of the COT of the IAP has a conjugate symmetric COT in Newfoundland margin. This assumption is central to understand how previous works interpret the tectonic structure and the succession of detachments.

Based on our data, the COT of the TAP does not have a conjugate in Newfoundland, because we observe the entire system frozen after the magmatic episode related to the inception of the J-anomaly propagated across the plate PIAB, truncated Domain III from the conjugate margin and changed the position of the centre of extension (Chapter 8 and next section). The J-magnetic anomaly delineating the magma propagation that cut the TAP extends across the IAP (Fig. 9.1). Thus, it is possible that it also ended extension in the TAP and may mean that the IAP does not have a conjugate structure in the Newfoundland margin. The existing seismic lines and drilling do not demonstrate the presence or extent of the COT with a mantle exhumed in the conjugate segment of the Newfoundland margin (e.g. Funck et al., 2003; Hopper et al., 2004; Van Avendonk, et al. 2006; Lau et al., 2006a, 2006b; Shillington et al., 2006). On the conjugate Newfoundland basin margin, serpentinized mantle has been suggested to exist beneath rifted continental and oceanic crust (Reid, 1994), whereas exhumed mantle has been restricted drilled at ODP Site 1277 (Leg 210, Shipboard Scientific Party 2004). Later studies modelled the margin by forward modelling of sparse WAS data sets. These studies suggest that the transition zone basement does not resemble most images of exhumed peridotite off Iberia. MCS profiles, together with coincident wide-angle seismic refraction data, tentatively suggest that the majority of transitional basement is thinned continental crust (Van Avendonk, et al. 2006). This crust would have been emplaced during the late stages of rifting, with a seaward increase in the influence of intrusions or mantle serpentinization (Shillington et al., 2006), whereas in the northern part of the margin, it is formed by 3-4-km-thick oceanic crust (Hopper et al., 2004). Despite the debate about the characterization of the nature of the basement in the Newfoundland margin, there are numerous works proposing a symmetric conjugate structure that is used in kinematic reconstructions (e.g. Nirrengarten et al., 2017; 2018; Szameitat et al., 2018; Causer et al. 2020).

The first models presented to explain exhumation at the COT of the IAP propose a succession of detachments cutting sequentially every ~5 km (Reston and McDermott, 2011). This model has also been applied with detachments every 10-20 km for the ultra-slow SW Indian Ridge, largely based on seafloor morphology and dredge samples (Sauter et al., 2013). In contrast, in the TAP we do not observe dipping intra-mantle features as in the IAP. The difference cannot be attributed solely to data quality, because FRAME data were collected with a 6-km long streamer and IAM-9 with a 4.5 km long streamer. The IAM source is larger, but the FRAME source of ~4800 c.i. images well the Moho in different locations and a depth similar to the expected dipping reflections and thus it does not appear to be an energy penetration issue. Thus, the IAP and TAP structures are different. In the TAP

the images of the entire domain, i.e. the whole area of mantle exhumation in this sector of the West Iberia - Newfoundland conjugate margins can be interpreted as a single detachment fault with an exhumed sector of over ~30 km and a ~15 km wide root zone (Fig. 9.4).

In this region, the water had circulated through the faults reaching the ductile-fragile transition (DFT) depth and, therefore, giving way to mantle serpentinization. It has been shown that the depth of the DFT in the context of ultra-slow spreading is around ~17 km (Grevemeyer et al. 2019). Nowadays, the configuration of this part of the FRAME-2 profile under Domain I, II and III, shows that the isovelocity contour of 8.0 km/s is around 15 km depth, so we propose that this limit of velocity could have corresponded to the DFT during the mantle exhumation, under a context of slow- and ultraslow-spreading.

9.4.4. J-anomaly basement

The 1D Vp-depth gradients in this domain are characteristic of oceanic crustal structure with Layer 2 and Layer 3 (Chapter 8). The oceanic igneous crust is about 6-8 km thick in Domain IV, with the 8-km segment somewhat thicker than typical 6-km-thick oceanic crust. The seismic images display some correspondence to the Vp model (Fig 9.6b). The uppermost intra-basement subhorizontal reflective layering, represented by a low-frequency band, has laterally homogeneous velocity between 4.8 to 5.0 km/s (blueish colours in Fig. 9.6b). The seismic image in Domain IV displays an overall different upper crustal geometry because there is no evidence of significant faulting or rotated layering. The slightly anomalous thick igneous crust and lack of faulting supports a domain formed by intense magmatism (Layer 3) and extrusive volcanism (Layer 2). These observations support that most of the plate opening was assimilated by magmatic intrusions and minor faulting.

The abrupt change display in the images from extended continental crust of Domain III to magmatic oceanic crust of Domain IV in a few kilometres further supports the model of spreading centre propagation along the J-anomaly causing the sudden termination of rifting (Chapter 8).

The volcanic upper basement can be defined as a unit that laterally changes in thickness creating a smooth basement topography. This upper unit produces thin sub-horizontal patterns of continuous reflections, possibly composed by successive volcanic units or volcanoclastic rocks. The base of these volcanic units is not a sharp boundary, although it can be identified by a change in the reflectivity pattern, as the volcanic units show higher reflectivity than the underlying middle crust (Fig. 9.6a). These volcanoclastic rocks are probably related to the Ashton volcano (Fig. 9.1), and have been sampled and dated as Cenomanian, between 96-99 Ma (Merle et al., 2006; 2009).

9.4.5. Cretaceous Magnetic Quiet Zone

The crust formed during the Cretaceous Magnetic Quiet Zone extends under the flat top of the Madeira Tore Rise, with comparatively intense normal faulting and gradual westward thinning of the basement (Fig. 9.7a, CMP 45000 – 50000).

Transition from Domain IV to V shows that the layering associated with magmatism disappears and extensional tectonics becomes more important. Thus, the observations suggest a change in the style of oceanic expansion from Domain IV to V.

We suggest that the opening and formation of new oceanic crust in Domain V could be characterized by a low extension rate and reduced magma production. This is supported by the change in basement structure from a layered uppermost basement to a TOB formed by a unique strong and continuous reflection.

We propose that after the magmatic pulse forming the J-anomaly, oceanic crust formed under new conditions during the Cretaceous Magnetic Quiet Zone. The spreading rate in this zone is unknown. However, the change in spreading centre processes may be explained by a decreased expansion rate from Domain IV to V.

9.5. In summary

The FRAME deep seismic survey shows for the first time across the entire Tagus Abyssal Plain the configuration of the basement, as well as the relations between the different crustal domains. This structural configuration gives clues on the geodynamic evolution of this basin.

Based on these results, we can define five different basement domains coexisting at the Tagus Abyssal Plain: (i) two thin continental domains, (ii) an exhumed mantle domain and (iii) two oceanic domains. The boundaries between these domains can be either a smooth transition or a well-defined tectonic structure.

The thin continental domain is located at the easternmost part of the seismic line and includes two different domains. It presents thickness variations, being characterized by a basement thickness of ~1 s TWT under the lower slope that is 100 km-long (Domain I) and by a basement thickness of ~2 s TWT under the TAP (Domain III). We propose that both domains are part of the same type of continental crust, affected by different degrees of extension. Thus, we propose that they represent together a pair of conjugate margins.

Between these two continental domains, we find an exhumed mantle domain (or Domain II). It is characterized by a basement that is ~4.5 s TWT-thick, with layered reflections on its lower part associated to serpentinization fronts. We suggest that this domain opened by the action of a ~30 km detachment fault that exhumed the mantle from east to west during a first stage of extension.

The oceanic crust domains IV and V are located at the westernmost part of the seismic transect, across the Madeira-Tore Rise. The basement has a thickness of ~3 s TWT in Domain IV, which corresponds with location of the J-anomaly. Intra-crustal reflections and basement faults are common in this basement. However, Domain V corresponds to the oceanic crust that formed under new conditions, as the Cretaceous Magnetic Quiet zone, where expansion rate was lower and it was heavily influenced by the tectonics.

The crustal domains of the Tagus Abyssal Plain are hence the result of extensional processes in a

continental drift context, which modified their crustal characteristics until they reached the current configuration. The geodynamic context is characterised by two main episodes of rifting that led at the end to the opening of the North Atlantic Ocean.

References

Afilhado, A., Matias, L., Shiobara, H., Hirn, A., Mendes-Victor, L., Shimamura, H. (2008). From unthinned continent to ocean: The deep structure of the West Iberia passive continental margin at 38°N. Tectonophysics, 458(1–4), 9–50. doi.org/10.1016/ j.tecto.2008.03.002.

Beslier, M. O. (1996). Data report: Seismic line LG12 in the Iberia Abyssal Plain, Proc. ODP Sci. Results, 149, 737– 739.

Boillot, G., Winterer, E.L., Meyer, A.W. (1987a). Introduction, objectives, and principal results: Ocean Drilling Program Leg 103, west Galicia Margin. Proc. ODP, Init. Repts., 103: College Station, TX (Ocean Drilling Program), doi: 10.2973/odp.proc.ir.103.

Brune, S., Heine, C., Pérez-Gussinyé, M., and Sobolev, S. V. (2014). Rift migration explains continental margin asymmetry and crustal hyper-extension. Nature Communications, 5(1), doi:10.1038/ncomms5014.

Buck, W.R. (1988). Flexural rotation of normal faults. Tectonics, 7(5), pp.959-973.

Dean, S. M., Minshull, T. A., Whitmarsh, R. B. and Louden, K. E. (2000). Deep structure of the ocean-continent transition in the southern Iberia Abyssal Plain from seismic refraction profiles: The IAM-9 transect at 40!200N. J. Geophys. Res. Solid Earth 105, 5859–5885.

Funck, T., Hopper, J.R., Larsen, H.C., Louden, K.E., Tucholke, B.E. and Holbrook, W.S. (2003). Crustal structure of the ocean-continent transition at Flemish Cap: Seismic refraction results, J. geophys. Res., 108 (B11), 2531, doi: 10.1029/2003JB002434.

Grevemeyer, I., Hayman, N. W., Langz, D., Peirce, C., Papenberg, C., Van Avendonk, H.J.A., Schmid, F., Gómez de La Peña, L. and Dannowski, A. (2019). Constraining the maximum depth of brittle deformation at slow- and ultraslow-spreading ridges using microseismicity. Geology, 47, 1069–1073, doi: 10.1130/G46577.1.

Henning, A. T., Sawyer, D. S. and Templeton, D. S. (2004). Exhumed upper mantle within the ocean-continent transition of the Northern West Iberia margin: Evidence from prestack depth migration and total tectonic subsidence analyses, J. Geophys. Res., 109, B05103, doi:10.1029/2003JB002526.

Hopper, J.R., Funck, T., Tucholke, B.E., Larsen, H.C., Holbrook, W.S., Louden, K.E., Shillington, D. and Lau, H. (2004). Continental breakup and the onset of ultraslow seafloor spreading off Flemish Cap on the Newfoundland rifted margin. Geology, 32(1), pp.93-96.

Hopper, J. R., Funck, T. and Tucholke, B. E (2007). Structure of the Flemish Cap margin, Newfoundland: insights into mantle and crustal processes during continental breakup. Geol. Soc. London Spec. Publ. 282, 47–61.

Klitgord, K.D., and Schouten, H. (1986). Plate kinematics of the central Atlantic. Geol. N. Am., 1000, 351–378.

Krawczyk, C. M., Reston, T. J., Beslier, M. O., and Boillot, G. (1996). Evidence for Detachment Tectonics on the Iberia Abyssal Plain rifted margin, in Proceedings of the Ocean Drilling Program, Scientific Results, vol. 149, edited by R. B. Whitmarsh et al., pp. 603– 615.

Lau, K.H., Louden, K.E., Funck, T., Tucholke, B.E., Holbrook, W.S., Hopper, J.R. and Christian Larsen, H. (2006). Crustal structure across the Grand Banks—Newfoundland Basin Continental Margin—I. Results from a seismic refraction profile. *Geophysical Journal International*, *167*(1), pp.127-156.

Lau, K.H., Louden, K.E., Deemer, S., Hall, J., Hopper, J.R., Tucholke, B.E., Holbrook, W.S. and Christian Larsen, H. (2006). Crustal structure across the Grand Banks—Newfoundland Basin Continental Margin—II. Results from a seismic reflection profile. *Geophysical Journal International*, *167*(1), pp.157-170.

Manatschal, G., Froitzheim, N., Rubenach, M., Turrin, B. (2001). The role of detachment faulting in the formation of an ocean-continent transition: insights from the Iberia Abyssal Plain from: Wilson, R.C.L.,

Manatschal, G. (2004). New models for evolution of magma-poor rifted margins based on a review of data and concepts

from West Iberia and the Alps. International Journal of Earth Sciences, 93(3), pp.432-466.

Mauffret, A., Mougenot, D., Miles, P.R., Malod, J.A. (1989). Cenozoic deformation and Mesozoic abandoned spreading center in the Tagus Abyssal-Plain (West of Portugal) - results of a multichannel seismic survey. Canadian Journal of Earth Sciences 26 (6), 1101–1123.

Merle, R. (2006). Age and origin of Tore-Madeira Rise: Beginning of Atlantic Ocean spreading or hotspot track. Petrology, Geochemistry, U–Pb Geo- chronology and Pb–Sr–Hf isotopes (PhD thesis). University of Nantes, Nantes, France.

Merle, R., Jourdan, F., Marzoli, A., Renne, P. R., Grange, M., and Girardeau, J. (2009). Evidence of multi-phase Cretaceous to Quaternary alkaline magmatism on Tore-Madeira Rise and neighbouring seamounts from 40Ar/39Ar ages. Journal of Geological Society of London, 166, 879–894.

Mougenot, D., (1989). Geologia da margem portuguesa. Documentos tecnicos, Instituto Hidrografico, Lisboa, Portugal, 259 pp.

Olivet, J.-L. (1996). La cinématique de la plaque Ibérie, Bull. Cent. Rech. Explor. Prod. Elf Aquitaine, 20, 131– 195.

Pérez-Gussinyé, M., Ranero, C. R., Reston, T. J. and Sawyer, D. (2003). Mechanisms of extension at nonvolcanic margins: evidence from the Galicia interior basin, west of Iberia. J. Geophys. Res. 108, 2245.

Péron-Pinvidic, G., Manatschal, G., Minshull, T.A., Sawyer, D.S. (2007). Tectonosedimentary evolution of the deep Iberia-Newfoundland margins: Evidence for a complex breakup history. Tectonics 26, 1T19, doi:10.1029/2006TC001970.

Pickup, S., Whitmarsh, R.B., Fowler, C.M.R., and Reston, T.J. (1996). Insight into the nature of the ocean-continent transition off West Iberia from a deep multichannel seismic reflection profile: Geology, v. 24, p. 1079–1082, doi:10.1130/0091-7613(1996)024<1079:IITNOT>2.3.CO;2.

Pinheiro, L.M., Whitmarsh, R.B., Miles, P.R. (1992). The ocean–continent boundary off the western continental margin of Iberia—II. Crustal structure in the Tagus abyssal plain. Geophys. J. Int. 109 (1), 106–124.

Prada, M., Sallarès, V., Ranero, C.R., Vendrell, M.G., Grevemeyer, I., Zitellini, N. and de Franco, R. (2014). Seismic structure of the Central Tyrrhenian basin: Geophysical constraints on the nature of the main crustal domains. *Journal of Geophysical Research: Solid Earth*, *119*(1), pp.52-70.

Ranero, C. R., and Pérez-Gusinyé, M. (2010). Sequential faulting explains the asymmetry and extension discrepancy of conjugate margins, Nature, Vol. 468, pp. 294-300, doi: 10.1038/nature09520.

Reid, I. D. (1994). Crustal structure of a nonvolcanic rifted margin east of Newfoundland. Journal of Geophysical Research, 99(B8), 15161, doi:10.1029/94jb00935.

Reston, T.J. (1996). The S reflector west of Galicia: The seismic signature of a detachment fault. Geophys. J. Int. 127, 230T244, doi:10.1111/j.1365-246X.1996.tb01547.

Reston, T.J. (2009). The structure, evolution and symmetry of the magma-poor rifted margins of the North and Central Atlantic: A synthesis. Tectonophysics 468, 6T 27, doi: 10.1016/j.tecto.2008.09.002.

Reston, T. J., and McDermott, K. G. (2011). Successive detachment faults and mantle unroofing at magma-poor rifted margins. Geology, 39 (11), 1071–1074, doi: 10.1130/g32428.1

Rovere, M., Ranero, C. R., Sartori, R., Torelli, L., Zitellini, N. (2004). Seismic images and magnetic signature of the Late Jurassic to Early Creta- ceous Africa–Eurasia plate boundary off SW Iberia. Geophysical Journal International, 158, 554–568.

Sallarès, V., Martínez-Loriente, S., Prada, M., Gràcia, E., Ranero, C., Gutscher, M.A., Bartolome, R., Gailler, A., Dañobeitia, J.J. and Zitellini, N. (2013). Seismic evidence of exhumed mantle rock basement at the Gorringe Bank and the adjacent Horseshoe and Tagus abyssal plains (SW Iberia). *Earth and Planetary Science Letters*, *365*, pp.120-131.

Sauter, D., Cannat, M., Rouméjon, S., Andreani, M., Birot, D., Bronner, A., Brunelli, D., Carlut, J., Delacour, A., Guyader, V. and MacLeod, C.J. (2013). Continuous exhumation of mantle-derived rocks at the Southwest Indian Ridge for 11 million years. *Nature Geoscience*, *6*(4), pp.314-320.

Shillington, D.J., Holbrook, W.S., Van Avendonk, H.J., Tucholke, B.E., Hopper, J.R., Louden, K.E., Larsen, H.C. and Nunes, G.T. (2006). Evidence for asymmetric nonvolcanic rifting and slow incipient oceanic accretion from seismic reflection data on the Newfoundland margin. *Journal of Geophysical Research: Solid Earth*, *111*(B9).

Shipboard Scientific Party, 2004. Leg 210 summary, in Proc. Ocean Drill. Program, Init. Repts., Vol. 210, pp. 1–78, eds Tucholke, B.E., Sibuet, J.-C., Klaus, A., Ocean Drilling Program, College Station, Texas.

Sibuet, J.C., Srivastava, S. P., and Spakman, W. (2004). Pyrenean orogeny and plate kinematics. Journal of Geophysical Research: Solid Earth, 109 (B8), doi:10.1029/2003jb002514.

Srivastava, S.P., Sibuet, J.C., Cande, S., Roest, W.R. and Reid, I.D. (2000). Magnetic evidence for slow seafloor spreading during the formation of the Newfoundland and Iberian margins. *Earth and Planetary Science Letters*, *182*(1), pp.61-76.

Sawyer, D., Whitmarsh, R., and Klaus, A. (1994). Iberia Abyssal Plain Sites 897-901, paper presented at Proceedings of the Ocean Drilling Program Initial Rep.

Tucholke, B. E., and Sibuet, J.C. (2007). Leg 210 synthesis: tectonic, magmatic, and sedimentary evolution of the Newfoundland-Iberia rift, in Proceedings of the Ocean Drilling Program, Scientific Results, vol. 210, edited by B. E. Tucholke, J.-C. Sibuet, and A. Klaus.

Van Avendonk, H.J., Holbrook, W.S., Nunes, G.T., Shillington, D.J., Tucholke, B.E., Louden, K.E., Larsen, H.C. and Hopper, J.R. (2006). Seismic velocity structure of the rifted margin of the eastern Grand Banks of Newfoundland, Canada. *Journal of Geophysical Research: Solid Earth*, *111*(B11).

Whitmarsh, R. B., and Sawyer, D. S. (1996). The ocean-continent transition beneath the Iberia Abyssal Plain and continental-rifting to seafloor-spreading processes: Proceedings of the Ocean Drilling Program, Scientific results, Volume 149: College Station, Texas, Ocean Drilling Program, p. 713–733.

Whitmarsh, R. B., M.-O. Beslier, P. J. Wallace, and Shipboard Scientific Party (1998). Sites 1065–1070, Proc. Ocean Drill. Prog. Initial Rep.,173, 65–294.

Zelt CA, Sain K, Naumenko JV, Sawyer DS. (2003). Assessment of crustal velocity models using seismic refraction and reflection tomography. Geophysical Journal International. Jun 1;153(3):609-26.

Part IV
DISCUSSION

Chapter 10

Discussion

10.1. Rifting and quality models

In this thesis, we focus on the study of how continents rift apart and form rifted margins. The detailed study of rifted margins is key to understand some of the most important tectonic and geodynamic processes on Earth that lead to the formation and evolution of oceans.

Focussing on the large-scale structure of the continental margins as seen in conventional vintage seismic data, the vast majority of previous studies have made the interpretation of these geological settings based on a unique conceptual model that still represents the current paradigm of knowledge in numerous text books. This model proposes that progressive continental rifting ends in a complete lithosphere breakup followed by sea-floor spreading at a mid-ocean ridge. In more recent models, it is also acknowledged that continental mantle unroofing -without substantial simultaneous magmatism- could also occur prior to sea-floor spreading, producing regions of exhumed mantle. This process leads to the formation of a conjugate pair of rifted margins with the ocean basins between them formed by exhumed mantle and/or new oceanic crust. Thus, it has been proposed that magma-poor rifted margins architecture is characterized by a template that consists of a set of structural rift domains (Fig. 10.1). From continent to ocean these are (i) proximal domain, (ii) necking domain, (iii) hyperthinned domain, (iv) exhumed mantle domain and (v) oceanic domain (e.g. Péron-Pinvidic and Manatschal, 2008; Sutra and Manatschal, 2012; Péron-Pinvidic et al., 2013) (Fig. 10.1).

However, vintage seismic data provide ambiguous information, which cannot realistically constrain the nature of the rocks of the basement. As a result, assumptions based on pre-conceived models of rock type and composition must be applied in order to interpret the data. The combination of modern marine geophysical data, including Wide-Angle Seismic (WAS), Multi-Channel Seismic (MCS) reflection and gravity data provide complementary information. Using those data sets in combination with current methodologies of seismic joint tomographic inversion provide structural models and map physical properties with unprecedented detail. This approach allows to re-define the structure of the rifted margins based on objective, data-based criteria. The interpretation of these data provides

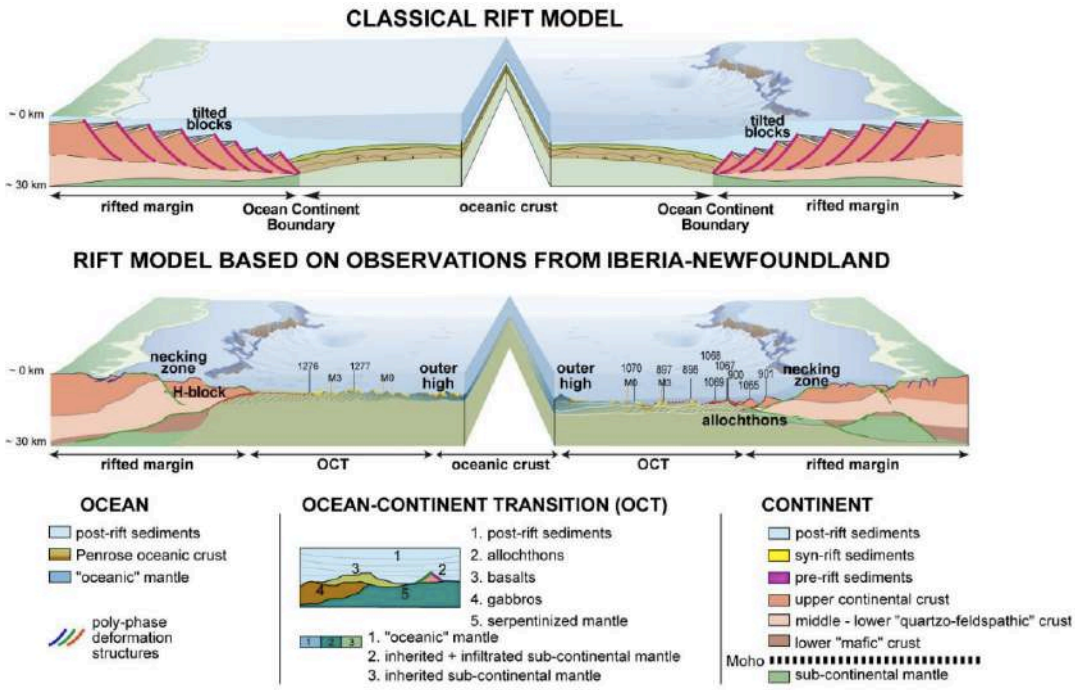

Figure 10.1 - Schematic three-dimensional representations of rifted margins. (a) Classical representation showing pre-, syn-and post-rift sediment architecture over uniformly stretched continental crust, affected by high-angle normal faults in the upper crust and ductile deformation in the lower crust, juxtaposed against a three layer Penrose type oceanic crust. (b) Representation of the structure of the Iberia-Newfoundland rifted margins as deduced from seismic sections and drill hole data. Major differences to the classical rift model are the occurrence of mantle exhumation along top-basement detachment faults in the COT. From Manatschal et al. (2010).

detailed information on the spatial distribution of the geological domains in the area, allowing to better understanding their process of formation and the ensuing deformation.

Although some of the models have been used as book examples to interpret rifted margin in general, here we focus the review on their ability to explain geological observations and geophysical data acquired in the Gulf of Lions (Western Mediterranean) and the Tagus Abyssal Plain (West Iberia margin). We propose the following topics, integrating published results with new results obtained during this PhD work, as the main aspects to consider for a review of the conceptual model:

10.1.1. The Gulf of Lions

Different interpretations of the basement nature of the Gulf of Lions have been proposed by a number of authors (e.g. Pascal et al., 1993; Contrucci et al., 2001; Gailler et al. 2009). Overall, they propose that the transition between the thinned continental crust and the oceanic crust is characterized by a domain formed by high P-wave velocity (Vp) rocks. Based on the velocity structure, the most recent of these studies interpreted it as a body made of exhumed lower crust. For the lower crust exhumation to take place, the formation of large structures known as detachment faults is inferred based on seismic images oriented NW-SE (Fig. 10.3a,b). Jolivet et al. (2015) and Granado et al. (2016), in Figure 10.2 a and b respectively, interpreted a 100 km-long lens of exhumed lower crust with a fairly constant thickness of around 5 km. If this interpretation were correct, the top of basement of the

exhumed lower crust imaged in these profiles should represent the exhumed segment of the detachment fault. The idea of lower crust exhumation is based on the study done by Moulin et al. (2015), who reinterpreted an MCS image and remodelled a WAS profile presented before by Gailler et al. (2009) using forward modelling, in Figure 10.3b and a correspondingly. The high velocity body had previously been identified by Gailler et al. (2009), Pascal et al. (1993), and Contrucci et al. (2001) but, instead of lower crustal exhumation, they proposed an alternative hypothesis to explain its presence in the transition zone between the continental and the oceanic crust. Gailler et al. (2009) preferred hypothesis is that this high-velocity zone represents upper mantle material exhumed and serpentinized during the initial opening of the basin (Fig. 10.2). As it shows Figure 10.3, the previous studies carried by Gailler et al. (2009) and Moulin et al. (2015) the Gulf of Lions margin could be divided in three main domains as also shows our final Vp model (Fig. 10.3) but their petrological nature is interpreted differently, as explained before.

We use the same geophysical data set as Gailler et al. (2009) and Moulin et al. (2015), but we have applied a new modelling approach with joint inversion of first arrival and WAS reflections, not done in the previous works, and we have also added a new modelling technique that jointly inverts MCS with WAS travel-times, as described in Chapter 5: *Travel-time Tomography*. This methodological approach has provided a new Vp model of improved resolution that roughly agrees with the distribution of crustal domains proposed so far, but provides additional detail and quantitative constraints on the distribution of seismic velocity as well as on the definition of the sharp lithological boundaries between the different domains. In contrast to previous models, our approach also allows estimating the uncertainty of the model parameters, which in turn provides more objective, data-based information on their likely petrological nature. In detail our results have substantial differences with the previous models (Fig. 10.3) and therefore on the interpretation.

The new Vp model across the Gulf of Lions is framed in a back-arc setting where a 30 km of continental crust progressively thins through a number of faulted and tilted blocks until it breaks up giving way to oceanic crust. Our interpretation of an oceanic crustal nature instead of exhumed mantle (Gailler et al., 2009) or lower continental crust (e.g. Moulin et al., 2015) is based on the well-resolved two layer vertical Vp gradient and on the location of the sharp velocity contrasts at the top and at the base (Moho) of the body. The resulting oceanic crust is <~5 km-thick, and extends for ~100 km. Based on the spatial distribution of Vp anomalies, we interpret that melt production was gradual and that emplacement in the crust initiated by underplating of the continental crust at the locus of thinning.

Our interpretation agrees with an eastward rifting of the Gulf of Lions related to roll-back of the west-directed Apenninic subduction zone (Cohen, 1980; Le Douaran et al., 1984; Rehault et al., 1984; Gueguen et al., 1998; Jolivet et al., 2000; 2006; 2015; Granado et al., 2016). Extension driven by the retreat of the subduction slab causing the eastward rotation of the Corsica-Sardinia block and produced anomalously thin oceanic crust, bounded at its base by a clear Moho reflection.

Furthermore, the oceanic crust is located between two domains of continental crust. East of the oceanic crust we interpret a thin continental crust that extends over the Ligurian Basin. This is supported by recent work further north (Dannowski et al., 2020).

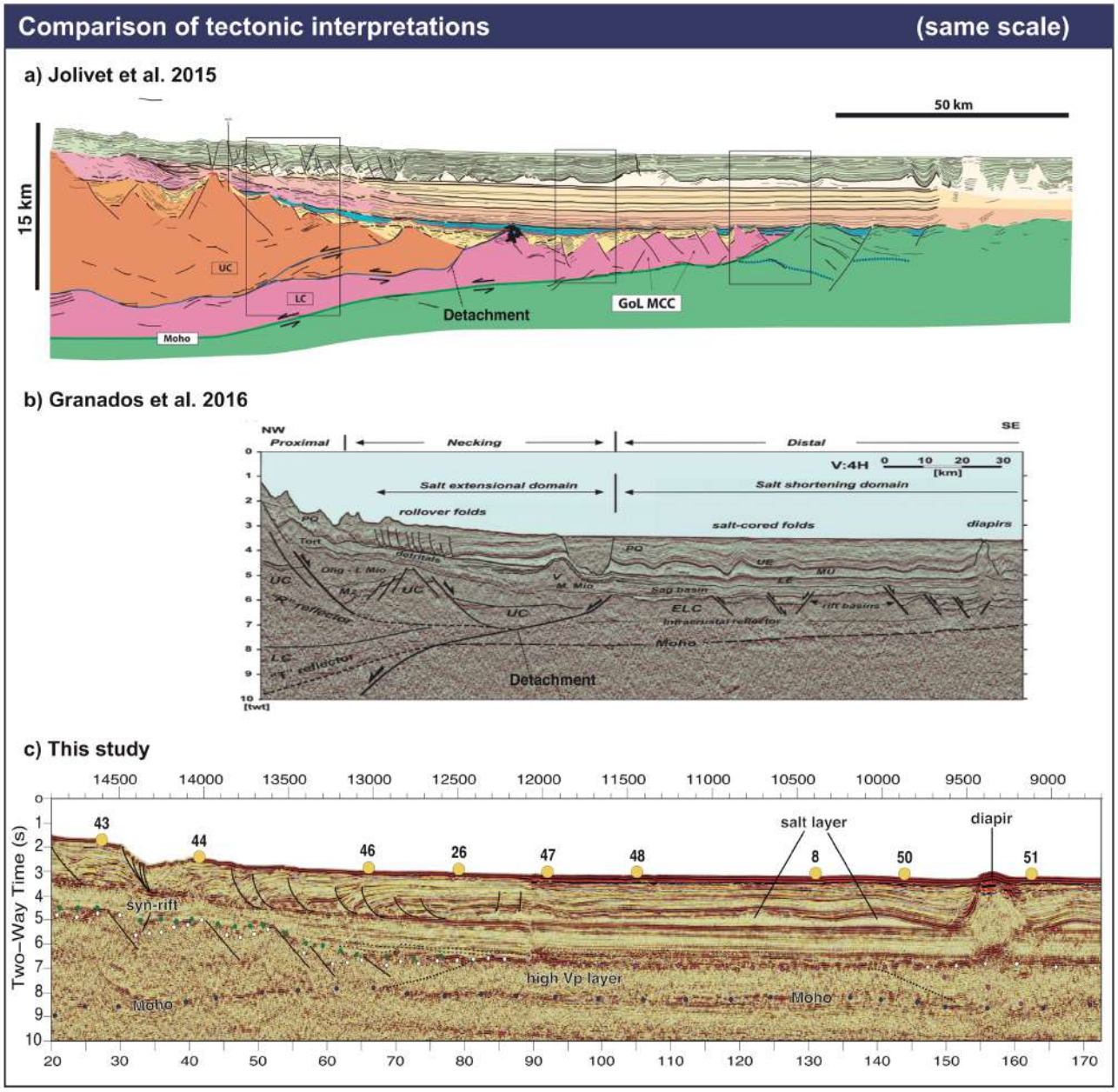

Figure 10.2 - Comparison of different tectonic interpretations across the Gulf of Lions. (a) Tectonic interpretation of the MCS line acquired by TGS-NOPEC M/V Zephir 1 in 2001, by Jolivet et al. (2015). (b) Tectonic interpretation of the MCS line from the SPBAL01 survey acquired by Spectrum Energy's vessel Polar Princes on November 2001, by Granado et al. (2016). (c) Tectonic interpretation taking into account the results of the Vp modelling in Fig. 10.3c, from this work.

◄ *Figure 10.3 - Comparison of different P-waves velocity models across the same seismic line in the Gulf of Lions (adjusted at the same scale). (a) Trave-time tomography of WAS first arrivals, by Gailler et al. (2009) and a representation of velocity and Moho depth uncertainties. (b) Forward modelling using WAS first arrivals and MCS reflections, by Moulin et al. (2015). (c) Joint travel-time tomography (MCS + WAS) from this work and the uncertainties of the velocities and each inverted horizon.*

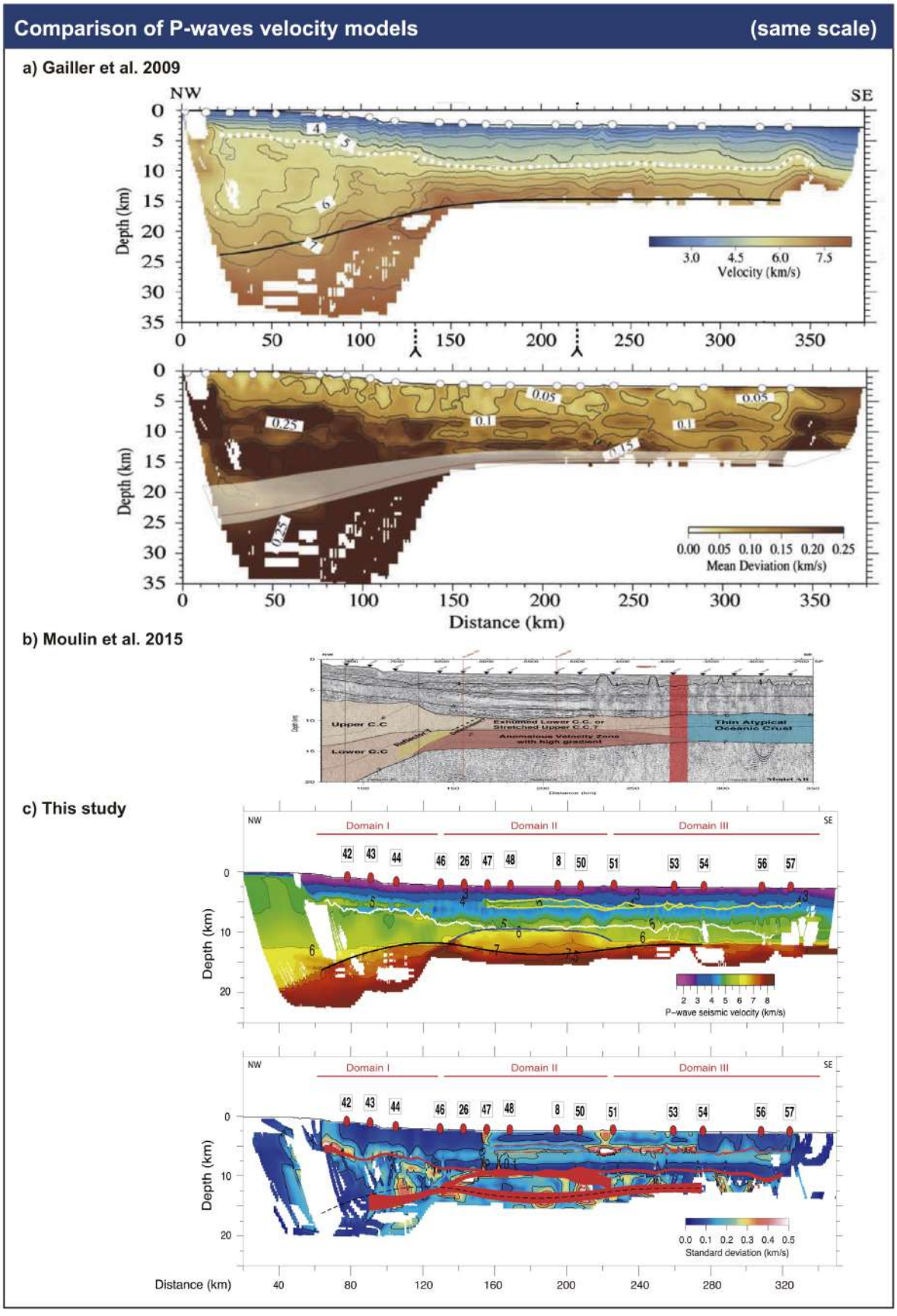
Comparison of P-waves velocity models
(same scale)
a) Gailler et al. 2009
NW
SE
Depth (km)
Velocity (km/s)
Mean Deviation (km/s)
Distance (km)
b) Moulin et al. 2015
Upper C.C
Lower C.C
Thin Atypical Oceanic Crust
c) This study
Domain I
Domain II
Domain III
P-wave seismic velocity (km/s)
Standard deviation (km/s)

10.1.2. The Tagus Abyssal Plain

Studies have been improving our knowledge on the structure and evolution of the West Iberia margin characterization since the 80's. However, there are still important gaps of knowledge, particularly in the southern part, across the Tagus Abyssal Plain (TAP). The main results presented in this thesis work are based on seismic data acquired during the FRAME survey (July and September 2018) that aimed at studying the distribution of geological domains based on the physical properties and the tectonic structure of the basement. The joint interpretation of the Vp, density and tectonic structure obtained with the WAS, gravity and MCS data, has led to a radically new definition of geological domains in the TAP as compared to what has been previously proposed and accepted to constitute a paradigm.

Previous interpretations of the TAP based on seismic data assumed a basement mainly formed by oceanic crust (e.g. Afilhado et al., 2008; Fig. 10.4a). Later, Bronner et al. (2011) and Nirrengarten et al. (2017) redefined the nature of the domains reinterpreting the published Vp model from Afilhado et al. (2008) to propose that most of the TAP is formed by exhumed mantle (Fig. 10.4b). In consequence, most of the recent maps from the region, and related kinematic models, typically display exhumed mantle in contact with oceanic crust in this basin (e. g. Nirrengarten et al., 2017; Szameitat et al., 2018). In contrast, the results of this PhD work, using far superior geophysical data, support that the basement under the TAP is fundamentally composed of thin continental crust and a much smaller extent of exhumed mantle that previously proposed (Fig. 10.4c). The previous interpretations are based on geophysical data of limited resolution and accuracy compared with those obtained in the FRAME project for this thesis. Our results implicitly show that the nature of the basement cannot be univocally constrained using sparsely sampled OBS profiles, as in Afilhado et al. (2008), or based on potential field modelling alone (Bronner et al., 2011; Nirrengarten et al., 2017). The conclusion is that these works necessarily have a large degree of unresolved uncertainty in the results and a high degree of subjectivity in their interpretation of the actual structure of the margin, and both problems have being substantially reduced in our study.

As described in Chapter 8, our results show evidence for the presence of basement rocks of different nature flooring the TAP. There is continental crust as thin as ~4 km thick under the lower slope that extends for over ~100 km that transitions into a ~70 km-wide exhumed mantle domain that appears to have been exhumed along a 30-km long detachment fault. In contrast to what is proposed in previous models, the exhumed mantle domain transitions again to a continental crust one to the west of the TAP basin. In contrast to that situated to the east, this domain might have some magmatic input at its base. Westward from this domain and across the Madeira-Tore Rise, we found a two-layered velocity structure typical of oceanic crust. This ≤8-km thick crust is slightly thicker than normal, particularly at the J-anomaly, and the depth-velocity distribution indicates a lower crust with slower average velocity than for typical oceanic Layer 3. Based on the observed anti-correlation between Vp and crustal thickness, we conclude that it is likely it corresponds to what now represents the eastern flank of the Madeira-Tore Rise, and that its anomalous structure might reflect the influence of a fertile geochemical anomaly in the mantle source. The westernmost segment of the Cretaceous Magnetic Quite zone displays a thin ocean crust that resembles that formed in an ultra-slow spreading magmatic setting strongly influenced by tectonics and limited magmatism.

Previous models suggesting the presence of exhumed mantle in the West Iberia margin are based on the recovery of serpentinized peridotites in the Ocean Drilling Project (ODP) site 637 (Boillot et al. 1987b; Shipboard Scientific Party, 1987a), located in the westernmost part if the Deep Galicia basin, and in ODP site 1068 (Shipboard Scientific Party, 1998c), in the Iberia Abyssal Plain. It has been interpreted that these serpentinites correspond to the basement of the COT, which resulted in faulting propagated towards the future ocean (e.g. Manatschal et al. 2001). In the southern IAP, the COT has been interpreted based on a WAS model as a >150 km wide zone of exhumed mantle rocks located between extended continental crust and the onset of anomalously thin oceanic crust (Dean et al., 2000; Minshull et al., 2014). Slightly southward from these lines but still in the IAP, the FRAME-3 WAS profile also shows a ~140 km-wide exhumed mantle domain that transitions into a 6 km-thick oceanic crust (Grevemeyer et al., in prep.).

In the TAP, vintage WAS data indicated the presence of a COT zone formed by a ~30 km-wide exhumed mantle domain (Pinheiro et al., 1992). A modern WAS profile acquired in the southernmost part of the TAP indicates that the sediment lays directly on basement made of serpentinited mantle rock (Sallarès et al., 2013a). Mantle exhumation is also interpreted beneath the Gorringe Bank and the north-western part of the Horseshoe Abyssal Plain (Sallarès et al., 2013a). They propose that the serpentine rock band have a similar nature and possibly origin to the IAP ocean–continent transition, which was probably generated during the earliest phase of the North Atlantic opening that followed continental crust breakup (Early Cretaceous).

The results obtained along transect 2 the FRAME experiment show that under the Tagus Abyssal Plain the basement contains a pair of original conjugate margins formed by extended continental crust with an overall crustal and tectonic asymmetric structure. The joint analysis of velocities and densities with observations of the tectonic structure shows how both continental margins transition rather abruptly to what has been interpreted as exhumed mantle. We interpret this structure as the result of the first extensional pulse in the basin, with the two continental crustal domains located at either side of the exhumed mantle corresponding to the original conjugate margins. Later, this first pulse of extension was cut by a rift jump possibly caused with the presence of the J-anomaly, resulting in the migration of the deformation axis to the west and leading to the formation of the mid-Atlantic ridge and to the opening of the North Atlantic basin. Any plausible regional geodynamic model should explain how and why these different crustal domains coexist in the basin and the particular evolution of each of them.

In summary, the structure defined with the data set modelled in this thesis indicates a spatial distribution of rock types that implies a temporal evolution of the basin in two different phases: the first with continental crust extension until amagmatic mantle exhumation, and the second starting with a magmatic pulse related with the J-anomaly that ended with the establishment of the mid-Atlantic ridge and the formation of ocean crust. This spatial distribution of crust types and the inferred temporal evolution are in stark contrast to current models of lithospheric extension (e.g. Iberia Abyssal Plain) where continental rifting is followed by mantle exhumation and oceanization. Commonly accepted models studying the continent to ocean transition (involving mantle unroofing) typically postulate a continuum from continental crust extension, mantle exhumation and eventual

oceanic crust formation by gradual instauration of a decompression melt system (e.g. Pérez-Gussinyé et al., 2006). To explain this particular configuration of the basement, in the following section we examine the potential mechanisms that may have led to the formation of these domains in the Tagus Abyssal Plain.

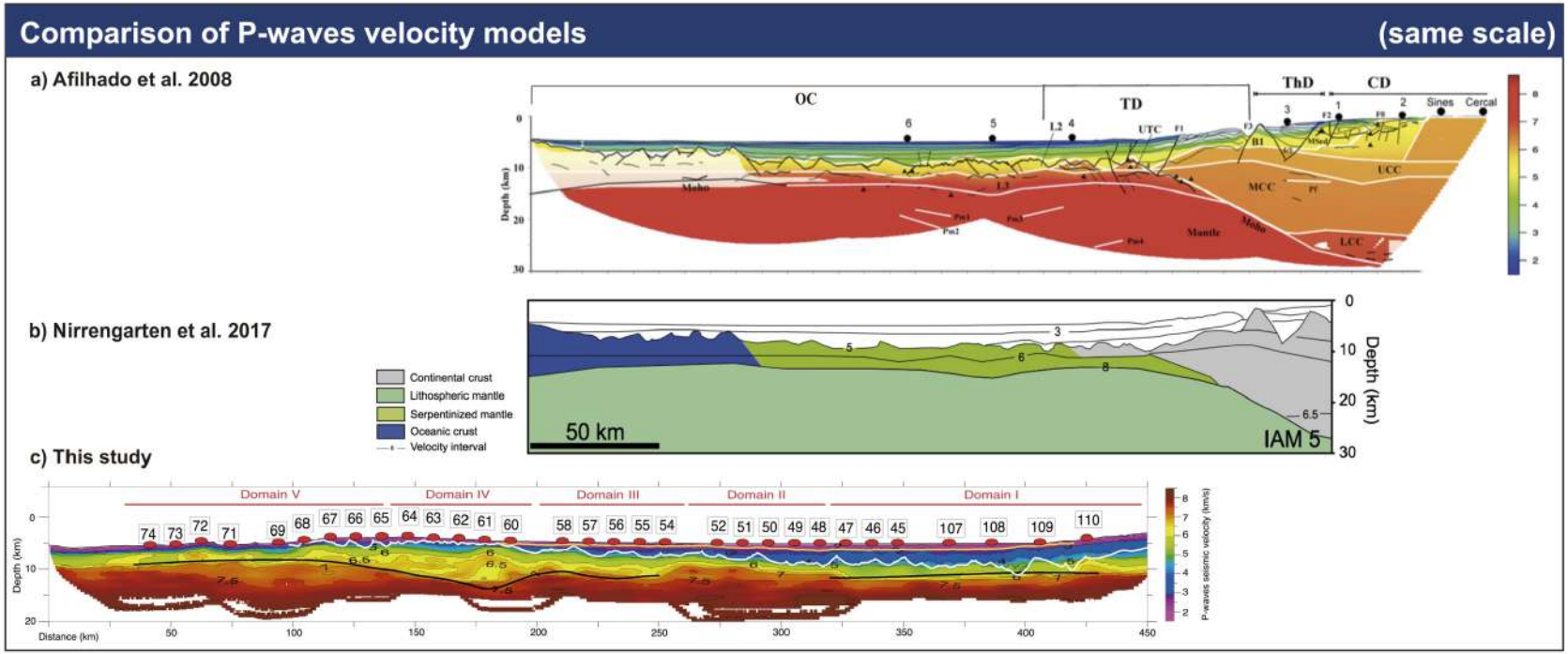

Figure 10.4 - Comparison of different interpretations of the nature of the basement across the Tagus Abyssal Plain (adjusted at the same scale). (a) Forward modelling using WAS first arrivals and MCS reflections of the IAM-5, by Afilhado et al. (2008). (b) Interpretation of the basement nature of the IAM-5, by Nirrengarten et al. (2017). (c) Joint travel-time tomography (MCS + WAS) from this work.

10.2. Implication for plate kinematics

In this section, we carry out a study of the kinematic evolution of the study area. To accomplish this goal, we review previous kinematic reconstructions proposed by different authors and compared them with the new geophysical data and models. In the kinematic reconstruction, we focus on the evolutionary steps and processes that explain the evolution of the Atlantic more than on those having taken place in the Mediterranean area, because they are not central for this work.

10.2.1. The Gulf of Lions

During the last three decades, a number of reconstructions of the tectonic evolution of the Western Mediterranean basins have been proposed and published (Rehault et al., 1984; Dewey et al., 1989; Lonergan and White, 1997; Gueguen et al., 1998; Frizon de Lamotte et al., 2000; Jolivet and Faccenna, 2000; Gelabert et al., 2002; Rosenbaum et al., 2002; Spakman and Wortel, 2004; Jolivet et al., 2009; Gutscher et al., 2012; Vergés et al., 2012; Chertova et al., 2014; Faccenna et al., 2014; van Hinsbergen et al., 2014) (Fig. 10.5 and Fig. 10.6). They all share the concept that slab rollback is the main process that triggered the opening of the Western Mediterranean basins. Those geodynamic models can be divided in two classes: 1) continuous slab models and 2) segmented slab models. The first ones consider the subduction rollback of a unique and continuous slab from the north Apennines to the Betic- Rif region (Rehault et al., 1984; Faccenna et al., 2004; Schettino and Turco, 2006; Jolivet et al., 2009; Carminati et al., 2012; Faccenna et al., 2014). The second ones consider the subduction rollback of a segmented slab that evolves in a different way depending on the regional stresses acting on each time (Wortel and Spakman, 2000; Spakman and Wortel, 2004; Vergés et al., 2012; Chertova et al., 2014; van Hinsbergen et al., 2014). Although the differences between these evolutionary models are evident, both models consider that the opening of the Western Mediterranean basins starts in the NE of the Liguro-Provençal Basin at Oligocene times followed by the opening of the Valencia Trough Basin, the Algero-Baleric Basin and finally the Alboran and Tyrrhenian Basin (Gómez de la Peña et al., 2020).

Although all these kinematic and geodynamic models differ in a number of details, they all consider a similar distribution of geological domains, as defined in the previous section. Broadly, most of these studies interpret a transition zone across the Gulf of Lions with debated petrological nature bounded by thinned continental crust towards the continent and by oceanic crust towards the centre of the basin (Fig. 10.7). In contrast, our data and models strongly suggest that, instead of exhumed continental mantle or lower continental crust, this high-velocity body is a thin oceanic crust. South and eastwards from this body, we find solid evidence for the presence of thinned continental crust, which also contrasts with all previous models that suggested that the central part of the Ligurian and Provençal basins is floored by oceanic crust (e.g. Mauffret et al., 1995; Jolivet et al., 2015). Interestingly, recent results from Dannowski et al. (2020) from a nearby MCS and WAS profile, also support that the central part of the Ligurian Basin is floored by thin continental crust rather than oceanic crust (location in pink, Fig. 10.8). Also, according to ESP's experiments (Fig. 10.8), this region has upper crustal velocities ranging from 6-6.2 km/s and lower crustal velocity anomalously high in the Gulf of Lions deep margin, suggesting that may be part of the oceanic crust. Thus, the combination of modern, high-quality data and state-of-the-art geophysical techniques, allow redefining the nature of

the geological domains in the area, challenging the prevailing conceptual models of margin formation and evolution not only at the regional level but also at a global and fundamental one.

The data and models presented here are not enough to re-define the kinematics of the opening of the Gulf of Lion margin. However, we suggest that the restriction of oceanic crust in a narrow domain should be related to episode when the back-arc extension jumped eastwards to form the Tyrrhenian. That jump must have ceased seafloor spreading and oceanization in this region of the Liguro-Provençal basin. A new kinematic model for the whole opening history of the Western Mediterranean basins is beyond the scope of our data and work and would require integration with other datasets from the Gulf of Lions, and a new study of the West Sardinia and Corsica margins. Additionally, the findings of our work should be integrated into new reconstructions, while existing ones need to be reviewed.

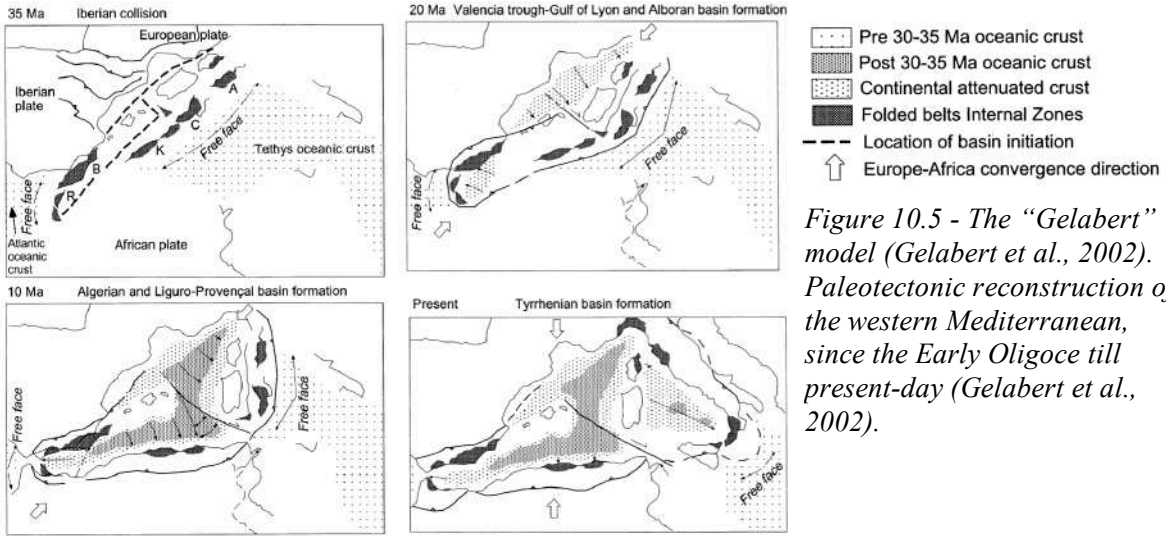

Figure 10.5 - The "Gelabert" model (Gelabert et al., 2002). Paleotectonic reconstruction of the western Mediterranean, since the Early Oligoce till present-day (Gelabert et al., 2002).

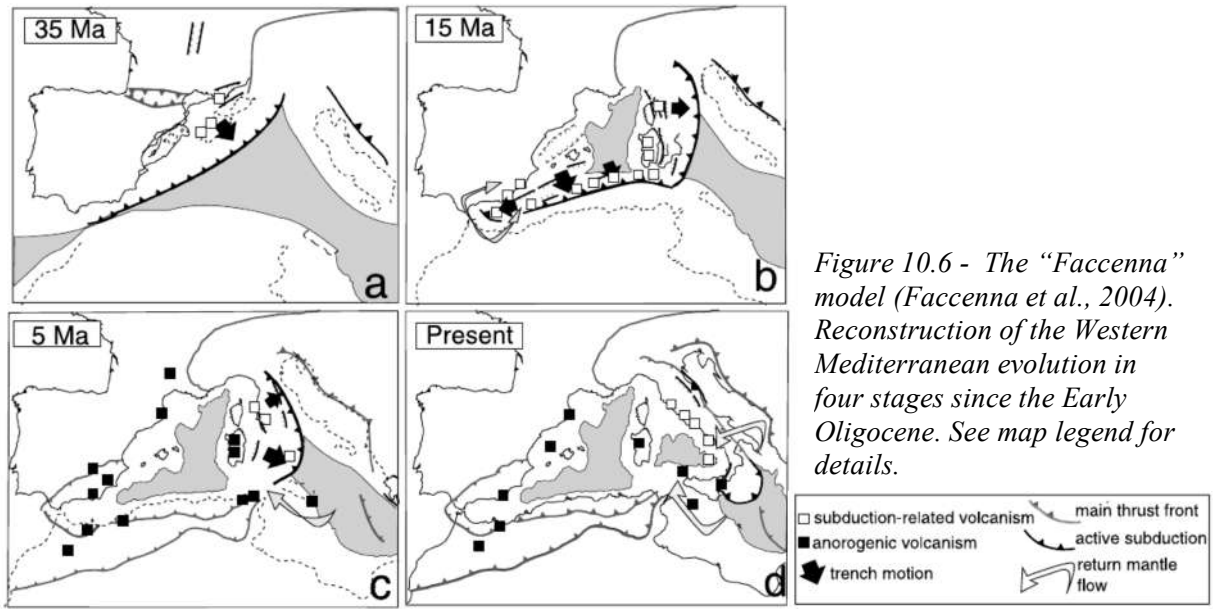

Figure 10.6 - The "Faccenna" model (Faccenna et al., 2004). Reconstruction of the Western Mediterranean evolution in four stages since the Early Oligocene. See map legend for details.

a) Mauffret et al. (1995)

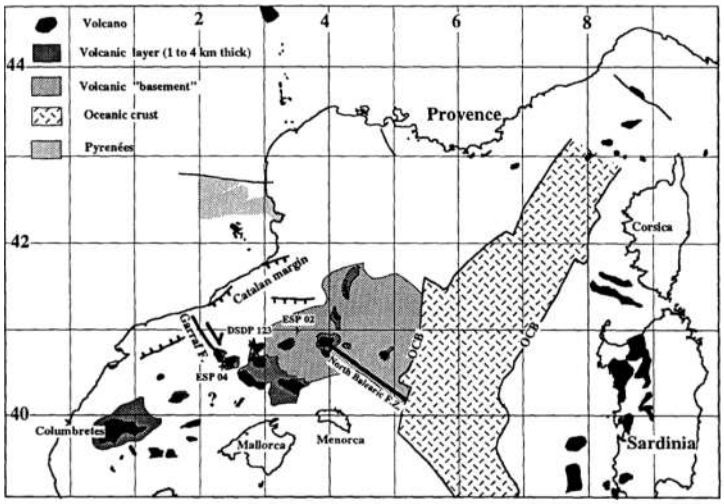

b) Jolivet et al. (2015)

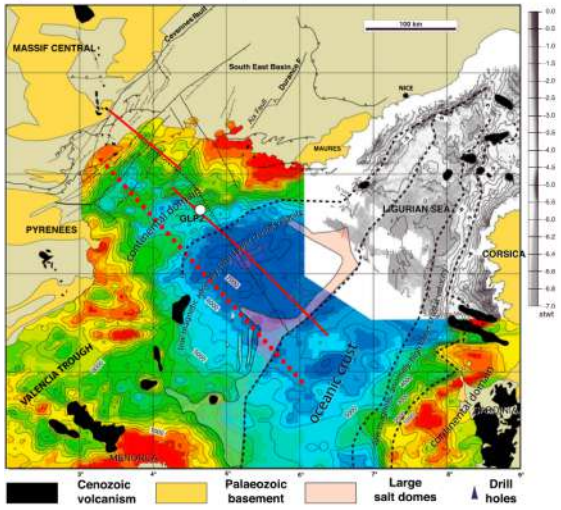

c) Granado et al. (2016)

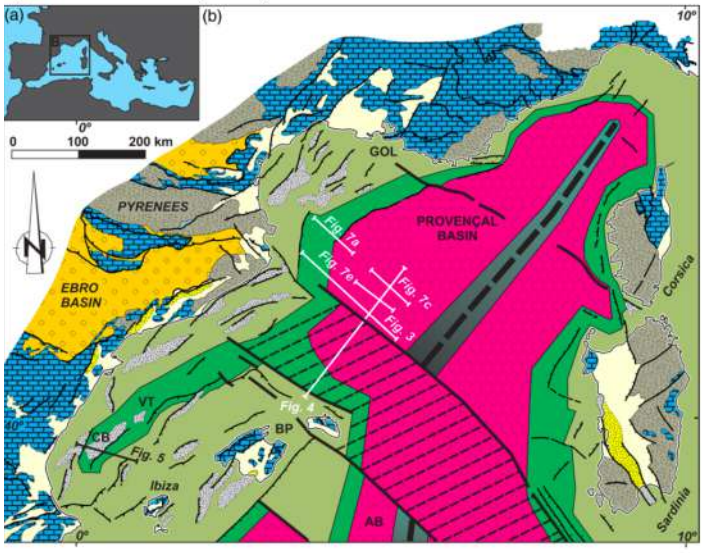

Figure 10.7 - Compilation of the three different domains across the Gulf of Lions and the Ligurian Basin (a) from Mauffret et al. (1995), (b) from Jolivet et al. (2015) and (c) from Granado et al. (2016). All studies show that the oceanic crust is more or less widely extended in a NE-SW direction along the Ligurian Basin, the Gulf of Lions and the Provençal Basin.

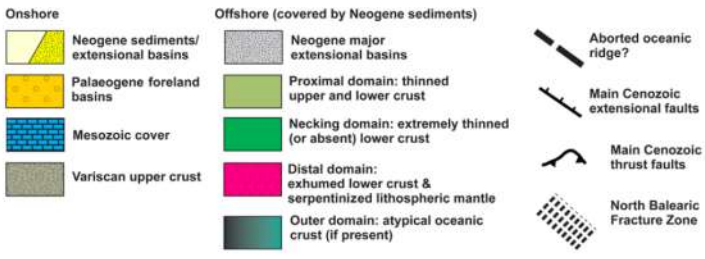

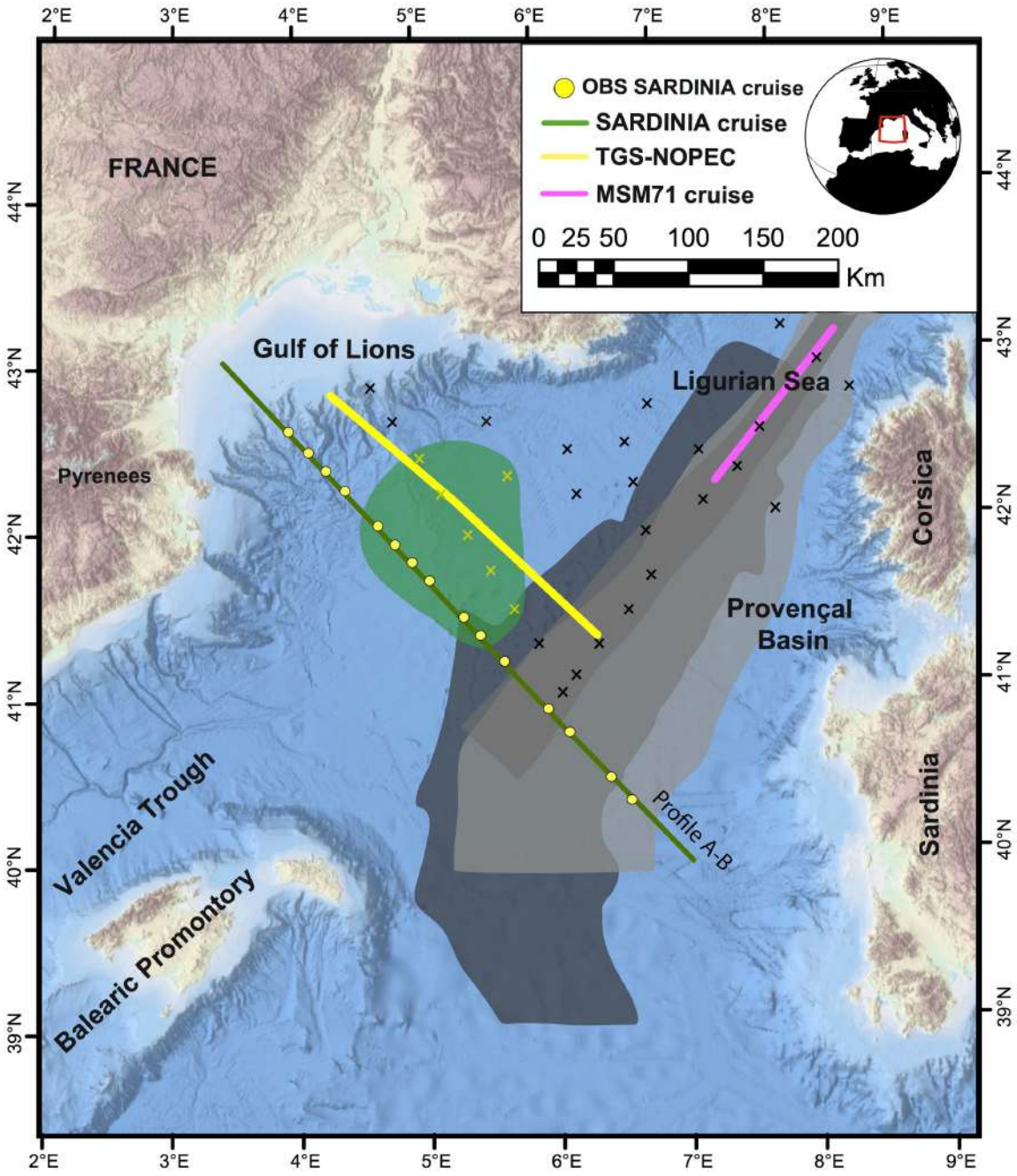

Figure 10.8 - Bathymetric and topographic map of the Gulf of Lions (SE France). It is bounded by the Ligurian Sea (NE), the Provençal Basin and Corsica-Sardinia continental margin (E), the Algero-Balearic Basin (S) and the Valencia Trough and the Balearic Promontory (SW). Green line corresponds to three WAS profiles acquired on the N/O Atlante during the Sardinia cruise (2006), yellow dots correspond to the position of every seafloor instrument (Gailler et al., 2009). Yellow line corresponds to a MCS line acquired by TGS-NOPEC M/V Zephir 1 in 2001 (Jolivet et al., 2015) and pink line corresponds to a wide-angle and multi-channel seismic line acquired by the German research vessel Maria S. Merian (Kopp et al., 2018). Cross correspond to marine ESPs (expanding spread profiles, CROC II cruise 1981): in yellow with oceanic crust velocities and black with continental crust velocities. The ESP have been useful to complement our study and helped us delineate the limits of the different crustal domains. The green area represents the extension of the oceanic domain from this work. The areas in shades of grey represent the location and extension of oceanic crust from Mauffret et al. (1995), Jolivet et al. (2015) and Granado et al. (2016).

10.2.2. The Tagus Abyssal Plain

The plate kinematic evolution of Iberia during the Mesozoic has been the subject of a debate (e.g. Sibuet et al., 2004; Neres et al., 2013; Vissers and Meijer, 2012). The numerous studies are based on several independent geological and geophysical methods, and have not yet resulted in a satisfactory accepted evolutionary model (Fig. 10.9). The limitations associated with individual constraints cause large uncertainties in the resulting plate motion models. The M-sequence of magnetic anomalies along the Newfoundland and West Iberian margins has constituted a first-order constraint on the motion of Iberia during the Mesozoic (Vissers and Meijer, 2012; Sibuet et al., 2004). Different geodynamic models have been proposed to explain the opening of the North Atlantic Ocean taking into account these constraints, including also the formation of the Tagus Abyssal Plain. These geodynamic models can be divided in two main groups depending on their fundamental working hypothesis:

i. J-anomaly is interpreted as an isochron (M0), thus associated with the formation of the first oceanic crust across the West Iberia margin and its conjugated margin (Fig. 10.10).

ii. J-anomaly is not interpreted as an isochron (M0). Instead, it is thought to correspond to an edge effect resulting from the juxta-position of an exhumed mantle domain and a magmatic oceanic domain (Fig. 10.11).

The age of final breakup and formation of first oceanic crust is particularly uncertain. Drilling results and breakup unconformity identifications date the onset of seafloor spreading at the Aptian–Albian transition (113 Ma) (Tucholke et al., 2007; Boillot et al., 1988). This is significantly younger than the age of the oldest isochrons interpreted from magnetic reversal anomalies offshore of Iberia (Srivastava et al., 2000). This discrepancy means that the interpretation of these anomalies in terms of M-sequence isochrons is disputed. Although they have been interpreted by some studies as markers of the first oceanic lithosphere (e.g. Vissers and Meijer, 2012; Sibuet et al., 2004), others authors have speculated that they might instead represent the fingerprint of igneous bodies located within zones of exhumed mantle (e.g. Sibuet et al., 2007, 2012).

The first group of kinematic models used the J-anomaly as a marker of the M0 isochron (Sibuet, 2004; Srivastava et al., 2000; Vissers and Meijer, 2012b), and assumed that oceanic magnetic anomalies are the best spatiotemporal constraints for plate kinematic modelling, although some magnetic anomalies also exist on exhumed mantle domains (Russell and Whitmarsh, 2003; Sibuet et al., 2007). Most of the regional kinematic reconstructions have been made based on this model (Fig. 10.10).

However, the Iberian Plate motion, before and during the Cretaceous normal polarity superchron, has often been questioned (Barnett-Moore et al., 2016; Le Pichon and Sibuet, 1971; Olivet, 1996; Rosenbaum et al., 2002; Sibuet, 2004; Vissers and Meijer, 2012b). This controversy is mostly related to different interpretations and restorations of the J-anomaly offshore the Iberia and Newfoundland rifted margins (Bronner et al., 2011; Tucholke and Sibuet, 2012).

The first-order kinematic reconstructions of the rifting, breakup, and seafloor spreading of the southern North Atlantic are based on the westward motion of the North American Plate relative to the Iberian/Eurasian Plate from Jurassic time to present. Most of the models (Jammes et al., 2009; Olivet, 1996; Sibuet, 2004; Vissers and Meijer, 2012a) agree on the closure of the southern North Atlantic and on the initial Triassic plate configuration (Fig. 10.9).

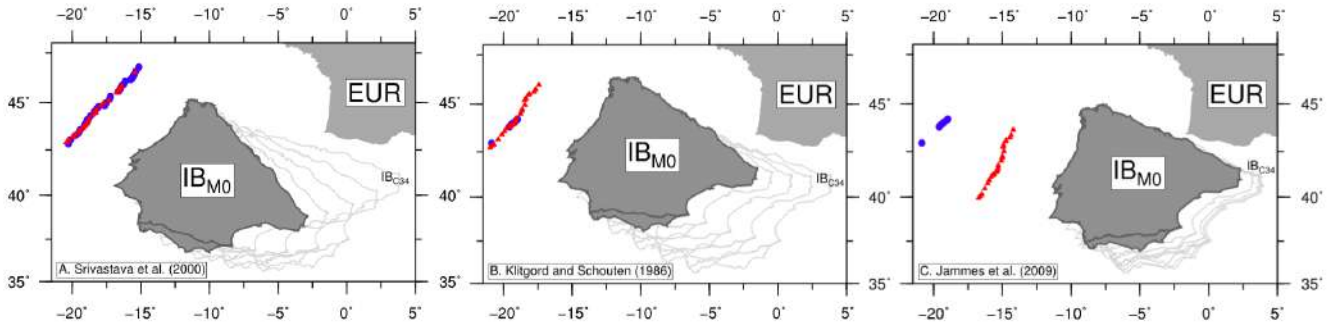

Figure 10.9 - Illustration of the three different rotation scenarios for the opening of the North Atlantic. (a) the "Srivastava" model or "scissor-type" opening of the Bay of Biscay (Vissers and Meijer, 2012; Sibuet et al., 2004; Srivastava et al., 2000) the "Klitgord and Schouten" model (Handy et al., 2010; Stampfli et al., 2002; Olivet, 1996; Le Pichon and Sibuet, 1971; Klitgord and Schouten, 1986), and (c) the "Jammes" model (Jammes et al., 2009) (modified from Barnett-Moore et al., 2016).

Currently, published plate kinematic models of Iberia fall into one of three major competing end-member models: (1) the "Srivastava" model (Vissers and Meijer, 2012; Sibuet et al., 2004; Srivastava et al., 2000), (2) the "Klitgord and Schouten" model (Handy et al., 2010; Stampfli et al., 2002; Olivet, 1996; Le Pichon and Sibuet, 1971; Klitgord and Schouten, 1986), and (3) the "Jammes" model (Jammes et al., 2009).

(1) The first argues for ~200-500 km of convergence along the Iberia-Eurasia plate boundary as a result of Iberia's ~35° counter clockwise rotation during the Cretaceous, often described as a scissor-type opening of the Bay of Biscay.

(2) The second describes a dominant left-lateral strike-slip motion along the Iberia-Eurasia plate boundary, approximated at present-day by the North Pyrenean Fault.

(3) The third implies transtensional motion along the Iberia-Eurasia plate boundary until the earliest Albian, which is then followed by an onset in minor orthogonal extension between Iberia and Eurasia, continuing until C34.

More recent studies question the validity of the magnetic anomalies and the "thin oceanic crust" (e.g. Bronner et al., 2011; Nirrengarten et al., 2017; Szameitat et al., 2018 in Fig. 10.11b). Debates questioning the validity of this particular interpretation arise from the nonvolcanic nature of the margin and the difficulties in distinguishing the different crustal types, i.e., continental and oceanic, from the exhumed subcontinental mantle lithosphere (Tucholke et al., 2007). These studies suggest that the magnetic anomalies interpreted as M-sequence are not a solid diagnostic for the presence of oceanic crust. Instead, they propose that the anomalies are created by susceptibility contrasts between zones of highly extended continental crust and exhumed mantle in the basin floor. Similarly, it has

been proposed that the high-amplitude J-anomaly might coincide with a zone of exhumed mantle punctuated by significant volcanic additions together with interbedded volcanics and sediments (e.g. Bronner et al., 2011). Based on a compilation of seismic and geochronological data, Nirrengarten et al. (2017) argued that the J-anomaly may not correspond to an oceanic magnetic anomaly and therefore should not be used as such for kinematic restorations. Later, Causer et al. (2020) proposed that in the southern part of the Newfoundland margin, the J-anomaly could be a product of mantle dynamics preceding plate rupture (Fig. 10.11c).

A new model is supported by this PhD work showing that there is a pair of conjugated margins from an aborted rift system under the TAP. This observation does not support the classical model of opening Iberia-Newfoundland where the pair of conjugate margins are at both sides of the ocean. In consequence, the evidence that there is a block of continental crust westwards of a narrow exhumed mantle domain poses new constraints that challenge the prevailing conceptual model of extension in this iconic continental margin. Further, it supports that the faint magnetic anomalies interpreted as the M series, if real anomalies and not the product of spurious ship tracks are not caused by oceanic crust lineaments.

Therefore, previous rifting models proposing that the TAP, and the West Iberia margin, is symmetric with respect to its conjugate Newfoundland margin are not correct. Thus, the related kinematic models assume a rift opening that is symmetric between the two pair of conjugate margins. In light of our results, we propose that all the formation and evolutionary models of the West Iberia margin must be revised, because the basic assumption of a symmetric lithospheric structure is incorrect. Consequently, the assumption of a symmetric opening for the North Atlantic rift is unfeasible.

The data and models presented in this thesis do not provide enough information to re-define the kinematics of the opening of the whole North Atlantic system. However, the observations point to a multiphase evolution at least in the TAP area, that includes: 1) a NE-SW regional opening and continental rifting of the easternmost part of the TAP leading to mantle exhumation along a unique detachment fault, 2) a ridge jump that moved the axis of extension and deformation toward the west, related to or caused by the inception of the J-anomaly, and 3) oceanic spreading, which resulted in the establishment of the mid-Atlantic ridge and the generation of oceanic crust. This sequence of events explains the crustal domains, physical properties and tectonic structure across the TAP observed in our seismic data.

As in the case of the Gulf of Lions, a new kinematic model for the rift and early oceanic spreading history of the North Atlantic Ocean is beyond the scope of this work. the new model requires the integration and re-evaluation of existing datasets from the rest of the basins that form the West Iberian margin, because our results also support that there exists a north-south lithospheric segmentation that must have affected the formation.

Detailed modelling of new seismic lines in all the basins could contribute to its knowledge that currently is poorly studied in the literature. Moreover, the findings of our work should be integrated into new reconstructions, while existing ones need to be reviewed.

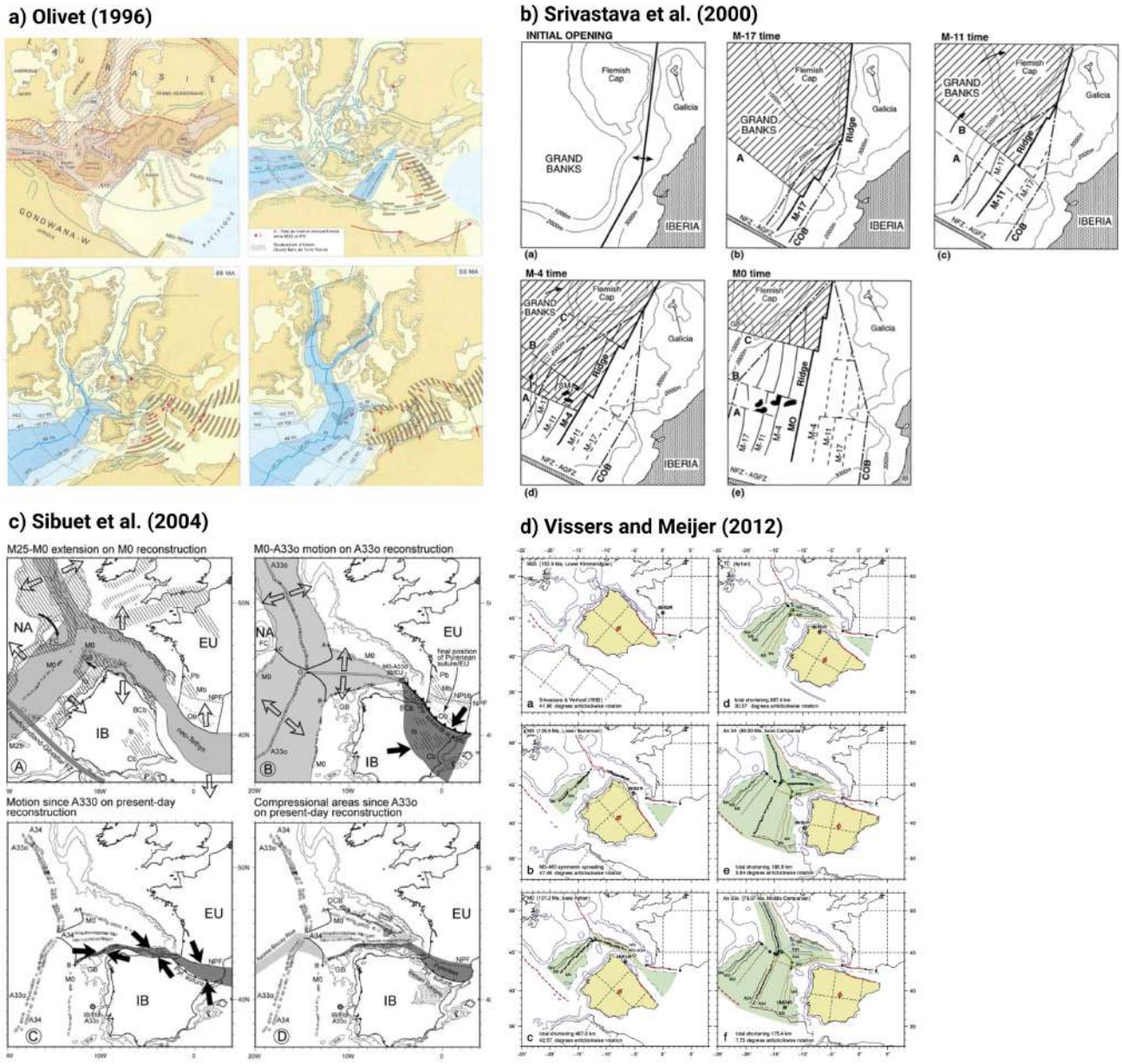

Figure 10.10 - Compilation of different kinematic reconstructions from the North Atlantic ocean: (a) from Olivet et al. (1996), (b) from Srivastave et al. (2000), (c) from Sibuet et al. (2004) and (d) from Vissers and Meijer, 2012. All these models used the J-magnetic anomaly as an isochron (M0).

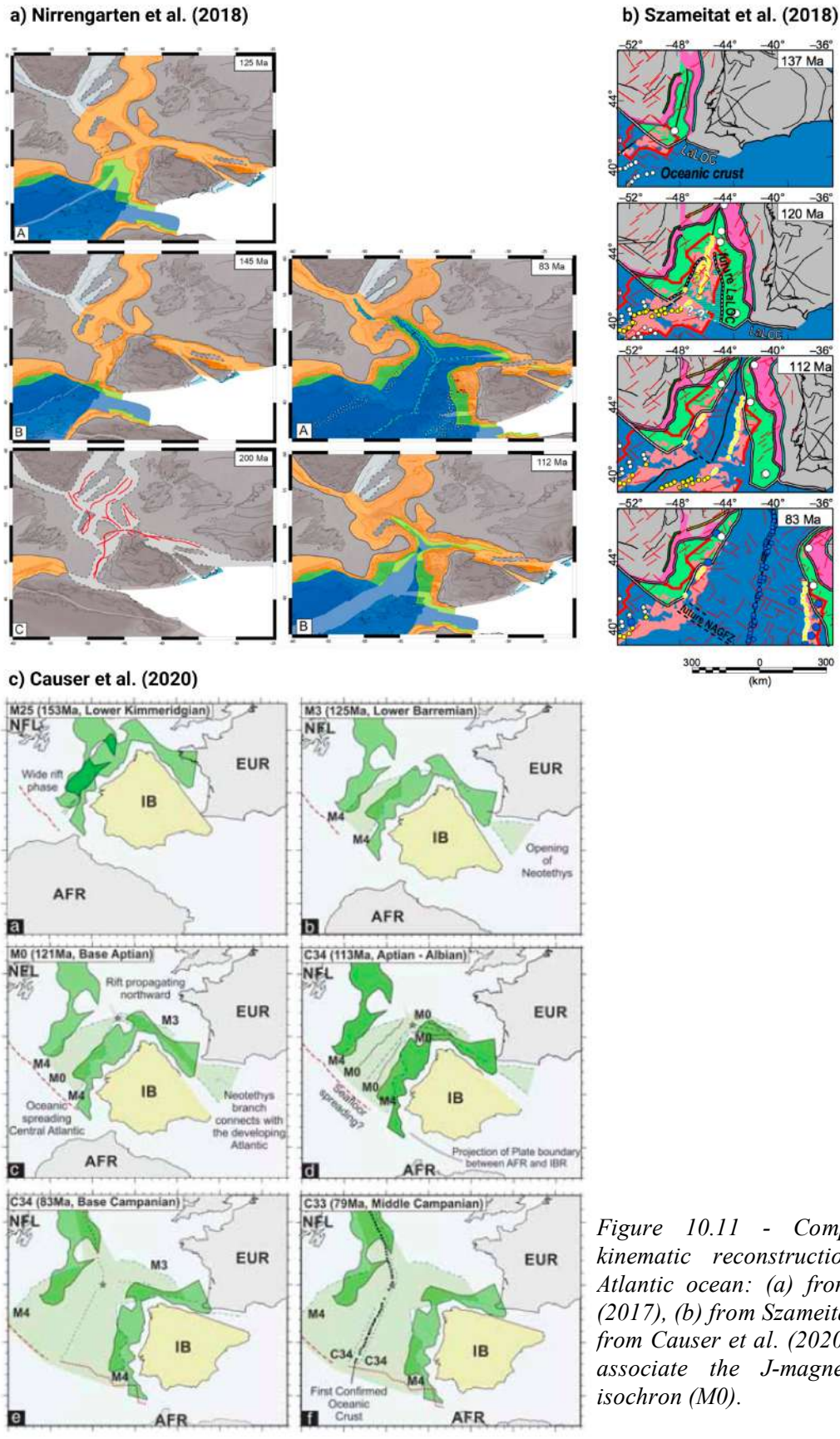

Figure 10.11 - Compilation of different kinematic reconstructions from the North Atlantic ocean: (a) from Nirrengarten et al. (2017), (b) from Szameitat et al. (2018) and (c) from Causer et al. (2020). These model do not associate the J-magnetic anomaly to an isochron (M0).

References

Afilhado, A., Matias, L., Shiobara, H., Hirn, A., Mendes-Victor, L., and Shimamura, H. (2008). From unthinned continent to ocean: The deep structure of the West Iberia passive continental margin at 38°N. Tectonophysics, 458(1–4), 9–50, doi: 10.1016/ j.tecto.2008.03.002.

Barnett-Moore, N., Hosseinpour, M., and Maus, S. (2016). Assessing discrepancies between previous plate kinematic models of Mesozoic Iberia and their constraints. Tectonics, 35(8), 1843–1862, doi: 10.1002/2015tc004019.

Boillot, G. and Malod, J. (1988). The north and north-west Spanish continental margin: a review. Revista de la Sociedad Geológica de España, 1(3-4), 295-316.

Boillot, G., Recq, M., Winterer, E.L., Meyer, A.W., Applegate, J., Baltuck, M., Bergen, J.A., Comas, M.C., Davies, T.A., Dunham, K. and Evans, C.A., 1987. Tectonic denudation of the upper mantle along passive margins: a model based on drilling results (ODP leg 103, western Galicia margin, Spain). Tectonophysics, 132(4), pp.335-342.

Bronner, A., Sauter, D., Manatschal, G., Péron-Pinvidic, G. and Munschy, M. (2011). Magmatic breakup as an explanation for magnetic anomalies at magma-poor rifted margins, Nature Geoscience, 4(8), 549.

Carminati, E., Lustrino, M., Doglioni, C. (2012). Geodynamic evolution of the central and western Mediterranean: Tectonics vs. igneous petrology constraints. Tectonophysics 579, 173–192, doi: 10.1016/j.tecto.2012.01.026

Chertova, M. V., Spakman, W., Geenen, T., Van Den Berg, A. P., Van Hinsbergen, D.J.J. (2014). Underpinning tectonic reconstructions of the western Mediterranean region with dynamic slab evolution from 3-D numerical modeling. J. Geophys. Res. Solid Earth 119, 5876–5902, doi: 10.1002/2014JB011150

Cohen, C.R. (1980). Plate tectonic model for the Oligo-Miocene evolution of the Western Mediterranean. Tectonophysics 68, 283–311.

Contrucci, I., Nercessian, A., Béthoux, N., Mauffret, A. and Pascal, G. (2001). A Ligurian (western Mediterranean Sea) geophysical transect revisited. Geophysical Journal International, 146(1), pp.74-97.

Dannowski, A., Kopp, H., Grevemeyer, I., Lange, D., Thorwart, M., Bialas, J., and Wollatz-Vogt, M. (2020). Seismic evidence for failed rifting in the Ligurian Basin, Western Alpine domain. Solid Earth, 11(3), 873–887, doi: 10.5194/se-11-873-2020.

Dean, S. M., Minshull, T. A., Whitmarsh, R. B., and Louden, K. E. (2000). Deep structure of the ocean-continent transition in the southern Iberia Abyssal Plain from seismic refraction profiles: The IAM-9 transect at 40°200N. Journal of Geophysical Research, 105(B3), 5859, doi: 10.1029/1999JB900301.

Dewey, J. F., Helman, M. L., Turco, E., Hutton, D. H. W. and Knott, S. D. (1989). Kinematics of the western Mediterranean. Alpine Tectonics, vol. 45, edited by P. Cowardm, D. Dietrich, and G. Park, pp. 265–283, Geological Society Special Publication, London.

Faccenna, C., Piromallo, C., Crespo-Blanc, A., Jolivet, L., Rossetti, F. (2004). Lateral slab deformation and the origin of the western Mediterranean arcs. Tectonics 23, n/a-n/a, doi: 10.1029/2002TC001488.

Faccenna, C., Becker, T.W., Auer, L., Billi, A., Boschi, L., Brun, J.P., Capitanio, F.A., Funiciello, F., Horvàth, F., Jolivet, L., Piromallo, C., Royden, L., Rossetti, F., Serpelloni, E. (2014). Mantle dynamics in the Mediterranean. Rev. Geophys. 52, 283– 332. doi:10.1002/2013RG000444.

Frizon de Lamotte, D., Saint Bezar, B., Bracène, R., Mercier, E. (2000). The two main steps of the Atlas building and geodynamics of the western Mediterranean. Tectonics 19, 740–761.

Gailler, A., Klingelhoefer, F., Olivet, J. L., Aslanian, D. (2009). The Sardinia scientific party, and Technical OBS team. Crustal structure of a Young margin pair: New results across the Liguro-Provençal Basin from wide-angle seismic tomography. Earth Planet. Sci. Lett., 286, 333–345,doi: 10.1016/j.epsl.2009.1007.1001.

Gelabert, B., Sàbat, F., and Rodríguez-Perea, A. (2002). A new proposal for the late Cenozoic geodynamic evolution of the western Mediterranean: Terra Nova, v. 14, no. i, p. 93–100.

Gomez de la Peña, L., Ranero, C. R., Gràcia, E., and Booth-Rea, G. (2020). The evolution of the westernmost Mediterranean basins. Earth-Science Reviews, 103445, doi:10.1016/j.earscirev.2020.103445.

Granado P., Urgeles R., Sàbat F., Albert-Villanueva E., Roca E., Muñoz J. A., Mazzuca N., Gambini R. (2016). Geodynamical framework and hydrocarbon plays of a salt giant: the NW Mediterranean Basin. Petroleum Geoscience, 22, 309-321, doi:10.1144/petgeo2015-084.

Gueguen, E., Doglioni, C., Fernandez, M. (1998). On the post-25 Ma geodynamic evolution of the western Mediterranean. Tectonophysics 298, 259–269, doi: 10.1016/S0040-1951(98)00189-9.

Gutscher, M.A., Dominguez, S., Westbrook, G.K., Le Roy, P., Rosas, F., Duarte, J.C., Terrinha, P., Miranda, J.M., Graindorge, D., Gailler, A., Sallares, V., Bartolome, R. (2012). The Gibraltar subduction: A decade of new geophysical data. Tectonophysics 574–575, 72–91, doi: 10.1016/j.tecto.2012.08.038

Handy, M. R., Schmid, S. M., Bousquet, R., Kissling, E., and Bernoulli, D. (2010). Reconciling plate-tectonic reconstructions of Alpine Tethys with the geological–geophysical record of spreading and subduction in the Alps, Earth Sci. Rev., 102, 121–158.

Jammes, S., Manatschal, G., Lavier, L., and Masini, E. (2009). Tectonosedimentary evolution related to extreme crustal thinning ahead of a propagating ocean: Example of the western Pyrenees, Tectonics, 28, TC4012, doi: 10.1029/2008TC002406.

Jolivet, L., and Faccenna, C. (2000). Mediterranean extension and the Africa-Eurasia collision. Tectonics, 19(6), 1095–1106, doi: 10.1029/2000TC900018.

Jolivet, L., Augier, R., Robin, C., Suc, J.P., Rouchy, J.M. (2006). Lithospheric-scale geodynamic context of the Messinian salinity crisis. Sediment. Geol. 188–189, 9–33, doi: 10.1016/j.sedgeo.2006.02.004.

Jolivet, L., Faccenna, C., Piromallo, C. (2009). From mantle to crust: Stretching the Mediterranean. Earth Planet. Sci. Lett. 285, 198–209, doi: 10.1016/j.epsl.2009.06.017.

Jolivet, L., Gorini, C., Smit, J. and Leroy, S. (2015). Continental breakup and the dynamics of rifting in back-arc basins: the Gulf of Lion margin. Tectonics, 34, 662–679, doi:10.1002/2014TC003570.

Klitgord, K., and Schouten, H. (1986). Plate kinematics of the central Atlantic, Geol. North Am., 1000, 351–378.

Kopp, H., Lange, D., Thorwart, M., Paul, A., Dannowski, A., Petersen, F., Aubert, C., Beeck, F., Beniest, A., Be- sançon, S., Brotzer, A., Caielli, G., Crawford, W., Deen, M., Lehmann, C., Marquardt, K., Neckel, M., Papanagnou, L., Schramm, B., Schröder, P., Steffen, K.-P., Wolf, F., and Xia, Y.: RV MARIA S. MERIAN Fahrtbericht/Cruise Report MSM71 LOBSTER: Ligurian Ocean Bottom Seismology and Tectonics Research, Las Palmas (Spain) – Heraklion (Greece) 07.02.–27.02.2018, GEOMAR Report, N. Ser. 041. GEOMAR Helmholtz-Zentrum für Ozeanforschung Kiel, Kiel, Germany, 47 pp., doi: 10.3289/GEOMAR_REP_NS_41_2018, 2018.

Le Douaran, S., Burrus, J., Avedik, F. (1984). Deep structure of the North-Western Mediterranean Basin: results of a two-ship seismic survey. Mar. Geol. 55, 325–345.

Le Pichon, X., and Sibuet, J.-C. (1971). Western extension of boundary between European and Iberian plates during the Pyrenean orogeny, Earth Planet. Sci. Lett., 12, 83–88.

Lonergan, L., and White, N., (1997). Origin of the Betic-Rif mountain belt. Tectonics 16, 504–522.

Manatschal, G., Froitzheim, N., Rubenach, M., and Turrin, B. D. (2001). The role of detachment faulting in the formation of an ocean-continent transition: insights from the Iberia Abyssal Plain. Geological Society, London, Special Publications, 187(1), 405-428.

Manatschal, G., Sutra, E., and Péron-Pinvidic, G. (2010). The lesson from the Iberia-Newfoundland rifted margins: how applicable is it to other rifted margins. CM 2010 Abstracts, 2, 27-37.

Martínez-Loriente, S., Sallarès, V., Gràcia, E., Bartolome, R., Dañobeitia, J. J., and Zitellini, N. (2014). Seismic and gravity constraints on the nature of the basement in the Africa-Eurasia plate boundary: New insights for the geodynamic evolution of the SW Iberian margin. Journal of Geophysical Research: Solid Earth, 119(1), 127-149.

Mauffret, A., Pascal, G., Maillard, A., and Gorini, C. (1995). Tectonics and deep structure of the north-western Mediterranean Basin. Marine and petroleum geology, 12(6), 645-666.

Minshull, T., Dean, S., and Whitmarsh, R. (2014). The Peridotite Ridge province in the southern Iberia Abyssal Plain: Seismic constraints revisited, J. Geophys. Res. Solid Earth, 119, 1580–1598, doi: 10.1002/2014JB011011.

Moulin, M., Klingelhoefer, F., Afilhado, A., Schnurle, P., Rabineau, M., Berlier, M.O. and Feld, A. (2015). Deep crustal structure across a young passive margin from wide-angle and reflection seismic data (The SARDINIA Experiment) – I. Gulf of Lion's margin. Bulletin Société Géologique de France, 186, 309–330.

Neres, M., Miranda, J., and Font, E. (2013). Testing Iberian kinematics at Jurassic-Cretaceous times, Tectonics, 32, 1312–1319, doi:10.1002/tect.20074.

Nirrengarten, M., Manatschal, G., Tugend, J., Kusznir, N. J., and Sauter, D. (2017). Nature and origin of the J-magnetic anomaly offshore Iberia-Newfoundland: Implications for plate reconstructions. Terra Nova, 29(1), 20–28, doi: 10.1111/ter.12240.

Olivet, J.L. (1996). La cinématique de la plaque Ibérie, Bull. Cent. Rech. Explor. Prod. Elf Aquitaine, 20, 131– 195.

Pascal, G.P., Mauffret, A., Patriat, P. (1993). The ocean–continent boundary in the Gulf of Lion from analysis of expanding spread profiles and gravity modelling. Geophys. J. Int. 113, 701–726.

Pérez-Gussinyé, M., Morgan, J. P., Reston, T. J., and Ranero, C. R. (2006). The rift to drift transition at non-volcanic margins: Insights from numerical modelling. Earth and Planetary Science Letters, 244(1-2), 458-473.

Péron-Pinvidic, G., and Manatschal, G. (2008). The final rifting evolution at deep magma-poor passive margins from Iberia-Newfoundland: a new point of view. International Journal of Earth Sciences, 98(7), 1581–1597, doi: 10.1007/s00531-008-0337-9.

Péron-Pinvidic, G., Manatschal, G., Osmundsen, P.T. (2013). Structural comparison of archetypal Atlantic rifted margins: A review of observations and concepts. Mar. Pet. Geol. 43, 21T47, doi: 10.1016/j.marpetgeo.2013.02.002.

Pinheiro, L. M., Whitmarsh, R. B., and Miles, P. R. (1992). The ocean-continent boundary off the western continental margin of Iberia-II. Crustal structure in the Tagus Abyssal Plain, Geophys. J. Int., 109, 106–124.

Rehault, J., Boillot, G., Mauffret, A. (1984). The Western Mediterranean Basin: geological evolution. Mar. Geol. 55, 447–477.

Rosenbaum, G., Lister, G., and Duboz, C. (2002). Reconstruction of the tectonic evolution of the Western Mediterranean since the Oligocene, J. Virtual Explor., 8, 107–130, doi: 10.3809/jvirtex.2002.00053.

Russell, S. M., and Whitmarsh, R. B. (2003). Magmatism at the west Iberia non-volcanic rifted continental margin: evidence from analyses of magnetic anomalies. Geophysical Journal International, 154(3), 706-730.

Stampfli, G., Borel, G., Marchant, R., and Mosar, J. (2002). Western Alps geological constraints on western Tethyan reconstructions, J. Virtual Explorer, 8, 77–106.

Sallarès, V., Martínez-Loriente, S., Prada, M., Gràcia, E., Ranero, C., Gutscher, M.A., Bartolome, R., Gailler, A., Dañobeitia, J.J. and Zitellini, N. (2013). Seismic evidence of exhumed mantle rock basement at the Gorringe Bank and the adjacent Horseshoe and Tagus abyssal plains (SW Iberia). Earth and Planetary Science Letters, 365, pp.120-131.

Schettino, A., and Turco, E. (2006). Plate kinematics of the Western Mediterranean region during the Oligocene and Early Miocene. Geophysical Journal International, 166(3), 1398-1423.

Sibuet, J.C. (2004). Pyrenean orogeny and plate kinematics. Journal of Geophysical Research, 109, B08104, doi: 10.1029/

2003JB002514.

Sibuet, J.C., Srivastava, S. P., Enachescu, M., and Karner, G. D. (2007). Early Cretaceous motion of Flemish Cap with respect to North America: Implications on the formation of Orphan Basin and SE Flemish Cap Galicia Bank conjugate margins. Geological Society of London, Special Publication, 282(1), 63–76, doi: 10.1144/SP282.4.

Sibuet, J.C., Rouzo, S., and Srivastava, S. (2012). Plate tectonic reconstructions and paleogeographic maps of the central and North Atlantic oceans. Canadian Journal of Earth Sciences, 49(12), 1395-1415.

SHIPBOARD SCIENTIFIC PARTY 1998c. Site 1068. In: Whitmarsh, R. B., Beslier, M.-O. et al. (eds) Proceedings of the ODP, Initial Reports,103. Ocean Drilling Program, College Station, TX, 163 – 218, doi: 10.2973/odp.proc.ir.173.106.1998.

SHIPBOARD SCIENTIFIC PARTY 1987a. Site 637. In: Boillot, G., Winterer, E. L. et al. (eds) Proceedings of the ODP, Initial Reports,103. Ocean Drilling Program, College Station, TX, 123 – 219, doi: 10.2973/odp.proc.ir.103.108.1987.

Spakman, W., and Wortel, R. (2004). A tomographic view on western Mediterranean geodynamics. In The TRANSMED atlas. The Mediterranean region from crust to mantle (pp. 31-52). Springer, Berlin, Heidelberg.

Srivastava, S. P., Sibuet, J. C., Cande, S., Roest, W. R., and Reid, I. D. (2000). Magnetic evidence for slow seafloor spreading during the formation of the Newfoundland and Iberian margins. Earth and Planetary Science Letters, 182(1), 61–76.

Sutra, E., Manatschal, G. (2012). How does the continental crust thin in a hyperextended rifted margin? Insights from the iberia margin. Geology 40, 139T 142, doi: 10.1130/G32786.1.

Szameitat, L. S. A., Ferreira, F. J. F., Manatschal, G., and Helbron, M. D. C. P. L. (2018). Evidence of mantle inheritance on the Ultra-Distal Western Iberian Margin from transformed total Magnetic Anomaly. Brazilian Journal of Geophysics, 36(3), 307-316.

Tucholke, B., Sawyer, D., and Sibuet, J.-C. (2007). Breakup of the Newfoundland–Iberia rift, Geol. Soc. Lond. Spec. Publ., 282, 9–46.

Tucholke, B. E., and Sibuet, J.-C. (2012). Problematic plate reconstruction, Nat. Geosci., 5, 676–677.

Van Hinsbergen, D.J.J., Vissers, R.L.M., Spakman, W. (2014). Origin and consequences of western Mediterranean subduction, rollback, and slab segmentation. Tectonics 33, 393–419, doi:10.1002/2013TC003349.

Vergés, J., and Fernàndez, M., (2012). Tethys–Atlantic interaction along the Iberia–Africa plate boundary: The Betic–Rif orogenic system. T ectonophysics 579, 144–172, doi: 10.1016/j.tecto.2012.08.032

Vissers, R., and Meijer, P. T. (2012). Mesozoic rotation of Iberia: Subduction in the Pyrenees?. Earth Sci. Rev., 110, 93–110.

Wortel, M.J., Spakman, W. (2000). Subduction and slab detachment in the Mediterranean- Carpathian region. Science 290, 1910–1917, doi: 10.1126/science.290.5498.1910.

Part V
CONCLUSIONS & FORWARD LOOK

Chapter 11

Conclusions

The results obtained from the processing, modelling and analysis of the different datasets present in this work has permitted to determine the nature of the basement and to elucidate the formation mechanisms of two classical examples of rifted margins.

Further, the results shown in this thesis shed new light on the geodynamic processes that governed the first stages of the opening of the Gulf of Lions and Ligurian basin in the Western Mediterranean during the Oligocene, as well as for the opening of Tagus Abyssal Plain, in West Iberia, during the Jurassic. In the latter case, my results allowed to propose a new view concerning its evolution into the breakup of the North Atlantic Ocean.

The most relevant findings of this research are summarized below.

11.1. General conclusions of the work

1) To characterize the structure and nature of the basement, I have applied a novel approach that allows reducing the uncertainty of the P-wave (Vp) model compared to most previous approaches. I have performed a joint refraction and reflection travel-time tomography to a combined set of travel-times from Wide-Angle Seismic (WAS) refracted and reflected phases together with reflections from spatially coincident Multi-Channel Seismic (MCS) data. This new tomographic approach provides the sediment velocity structure and top of basement geometry with high accuracy, and helps to better constraining the velocity-depth definition of basement layers and the limits between the different geological domains, especially across the COT zone.

2) The integration of MCS and WAS data into a joint travel-time inversion scheme allows to significantly reducing the basement velocity uncertainty, so that their petrological nature can be more objectively defined. The improved statistical analysis of velocity uncertainty further helps to provide realistic bounds to the velocity and velocity-derived properties of each layer

and segment of the profiles.

3) The Vp models obtained from the combination of WAS and MCS data, together with complementary information from gravity modelling and the Vp-depth profiles reveal different, well-constrained basement affinities in the Gulf of Lions and the Tagus Abyssal Plain. The new constrains concerning the petrological nature and settings of the crustal domains have important structural and geodynamic implications for both basins.

4) The combined interpretation of the Vp model with the MCS seismic image yields a new interpretation of the tectonic architecture and crustal structure of the Gulf of Lions and the Tagus Abyssal Plain areas with implications for the surrounding basins.

11.2. Specific conclusions for each margin

11.2.1. The Gulf of Lions

Based on the crustal properties derived from the 2D Vp tomography model and the tectonic structure observed in the MCS profile, the basement in the Gulf of Lions - Ligurian margin can be divided in three different domains:

(i) Continental domain: this domain is interpreted to be constituted by rifted continental crust, thinning from ~20 km beneath the continental platform to ~5 km thick oceanwards, at the boundary with the oceanic crust domain, implying a stretching factor (β) of ~8.

(ii) Oceanic domain: this domain was previously interpreted as a transitional domain containing exhumed mantle rocks and/or exhumed lower crustal rocks. However, the models obtained here indicate that it more likely is a ~5 km-thick lens of oceanic crust. Based on of partial decompression melting models, we show that the presence of a 5 km-thick oceanic crust is consistent with the amount of lithospheric stretching observed along the margin.

(iii) Thin continental domain: my results support the presence of ultra-thin (<4 km) continental crust, rather than the previously inferred oceanic crust, for this domain.

The structure across the deep-water region of the Gulf of Lions obtained from joint refraction and reflection tomography has allows a better accuracy and resolution in the definition crustal structure and properties as compared to previous approaches. The models in this work support the presence of an abrupt COT (<10 km-wide) on either side of a ~100 km-wide segment of anomalously thin (<5 km) oceanic crust. I propose that the confinement of oceanic crust to a narrow domain, between two continental-crust domains, may be a consequence of limited back-arc spreading that stopped when extension jumped eastwards to form the Tyrrhenian basin, abruptly ceasing the oceanization process in this region of the Liguro-Provençal basin.

11.2.2. The Tagus Abyssal Plain

My results indicate that basement of the Tagus Abyssal Plain (TAP) segment of the West Iberia margin has five domains showing three different crustal structure and rock properties (Vp and density). From east to west, Domains I and III are made of extended continental crust, whilst Domain II is a ~60 km-wide segment made of partly serpentinized exhumed mantle rocks. Westwards, there is Domain IV, which presents a 7-9 km thick segment of slightly thickened oceanic crust coinciding with the location of the J-magnetic anomaly. Finally, Domain V appears to be formed by oceanic crust thinning westwards from 6 to 3 km. My interpretation is that this domain was formed during the Cretaceous Magnetic Quiet Zone (CMQZ), possibly at ultra-slow spreading rates.

I have also characterized the tectonic structure of the basin from the interpretation of the MCS seismic image. From the 2D Vp model and the tectonic characterization, the FRAME-2 profile has allowed performing for the first time a comprehensive study of the crustal configuration of the TAP. The data analysis supports the presence of three different crustal domains coexisting at the margin:

(i) Ultra-thin continental domains, which are represented by Domain I and Domain II. Domain I is found mostly under the eastern half of the TAP and Domain II under the westernmost sector of the TAP. Both domains present thickness variations and show a crustal basement mostly cut by normal faults dipping westwards for Domain I and dipping eastwards for Domain III. We propose that both domains are part of the same crust, but they are affected by different degrees of extension. Thus, we propose that together they represent a pair of conjugate margins.

(ii) Exhumed mantle domain, located under the central part of the TAP. Domain III is made of exhumed mantle, partially serpentinized in the upper 6-8 km. This domain is younger than the continental domains on either side. We interpret that this domain opened by the action of a ~30 km detachment fault that exhumed the mantle from east to west during the first stage of extension.

(iii) Oceanic crust domains are found at the westernmost part of the seismic profile, under the Madeira-Tore Rise (Domain IV and Domain V). The basement has a thickness of 7-9 km at the location of the J-anomaly and does not show a tectonic structure (Domain IV). However, oceanwards, the oceanic crust (Domain V) thins until it reaches a thickness of 3 km. We interpret that this domain formed under different conditions from Domain IV. Domain V formed under a lower expansion rate and a strong influence of extensional tectonics.

The distribution of basement domains in the TAP is at odds with evolutionary models of magma-poor margins that have been previously applied to the West Iberia margin. In these models, continental breakup is followed by mantle exhumation, promoting asthenospheric rise and the subsequent establishment of a stable spreading system. In our work, we propose that the origin of the Tagus Abyssal Plain and the configuration of its domains resulted from a more complex geodynamic evolution.

The proposed model includes five stages of deformation, in which mantle exhumation through a detachment fault stopped continental rifting of an asymmetric margin system. After this, a jump in the location of the extensional axis accompanied by a first pulse of magmatism gave birth to seafloor spreading centre, which continued to develop as an ultra-slow spreading centre during the CMQZ.

The main features of these stages are briefly exposed below:

I. The first stage consists of an asymmetric continental crustal thinning by sequential normal faulting. During this stage, the upper mantle Vp supports partial serpentinization of the uppermost 8-10 km was facilitated by faults reaching the mantle on either conjugate sides of the margin. However, despite the presence of weak serpentine in the mantle, none of the faults that cut the boundary developed to exhume the mantle.

II. During the second stage, it appears to have occurred a change in the direction of extension, possibly causing a change in the strike of the faults. This would have also rotated the strike of structures in the westernmost continental crust domain. We propose that this change caused the continental fault system to stop, and a newly oriented fault system caused the final continental breakup and initiated the exhumation of the mantle.

III. In the third stage, the fault that initiated at the end of the previous stage extended further, exhuming mantle to the paleo-seafloor along a ~30 km long heave. It has associated a symmetric high, producing a core complex-type of detachment geometry.

IV. In the fourth stage, most of the plate opening was assimilated by the creation of a new magmatic crust. The first pulse corresponds to the J-anomaly sector, where fault activity is minimal. At this stage, a ridge jump and the subsequent spreading centre propagation caused the sudden termination of the rift described in the stage (I, II and III) and led to the formation of oceanic crust. The oceanic igneous crust in this domain is about ~8-9 km and shows the characteristic Penrose-type structure with Layer 2 and Layer 3.

V. Finally, in the last stage, the igneous oceanic crust thins indicating the establishment of an ultra-slow spreading centre with reduced magma production. My interpretation is that thin crust was formed during the Cretaceous Magnetic Quiet Zone, with an interplay of reduced magmatism and intense extensional faulting.

Thus, the 3D development of the rift-to-drift system of West Iberia does not appear to conform to the gradual 2D lithospheric thinning envisioned by most current conceptual models of the evolution of magma-poor margins presented in the literature.

Chapter 12

Forward look

The results of this thesis provide novel information, of unprecedented accuracy and detail, concerning the spatial distribution, limits and petrological nature of the geological domains of two widely studied rifted margins. I have described the configuration and characteristics of these domains, along with a conceptual model that attempts to explain how extension leads to the formation of stretched continental crust, oceanic crust, and mantle exhumation in the case of the West Iberia margin. However, and as stated in previous chapters, additional geological and geophysical information would help to address the open questions arising from these new findings. In particular, I consider that some remodelling of existing data is needed, but also the acquisition of new geophysical data in key areas. This new data could be combined with numerical modelling to shed new light on the nature and formation processes of the different geological domains.

12.1. The Gulf of Lions

The geological domains in the Gulf of Lions (GoL) basin have been inferred based on a single geophysical transect. Consequently, their boundaries, distribution and petrological nature remain poorly constrained. To solve this issue, I propose the following:

First, remodelling another published seismic profile located in the conjugated margin of the Gulf of Lions: the **profile G-H** (Fig. 12.1). This profile is a coincident WAS and MCS transect acquired in 2006 by Ifremer Institute across the Sardinia margin, as part of the same survey as profile A-B, modelled in this thesis. This profile has already been modelled by travel-time tomography by Gailler et al. (2009). Later, Afilhado et al. (2008) remodelled the data using forward modelling. The resulting velocity models display a high-velocity zone beneath the continental slope and the proximal part of the deep basin (~100–140 km distance), which coincides with the transition to a thinner crust. I propose to apply a joint refraction and reflection travel-time tomography, as I did with profile A-B. This should provide a better constrain of the geological domains as well as the geometry of the main reflectors (e.g. top of the basement and the Moho) from the Sardinia margin. Together with the

recently published results from the Ligurian Basin obtained by Dannowski et al. (2020) (Fig. 12.1), this new analysis will surely help to better understand the geology and geodynamic evolution of this part of the Western Mediterranean.

Within this work, I have shown the importance of resolving the deep crustal structure and rock properties to understand basin evolution. Although MCS data provide relatively high-resolution information along the profile, the MCS profiles alone do not allow constraining the nature of the crust, especially of its deepest parts. MCS data provide information on the approximate thickness and reflectivity structure, which can be complemented using supplementary information from wells and dredges to better characterize the sediments and uppermost part of the crust. However, if the objective is unequivocally defining the Gulf of Lions crustal domains and their boundaries, I need to incorporate the information from the WAS-based velocity models. Thus, I suggest using the grid of 2D MCS profiles SPBAL01 in the Gulf of Lions (Fig. 12.1), which was processed by Spectrum Energy Ltd, to extend the domains interpreted in the modelled profile from this thesis to the rest of

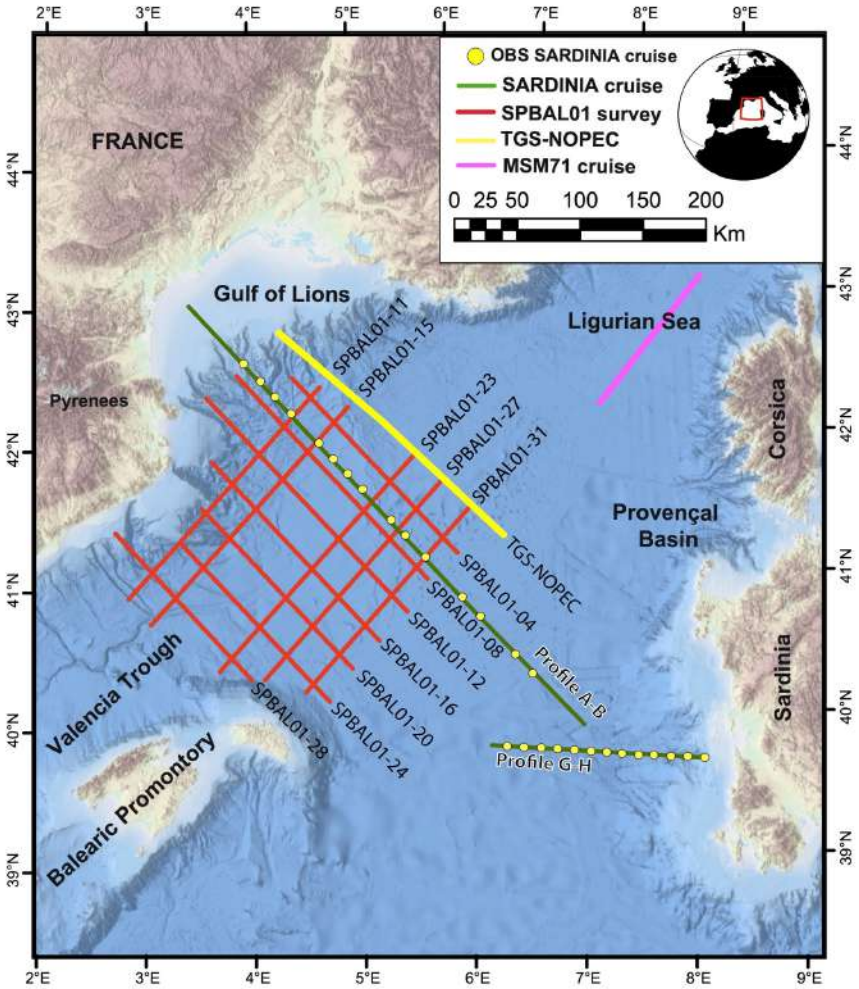

Figure 12.1 - Bathymetric and topographic map of the Gulf of Lions (SE France). It is bounded by the Ligurian Sea (NE), the Provençal Basin and Corsica-Sardinia continental margin (E), the Algero-Balearic Basin (S) and the Valencia Trough and the Balearic Promontory (SW). Lines in red correspond to MCS profiles SPBAL01. Green lines correspond to two WAS profiles from the Sardinia cruise (2006) and the yellow dots correspond to the position of every seafloor instrument (Gailler et al., 2009). Yellow line corresponds to a MCS line acquired by TGS-NOPEC (Jolivet et al., 2015). Pink line corresponds to the WAS profile from Dannowski et al. (2020). Modified from Viñas (2017).

the basin (Fig. 12.2), going from a 2D approach to a 3D view of the geology of the Gulf of Lions. For instance, I have identified the major tectonic features across the profile (Fig. 12.2c). Thus, the idea of a future work would be to identify the same main features first, in the nearest lines (e.g. SPBAL01-08 to the south and PBAL01-04 to the north) and then, moving progressively to all the seismic dataset. Consequently, the seismic interpretation of the MCS grid will allow defining the limits of the different crustal domains (continental or oceanic). This will allow framing, in turn, the results in the context back-arc extensional processes during the formation of the Western Mediterranean basins. The new distribution will permit to have enough information for future kinematic models of the zone.

Besides, I propose the acquisition of a new geophysical transect including both MCS and WAS data. The new profile (**LIGUR-1** in Fig 12.3) would go from Valencia Through to the Ligurian Sea,

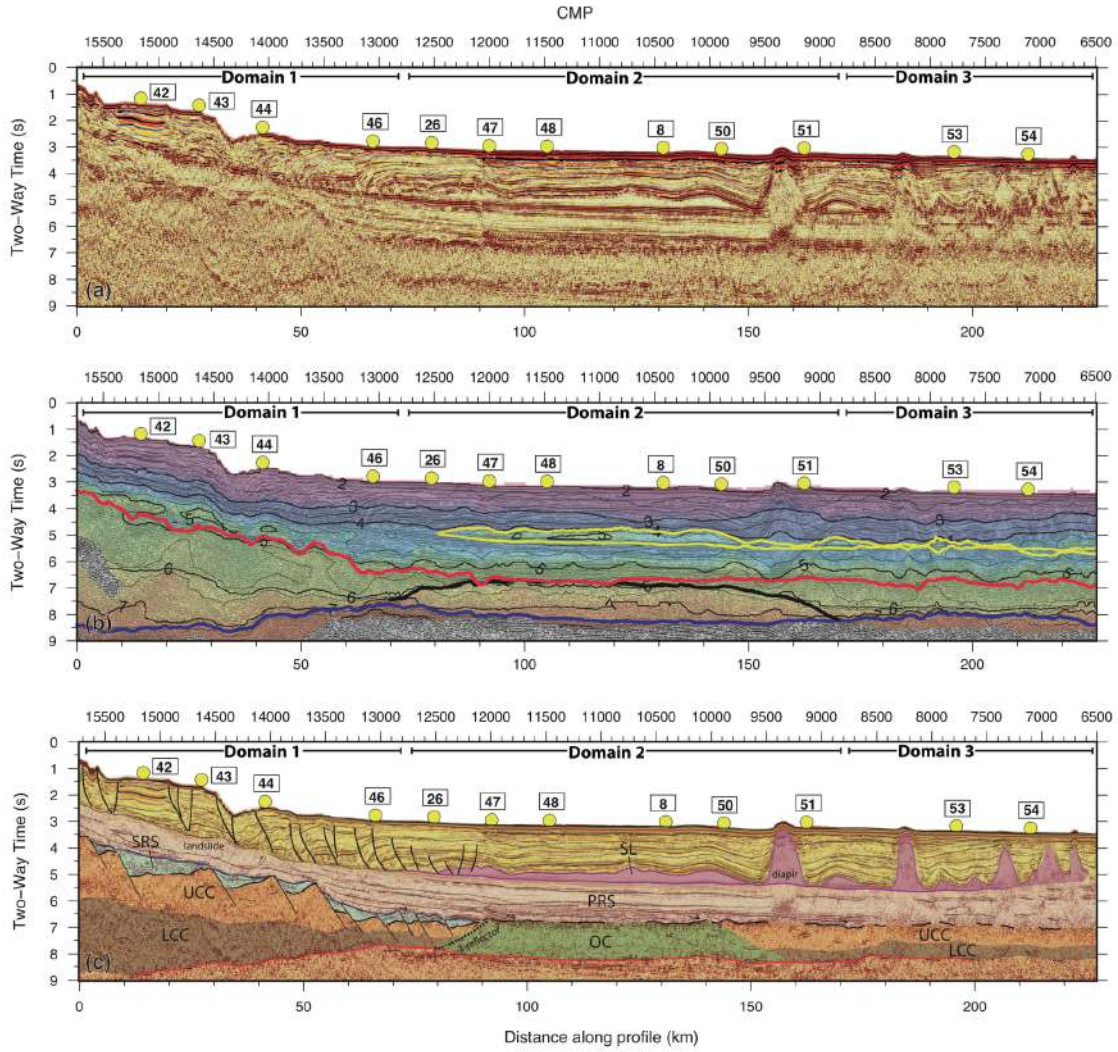

Figure 12.2 - (a) Post-stack time migration image of profile A-B, yellow circles represent the OBS/H location. (b) Same MCS image of profile A-B overlaid with the P-wave velocity model converted to TWT. Yellow circles represent the OBS/H location and yellow, red, black and blue lines correspond to the geometry of the inverted horizons: base and top of the layer of salt, the basement top, the top of the high-velocity zone and the Moho, respectively. (c) Tectonic interpretation of profile A-B. The seismic characteristics observed in the profile A-B can be extrapolated to the SPBAL01 lines. The whole seismic interpretation of these lines will be useful to complement our study and help to delineate the limits of the different crustal domains in the Gulf of Lions area. UCC: upper continental crust, LCC: lower continental crust, OC: oceanic crust, PRS: post-rift sediments, SRS: syn-rift sediments and SL: salt layer. Yellow circles represent the OBS/OBH location.

crossing the high-velocity zone, interpreted in this thesis as oceanic crust (green area in Fig. 12.1), and the zone with Expanded Spread Profiles (ESP) showing high velocities (yellow crosses in Fig. 12.3) (Le Douaran et al., 1984; Pascal et al., 1993). This profile would allow us to observe if this body has a lateral continuity along the margin of the Gulf of Lions. Finally, I propose to acquire a second WAS profile coincident to SPABAL01-20 MCS profile, perpendicular to LIGUR-1 and parallel to profile A-B (Fig. 12.3). The resulting modelling may help to confirm if the western section of the Gulf of Lions is floored by oceanic crust but also, to image and map the transition between the Gulf of Lions and the Valencia Through.

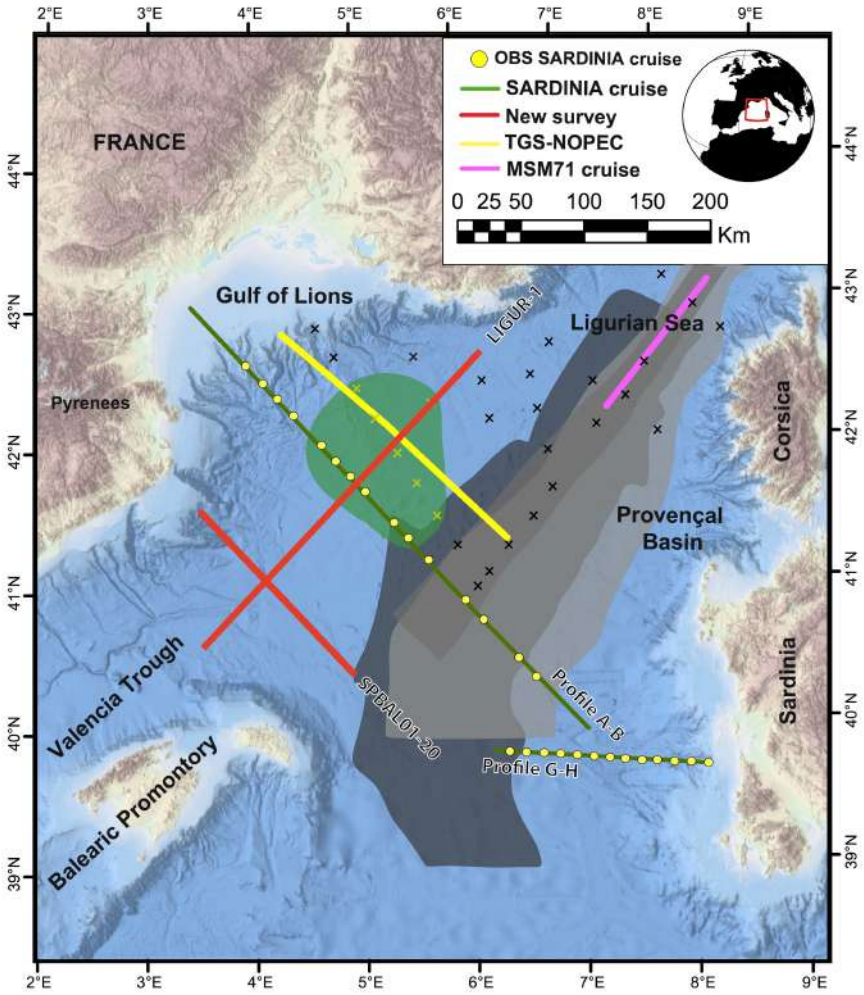

Figure 12.3 - Bathymetric and topographic map of the Gulf of Lions (SE France). The proposed new surveys are depicted with red lines: WAS profiles (LIGUR-1 WAS and MCS data and SPBAL01-20 only WAS data). The green area represents the extension of the oceanic domain from this work. The areas in shades of grey represent the location and extension of oceanic crust from Mauffret et al. (1995), Jolivet et al. (2015) and Granado et al. (2016).

12.2. The Tagus Abyssal Plain

In the case of the Tagus Abyssal Plain, we have modelled a single profile that crosses the entire basin. However, during the FRAME survey another ~360 km long WAS profile was also acquired further north (i.e. FRAME-3 in Fig. 12.4). It extends towards the ocean basin at its westernmost part and towards the Iberian Abyssal Plain at east. A total of 30 OBS/H were deployed along this profile to record the airgun shots, with an average spacing of ~10 km along the whole profile. I recommend to complement the existing data with a new coincident MCS profile to be able to apply the joint travel-time tomography, presented in this thesis. The new approach would provide information on the east-west variations of the crustal structure across the Iberia Abyssal Plain, and on the transition between the different domains, but especially across the J-anomaly, which has been also identified in this basin. Profiles FRAME-3 and FRAME-2 are parallel. Thus, the geophysical data would help to explore the latitudinal extension of their different domains and its relationship with their other adjacent margins.

In the same way, we can complement the existing data with a new modern WAS profile of similar instrument spacing as FRAME-2 and FRAME-3 along **IAM-5** (Afilhado et al., 2008) (Fig. 12.4). This would permit to apply a joint WAS and MCS inversion also along this profile, providing information on the crustal nature and structure beneath the eastern part of the Tagus Abyssal Plain, and giving new constraints to better understand the mechanism of thinning of the continental crust, particularly in this region.

Further, I recommend to complement the existing data with two long geophysical transects along which WAS, MCS and gravity data would be acquired (Fig. 12.4). The proposed **TRAN-1 profile** runs parallel to FRAME-2 and FRAME-3 profiles, along the transition between the Tagus and Iberia Abyssal Plain. The location of this profile, would allow us to know how the transition occurs between the two main basins that form the southern West Iberia (Fig. 12.4). Moreover, it can provide a way to link the geological features observed in FRAME-2 and FRAME-3 profiles.

The **TAP-1 profile** is parallel to FRAME-2 and IAM-5. The location is constrained by the presence of two seamounts (the Ashton and Gago Coutinho seamounts; Merle et al., 2018). However, the modelling of this profile would provide additional information on the nature of the basement beneath this area, which could be compared with the results obtained along the FRAME-2 and IAM-5 profiles. The results would permit to further constrain the geodynamic model for the Tagus Abyssal Plain, proposed in this thesis.

Rock samples of the basement in the area are scarce. Sampling is distributed mainly along the northern part of the margin, between the Iberia Abyssal Plain (IAP) and the Galicia Deep basin and they have been drilled to constrain the nature of the basement. The most relevant points in this thesis are the definition of the nature of the crust beneath the Tagus Abyssal Plain. However, the observation from this basin is constrained only with crustal velocity and density information. To better constrain the petrological nature of these domains it is necessary to drill and perform geochemical analysis of the samples. For that reason, I propose **E1** and **J1** as two potential locations for Integrated Ocean Discovery Program (IODP) drilling sites (Fig. 12.4). The location of these two perforation sites is

based on the information provided by the MCS images and the Vp models obtained in this work. The drilling depth would be ~7 km and ~5 km, respectively. The first drilling site is located in the centre of the Tagus Abyssal Plain (E1 in Fig. 12.4), as it is the point with the shallower basement and a thinner sedimentary sequence. The goal of this hole would be to investigate the presence of exhumed mantle during the formation of this region. Additionally, it would put an end to the lack of petrological information in the Tagus Abyssal Plain, providing in turn, invaluable information on the nature of some structural highs in this domain. The second drilling site is J1, located westernmost limit of the TAP and coinciding with the domain interpreted in this work as the J-anomaly (Fig. 12.4). The main goal of this hole is to ground-truth the nature of the basement in this domain, to check if it corresponds to the first oceanic crust formed in the West Iberia margin.

Finally, we propose to carry out further analysis on the J-anomaly, by including samples from the Vp model of the FRAME-3 profile and the new geophysical profiles, proposed before, to enrich the the *H-Vp* diagrams. The new information will probably shed new light into the nature and process of formation of the J-anomaly along the West Iberia. The goal is confirming if its formation was triggered by the presence of a short-lived compositional anomaly in the mantle source, as we suggest in this work.

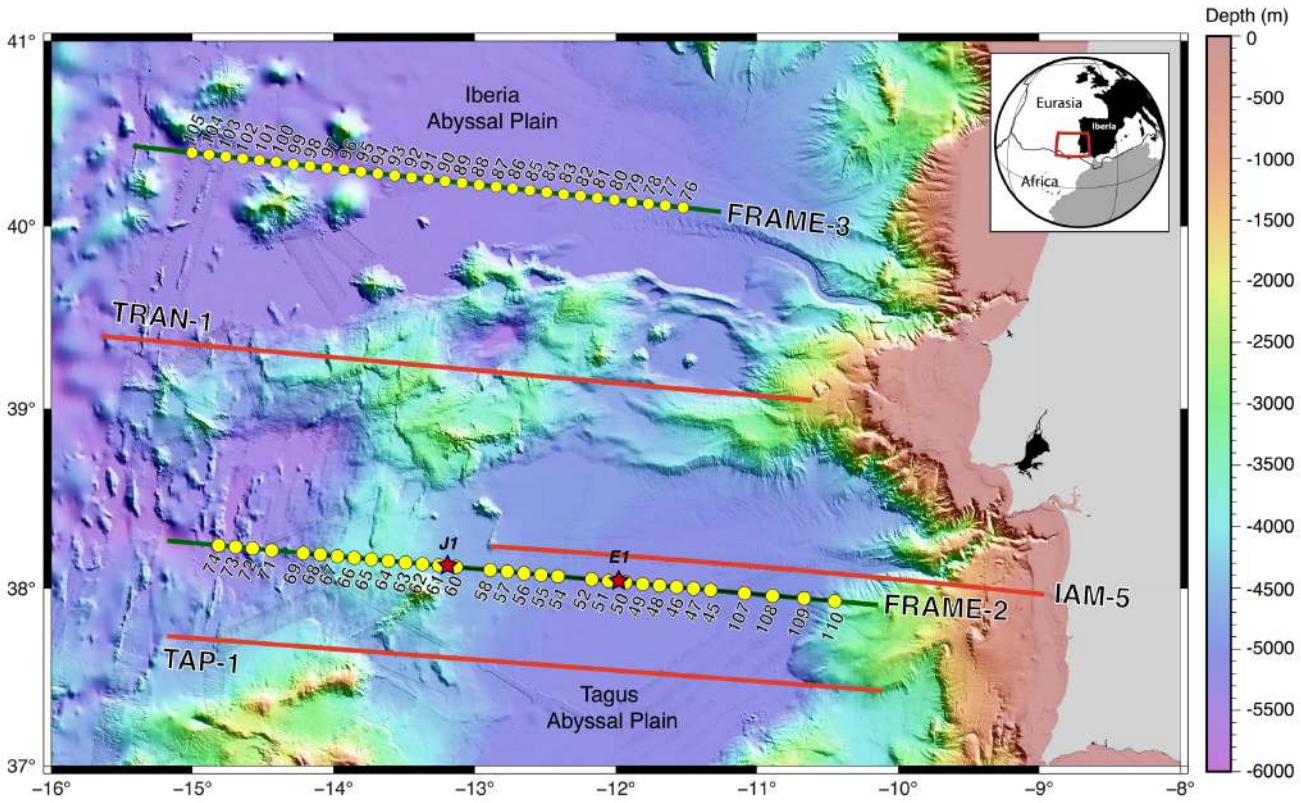

Figure 12.4 - Bathymetric map of the central and southern West Iberia margin including two seismic profiles. Green lines correspond to WAS profiles (FRAME-2 and FRAME-3) acquired during Leg-2 from the FRAME (2018) cruise, while the coincident thin black line in profile FRAME-2 correspond to the MCS profile acquired during the Leg-1. The proposed new surveys are depicted with red lines: WAS profiles (TRAN-1 and TAP-1 with coincident WAS and MCS data, and WAS data for the IAM-5 profile) and red star: new well (J1 and E1).

References

Afilhado, A., Matias, L., Shiobara, H., Hirn, A., Mendes-Victor, L., and Shimamura, H. (2008). From unthinned continent to ocean: The deep structure of the West Iberia passive continental margin at 38°N. Tectonophysics, 458(1–4), 9–50, doi:10.1016/ j.tecto.2008.03.002.

Dannowski, A., Kopp, H., Grevemeyer, I., Lange, D., Thorwart, M., Bialas, J., and Wollatz-Vogt, M. (2020). Seismic evidence for failed rifting in the Ligurian Basin, Western Alpine domain. Solid Earth, 11(3), 873–887, doi: 10.5194/se-11-873-2020.

Gailler, A., Klingelhoefer, F., Olivet, J. L., Aslanian, D. (2009). The Sardinia scientific party, and Technical OBS team. Crustal structure of a Young margin pair: New results across the Liguro-Provençal Basin from wide-angle seismic tomography. Earth Planet. Sci. Lett., 286, 333–345, doi: 10.1016/j.epsl.2009.1007.1001.

Lau, K. H., Louden, K. E., Funck, T., Tucholke, B. E., Holbrook, W. S., Hopper, J. R., and Christian Larsen, H. (2006). Crustal structure across the Grand Banks - Newfoundland Basin Continental Margin - I. Results from a seismic refraction profile. Geophysical Journal International, 167(1), 127-156.

Le Douaran, S., Burrus, J. and Avedik, F. (1984). Deep structure of the north-western Mediterranean Basin: Results of a two-ship seismic survey. Marine Geology, 55(3-4), pp.325-345.

Merle, R., Jourdan, F. and Girardeau, J. (2018). Geochronology of the Tore-Madeira Rise seamounts and surrounding areas: a review. Australian Journal of Earth Sciences, 65(5), pp.591-605.

Pascal, G.P., Mauffret, A., Patriat, P. (1993). The ocean–continent boundary in the Gulf of Lion from analysis of expanding spread profiles and gravity modelling. Geophys. J. Int. 113, 701–726.

Viñas, M. (2017). Tectonic structure and formation kinematics of the Western Mediterranean basins. PhD Thesis.

Appendix

A.1. Seismic tomography steps for the Vp models

A.1.1. Gulf of Lions modelling

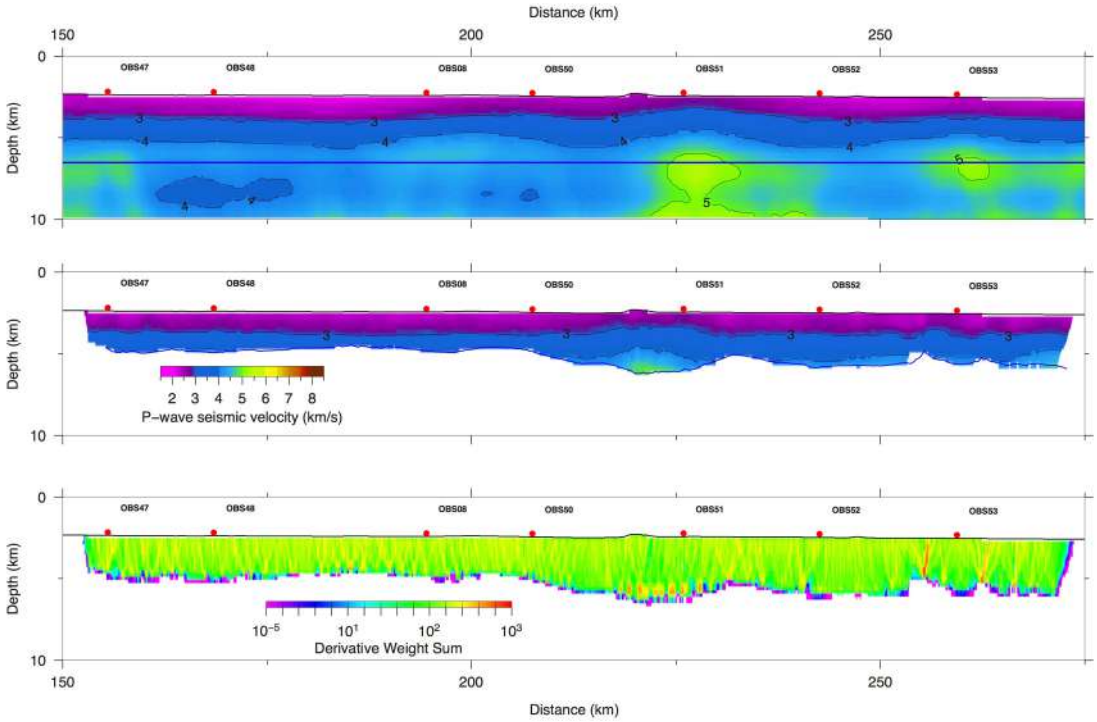

Figure A.1 - Step 1 of the layer-stripping. Inversion of the top of the salt layer and the overlying Vp structure using reflected travel-times from MCS data only. From top to bottom: initial 1-D Vp model, final 2-D Vp model and DWS from the final Vp model.

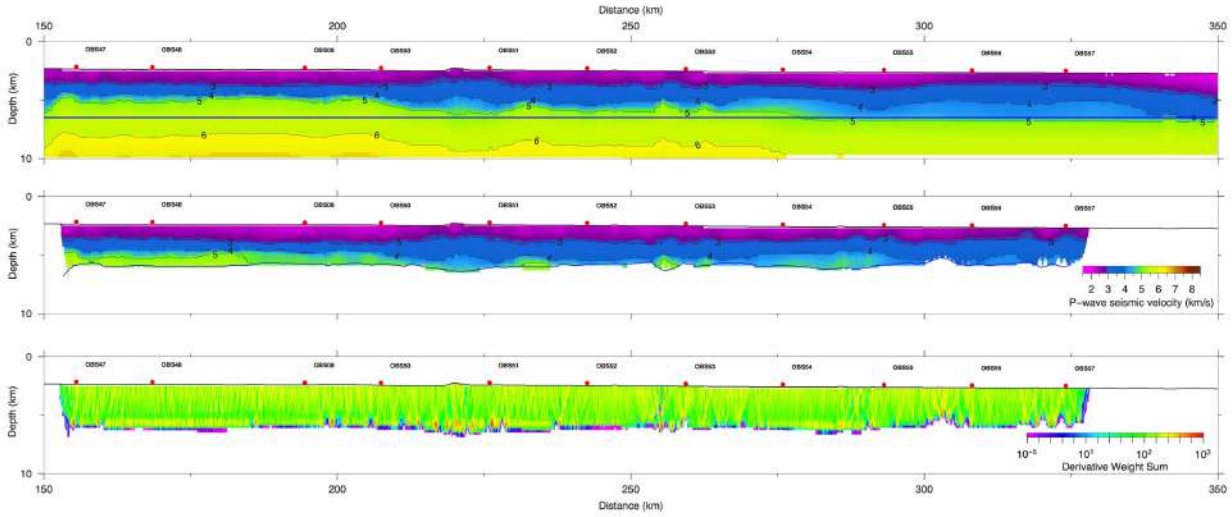

Figure A.2 - Step 2 for the layer-stripping. Inversion of the base of the salt layer and the overlying Vp structure using reflected travel-times from MCS data only. From top to bottom: initial 1-D Vp model, final 2-D Vp model and DWS from the final Vp model.

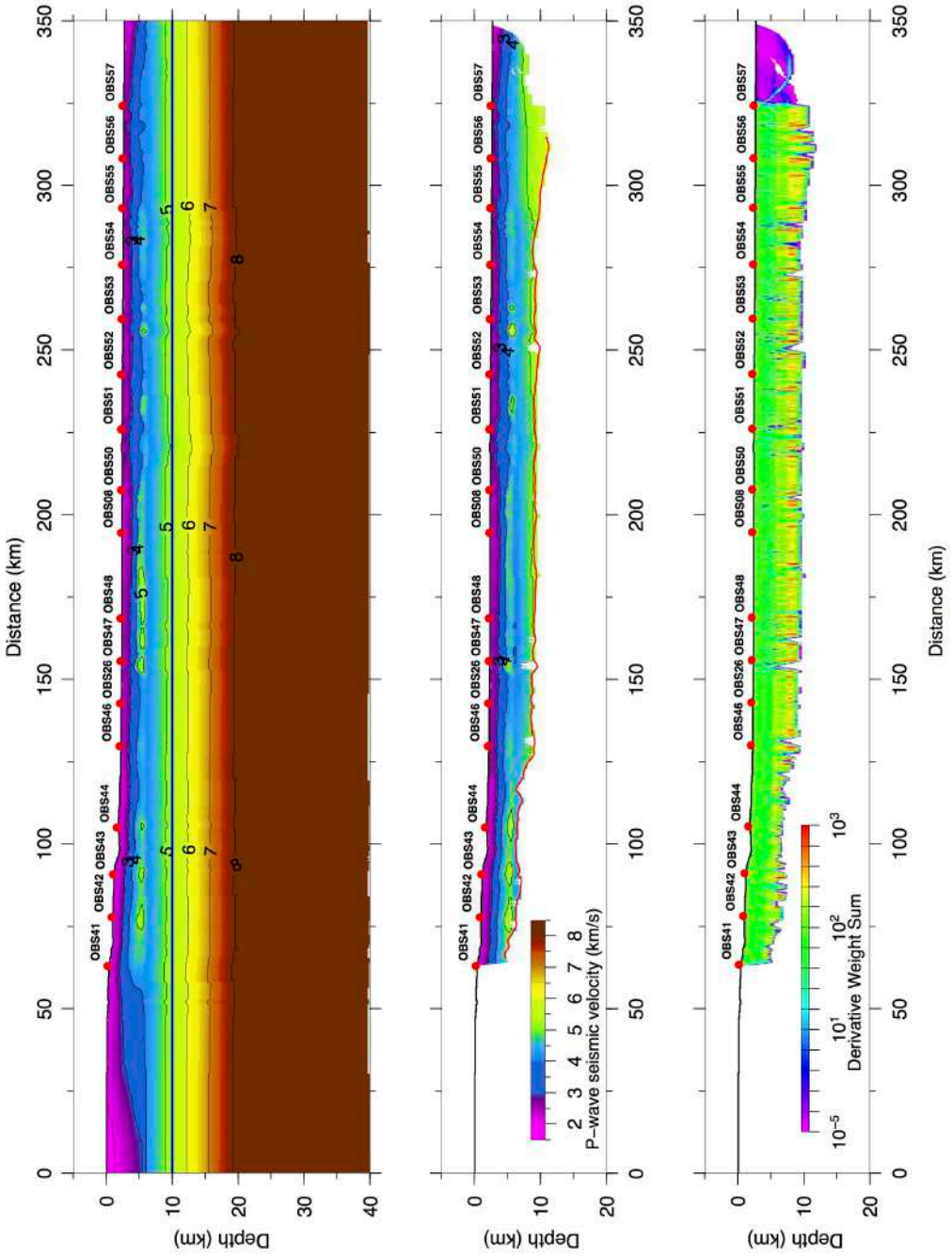

Figure A.3 - Step 3 for the layer-stripping. Inversion of the top of the basement and the velocity structure of the lower post-rift sedimentary unit using travel-times of reflected P-waves at the top of the basement from MCS data and Ps first arrival from WAS data. From top to bottom: initial 1-D Vp model, final 2-D Vp model and DWS from the final Vp model.

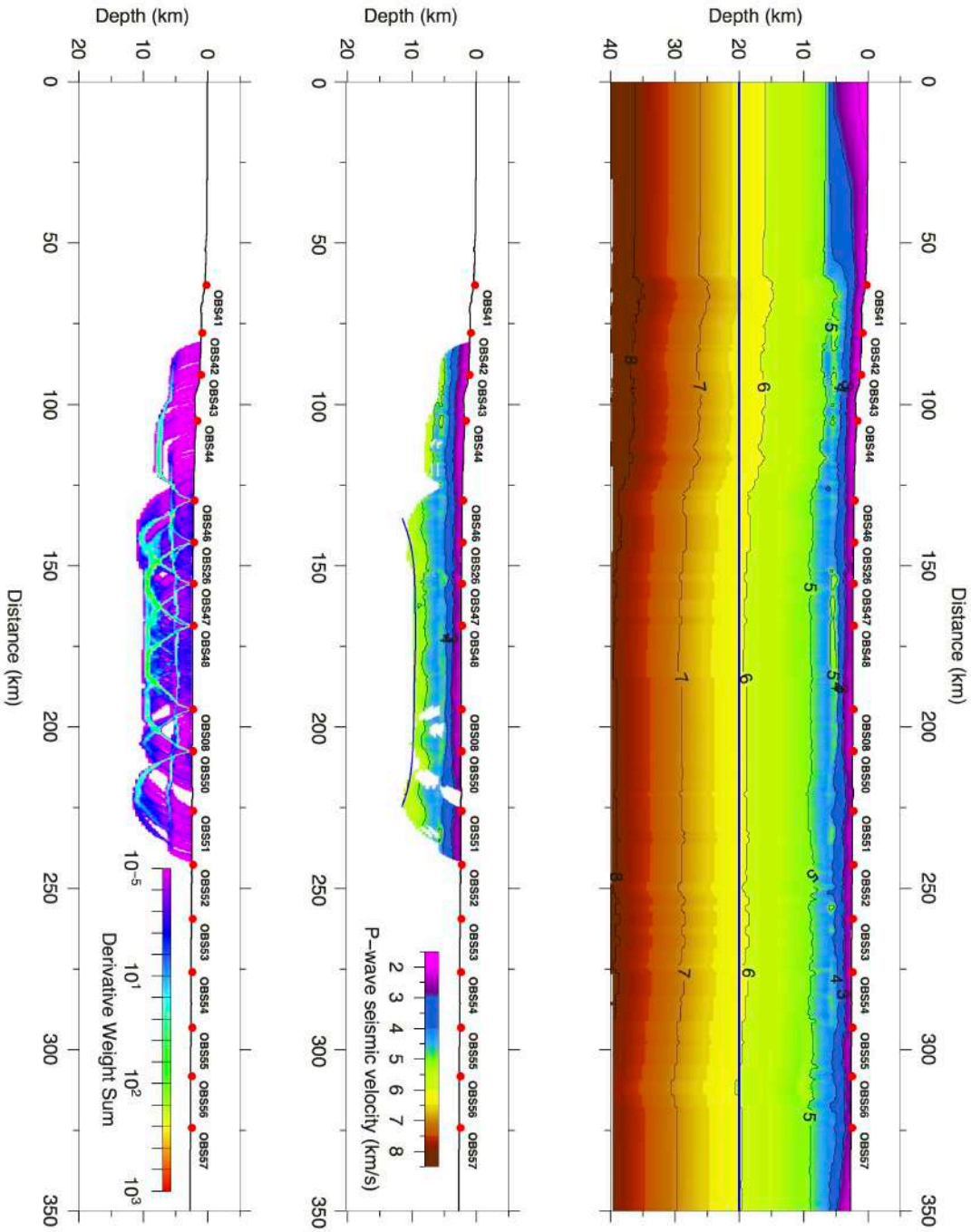

Figure A.4 - Step 4 for the layer-stripping. Inversion of the top of the HVL using Ps first arrival travel-times and PbP reflection travel-times from WAS data. From top to bottom: initial 1-D Vp model, final 2-D Vp model and DWS from the final Vp model.

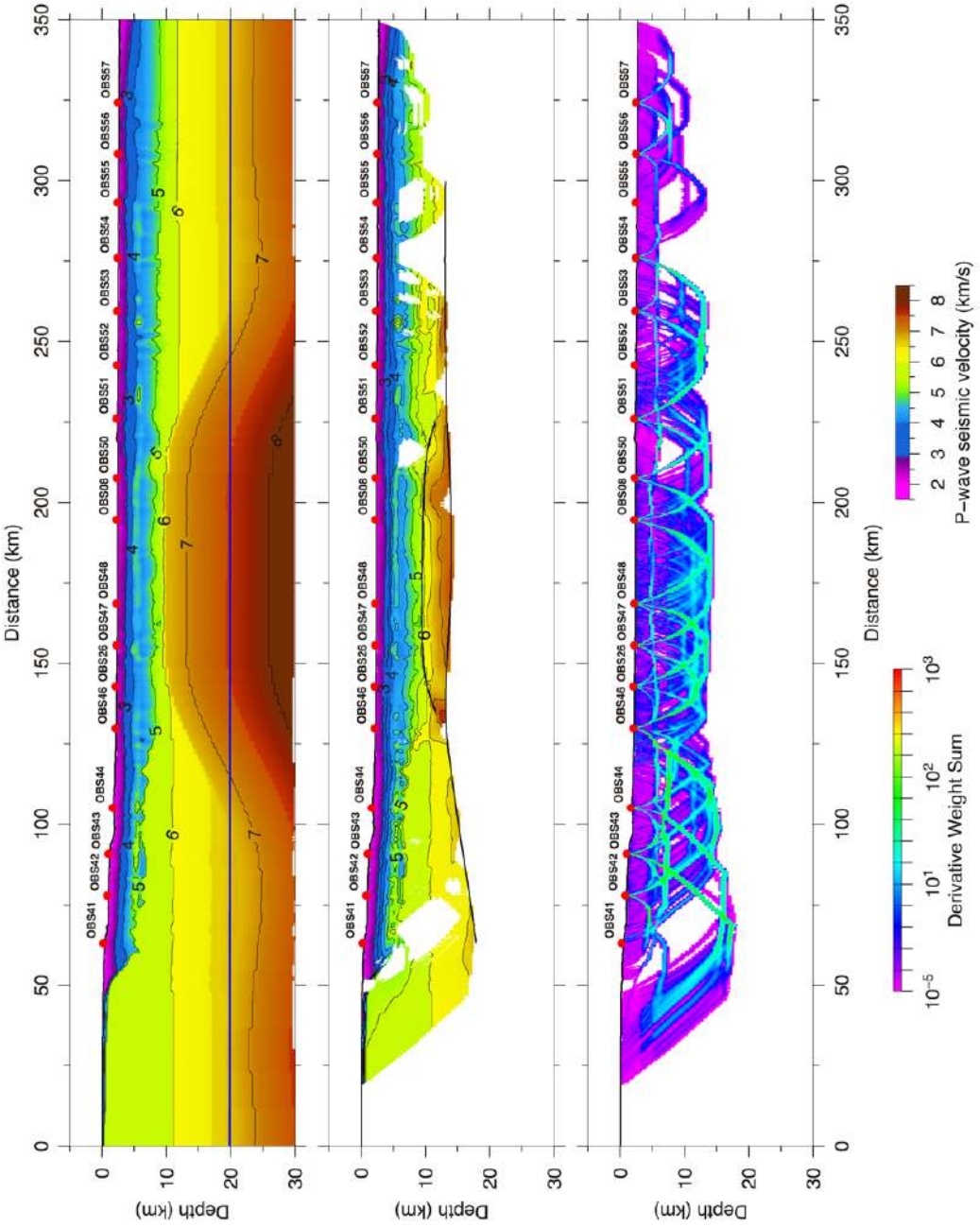

Figure A.5 - Step 5 for the layer-stripping. Inversion of the Moho and the Vp structure of the using Ps, Pb, and PmP travel-times from the WAS data. From top to bottom: initial 1-D Vp model, final 2-D Vp model and DWS from the final Vp model.

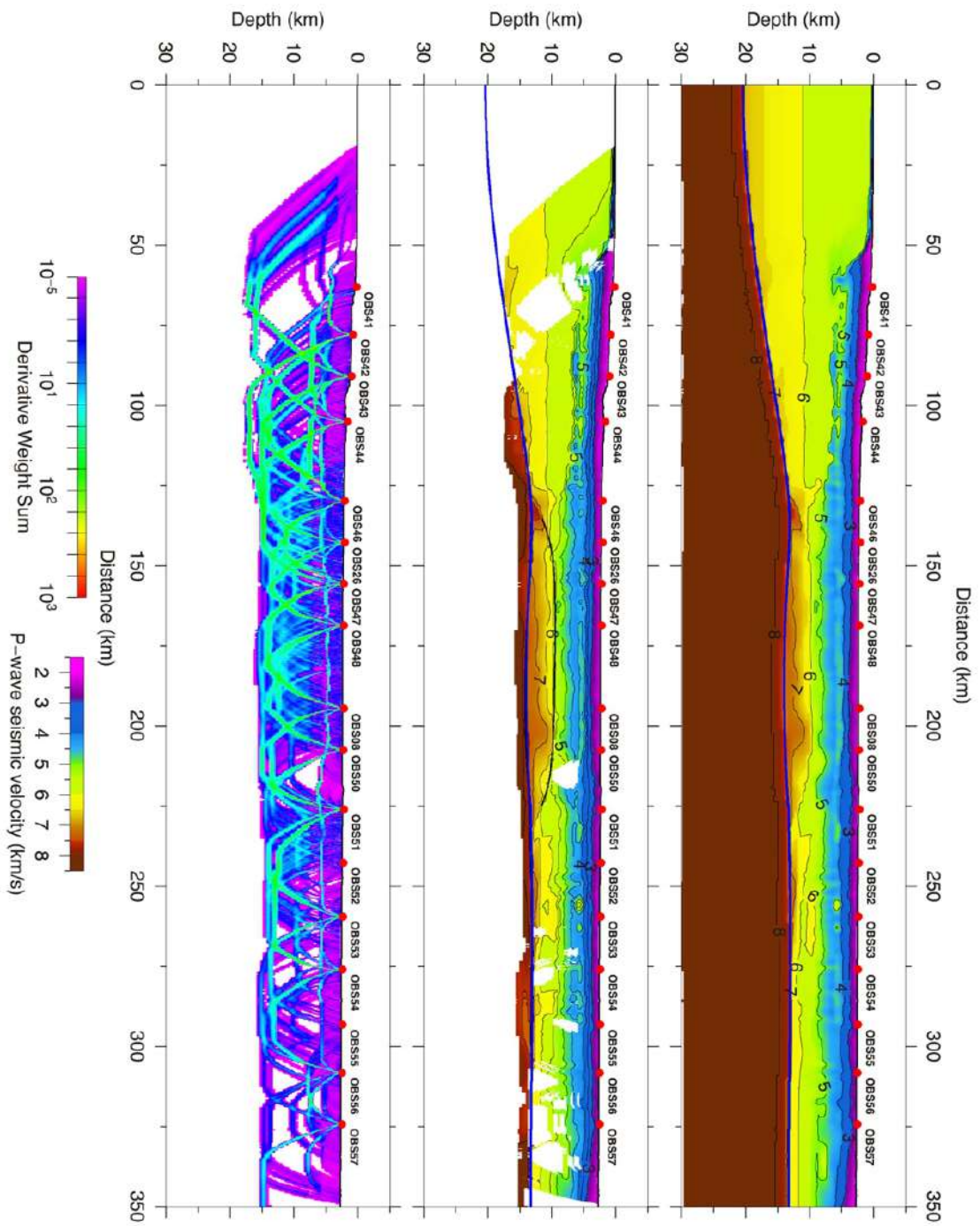

Figure A.6 – Step 6 for the layer-stripping. Inversion of the uppermost mantle velocity using all first arrival travel-times (i.e. Ps, Pb, Pn) and PmP reflections from the WAS data. From top to bottom: initial 1-D Vp model, final 2-D Vp model and DWS from the final Vp model.

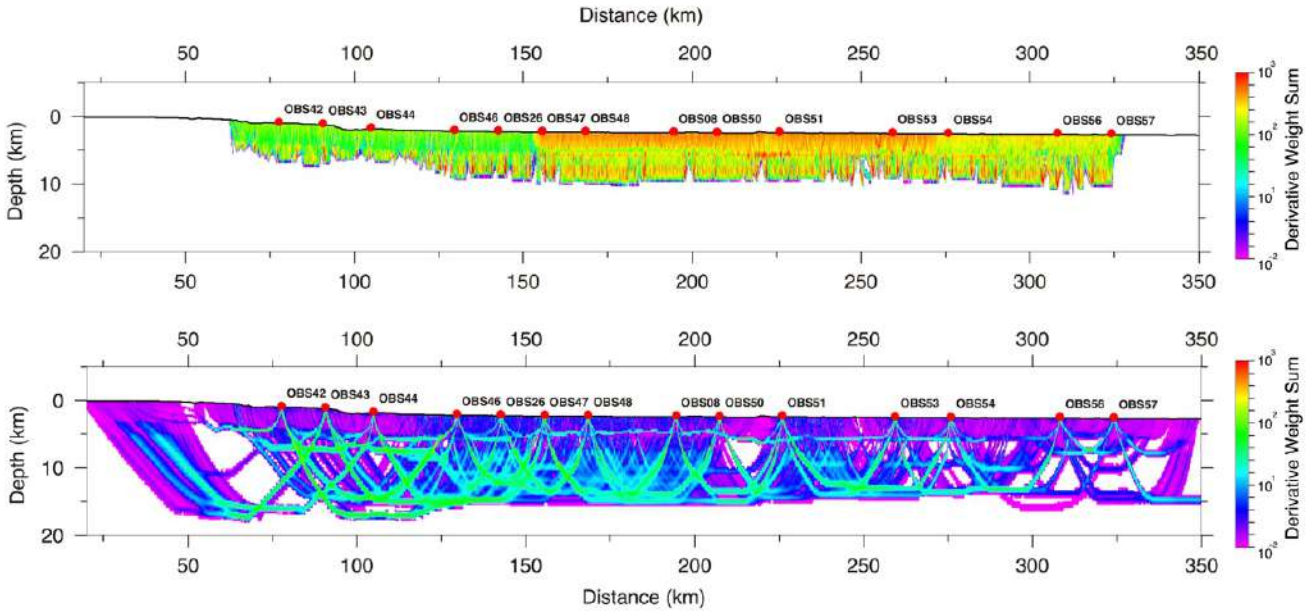

Figure A.7 – Derivative weight sum (~raytracing) from MCS travel-times (upper figure) and WAS travel-times (lower figure).

A.1.2. Tagus Abyssal Plain modelling

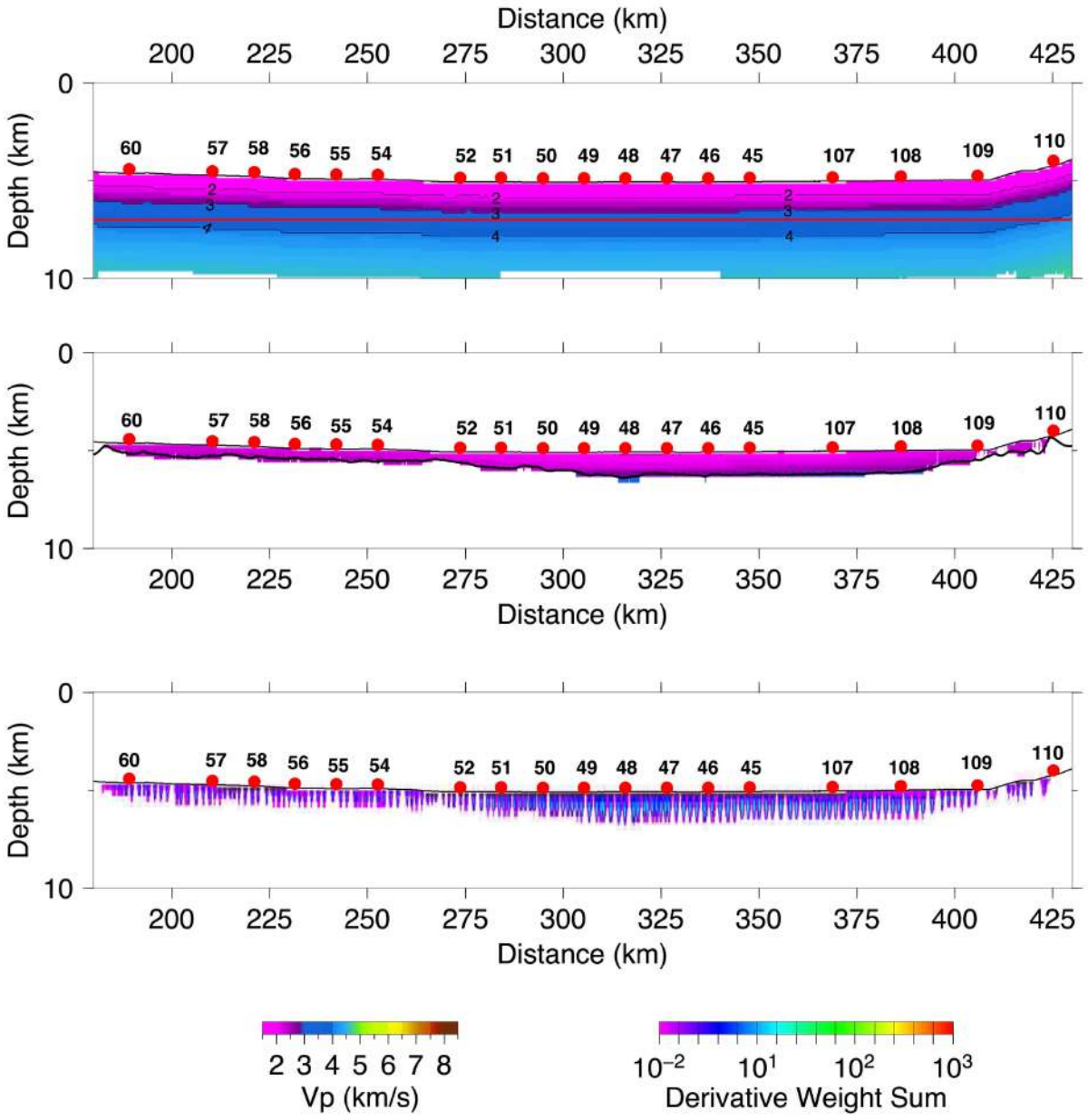

Figure A.7 - Step 1 for the layer-stripping. Inversion of the unconformity boundary and the overlying Vp structure corresponding to the upper sediment unit using reflected travel-times from MCS data only. From top to bottom: initial 1-D Vp model, final 2-D Vp model and DWS from the final Vp model.

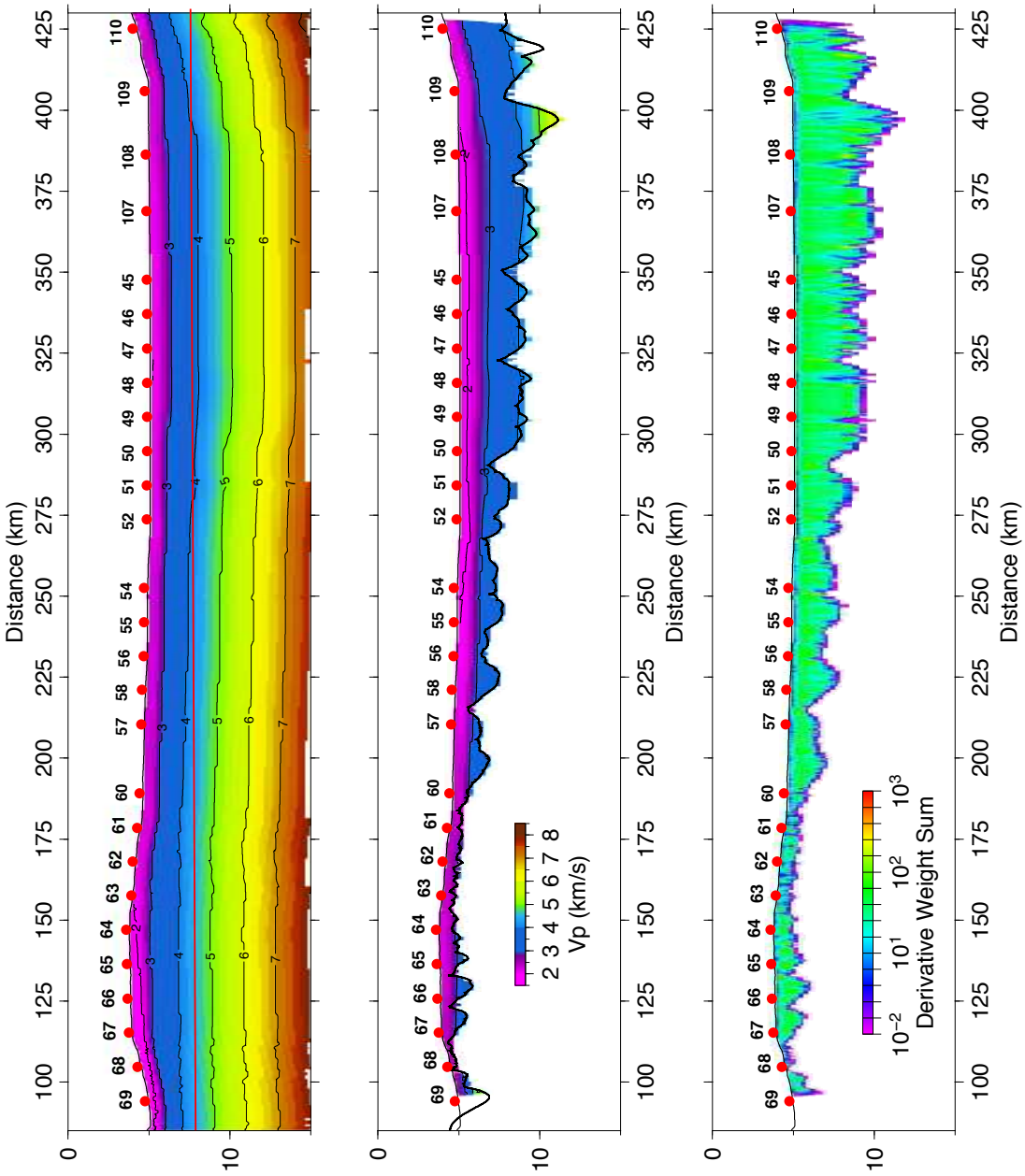

Figure A.8 - Step 2 for the layer-stripping. Inversion of the top of the basement and the velocity structure of the lower sedimentary unit using travel-times of reflected P-waves at the top of the basement from MCS data. From top to bottom: initial 1-D Vp model, final 2-D Vp model and DWS from the final Vp model.

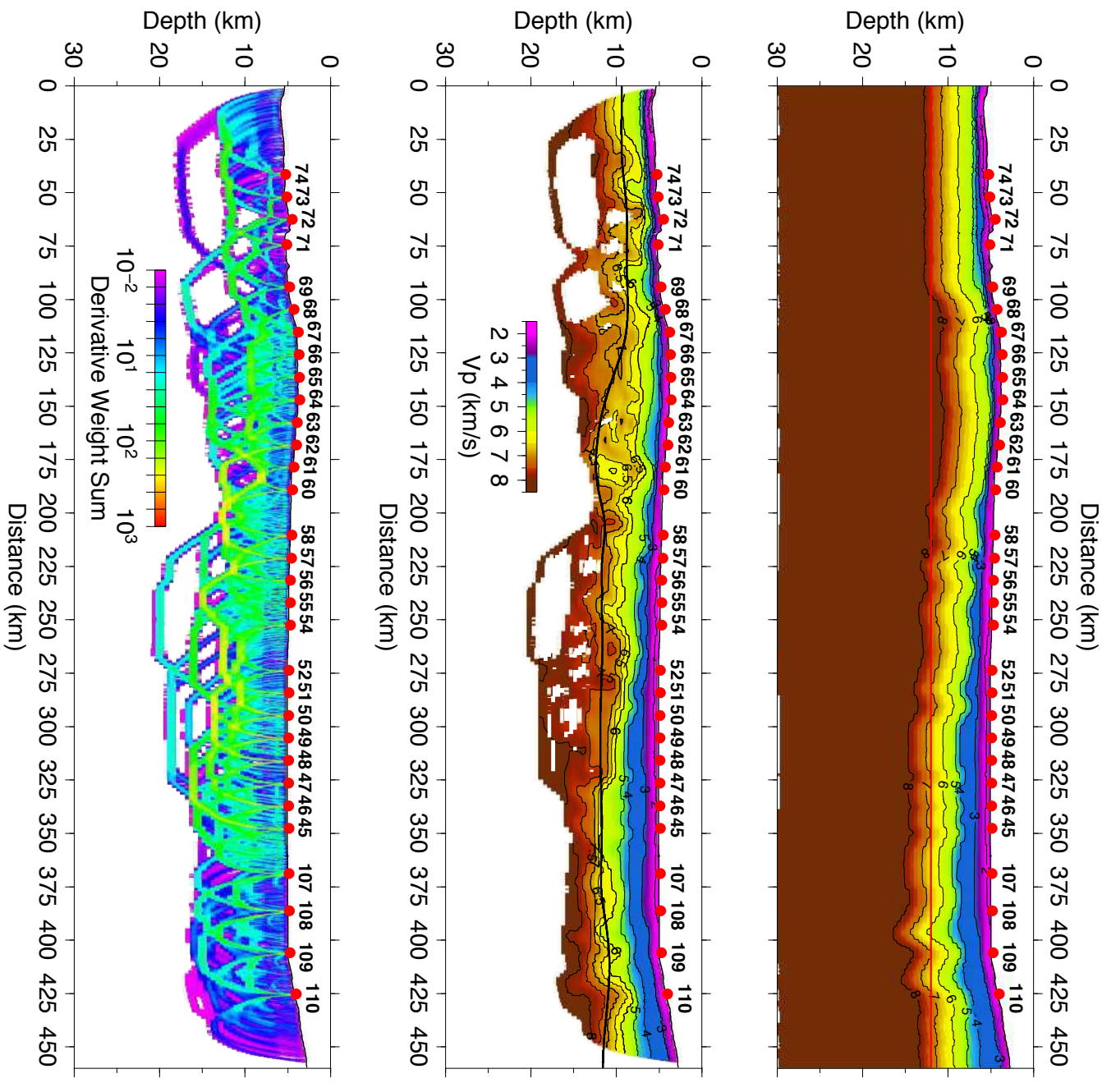

Figure A.9 - Step 3 for the layer-stripping. Inversion of the basement unit using Ps and Pg first arrival travel-times and PmP reflection travel-times from WAS data. From top to bottom: initial 1-D Vp model, final 2-D Vp model and DWS from the final Vp model.

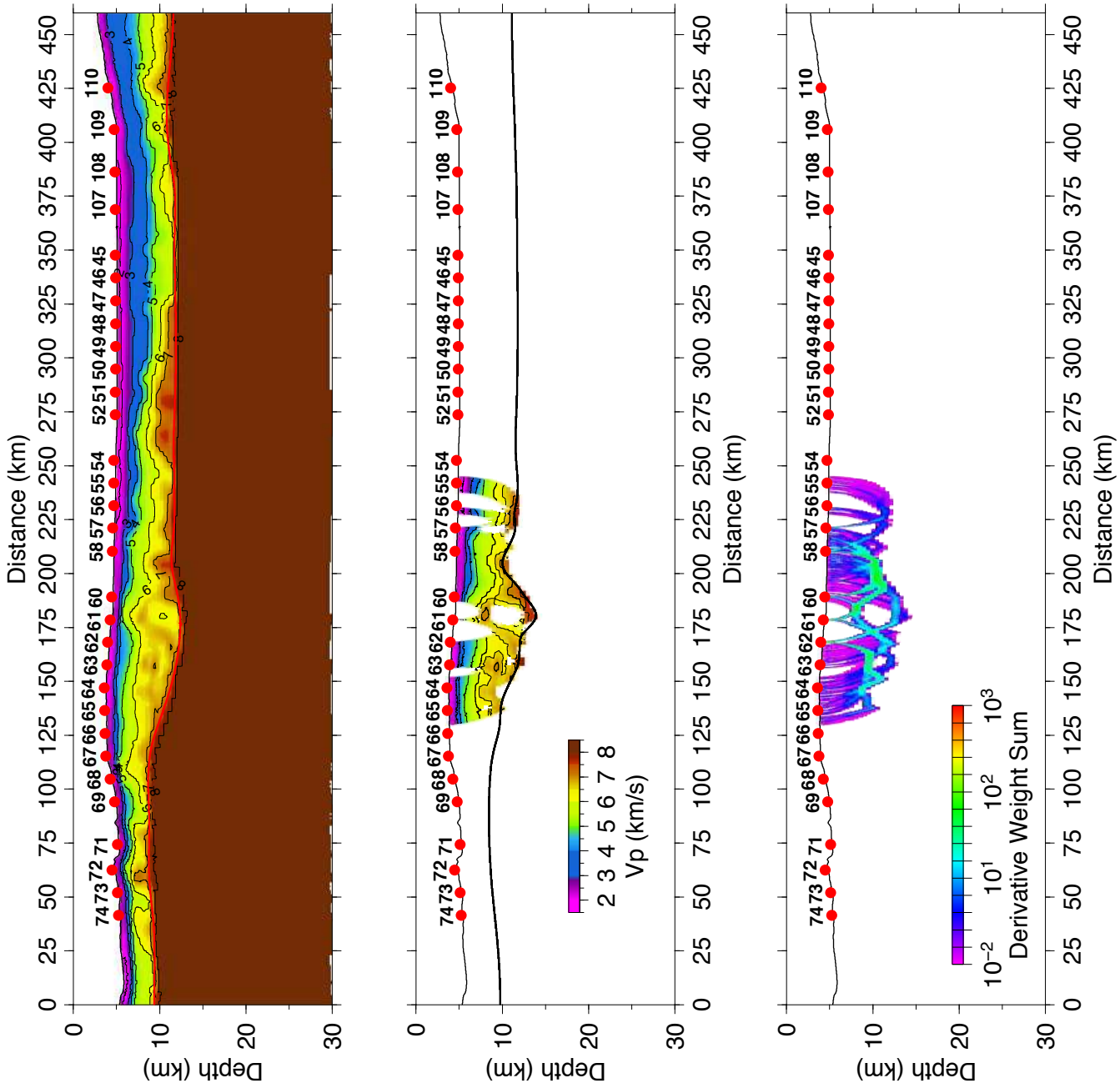

Figure A.10 – Intermediate step for the layer-stripping. Inversion of the PmP reflection travel-times from WAS data. Inversion of a few PmP reflection between OBS 54 and OBS69 where I was interested to make the boundary more sharp and abrupt. From top to bottom: initial 1-D Vp model, final 2-D Vp model and DWS from the final Vp model.

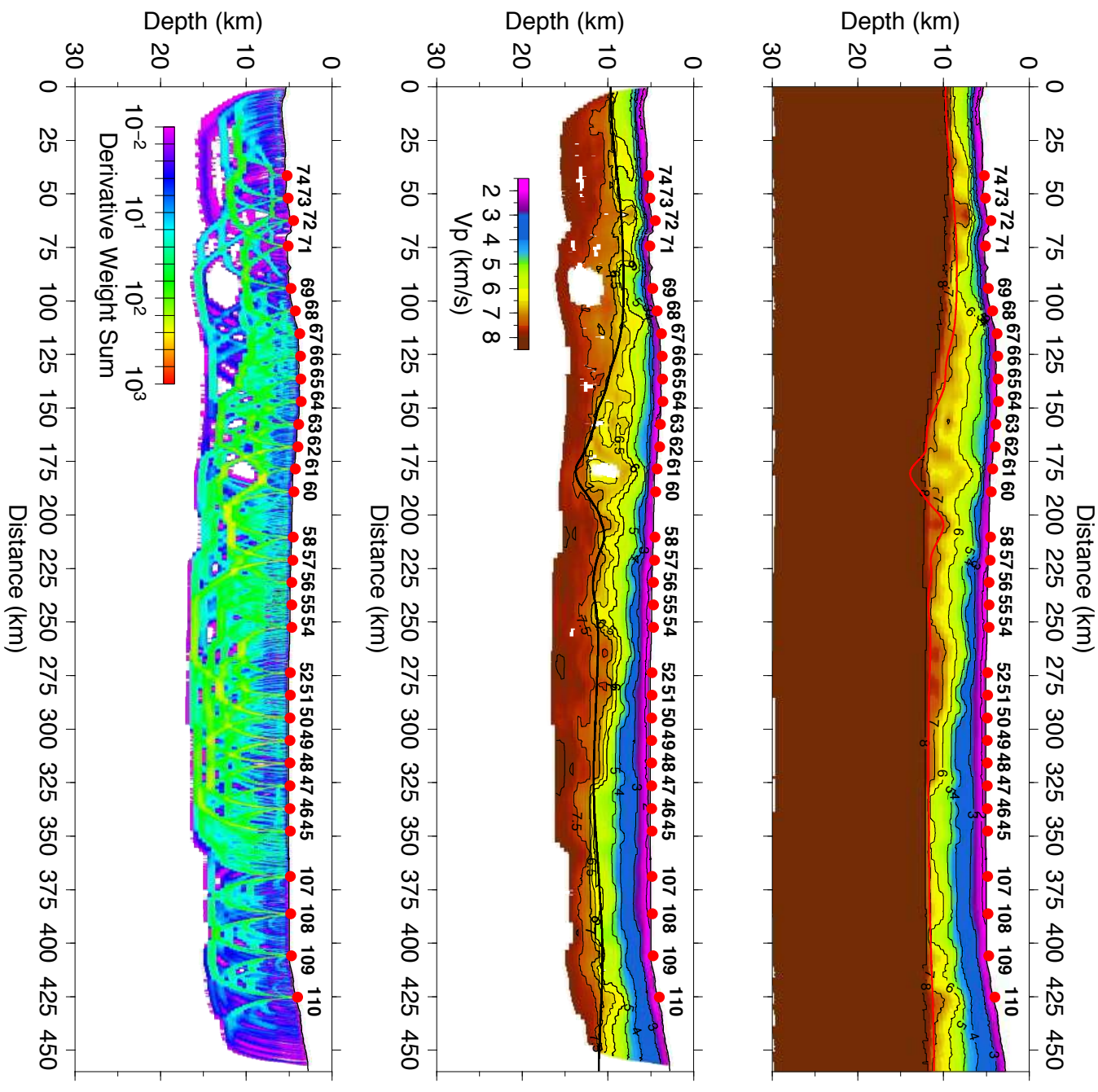

Figure A.11 – Step 4 for the layer-stripping. Inversion of the uppermost mantle velocity using all first arrival travel-times (i.e. Ps, Pg and Pn) and PmP reflections from the WAS data. From top to bottom: initial 1-D Vp model, final 2-D Vp model and DWS from the final Vp model.

A.2. Travel-time residuals (RMS) for the MCS picking data

A.2.1. Gulf of Lions modelling

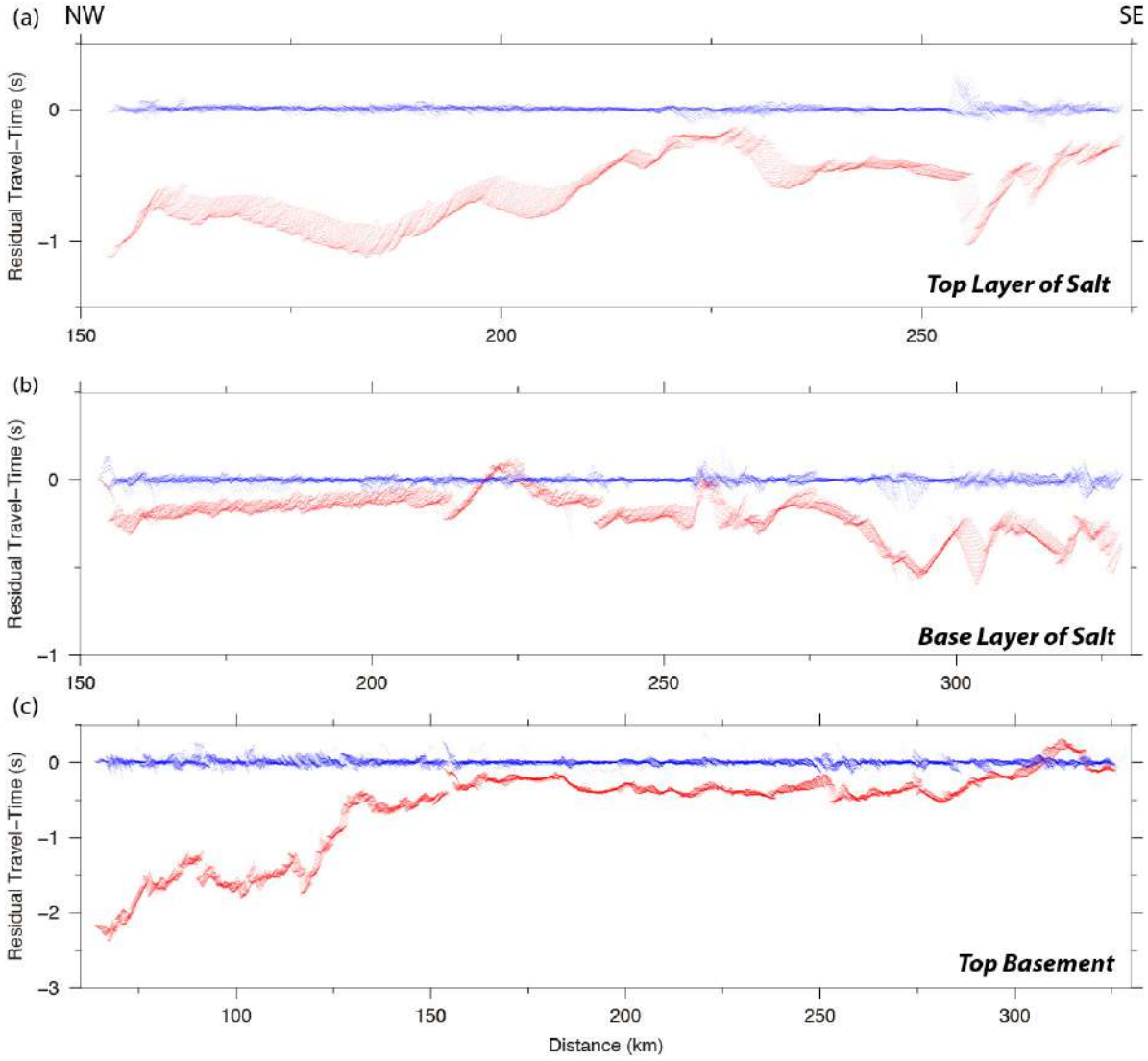

Figure A.12 - Root mean squared (r.m.s.) residual between the observed and synthetic travel-times: in red the r.m.s values for the first iteration and in blue the r.m.s values for the last iteration. (a) r.m.s values for the top of the salt layer along the profile (b) r.m.s values for the base of the salt layer along the profile and (c) r.m.s values for the top of the basement along the profile.

A.2.2. Tagus Abyssal Plain modelling

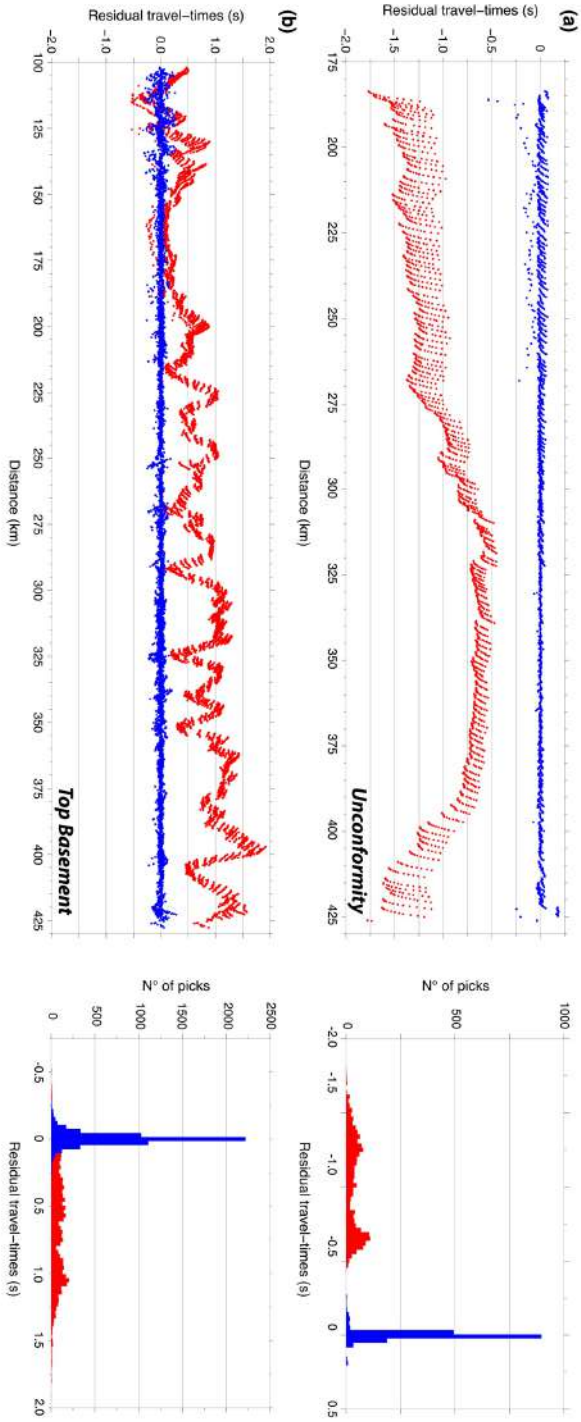

Figure A.13 - Root mean squared (r.m.s.) residual between the observed and synthetic travel-times: in red the r.m.s values for the first iteration and in blue the r.m.s values for the last iteration. (a) r.m.s values for the unconformity horizon along the profile (left) and respect to the number of picks (right) (b) r.m.s values for the top of the basement along the profile (left) and respect to the number of picks (right).

A.3. Root mean square (r.m.s) and picking uncertainty (χ^2)

A.3.1. Gulf of Lions modelling

Inversion step	r.m.s		χ^2	
	Initial value	Final value	Initial value	Final value
Top Salt	0.064	0.017	1034.99	0.783
Base Salt	0.234	0.019	137.403	0.948
TOB	0.839	0.033	783.578	1.249
Top HVL	1.323	0.064	791.224	1.322
Moho	1.034	0.077	495.263	1.419
Mantle	0.114	0.065	7.312	1.405

A.3.2. Tagus Abyssal Plain modelling

Inversion steps	r.m.s		χ^2	
	Initial value	Final value	Initial value	Final value
Unconformity	1.051	0.019	690.062	0.220
TOB	0.309	0.060	59.717	2.283
Moho	0.077	0.049	2.382	0.906
Mantle	0.217	0.055	30.568	1.380

A.4. Uncertainty analysis for the FRAME-2 profile

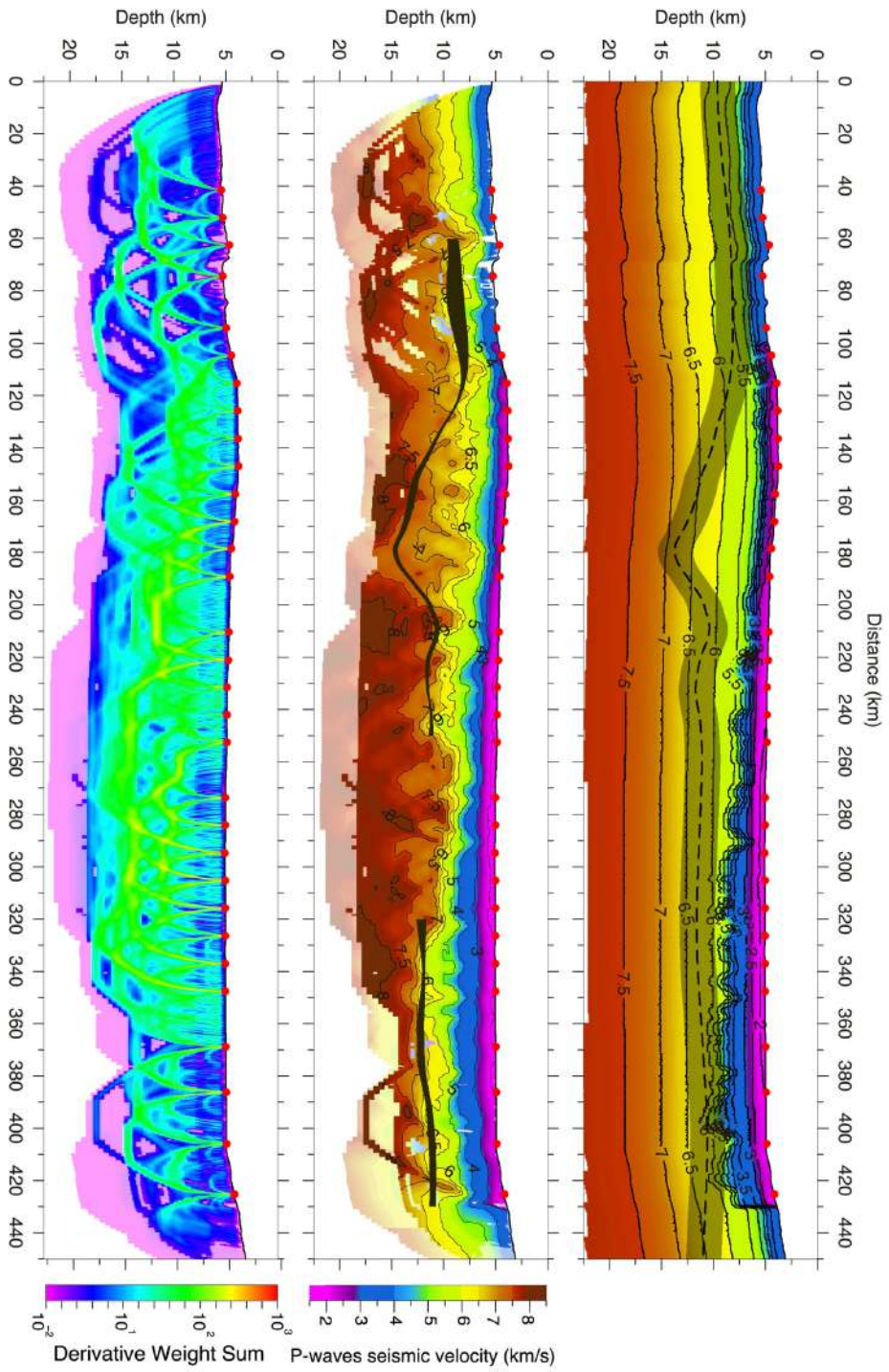

Figure A.14 - From top to bottom: (a) Initial 1D Vp model. Dashed black line represents the preferred basement top from Chapter 8 (Fig. 8.3a) and black shadow represents the ± 3 km static shift applied to the same preferred Moho. (b) Average Vp values from the Monte-Carlo analysis for FRAME-2 profile in Fig. 8.3d. The width of the dark band shows the standard deviation of the depth for the inverted horizon: the Moho. (c) Average derivative weight sum (DWS) of all the inversions of tomographic model in (b). Red circles display the receiver location, OBS/OBH.

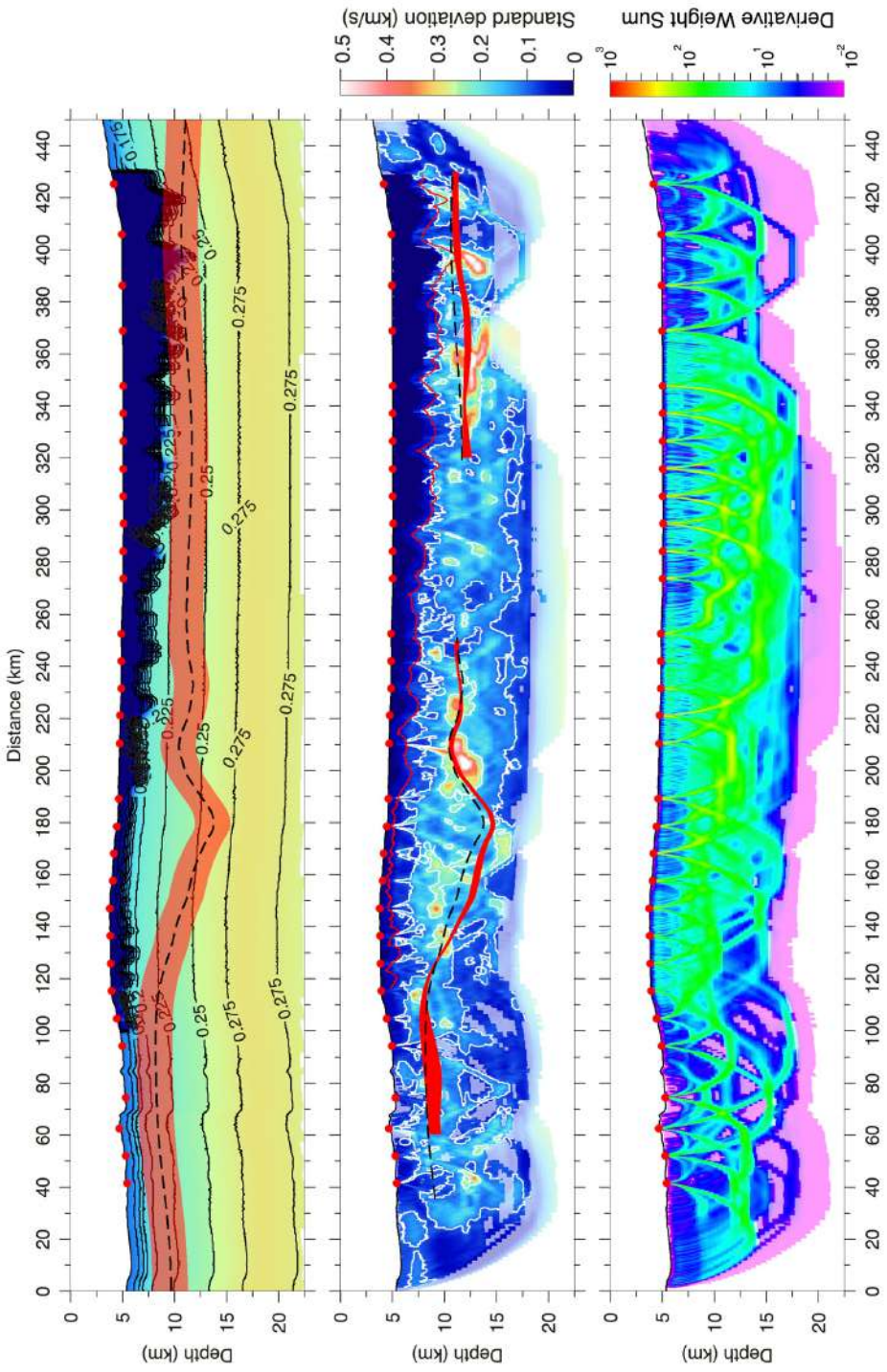

Figure A.15 - From top to bottom: (a) Initial 1D Vp model. Dashed black line represents the preferred basement top from Chapter 8 (Fig. 8.3a) and red shadow represents the ± 3 km static shift applied to the same preferred Moho. (b) Standard deviation of Vp values of the average solution of the Monte-Carlo analysis for profile FRAME-2. The width of the red band shows the standard deviation of the depth of the inverted horizons: the Moho. In dashed black line the preferred Moho from (a). (c) Average derivative weight sum (DWS) of all the inversions of tomographic model in (b). Red circles display the receiver location, OBS/OBH.

A.5. OBS cross-sections with the picked and the predicted travel times

A.5.1. Gulf of Lions modelling

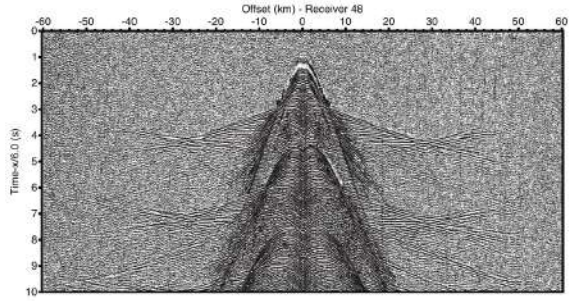
Offset (km) - Receiver 48
Time-x/6.0 (s)

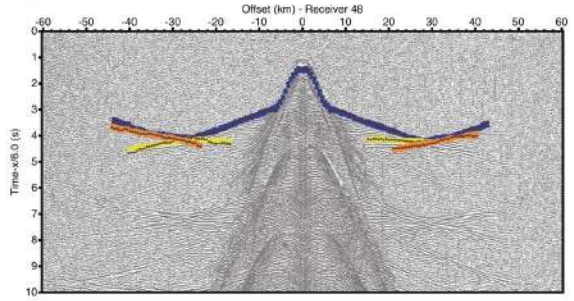
Offset (km) - Receiver 48
Time-x/6.0 (s)

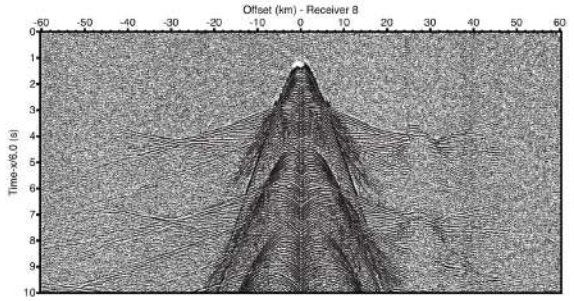
Offset (km) - Receiver 8
Time-x/6.0 (s)

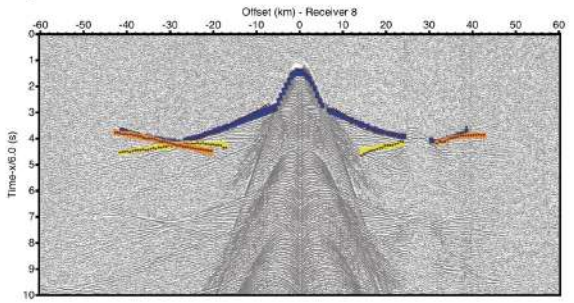
Offset (km) - Receiver 8
Time-x/6.0 (s)

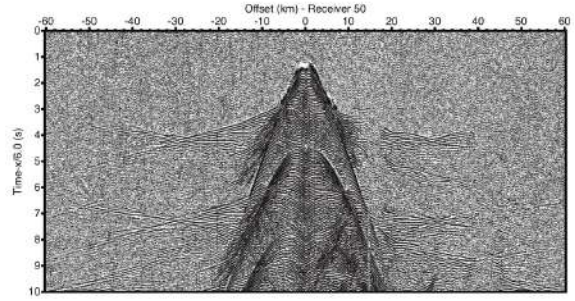
Offset (km) - Receiver 50
Time-x/6.0 (s)

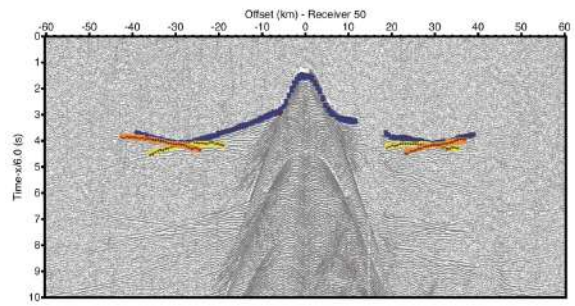
Offset (km) - Receiver 50
Time-x/6.0 (s)

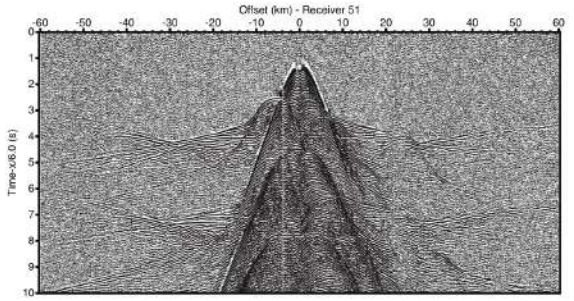
Offset (km) - Receiver 51
Time-x/6.0 (s)

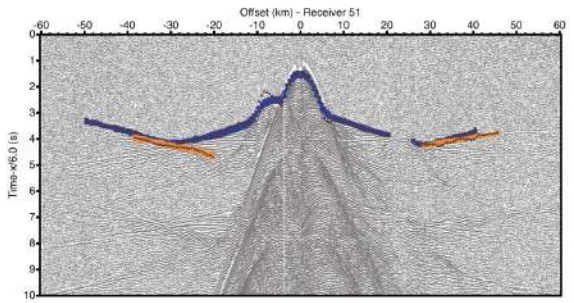
Offset (km) - Receiver 51
Time-x/6.0 (s)

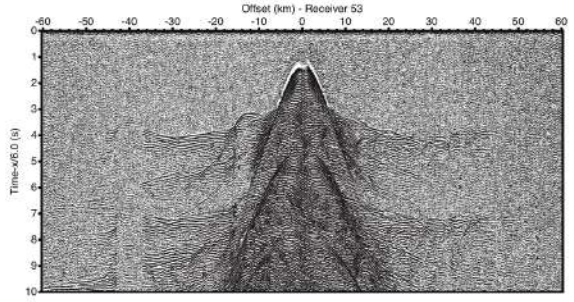
Offset (km) - Receiver 53
Time-x/6.0 (s)

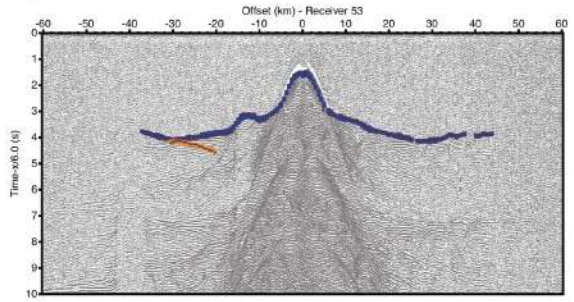
Offset (km) - Receiver 53
Time-x/6.0 (s)

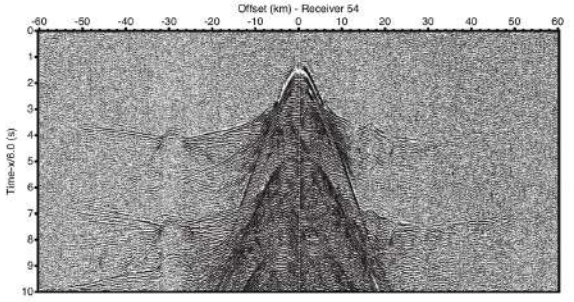
Offset (km) - Receiver 54
Time-x/6.0 (s)

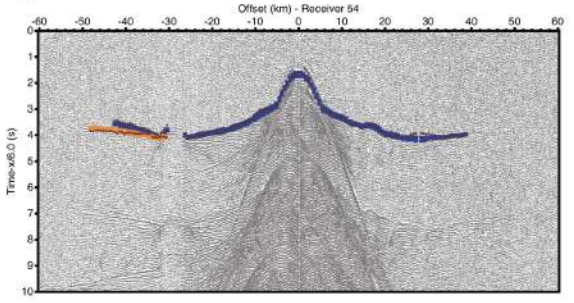
Offset (km) - Receiver 54
Time-x/6.0 (s)

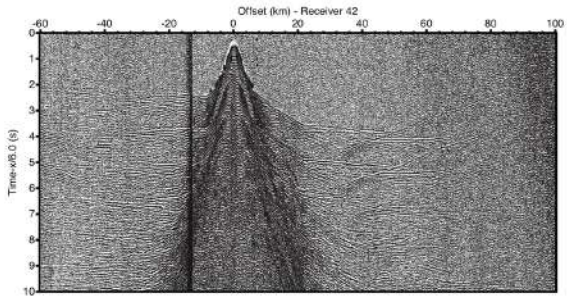
Offset (km) - Receiver 42
Time-x/6.0 (s)

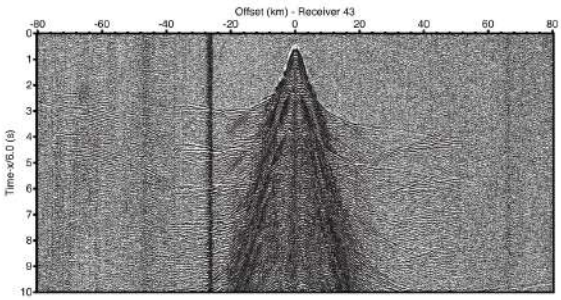
Offset (km) - Receiver 43
Time-x/6.0 (s)

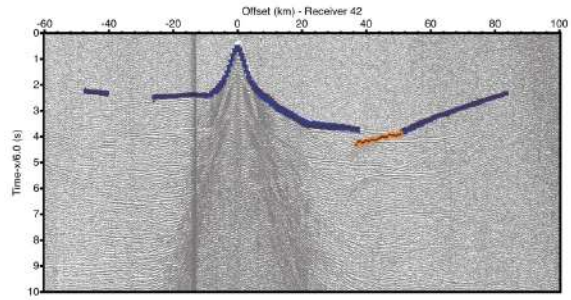
Offset (km) - Receiver 42
Time-x/6.0 (s)

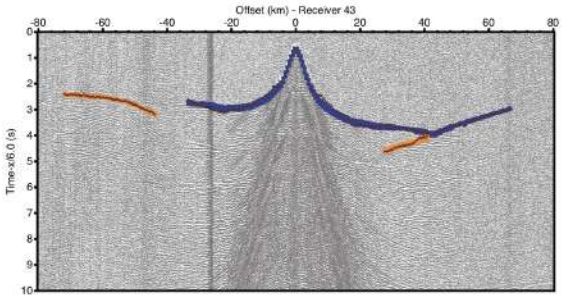
Offset (km) - Receiver 43
Time-x/6.0 (s)

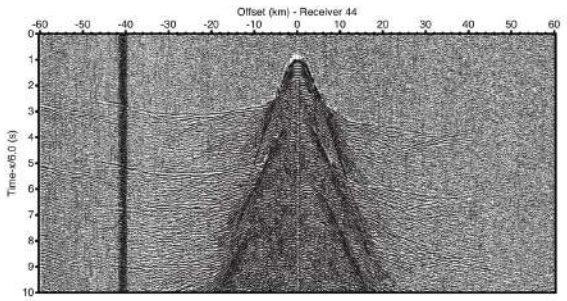
Offset (km) - Receiver 44
Time-x/6.0 (s)

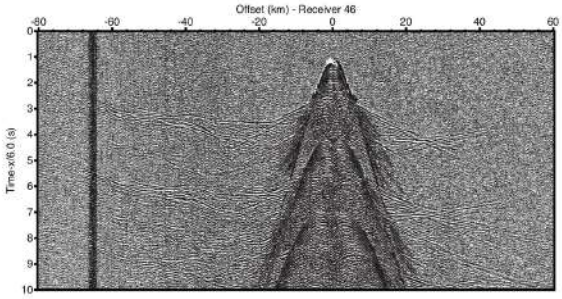
Offset (km) - Receiver 46
Time-x/6.0 (s)

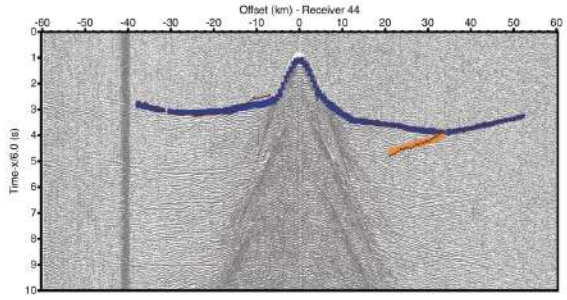
Offset (km) - Receiver 44
Time-x/6.0 (s)

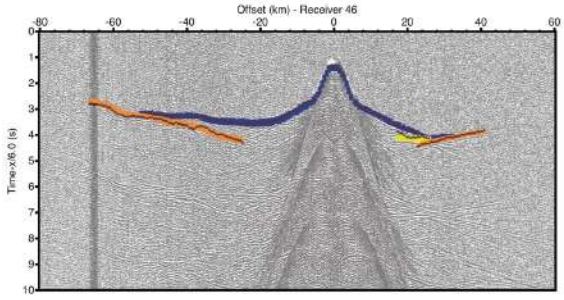
Offset (km) - Receiver 46
Time-x/6.0 (s)

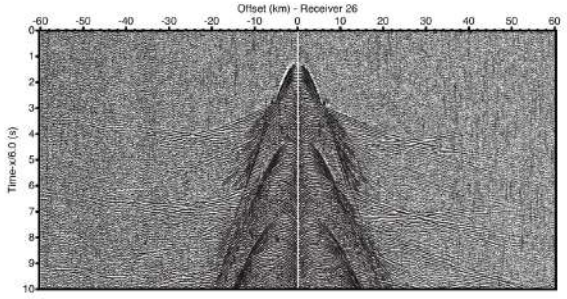
Offset (km) - Receiver 26
Time-x/6.0 (s)

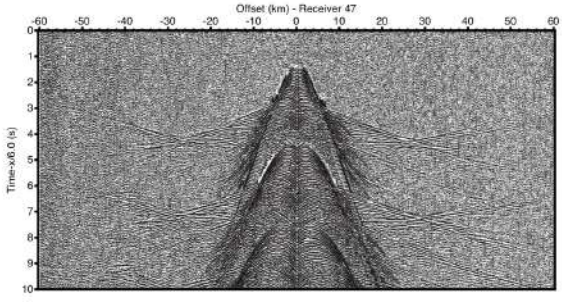
Offset (km) - Receiver 47
Time-x/6.0 (s)

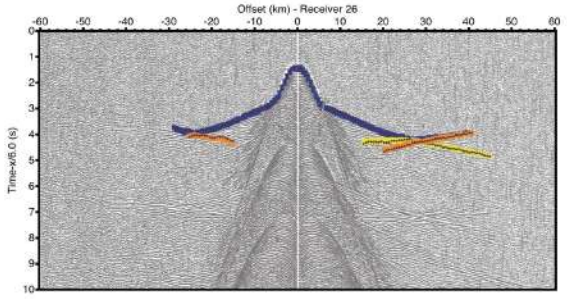
Offset (km) - Receiver 26
Time-x/6.0 (s)

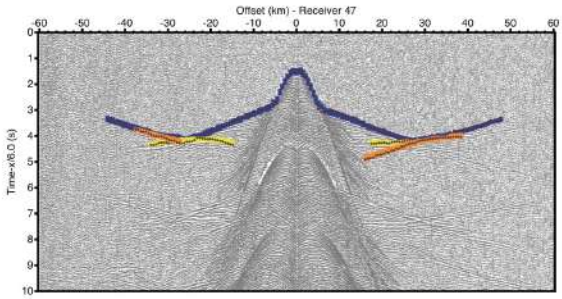
Offset (km) - Receiver 47
Time-x/6.0 (s)

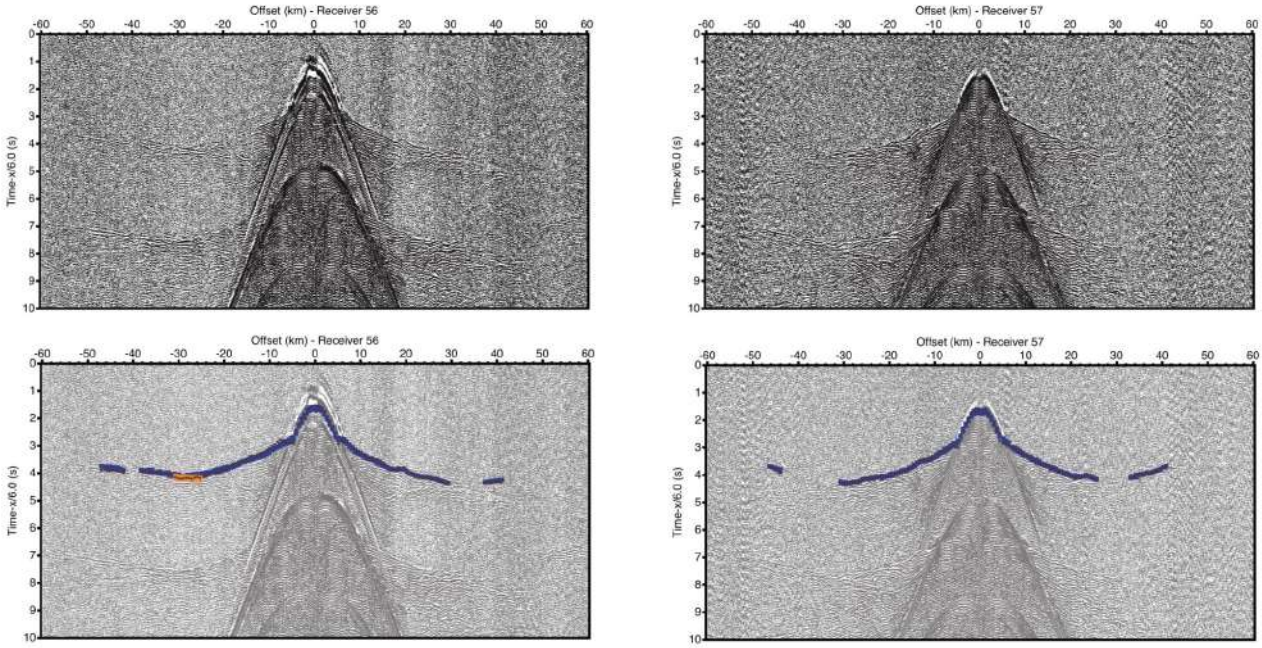
Offset (km) - Receiver 56
Offset (km) - Receiver 57
Offset (km) - Receiver 56
Offset (km) - Receiver 57
Time-x/6.0 (s)

A.5.1. Tagus Abyssal Plain modelling

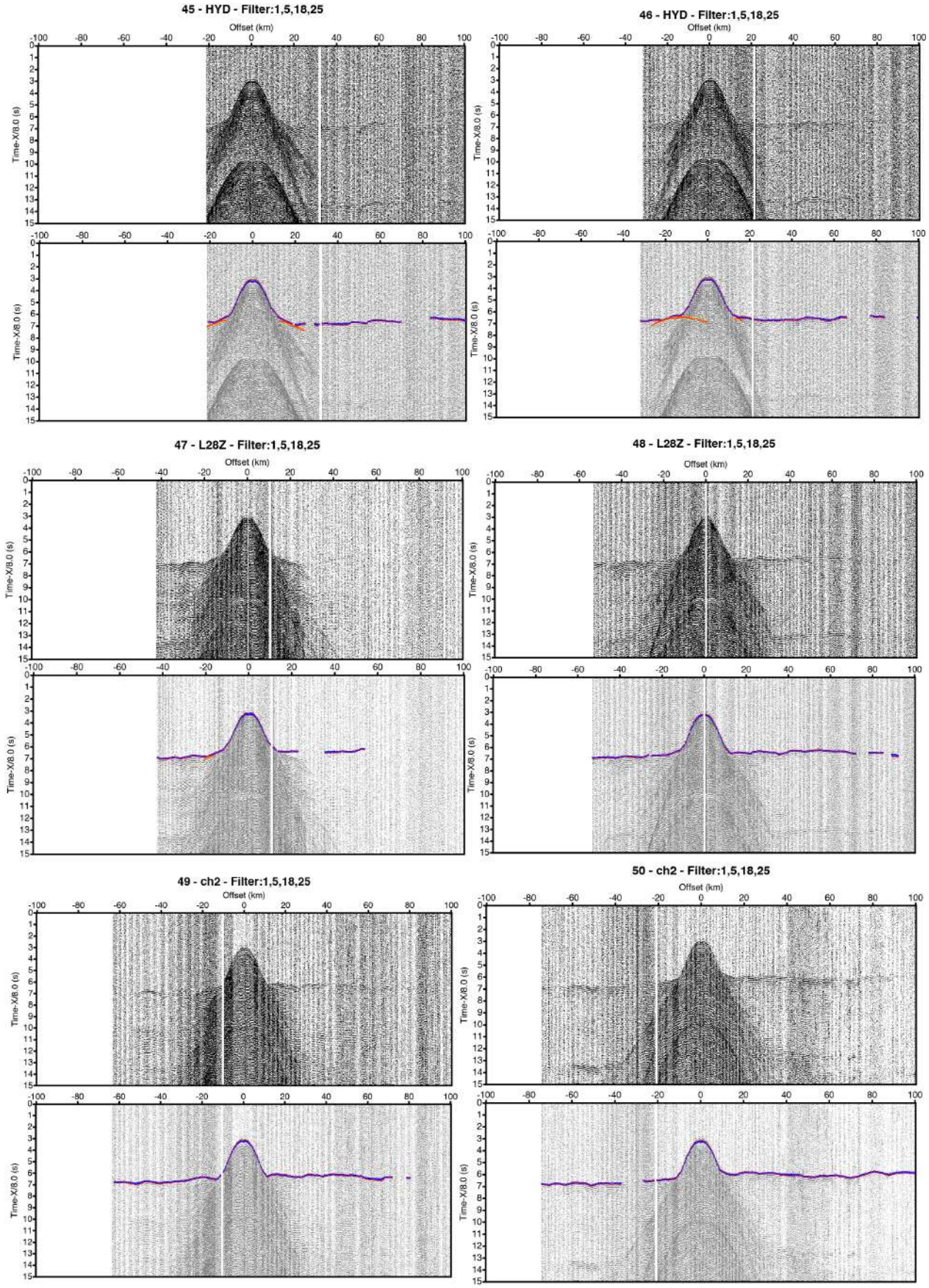
45 - HYD - Filter:1,5,18,25
46 - HYD - Filter:1,5,18,25
47 - L28Z - Filter:1,5,18,25
48 - L28Z - Filter:1,5,18,25
49 - ch2 - Filter:1,5,18,25
50 - ch2 - Filter:1,5,18,25
Offset (km)
Time-X/8.0 (s)

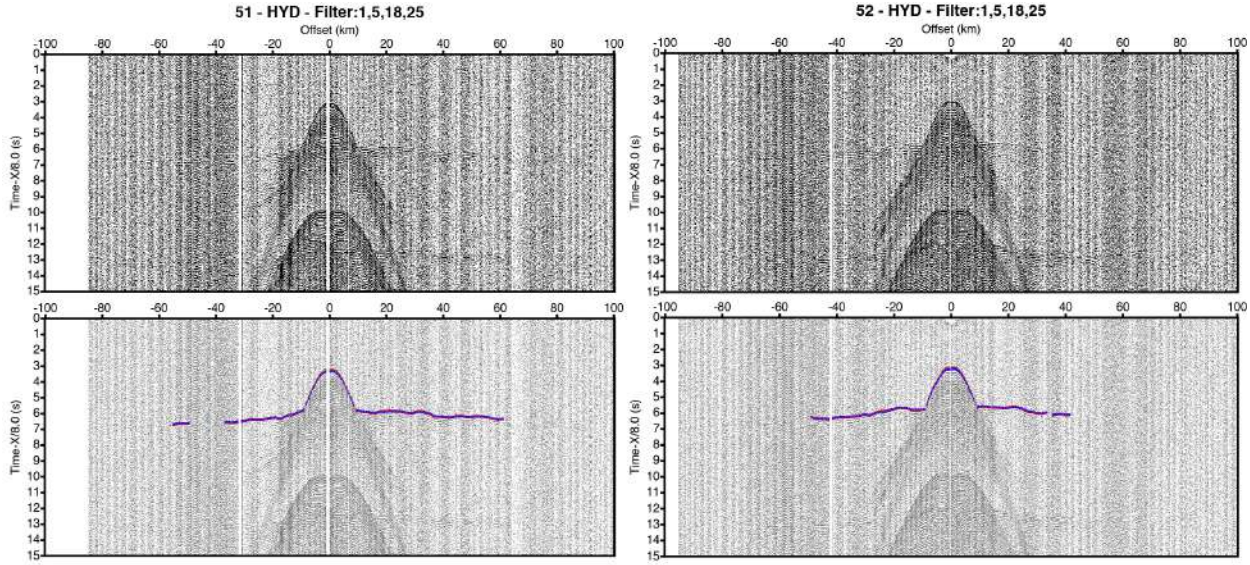
51 - HYD - Filter:1,5,18,25
Offset (km)
Time-X/8.0 (s)

52 - HYD - Filter:1,5,18,25
Offset (km)
Time-X/8.0 (s)

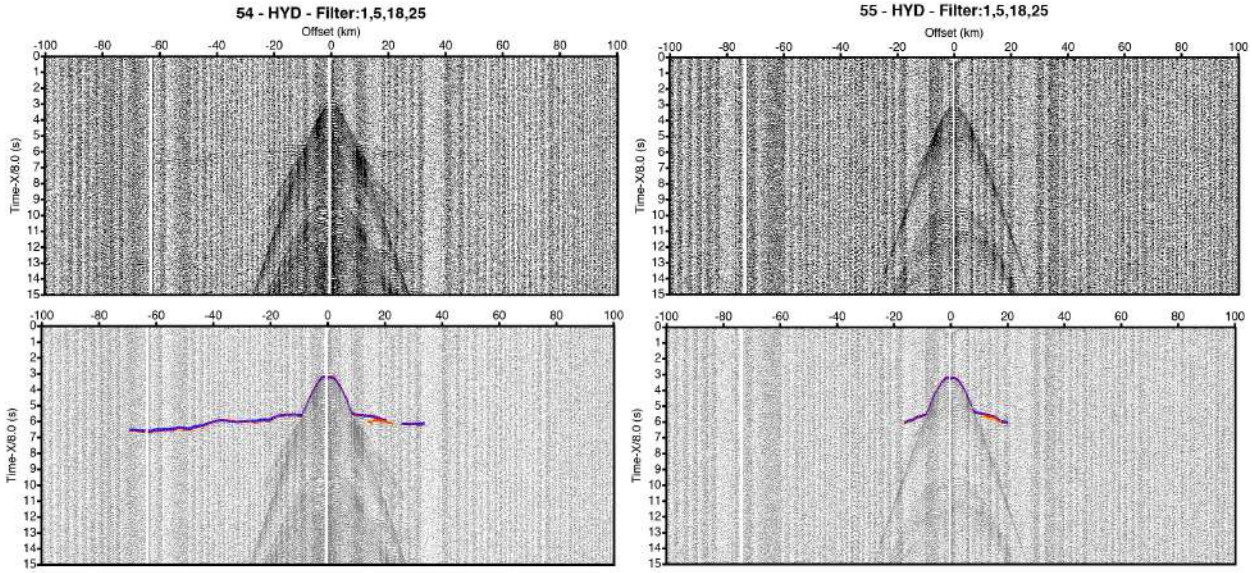
54 - HYD - Filter:1,5,18,25
Offset (km)
Time-X/8.0 (s)

55 - HYD - Filter:1,5,18,25
Offset (km)
Time-X/8.0 (s)

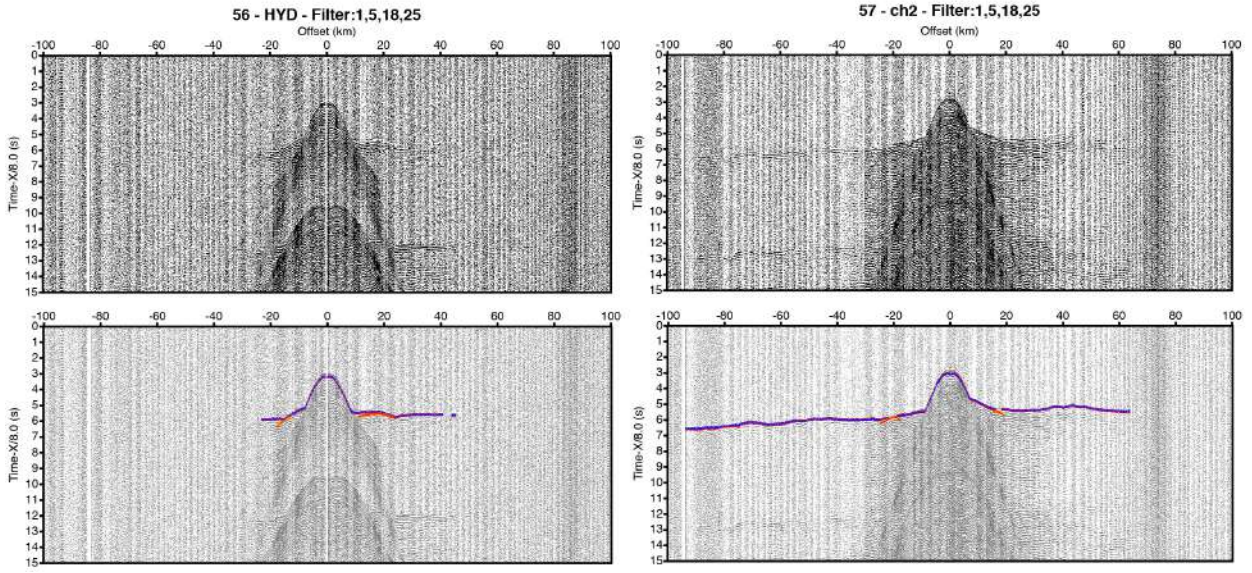
56 - HYD - Filter:1,5,18,25
Offset (km)
Time-X/8.0 (s)

57 - ch2 - Filter:1,5,18,25
Offset (km)
Time-X/8.0 (s)

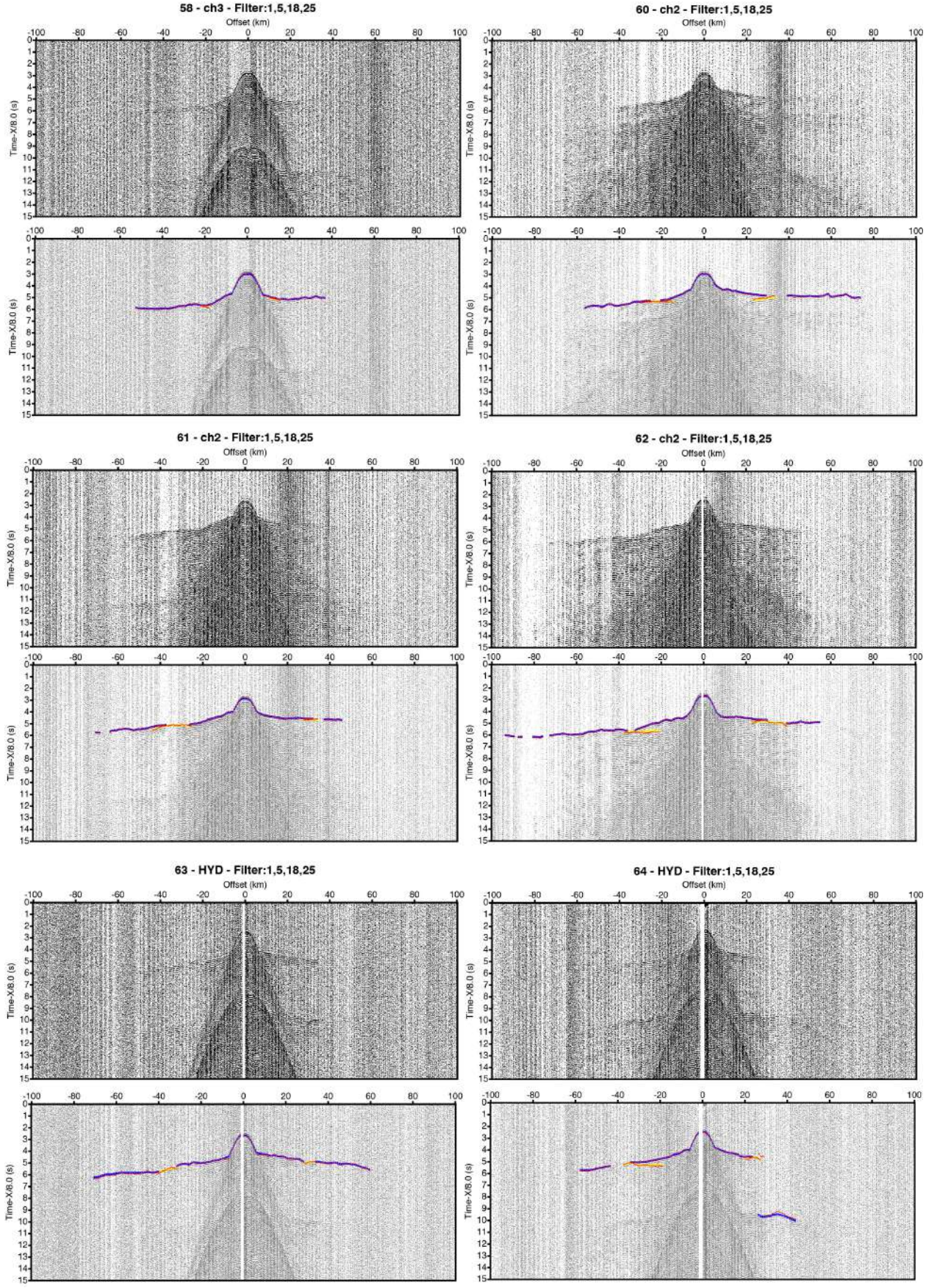
58 - ch3 - Filter:1,5,18,25
60 - ch2 - Filter:1,5,18,25
61 - ch2 - Filter:1,5,18,25
62 - ch2 - Filter:1,5,18,25
63 - HYD - Filter:1,5,18,25
64 - HYD - Filter:1,5,18,25
Offset (km)
Time-X/8.0 (s)

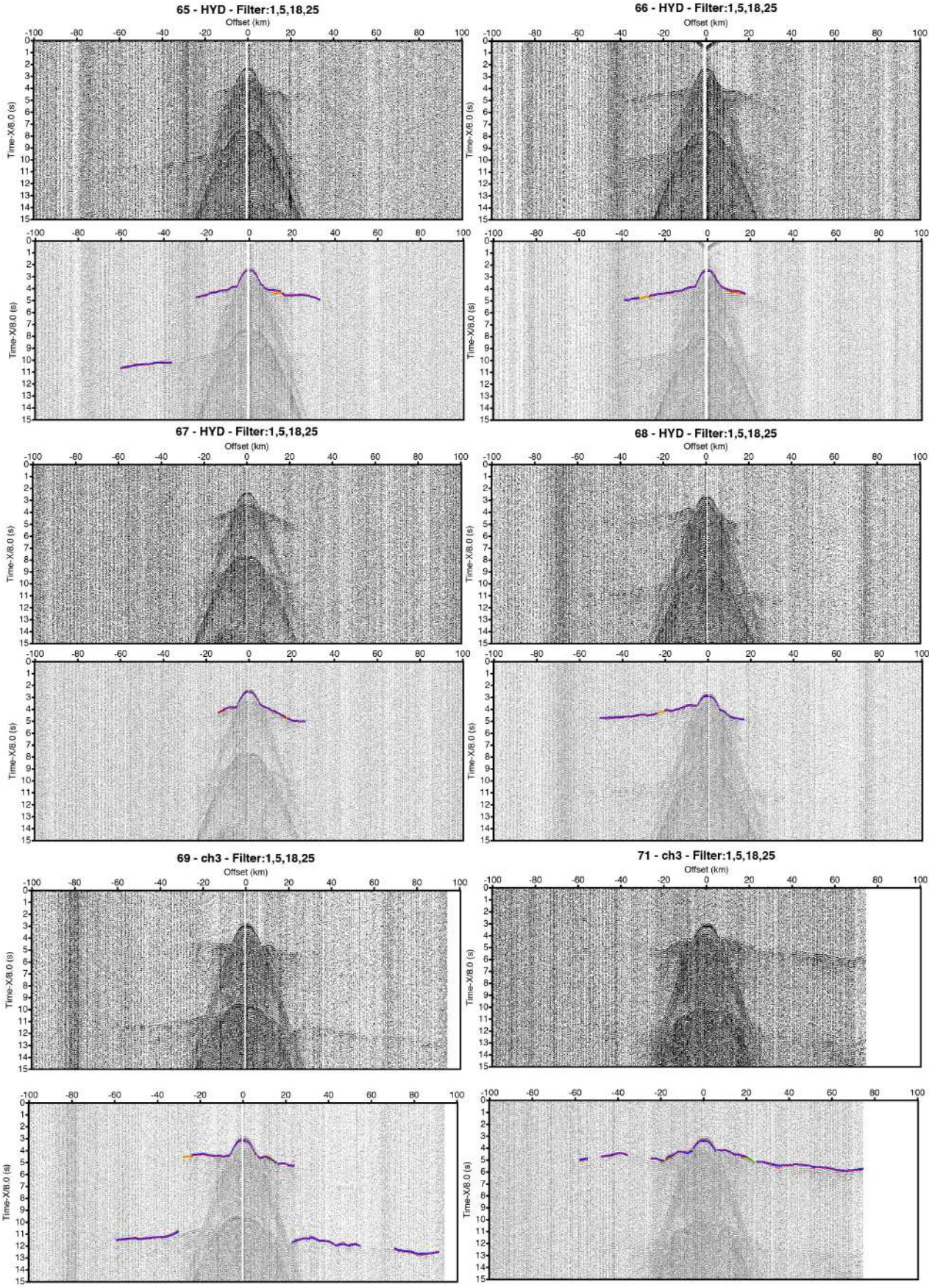
65 - HYD - Filter:1,5,18,25
66 - HYD - Filter:1,5,18,25
67 - HYD - Filter:1,5,18,25
68 - HYD - Filter:1,5,18,25
69 - ch3 - Filter:1,5,18,25
71 - ch3 - Filter:1,5,18,25
Offset (km)
Time-X/8.0 (s)

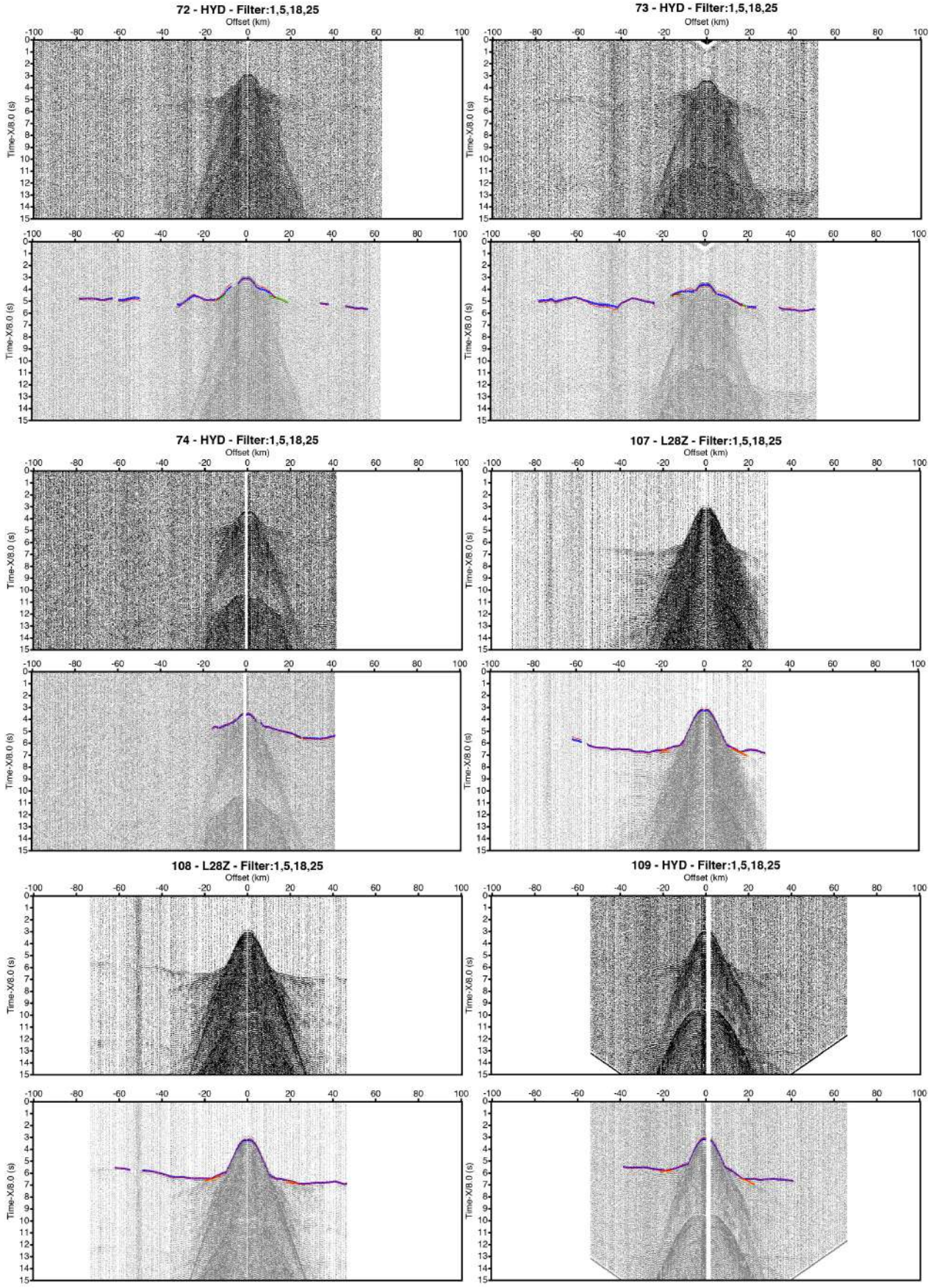
72 - HYD - Filter:1,5,18,25
73 - HYD - Filter:1,5,18,25
74 - HYD - Filter:1,5,18,25
107 - L28Z - Filter:1,5,18,25
108 - L28Z - Filter:1,5,18,25
109 - HYD - Filter:1,5,18,25
Offset (km)
Time-X/8.0 (s)

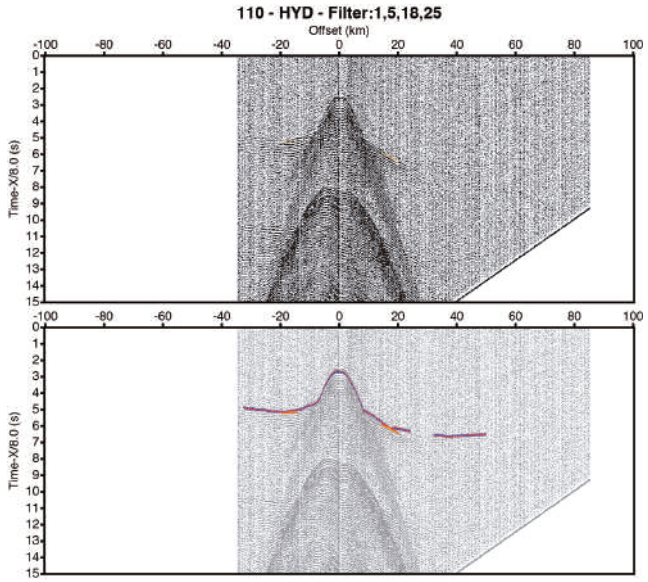
110 - HYD - Filter:1,5,18,25
Offset (km)
-100
-80
-60
-40
-20
0
20
40
60
80
100
Time-X/8.0 (s)
0
1
2
3
4
5
6
7
8
9
10
11
12
13
14
15

A.6. Multi-Channel Seismic (MCS) profiles

A.7. List of acronyms

AGC: Amplitude Gain Control
CDP: Common Depth Point
CMP: Common Mid-Point
CMQZ: Cretaceous Magnetic Quiet Zone
COT: Continent-Ocean Transition
DSDP: Deep Sea Drilling Project
ESP: Expanded Spread Profiles
FRAME: FoRmAtion of geological domains in the Western Iberian Margin and tectonic rEactivation of their limits
GO: Gorringe bank
GoL: Gulf of Lions
ICR: Intra Crustal Reflection
IMR: Intra Mantle Reflections
IAP: Iberia Abyssal Plain
Ifremer: Institut Français de Recherche pour l'Exploitation de la Mer
IODP: Integrated Ocean Discovery Program
JS: Josephine Seamount
MCS: Multi-Channel Seismic
Moho: Mohorovicic (crust – mantle boundary) discontinuity
NMO: Normal Move Out
OBH: Ocean Bottom Hydrophone
OBS: Ocean Bottom Seismometers
ODP: Ocean Drilling Programme
PIAB: Paleo Iberia-Africa Plate Boundary
r.m.s.: root mean squared
RV: Research Vessel
SDR: Seaward Dipping Reflectors
TAP: Tagus Abyssal Plain
TOB: Top Of the Basement
TT: Travel Time Tomography
TWT: Two-Way Travel-time
Vp: P-waves velocity
WAS: Wide-Angle Seismic